Receptivity & Transition in Boundary-Layers over Rigid & Compliant Surfaces

by

Reza Ali

A thesis submitted in partial fulfilment
of the requirements for the degree of
Doctor of Philosophy in Engineering

Supervisor: Professor P.W. Carpenter

University of Warwick, School of Engineering

October, 2003

Contents

Contents i

List of Figures xi

Acknowledgments xii

Declaration xiii

Abstract

1 Introduction 1

2 Boundary-Layer Receptivity 7

2.1 Forced & Natural Receptivity 7

2.1.1 Experimental Investigations 9

2.1.2 Theoretical & Numerical Investigations 11

2.2 Freestream Turbulence & Other Studies 13

2.3 Effect of Particulates on Receptivity Mechanisms 17

2.4 Effect of Surface Imperfections on Receptivity 21

3 Computational Model 23

3.1 Velocity-Vorticity (DNS) Formulation 24

3.1.1 Governing Equations 25

3.1.2 Boundary Conditions 27

3.1.3 Wall-normal co-ordinate mapping 29
3.1.4 Compliant Surface 30
3.2 Numerical Methods 32
3.2.1 Spatial & Spectral Discretisation 32
3.2.2 Temporal Discretisation 33
3.2.3 Numerical Treatment of Compliant Wall 33
3.3 Prescribed Velocity Profiles 36
3.3.1 Blasius Profile 36
3.3.2 Turbulent Velocity Profile 38
3.4 Code Validation 40

4 Klebanoff Mode Receptivity over Rigid & Compliant Surfaces 48
4.1 Particulate-Induced Receptivity 49
4.1.1 Excitation by Body Forces 49
4.1.2 Form of the Body Force 51
4.1.3 Streaky Structures over Rigid Surfaces (Code Validation) 53
4.2 Streaky Structures over Compliant Surfaces 59
4.2.1 A brief note on the selection of compliant wall properties 59
4.2.2 Development of Streaks over Compliant Surfaces 60
4.2.3 The Evolution of Streaks over Compliant Panels 68
4.2.4 Orthotropic Surfaces 85
4.2.5 A Brief Note on the Effects of Wall Damping 91
4.3 Chapter Summary 94

5 Effect of Wall Compliance on Near-Wall (Streaky) Structures in Turbulent Flow 96
5.1 Effects of Wall Compliance on Turbulence 97
5.2 Code Validation 101
5.2.1 A brief note on the modelling approach 101
5.2.2 Streaky Structures over Rigid Surfaces 103

5.3 Streaky Structures over Compliant Surfaces 108
5.3.1 Development of Near-Wall Structures over Compliant Surfaces . 108
5.3.2 Development of Near-Wall Structures over Compliant Panels . . 124
5.3.3 Effect of Orthotropicity 131
5.4 Chapter Summary 133

6 Effect of Surface Roughness over Rigid & Compliant Surfaces 135
6.1 Surface Roughness Receptivity 136
6.2 Wavy-wall formulation 139
6.3 Effect of Surface Roughness over Rigid Surfaces 142
6.3.1 Validation 142
6.4 Hydrodynamic Effects of Roughness over Compliant Walls 148
6.4.1 The Structure of Dolphin Skin 148
6.4.2 Hydrodynamic Effects 151
6.4.3 A Brief Note on the Hydrodynamic Significance of Cutaneous Ridges 162
6.4.4 Compliant Panels 162
6.4.5 A brief note on the effect of damping & orthotropicity 173
6.5 Chapter Summary 175

7 Conclusions & Recommendations for Future Work 177
7.1 Conclusions 177
7.2 Recommendations for Future Research 182
7.2.1 Computational Study 182
7.2.2 Experimental Study 183

A Effect of Particulates on Receptivity over Rigid & Compliant Surfaces 186
A.1 Particle Dynamics 187
A.2 Effect of a Moving Particle 195
A.3 Particle Interaction in a Boundary Layer 203

A.4 Summary 210

Bibliography **212**

List of Figures

1.1 Annotated diagram of flow over flat plate 2

2.1 Flow visualisation and decsription of (a). surface mounted and (b). elevated spheres in a boundary layer. 19

3.1 Adopted co-ordinate system. 25
3.2 Compliant surface modelled as plate-spring model 30
3.3 Mean flow profile as generated by the Blasius solver. 37
3.4 The inner regions of the turbulent boundary layer. 39
3.5 The full turbulent boundary layer. 39
3.6 Evolution of a Tollmien-Schlichting (T/S) wavepacket with time. 41
3.7 Comparison of normalised velocity profiles for a three-dimensional T/S wave calculated by linear theory and with our code over rigid surface. . 42
3.8 Variation of streamwise wavenumber α_r with streamwise location. . . . 43
3.9 Variation of two-dimensional growth rate, α_i, as a function of frequency over a compliant surface. 46
3.10 Neutral stability curve for a Blasius boundary-layer over a compliant surface (local parallel flow assumption). 47

4.1 Bodyforce simulation schematic. 50
4.2 Spanwise perturbation velocity contours at t=1000 over a rigid surface. 54
4.3 Streamwise velocity contours: Evolution of 'streaky structures' with time, t over a rigid surface. 55

4.4 Amplitude, maximum streak velocity, $|u|_{max}$, as a function time, t for R=1000. 56
4.5 Amplitude, maximum streak velocity, $|u|_{max}$, as a function of the spanwise wavenumber, β, for R=1000. 57
4.6 Streamwise velocity contours: Evolution of 'streaky structure' with time over a Kramer-type, wholly compliant surface. 61
4.7 Spanwise perturbation velocity contours and variation of u at t=1000 over (a) rigid surface, and a Kramer type (b) compliant surface. 63
4.8 Amplitude, maximum streak velocity, $|u|_{max}$, as a function of the spanwise wavenumber, β, over a rigid (a) & compliant surface (b). 64
4.9 Amplitude, maximum streak velocity, $|u|_{max}$, as a function of the spanwise wavenumber, β, over compliant surfaces of increasing flexibility at R=1000. 65
4.10 Spanwise wavenumber streak bearing limits, (β) as a function of the Reynolds number, R, for a wholly compliant surface. 66
4.11 Receptivity Coefficient (ReC) as a function of spanwise wavenumber, β, over compliant surfaces of increasing flexibility. 69
4.12 Embedded Compliant Panel 70
4.13 Spanwise perturbation velocity contours at t=1000 over (a) rigid surface, and Kramer type (b) wholly and (c) embedded compliant surfaces. . . . 72
4.14 Streamwise perturbation velocity contours, (a), and variation of u in the streamwise (b), and spanwise (c), directions for a streak generated over an embedded, Kramer-type, compliant panel at t=1000. 73
4.15 Receptivity Coefficient (ReC) as a function spanwise wavenumber, β, for embedded and wholly compliant surfaces of increasing flexibility. . . 74
4.16 Streamwise velocity contours: Evolution of 'streaky structure' with time over a Kramer-type, wholly compliant surface. 77

4.17 Amplitude, maximum streak velocity, $|u|_{max}$, as a function of the spanwise wavenumber, β, over a rigid (a) and compliant surface, (b), and panel (c) respectively. 78
4.18 Spanwise number streak bearing limits, (β) as a function of the Reynolds number, R, for compliant (a) surface and (b) panel. 79
4.19 Amplitude, maximum streak velocity, $|u|_{max}$, as a function of the spanwise wavenumber, β, over wholly and embedded compliant surface of increasing flexibility. 80
4.20 Receptivity Coefficient (ReC) as a function of spanwise wavenumber, β, over compliant surfaces (a), and panels (b) of increasing flexibility. . . . 82
4.21 Streamwise variation of energy components over a compliant panel. . . 84
4.22 Growth rates, ($-\alpha_i$) as a function of frequency, (W) for T/S waves generated over an orthotropic compliant surface. 87
4.23 Trace of near-wall structures and growth rate over a Kramer-type compliant surface with varying orthotropicity. 89
4.24 Amplitude of maximum streak velocity, $|u|_{max}$, as a function of the spanwise wavenumber, β, over wholly Kramer-type orthotropic and isotropic compliant surfaces. 90

5.1 Physical mechanism of near-wall structures in the transitional boundary layer. 98
5.2 Low-speed streaks in (a) rigid surface (z^+=51) and (b) compliant surface flat-plate turbulent boundary layer (z^+=49). 99
5.3 Amplitude, maximum streak velocity, $|u|_{max}$, as a function time, t^+ for R=1000. 104
5.4 Optimum spanwise wavelength, λ^+_{opt} as a function of the normal distance from the wall. 105
5.5 Maximum streak velocity, $|u_{max}|$, as a function of the spanwise wavelength of the body force, λ^+. 105

5.6 Spanwise perturbation velocity contours at t^+=50 over a rigid surface. . 106
5.7 Streamwise velocity contours: Evolution of 'streaky structures' with time, t^+ over a rigid surface. 107
5.8 Streamwise velocity contours: Evolution of 'streaky structures' with time, t^+ over a compliant surface with Lee-type properties. 110
5.9 Spanwise perturbation velocity contours at t^+=50 over (a) rigid surface and (b) compliant surface with Lee type properties. 111
5.10 Optimum streamwise streak spacing, λ^+_{opt} as a function of Reynolds number, R for Lee and Kramer-type surfaces. 112
5.11 Maximum streak velocity, u_{max}, as a function of the optimum spanwise wavelength of the body force, λ^+_{opt} for rigid and (Kramer-type) compliant surface. 113
5.12 Optimum streamwise streak spacing, λ^+_{opt} as a function of Reynolds number, R. 114
5.13 Maximum streak velocity, u_{max}, as a function of the optimum streamwise streak spacing, λ^+_{opt}. 115
5.14 Streamwise velocity contours at t^+=50 over (a) Lee *et al.* type and (b) Kramer-type surface. 117
5.15 Streamwise variation of energy components over a compliant surface. . 120
5.16 Reynolds stress, (Rs) as a function of wall-height, z/δ for different Reynolds numbers, R over a rigid surface. 121
5.17 Reynolds stress, (Rs) as a function of wall-height, z/δ for different Reynolds numbers, R over compliant surfaces. 122
5.18 Reynolds stress, (Rs) as a function of wall-height, z/δ for different Reynolds numbers, R over compliant surfaces with Choi properties . . . 123
5.19 Development of near-wall structure in a turbulent boundary layer over a Lee *et al.*-type compliant panel. 125
5.20 Streamwise variation of energy components over a compliant panel. . . 127

5.21 Reynolds Stress, (Rs) as a function of wall-height, z/δ for R=1348 over (a) compliant surfaces and (b) compliant panel. 128
5.22 Maximum streak velocity, $|u|_{max}$, as a function of the optimum streamwise streak spacing, λ^+_{opt}. 130
5.23 Maximum streak velocity, $|u|_{max}$, as a function of the optimum streamwise streak spacing, λ^+_{opt} over a Kramer-type compliant surface with varying orthotropicity. 132

6.1 Schematic of flow over a rough (wavy) wall. 137
6.2 Rough (wavy) wall simulation schematic. d is the spacing between the peaks; λ_S is the wavelength; and k, the roughness amplitude. 140
6.3 Neutral Stability Curves for surfaces of varying roughness over a rigid wall. 143
6.4 T/S wave development over smooth and wavy surfaces. 144
6.5 Growth rate of a T/S as a function of frequency f, over a surface with a fixed roughness height and varying wavelength. 146
6.6 T/S wave growth rate as a function of the roughness aspect ratio, AR over surfaces in the absence of compliance. 147
6.7 Cross-sectional view of dolphin skin. 149
6.8 Dolphin Skin Structure. 150
6.9 Neutral Stability Curves for surfaces of varying roughness over (a) compliant and (b) rigid walls. 153
6.10 Contour and velocity traces of T/S wave over a compliant surface with an imposed waviness of k=0.21mm for (a) R=750, (b) R=904 and (c) R=1100. 154
6.11 Growth of T/S wave over smooth and wavy surfaces over a rigid, (a), and compliance, (b), wall as a function of the spanwise (body forcing) wavenumber. 155

6.12 Growth rate as a function of the roughness aspect ratio, AR, for compliant and rigid surfaces. 158
6.13 Growth rate as a function of the frequency for surfaces of increasing compliance. 159
6.14 Neutral Stability Curves for a surfaces of varying compliance with a waviness of k^*=18.9. 160
6.15 Growth rate as a function of the roughness aspect ratio, AR, for surfaces of varying compliance. 161
6.16 Development of T/S wave over a compliant surface with cutaneous ridge geometry. 163
6.17 Growth rate as a function of frequency, f for surfaces of varying wavelength. 164
6.18 Waviness (roughness) imposed compliant panel test case under study. . 165
6.19 Neutral Stability Curves for surfaces of varying geometeries over a compliant panel. 167
6.20 Trace of the disturbance enstrophy, (a), and kinetic energy, (b), for a T/S travelling over a compliant panel. 168
6.21 Growth rate as a function of the roughness aspect ratio, AR, for surfaces of varying compliance. 169
6.22 Streamwise variation of energy components over a wavy and smooth compliant panel. 172

A.1 Drag coefficient of sphere as a function of the Reynolds Number 190
A.2 Temporal evolution of disturbances generated by a travelling, oscillating, particle unaffected by the boundary layer over a rigid wall. 197
A.3 Evolution of T/S and pseudo-particle wavepackets over a rigid and compliant wall. 198
A.4 Temporal evolution of disturbances generated by a travelling, oscillating, particle unaffected by the boundary layer over a compliant wall. 200

A.5 Variation of wall enstrophy with time for the particle-induced T/S disturbance over rigid and compliant surfaces. 201
A.6 Temporal evolution of wall-wavepacket over a compliant panel generated by a travelling, oscillating, psuedo-particle that is unaffected by the boundary layer 203
A.7 Temporal evolution of T/S wavepacket over a rigid and compliant wall generated by a travelling, oscillating, puesdo-particle interacting with the boundary layer 204
A.8 Evolution of T/S awavepackets, generated by an interactive and non-interactive particle in the presence and absence of compliance 205
A.9 Neutral-Stability Curves for particle-induced T/S disturbance over rigid and compliant surfaces. 206
A.10 Variation of wall enstrophy with time for the particle-induced T/S disturbance over rigid and compliant surfaces. 208

Acknowledgments

I would like to thank everyone that has helped me at Warwick. In particular, special thanks go to my supervisor and friend Peter Carpenter for his constant support, patience and generous supervision. Many thanks, I would not have come this far without your help, encouragement and loan of some very eclectic vinyl records! I'd also like to thank Chris Davies at Cardiff University, Duncan Lockerby at King's College, London, Peter Thomas at Warwick University and Tony Lucey at Curtin University, Australia for their help and advice.

I have been fortunate to have met and had the support from some very valued friends at Warwick. I am immensely indebted to my oldest and closest and longest suffering housemates(!) and friends: Alex (M.S.S.) and Pascal, who have been there right from the start during the MRes days. Thanks guys, you are the greatest and I have been very privileged to have lived through all our colourful ups and downs together! A big hello to Jason '(Dr.) D.J. K', Rai, Duncan and Gianni+Helen, who have in their own unique way, added to make my time here so enjoyable. To this, a special thanks to Karen for making perfect cups of tea and putting up with me before nine in the office and Rich for the occassional run- you never know, some day we might get the chance to run a marathon together! I'm certain our close friendships will continue and we'll all meet up soon, maybe even at the Royal Bengal for a ruby...

This thesis wouldn't be complete without special mention for the original occupants of the infamous Room F106*b*, namely Laney, Farzam, Zinedine and Martin. Good luck to Ross, Yan and Mark. Also, from my time at Reading University I'd particularly like to thank John Burton, Caroline Ellick, Hugh Campbell-Lendrum, Richard George and Jill+the little ones (Julliette+Julia). Finally, a very big thank you to my family.

Reza, Coventry, June 2003

This study was sponsored by *QinetiQ*, formerly the United Kingdom *Defence & Evaluation Research Agency*, Farnborough, whose support is gratefully acknowledged.

Declaration

This thesis, and the material in it, is my own work. It has not been submitted for a degree at any other university.

The following articles have been published, or in the progress of submission as a result of the work contained within this thesis:

Ali, R. & Carpenter, P.W. 2001 Klebanoff modes in Boundary-Layers over Compliant Surfaces. *Bull. Amer. Phys. Soc.* **46**(10),29.

Cros. A., Ali, R., LeGal, P., Thomas, P. J., Schouveiler, L., Carpenter, P. W., Chauve, M. P. & Davies, C. 2001 Transition of torsional Couette flow between a compliant rotating disc and a stationary rigid wall. in abstract volume for *IUTAM Symp, on Flow in Collapsible Tubes and Past Other Highly Compliant Boundaries*, 26-30th March, 2001, University of Warwick, Coventry, U.K.

Ali, R. & Carpenter, P.W. 2002 Dolphins & wavy surfaces: The hydrodynamic effects of cutaneous ridges. In abstract volume for *Biomimetics 7 Meeting: Achievements & future challenges*, 20th September, 2002, Centre for Biomimetics, University of Reading, Reading, U.K.

Ali, R. & Carpenter, P.W. 2002 Klebanoff modes in Boundary-Layers over Compliant Surfaces. *Bull. Amer. Phys. Soc.* **47**(10),52.

Thomas, P. J., Cros. A., Ali, R., LeGal, P., Schouveiler, L., Carpenter, P. W. & Chauve, M. P. 2002 Experiments on the Influence of Wall Compliance on the Laminar-Turbulent Transition of Torsional Couette Flow. *Bull. Amer. Phys. Soc.* **47**(10),137.

Zoueshtiagh, F., Ali, R., Colley, A. J., Thomas, P. J. & Carpenter, P. W. 2003 Laminar-Turbulent Boundary-Layer Transition over a Rough Rotating Disc. *Phys. Fluids.* **15**(8),2441.

Cros. A., Ali, R., LeGal, P., Thomas, P. J., Schouveiler, L., Carpenter, P. W. & Chauve, M. P. 2003 Effects of Wall Compliance on the Laminar-Turbulent Transition of Torsional Couette Flow. *J. Fluid Mech.* **481**, 177.

Thomas, P. J., Zoueshtiagh, F., Ali, R. & Carpenter, P. W. 2003 Boundary-Layer Transition over a Rough Rotating Disc. In abstract volume for *The 5th EUROMECH Fluid Mechanics Conference*, 24-28th August, Toulouse, France. pp.394

Carpenter, P. W., Ali, R., Davies, C. & Lockerby, D. A. 2003 A Simple Computational

Model for Studying the Control of Near-Wall Structures in Turbulent Boundary Layers. In abstract volume for *The 5th EUROMECH Fluid Mechanics Conference*, 24-28th August, Toulouse, France. pp.367

THOMAS, P. J., COLLEY, A. J., CARPENTER, P. W., ALI, R. & ZOUESHTIAGH, F. 2003 Measurement of Type-II-eigenmode destabilisation in boundary-layer transition over a rotating, compliant rotating disk. *Accepted for publication in Amer. Phys. Soc. 2004 Fluid Dynamics Division Meeting, New York.*

COLLEY, A. J., CARPENTER, P. W., THOMAS, P. J., ALI, R. & ZOUESHTIAGH, F. 2003 Experimental verification of Type-II-eigenmode destabilisation in boundary-layer transition over a compliant rotating disk. *Submitted for publication in J. Fluid Mech.*

ALI, R. & CARPENTER, P. W. 2003 Receptivity & transition in boundary layers over rigid and compliant walls. Tech. Report: 03/2, University of Warwick, Coventry, U.K.

Abstract

The generation of freestream turbulence by minute particulates and surface roughness over compliant walls in flat-plate, laminar and turbulent boundary layers is numerically investigated. The findings fill the gap in knowledge concerning the effect of such disturbances and are important for the development of compliant walls for marine applications.

The three-dimensional, boundary-layer disturbances, are modelled using a mixed spectral/ finite-difference, velocity-vorticity formulation of the Navier-Stokes equations. The compliant wall is modelled using a plate-spring model, where the displacement of the surface is restricted to the vertical direction. The fluid and wall codes are interactively coupled and numerical stability is achieved by combining the inertia terms together. The integrity of the code for rigid and compliant walls was demonstrated through the generation of Tollmien-Schlichting (T/S) waves. The particles were modelled as both stationary and moving body force(s), and roughness modelled spectrally as a wavy surface. The findings highlight favourable effects of wall-compliance. Both compliant walls, stretching across the entire domain, and a finite compliant panel embedded in a rigid wall were investigated. With regards to the latter, it was observed that, in general, the joins did not exert any additional adverse effects on the particle- and roughness-induced phenomena, and those that were induced could be easily controlled.

Klebanoff modes, which manifest themselves as streaky structures, were simulated in a laminar boundary layer, generated by a single stationary body force. The model was extended to show the development of similar near-wall structures in a turbulent boundary layer, providing for the first time quantitative agreement with experimental studies. The findings suggest compliant walls are less susceptible to bypass transition. The simulations also provide a possible explanation for observation of skin-friction drag reductions. A simple model describing the behaviour of moving particles, demonstrated local suppression of induced perturbations at the wall and revealed the faster-growing disturbance travelling with the particle.

Over rough surfaces, an oscillating body force was used as a T/S driver and the stability of the subsequent wave explored. In general, compliance has a stabilising effect, which is reduced as amplitude of the waviness is increased. The model was extended to ascertain the hydrodynamic effects of the minute cutaneous ridges observed over dolphin skin.

Chapter 1

Introduction

It is now widely accepted that compliant surfaces can be employed to postpone transition. The main concern in the present work is to bridge an important gap in the knowledge concerning the effects of compliant (and rigid) surfaces on *receptivity* mechanisms. In particular, the generation of freestream turbulence by vorticity, generated by suspension of minute particles, and rough(wavy) surfaces. Such concerns are pertinent to the development of compliant walls for practical use in marine applications. This chapter will serve as a brief introduction to the facets of this work.

Investigations to assess the capability of compliant surfaces to produce drag reduction were inspired by dolphins. Gray (1936) calculated that the dolphin was able to maintain anomalously high swimming speeds. He commented that its muscles would have to deliver as much as seven times more power per unit mass than any other mammalian muscle to achieve a swimming speed of 9m/s! This led Gray to conclude that somehow the dolphin must be capable of maintaining laminar flow, the so-called *Gray's Paradox*. Later, Kramer (1957, 1960a,b, 1962, 1965) conducted a series of experiments in which he covered solid bodies of revolution with rubber coatings which he believed at the time were representative of dolphin skin. We now know that his understanding of dolphin skin morphology was incorrect and that his surfaces did not quite replicate certain aspects of dolphin skin (Babenko & Surkina 1969; Carpenter *et al.* 2000). Kramer towed his bodies at high speed through sea-water and claimed considerable

drag reductions.

It is universally accepted that for low noise levels found in free flight and in natural marine environments, the boundary-layer can be divided into three regions (Figure 1.1). The initial laminar region is followed by a transitional region. This is composed of an initial localised receptivity or disturbance stage, followed by slow, exponential, downstream growth of the generated two-dimensional instability or Tollmien-Schlichting (T/S) wave. As soon as the wave reaches certain threshold amplitudes they assume three-dimensional spanwise periodic structures, i.e. non-linear effects set in. The three-dimensional disturbances grow rapidly to large amplitudes which triggers breakdown to 'random' turbulence. The amplification of T/S waves accounts for up to 80% transition process. (Other laminar-turbulent transition scenarios exist which will be described where relevant.)

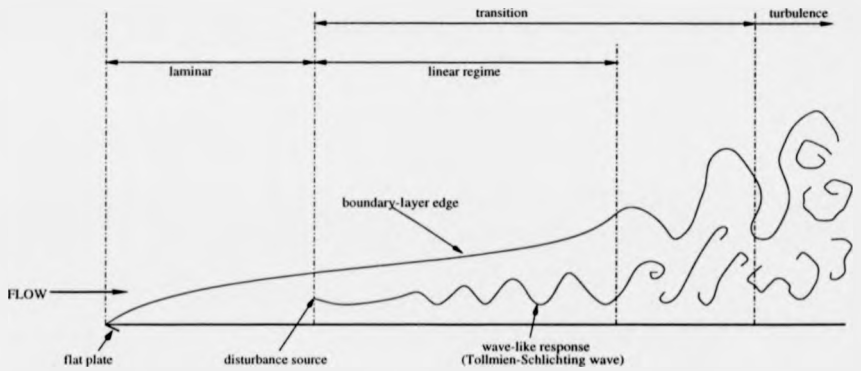

Figure 1.1: Annotated diagram of flow over flat plate

Kramer concluded that his coatings were able to postpone transition by suppressing the growth of small-amplitude T/S waves. However, theoretical studies by Benjamin (1960, 1963) and Landhal (1962) showed that whilst wall compliance could indeed suppress T/S growth, it was also possible to invoke flow-induced surface instabilities (FISI), which may limit or destroy any advantages gained from T/S stabilisation. It

was also shown that the inclusion of damping in the compliant coating would generate a destabilising effect on T/S waves, in direct opposition to Kramer's hypothesis. As a result of this, and the fact that experimentalists could not replicate Kramer's results, enthusiam died out as few believed in the worthwhile transition benefits obtainable from such coatings.

A theoretical investigation into Kramer's coating by Carpenter & Garrad (1985,1986) re-ignited the current interest in compliant surfaces. They noted that virtually no attempt had been made to model Kramer's coatings theoretically. Although the Benjamin and Landhal studies had indicated that T/S stabilisation was possible, they made no attempt to model Kramer's compliant coatings theoretically. What's more, most of the previous experiments had been conducted in a manner which would have been unlikely to test Kramer's concepts properly. Carpenter and Garrad modelled the coatings as a plate-spring model- essentially plates supported on a spring foundation with the effects of visco-elastic damping included. They showed that, in theory, substantial transition delay could be obtained from most of Kramer's coatings.

A series of experiments conducted by Gaster (1987) confirmed that reductions in T/S growth rates could be achieved. Gaster and his co-workers towed a relatively simple compliant panel embedded into a flat plate through a low-noise towing-tank facility. Their compliant coating was much simpler than the Kramer coatings. It was softer and consisted of two layers with a plate-like outer layer enclosing a softer layer. Good agreement between the measured growth and that predicted by a suitably modified linear stability theory was observed and represented the first laboratory observation that stabilisation of T/S waves leading to transition delay was possible with compliant coatings. Since then a large number of theoretical, numerical and experimental studies have shown that optimised compliant surfaces can be used to obtain significant transition delays, and highlighted the rich and complex diversity of fluid- and solid-based instabilities that have been identified. It is now theorised that, in principle, transition could be delayed indefinitely with the use of optimised multiple-panel compliant walls (Carpenter, 1998). Comprehensive reviews of the topic may be found by reference to

Carpenter (1990) and Riley *et al.* (1988) and more recently Carpenter (1998), Gad-el-Hak (1998, 2002) and Carpenter, Davies & Lucey (2000).

Our interest lies with numerical investigation of the effects of compliance on receptivity mechanisms, particularly when they are subjected to boundary-layer disturbances by freestream turbulence, generated through the introduction of minute particle(s) to the flow and also through imposed roughness. This is reminiscent of a marine environment. Although, the following chapter will describe receptivity in greater detail, a brief introduction is warranted here.

The study of receptivity can be used to improve the prediction of transition delay, as well as advancing general knowledge, both of which are major facets of our work. If we recall the transition region described in Figure 1.1, it can be noted that the first stage involves a localised receptivity stage followed by the linear growth of T/S waves. (If the boundary layer is subjected to sufficiently large excitations, the linear regime is avoided and turbulence is achieved through a bypass mechanism (Morkovin & Reshotko, 1990).) The receptivity stage describes processes in which environmental disturbances excite boundary-layer instabilities forcing transition to turbulence. Every transition path to turbulence involves a receptivity stage. The concept was first defined by Morkovin (1969a,b). Theoretical treatments have only recently been applied to the receptivity problem and have laid the foundations for numerical and experimental study. Owing to this, certain aspects of receptivity paths leading to transition are now well understood.

Very little is known regarding the receptivity of boundary layers over compliant surfaces and our study has addressed the effects that environmental factors have on receptivity paths and how they affect transition and control. In our study, it has been important to identify the instabilities or modes in which the boundary layer becomes more receptive to external disturbances. To anticipate the following chapters, we note here that there are a limited number of experimental (Hall, 1967; Blackwelder *et al.*, 1992; Vincent & Petrie, 1993; Lauchle *et al.*, 1995) and numerical studies (Saiki & Biringen, 1997) on the effect that surface-mounted and elevated (isolated) particles

have on the transition process within the boundary layer. These studies involve relatively large particles, (in excess of a third of the boundary-layer thickness), which induce a bypass-related receptivity mechanism. Note that *we are primarily interested in particles having a size which is only a tiny fraction of the boundary-layer thickness.*

An investigation of the effects of surface imperfections in the form of fixed waves in the compliant surface was also undertaken. The effects of roughness, especially in pipe flow, imposed over rigid surfaces, is well known. In general, if the roughness height is sufficiently small, no significant transitional effects are observed, whereas if the roughness height is sufficiently large, transition occurs. A literature review has revealed that only a handful of relevant numerical and experimental studies have been undertaken. Of these, there appears to be no standard definition of the roughness shape, height and distribution (Kendall, 1981; Reshotko & Leventhal, 1981; Corke *et al.*, 1986), making any comparison difficult. However, all the studies indicate that a bypass mechanism appears to explain the (almost) instantaneous transition observed (Floryan, 1997).

The findings within this thesis are based on results from numerical simulations. The computational (Direct Numerical Simulation (DNS)) study employs a novel velocity-vorticity code to investigate the receptivity phenomenon. The scheme is advantageous over other DNS in terms of computational efficiency and physical accuracy. The approach adopted here is based on scheme developed by Davies & Carpenter (1997, 2001), which is an advance on the scheme first developed by Fasel and his co-workers in the 1970s (Fasel, 1976, 1980; Fasel & Konzelmann, 1990; Fasel, Rist & Konzelmann, 1990). A key advantage of the method is that the wall vorticity is computed which is attractive when analysing the physics of such flows. The motion of the compliant panel is governed by the plate-spring model for our puposes. The fluid flow generates forces which drive the wall, while the resulting wall motion strongly influences the flow field. The fluid and wall motions are interactively coupled. Full details will be given in Chapter 3.

Layout of the thesis

This thesis is laid out as follows:

Chapter 2 provides a brief overview on particulate- and surface-induced receptivity phenomenon, based on a review of the available literature;

Chapter 3 describes the velocity-vorticity formulation adopted and the plate-spring model employed to model the dynamics of the compliant wall. The methodology adopted to interactively couple the codes will be described;

Chapters 4 and 5 are devoted to a description of the effects that wall compliance has on the development of so-called Klebanoff (K)-mode (or streaky structures) and near-wall structures in laminar and turbulent boundary layers respectively. (The K-mode refers to a boundary-layer structure that is believed to be indicative of bypass transition);

To our knowledge the study of the effects of surface roughness in the presence of compliance, is the first such of its kind. The study of such surface imperfections is challenging owing to the fact that various mechanisms may initate transition, namely the roughness distribution and geometry, flow conditions and level of compliance. A description and discussion of the phenomenon observed will be discussed in Chapter 6;

Finally, a brief synopsis of the key conclusions drawn from this work and a list of recommendations for future research are provided in Chapter 7.

Particulate matter has been suggested by some authorities to make the use of compliant walls for laminar flow control impossible in marine environments. A very brief summary of the conclusions from a study where boundary-layer disturbances are generated by moving particles over a compliant surface are also given in Chapter 7. Due to the preliminary and incomplete nature of this study these conclusions should be treated with some caution. Further details regarding the model to describe the particle dynamics, the coupling procedure to the fluid and compliant-wall aspects of the code and analysis may be found in Appendix A.

Chapter 2

Boundary-Layer Receptivity

This chapter will review particulate- and surface-induced receptivity phenomena. The first section will begin with a general discription of receptivity theory.

2.1 Forced & Natural Receptivity

Receptivity is the 'first stage' of the transition process and defines the processes in which environmental disturbances excite boundary-layer instabilites causing transition to turbulence (Morkovin, 1969a,b). Environmental disturbances are those which involve either acoustic waves or freestream turbulence, forcing transition by initiating various instability modes. It follows that there are a number of different situations and regions where a boundary layer becomes more receptive to such external disturbances. Receptivity is of fundamental importance as the initial amplitude of the disturbance dictates which transition path is taken. For example, a sufficiently large initial disturbance would trigger non-linear behaviour leading directly to turbulence through a bypass mechanism. If the initial amplitude is smaller, a more gradual sequence of instantaneous disturbances are initiated eventually leading to turbulence.

Little is known regarding the actual origins of disturbances in the boundary layer. Receptivity is different from the classical boundary-layer-stability eigenvalue problems, where the disturbances satisfy linear homogeneous equations. Instead, it can be defined

as an initial-value problem, i.e. it involves evaluation of the boundary-layer response to an externally imposed disturbance. Although the original Schubauer & Skramstad (1943) experiments may be described as an early receptivity study, the original, theoretical, treatment of receptivity was conducted by Gaster (1965).

From a practical viewpoint two main kinds of instability are important: The Tollmien-Schlichting (T/S) instabilty, which dominates two-dimensional boundary layers, and; The crossflow (CF) instability, which dominates three-dimensional boundary layers like that over a rotating-disc. Both can be excited by either stationary or non-stationary freestream perturbations, or various localised and non-localised surface non-uniformities.

Although, progress has been hampered by the complexity of the flow, certain aspects of the receptivity problem are now reasonably well understood. The reader is referred to Goldstein & Hultgren (1989), Leehey (1980), Nishioka & Morkovin (1986) and Saric, Reed & Kerschen (2002) for a comprehensive review. Kachanov (2000) describes some current three-dimensional disturbance studies. Arnal & Casalis (2000) offers a more applied review with respect to boundary-layer transition.

Kerschen (1989) defines two groups of boundary-layer receptivity. *Forced Receptivity* is where an unsteady, short-scale, disturbance directly excites instabilities within the boundary layer. An impulse excites the wavepacket within the boundary layer. *Natural Receptivity* involves environmental disturbance, such as the excitation of instability waves in a two-dimensional laminar shear layer by an incident acoustic wave. For interaction, the frequency and phase velocity of the acoustic wave(s) must coincide with the unstable frequencies of the boundary layer.

The study of receptivity is important for the prediction of transition. The most common transition-prediction methods, such as the e^n method, do not consider the receptivity stage. As it is sensible to base transition-point prediction on the local instability wave amplitude, there is a need to incorporate both receptivity and linear growth regimes. Such a method would include the influence of the unsteady motion in the whole boundary layer. For this reason it is important to develop theoretical

prediction methods for receptivity.

The various theoretical, experimental and numerical approaches will be briefly reviewed in the following sections.

2.1.1 Experimental Investigations

Receptivity experiments are difficult to perform as they require an environment where disturbance levels are low and laminar flow conditions extend over a wide Reynolds number range. A controlled periodic disturbance needs to be carefully introduced allowing a systematic study of the boundary-layer response. Typical examples include (controllable) wave-like disturbances in the form of surface roughness and vibration, or the use of acoustic methods. Schubauer & Skramstad's (1943) classic experiments involved stretching and vibrating a fine metallic ribbon close to the surface of a flat plate. The ribbon frequency was controlled to generate various instabilities and the disturbance traced downstream by monitoring the flow velocity. As the disturbance travels downstream, depending on local conditions it will grow or decay. If the disturbance grows, it may transform into turbulent flow. Their experiments confirmed the applicability of linear stability theory as an approach by which it is possible to ascertain when a flow is unstable to infinitesimal disturbances, i.e., conditions in which the flow must undergo transition from one type of motion to another.

In practice, it is difficult to make the disturbance weak enough for regular waves, and often difficult to detect Tollmien-Schlichting (T/S) waves at all. T/S waves cannot be easily observed in natural transition experiments as natural sources of disturbance tend to generate wavepackets in an almost random fashion temporally and spatially. Noise and other continually generating disturbances of other frequencies complicate matters further. It is important to minimise such disturbances as they can generate different receptivity mechanisms.

Goldstein & Hultgren (1989) group receptivity experiments into two categories. The first group is where the disturbances are locally introduced *into or just outside*

the boundary layer, (such as the Schubauer & Skramstad (1943) experiments). The second category is where disturbances are introduced some distance *outside* the boundary layer. This generates freestream disturbances which generate boundary-layer instability waves. These experiments are difficult to control and often lead to conflicting interpretation of results.

There are numerous examples of acoustically-induced transition. Schubauer & Skramstad (1943) experiments were the first to use an artificial disturbance, (in the form of a ribbon), to generate T/S waves. Kachanov *et al.* (1975) were first to highlight the rôle of modal vibrations in an acoustically excited boundary layer. Shapiro (1977) measured T/S amplitudes in a flat-plate boundary layer exposed to acoustic forcing. He found that the T/S wave amplitudes increased linearly with the imposed disturbance.

Many groups studied the phenomenon with the use of small roughness elements. Aizin & Polyakov (1979) used a roughness element in the form of a thin, narrow tape and observed a linear relationship between the roughness height and amplitude of the instability waves. Nishiokia & Morkovin (1986) described this as a *clear illustration of receptivity* to sound. Saric *et al.* (1991) investigated the same receptivity mechanism with a similar element and found that a roughness-height threshold existed below which the linear relationship held. Kosorygin & Polyakov (1990) demonstrated that T/S waves generated at a blunt edge could be cancelled by careful positioning of two-dimensional roughness strips in the downstream boundary layer. This was due to selective phase interference between the waves generated at the roughness and waves originating in the leading-edge region.

Zhou *et al.* (1994) investigated several roughness configurations and found that the level of the disturbance amplitude downstream depended on the ratio of the T/S wavelength to the streamwise length scale of the roughness. The maximum level of acoustic receptivity for a two-dimensional roughness element occurred when the width, (i.e. streamwise length scale), was half the local T/S wavelength. Breuer *et al.* (1996) used the background acoustic field to excite flow over a two-dimensional roughness

array placed inside a Blasius boundary layer. The background, unforced, (acoustic) excitation used in their work was more similar to a natural scenario than the periodic single-frequency excitation often used in acoustic receptivity experiments. They reported that the streamwise velocity spectra measured downstream from the roughness array contained a number of harmonics consistent with K-type transition.[1] With the removal of the roughness array, sub-harmonic transition was observed. This does not exclude the possibility that this behaviour was connected with the change in amplitude.

2.1.2 Theoretical & Numerical Investigations

Two main theoretical methodologies exist: one based on an infinite-Reynolds-number asympotic approach (Goldstein, 1985; Ruben, 1985; Zhigulev & Feberov, 1987); the other is based on classical stability theory. The latter is a simpler method that offers ease of (physical) interpretation. Early studies did not reveal what mechanism facilitated the transformation of the freestream disturbance wavelength at a particular frequency to the wavelength of the boundary-layer instability wave. As receptivity occurs in regions where the mean boundary-layer flow changes rapidly in the streamwise direction, this would invalidate the parallel-flow assumption of the Orr-Sommerfeld (O/S) equation.

It is reasonable to consider receptivity by assuming small-perturbation and parallel-flow approximations, but extending the analysis to three dimensions. Various methods exist to correct the O/S solutions and incorporate the effect of slow streamwise growth of the boundary layer. If the distance between the source and region of interest is small, the magnitude of these corrections will also be small. The mean flow is therefore assumed to be a function of a single spatial variable, namely the normal distance (y)

[1] K-type transition refers to the harmonic perturbations generated and studied by Klebanoff and his co-workers and reported in Schlichting & Gersten (2000). They are fundamentally different to the K-mode streaky structures discussed in later chapters, and manifest themselves as aligned, as opposed to staggered, Λ-vortices occuring in successive rows and generated when T/S waves reach a threshold amplitude. Further details may be found in Chapter 15 of Schlichting & Gersten (2000).

from the wall. After the application of a perturbation scheme to the Navier-Stokes (N/S) equations, a set of partial differential equations are derived, which the parallel-flow approximation makes separable. These reduce to a single, fourth-order, linear differential equation, the O/S equation.

Goldstein (1983,1985) and Goldstein *et al.* (1983) used the infinite-Reynolds number asympotic approach to identify crucial features of boundary-layer receptivity to freestream *sound.* They noted that the boundary layer only became receptive in regions of markedly non-parallel mean flow. Two different classes of receptivity, were identified in which non-parallel mean flow was instrumental in the generation of the T/S wave. Leading-Edge Receptivity represents the first class, and occurs when environmental disturbances rescale as they propagate through the strong streamwise pressure gradient found at the leading edge. At the leading edge, the boundary layer is thin and grows rapidly. Goldstein *et al.* (1983) found that the level of boundary-layer receptivity is dependent on the angle of incidence of acoustic waves onto the leading-edge region. Maximum and minimum levels of receptivity were found to correspond to acoustic waves propagating parallel to the mean flow, directly upstream and downstream respectively.

The second receptivity class occurs when the mean flow is forced to make rapid streamwise adjustments in the slowly growing region of the boundary layer downstream from the leading edge. Adjustments of the mean flow are often caused by changes in the wall boundary condition. For coupling to take place between an environmental disturbance and the instability wave, the streamwise length scale of the mean-flow adjustment must be of the same order as the local T/S mode wavelength. Using nonlinear, triple-deck equations as an asymptotic approximation to the N/S equations in this region, Goldstein (1985) was able to estimate the coupling between the acoustic and T/S waves in the Aizin & Polyakov (1979) experiment. There are two main problems with the asymptotic approach: comparison is difficult between experiment and theory, and the equations are only valid in the region close to the lower branch of the stability curve, restricting analysis. The finite-Reynolds-number theory was proposed

by Kerschen (1989), and later improved by Crouch (1992) and Choudhari & Streett (1992).

The basic concept is a simple one, that satisfies the disturbance propagation in a parallel shear flow. The flow is expanded as a regular series of small parameters, such as the amplitudes of the acoustic wave and surface profile, in the region where receptivity occurs. The lowest order of expansion would consist of the steady mean flow along the unsteady acoustic disturbance propagating through the boundary layer. By solving the steady O/S equation with the appropriate boundary condition to describe the surface, and defining the lowest-order acoustic disturbance as a Stokes flow solution, it is possible to find the mean-flow solution. It follows, owing to the mean-flow adjustment, that the highest order expansions consist of short-scale perturbations. The equations (in the streamwise direction) are reduced to a single ordinary differential equation upon the application of the Fourier transform and can then be solved. Various groups have studied acoustic receptivity using this method, and observed good agreement with experimental data.

2.2 Freestream Turbulence & Other Studies

Whereas acoustic receptivity appears to have undergone intense investigation, the same cannot be said for modelling and predicting freestream turbulence. Such experiments are relatively scarce. Kendall (1991) reports some of the said effects on the excitation and evolution of disturbances within the boundary layer. His experiments show that a distributed receptivity due to free-stream turbulence exists, but offers no detailed analysis as to what mechanisms are involved to excite the boundary layer. However, there is agreement on the appearance of streamwise elongated streaks, which characterise the flow. They were first observed by Klebanoff in an unpublished paper, (although his original results can be found in Kendall (1998)). Westin *et al.* (1994) compared several experimental studies and concluded that there appeared to be *no* link between the freestream turbulence level, boundary-layer fluctuations and the transitional Reynolds

number, for the streamwise velocity component. Earlier, Kendall (1985) experimentally investigated weak freestream turbulence and noted that the streak response linearly scaled with the turbulence level in the streamwise velocity component and freestream turbulence scales.

The importance of T/S waves for transition, initiated by freestream turbulence, is unclear. At high levels of freestream turbulence, T/S waves are difficult to identify and do not cause transition. In low freestream turbulence, wavepackets can be identified travelling at the same speed as T/S waves, with their amplitude scaling non-linearly with the turbulence level. If one introduces T/S waves with a boundary layer subjected to freestream turbulence, their amplification rate is smaller than in an undisturbed boundary layer (Boiko *et al.*, 1994).

This phenomenon has been studied in some depth. The common approach appears to apply parabolised stability equations to account for non-parallel effects on non-localised receptivity. Vortical freestream disturbances provide a distributed energy transfer to the natural eigenmodes when conditions are close to resonance. Downstream of this energy transfer, the travelling-wave solution is dominated by the natural eigenmode. Forcing from the vortical disturbances are concentrated in the outer region of the boundary layer. It is expected that vortical disturbances are associated with a weaker receptivity mechanism compared to acoustic forcing. In fact, Crouch (1994) notes that although the total receptivity amplitudes are approximately ten times larger than that for localised vortical receptivity, they are approximately fifty times *smaller* than that for non-localised acoustic receptivity. Crouch (1994) modelled the non-localised receptivity of the Blasius boundary layer and reported that the vortices replicate some of the characteristics of freestream turbulence with their interaction enhancing the receptivity mechanism.

Bertolotti (1997) used the same approach to investigate the response of the Blasius boundary layer to low-frequency, freestream three-dimensional vortical modes. His results echo that of Crouch (1994). He observed that when the vortical modes have a frequency equal to those of the unstable T/S waves, the scattering of vortical modes by

surface waviness produces only a weak response. When steady, low-frequency, vortical modes are considered, the emergence of K-modes are observed which cause a periodic spanwise modulation of the streamwise velocity. He concluded that the streak growth is related to non-modal growth. Note that the common scattering model does not explain the connection between freestream turbulence and T/S waves.

Recent work by Berlin & Henningson (1999) also identifies these 'streak' structures through a numerical study of non-linear receptivity mechanisms for freestream disturbances. They studied the interaction of vortical freestream disturbances within a laminar boundary layer. Unlike Bertolotti (1997), their emphasis was placed on the search for a mechanism that did not include a leading edge. They identified linear and non-linear receptivity mechanisms.

The non-linear mechanism was found to force streaks inside the boundary layer similar to those found experimentally. They were also observed for disturbances elongated in streamwise directions and for oblique freestream disturbances. It is argued that the boundary-layer response caused by the non-linear mechanism depended on the initial disturbance energy. This is comparable to that of the linear mechanism which was found to be only efficient for freestream vortices: the wall-normal velocity component of the freestream disturbances was found to be the most important for the receptivity mechanism (rather than the streamwise component). They identified a boundary-layer receptivity mechanism, in which three-dimensional disturbances in the freestream continue to force streaks inside the boundary layer. This may explain the difference between the experimental observations and previously suggested theories for the origin of streaks in the boundary layers subjected to freestream turbulence. It appears that the selection mechanism is dependent on the wavelength of the freestream turbulent scales. Note also that the linear mechanism dominates at low turbulence levels, and the non-linear mechanism at higher turbulence levels. No experimental verification at present has been shown, as the streak profiles in the boundary layer in either case are almost identical. (Kendall (1998) and Westin *et al.* (1994) have both reported problems.)

Although their results are similar to those obtained by Bertolotti (1997), Andersson, Berggren & Henningson (1999) note that Bertolotti used an incorrect scaling factor for the Reynolds number. This would explain the incorrect spanwise scales obtained. It may be finally noted that despite continued research, *the mechanism for T/S wave generation by freestream turbulence is still unknown.* A recent study by Meitz and Fasel, reported in Fasel (2002) attempts to address this. Whilst it has long been known that as the freestream turbulence is increased, (the amplitude of the K-mode increases, pushing transition further upstream (Kendall, 1998)), there has been no clear demonstration as to the relationship between the K-mode and any known transition mechanism. The observation made by Kendall (1998) that the growth of naturally occuring T/S wavepackets depended on their amplitude, and that their spanwise extent appeared to be related to the spanwise scale of the K-mode, prompted Fasel (2002) to perform a series of simplified direct numerical simulations of the streaks interacting with two-dimensional T/S waves. They demonstrated how the interaction between the two, formed three-dimensional wavepackets, which, when the amplitude of the disturbance reached a critical value generated a 'fundamental resonance-type' secondary instability prompting wavepacket breakdown into turbulent spots. They were able to chart the mechanism in considerable detail. They also showed that the 'periodic thickening and thinning of the boundary-layer', observed in Klebanoff's original experiments, (reported by Kendall (1998)), were primarily due to artifacts of the spanwise modulation of the streamwise velocity and not due to strong streamwise vortices. Note that the 'thickening and thinning' of the boundary-layer has not been observed by all experimentalists and as a result more study is required to confirm this. Additionally, there is a need for further study using more realistic generators of freestream disturbances, which is an aim of the present work.

2.3 Effect of Particulates on Receptivity Mechanisms

In a marine environment the main sources of disturbance would be freestream turbulence caused by minute particulate matter in sea water. Very little is known regarding these effects in a boundary layer over rigid or, let alone, compliant surfaces. Whilst most low-noise, clean, receptivity studies have been conducted in low-speed wind tunnels, very little work has been conducted in water (Colley *et al.*, 1998) and in particulate (marine-type) environments. Of the relevant studies, most focus on the initiation of the bypass mechanism and particle interaction during the turbulent phase with regard to bodies moving through *heavily laden* particulate environments. The latter is far from our present interest. However, a number of recent experimental and numerical studies have attempted to study the effect isolated particles have when they enter the boundary layer. These studies have also found that the bypass mechanism seems to be the receptivity path.

Saiki & Biringen (1997) examined the effect that an isolated, stationary, spherical particle would have on the transition process in a flat-plate boundary layer. Two cases are studied, a sub-critical case where hairpin vortices are observed shedding into the wake as they are convected downstream, and a super-critical case, where a turbulent wedge develops downstream of the sphere. Their computations indicate transition induced by a sphere is due to a bypass mechanism. Their results seem to agree with flow visualisations obtained by Blackwelder *et al.* (1992). The latter examined the influence a moving (isolated) sphere, with a diameter approximately a third of the boundary layer would have using a water-channel facility. Their flow visualisations revealed the production of a turbulent spot when an isolated particle entered the boundary layer. They concluded that the turbulent spots were produced by the particle wake rather than the particle itself, and suggested that the spot formation is inviscid in nature. This agrees with early experiments performed by Hall (1967) and Mochizuki (1961) who showed that the predominant mechanism was a form of bypass transition, (i.e.

the *direct seeding of turbulence* in the wedge in the boundary layer from the element).

Vincent & Petric (1993), motivated by an interest in the wake characteristics behind the sphere and development of the turbulent wedge, experimentally studied the effect that surface-mounted and elevated, stationary, spherical particles would have on the boundary layer. Laser doppler velocimetry was employed, and showed that, in general, the same features are observed for each configuration (Figure 2.1). For surface-mounted spheres, the flow field appeared to be dominated by horseshoe and trailing-vortex systems as Mochizuki (1961), Acarlar & Smith (1987) and Klebanoff, Cleveland & Tidstrom (1992) had observed. For the elevated case the wall appeared to have a stabilising influence on the hairpin vortices, and vortices are shed with fixed orientation, so the heads do not lift directly away from the plate without random irregular orientation. Where a turbulent wedge is formed, the trailing-vortex system rapidly gives way to hairpin vortex shedding in the near vicinity of the sphere. The development of the hairpin vortices is similar to that of turbulent bulges described by Falco (1977), and did not vary significantly. Hence, it was concluded that the horseshoe vortex that forms with the surface-mounted particle *does not* play a significant rôle in the wake development and turbulent-wedge process.

Studies where transition is investigated in low-density particle-laden environments over heated underwater bodies find that the transition location is determined by the location of the particle(s) within the body boundary layer (Lauche *et al*, 1995). This view is supported by the particle/body interaction model developed by Chen *et al.* (1979). This determines the occurence of turbulent spots due to particles captured in the boundary layer. Upon entering the boundary layer, the particle undergoes transient motion and the relative velocity between the particle and fluid becomes non-zero. A particle wake forms and this wake is suspected to cause the formation of a turbulent spot. This agrees with Blackwelder *et al.* (1992). Lauchle *et al.* find a preferred capture zone exists, in which free particles are most likely to enter the boundary layer. When the particles are in the freestream some of them cross streamlines and arrive near the surface substantially out of equilibrium with local boundary-layer flow resulting in

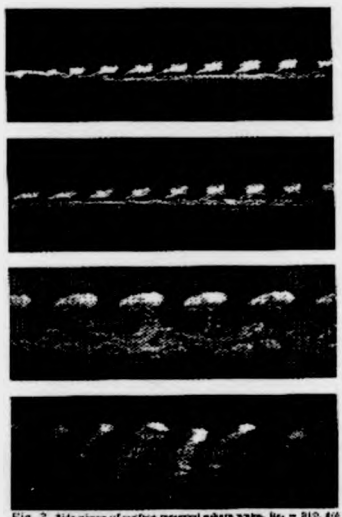

X	Top of Hairpin y/δ	Comments
1	—	no hairpin vortices
3	—	no hairpin vortices
5	—	vortex roll up starting
10	0.46-0.50	hairpin vortices form
20	0.80	hairpin vortices rising, boundary layer mainly near wall
50	1.16	disturbance near the wall, hairpin legs reattach to surface and flatten
100	1.40	hairpin legs beginning to break up
150	1.60	intermittent turbulent activity near wall
240	1.60	turbulent bulges, every 4th hairpin head moves toward plate

(a) surface mounted sphere

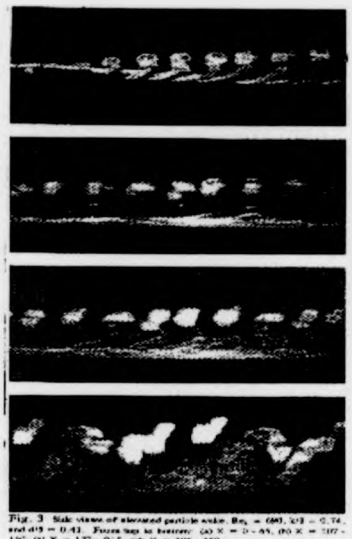

X	Top of Hairpin, y/δ	Comments
1	—	no horseshoe vortex, no hairpin vortices
3	—	1 Sd separation bubble attached to sphere
5	0.87	hairpin heads began to form and rise
10	1.13	hairpin heads rising, legs at height of bottom of sphere and moving toward plate
20	1.30	hairpin legs approach plate, heads rising
50	1.74	hairpin legs reattach to plate surface at X = 70, hairpin heads rising
150	2.17	boundary layer irregular near wall, turbulent bursts evident, every 4th vortex head is low
200	2.18	boundary layer chaotic, turbulent bulges effect hairpin heads, periodic pattern

(b) elevated sphere

Figure 2.1: Flow visualisation and description of (a) surface mounted, and (b) elevated spheres within a boundary layer (Vincent & Petrie, 1993). X represents the streamwise length, (y/δ), represents the depth of immersion of the sphere.

the creation of wakes that can lead to the formation of a turbulent spot.

More recent numerical and experimental studies have tended to focus on the bypass mechanism by studying isolated disturbances within the boundary layer. Breuer & Haritonidis (1990), Breuer & Landhal (1990), and Henningson, Lundbladh & Johansson (1993) observe algebraic temporal growth of disturbances, described as the lift-up mechanism. The development of this type of incipient turbulence is characterised by two parts: a wave portion (according to linear stability theory), and a transient portion which travels with the local mean velocity. The latter is associated with the lift-up mechanism, which generates horizontal perturbation velocity by vertical motion of particles in the presence of mean shear. This is activated by the three-dimensionality of the flow. The growth and dominance of the transient part leads to transition bypassing the T/S route. Saiki & Biringen (1997) observed that isolated disturbances are characteristic of particle-induced perturbations, linking transition caused by particles to three-dimensional disturbances.

We can conclude that the bypass mechanism can be described as a receptivity mechanism as it is initiated by external perturbations. Jacobs & Durbin (2001) simulate bypass induced by freestream turbulence by direct numerical simulation. Whereas it is generally agreed that there are three regions of concern: a buffeted laminar-layer (which is stable to peturbations); a region of intermittent turbulent spot formation (where localised perturbations trigger instabilities which generate turbulent spots); and finally a fully turbulent boundary-layer, there is some confusion as to the receptivity process. In particular, the coupling of freestream perturbations to boundary-layer modes. Jacobs & Durbin (1998) indicate that whilst low-frequency modes can penetrate the boundary layer, it is the case that they do not directly lead to instability, and are generated by decaying 'freestream motions'. In fact, low-frequency perturbations produce even lower-frequency boundary-layer modes that are amplified and elongated in the streamwise directions, producing the 'streaks' described earlier.

2.4 Effect of Surface Imperfections on Receptivity

The effect of surface roughness over rigid and compliant surfaces is pertinent to the development of marine flow systems. Various physical mechanisms, that initate the transition process, arise owing to surface geometry and roughness distribution and amplitude.

Existing literature deals with three classes of disturbance roughness: single-isolated, two-dimensional roughness, where separated wall-wakes are observed; single-isolated, three-dimensional roughness where a horseshoe vortex is induced and extends downstream; and surface imperfections, where no single predominant feature exist. In general, roughness favours transition. If the roughness height is sufficiently small, it has no effect and the walls are said to be hydrodynamically smooth. If the roughness height is sufficently large, transition occurs at the roughness element. For moderate roughness heights, transition occurs a certain distance downstream from the location of the roughness, with the distance decreasing with increasing roughness height (Floryan, 1997).

Experimental investigations are difficult, owing to problems of isolating and quantifying the distributed receptivity. Current experimental data lack a standard definition of the roughness shape, height and distribution (Kendall, 1981; Reshotko & Leventhal, 1981; Reshotko, 1984; Corke *et al.*, 1986), which makes comparison difficult. However, all the experiments conclude that there is a violent, almost instantaneous, transition from laminar conditions. The cause of this is presently unknown, but we suspect it is the result of a bypass mechanism.

Reshotko & Leventhal (1981) found that roughness, in the form of sand, moves the undeformed Blasius profile outward. They noted that the growth of disturbances occurs at frequencies lower than those for which T/S waves are unstable. Amplification appeared to have been driven by the local wake profile at the crest of distributed roughness elements. These observations appear to contradict early theoretical work where it is assumed that the distortion of the mean flow by roughness promoted instability

(Lessen & Gangwani, 1976; Singh & Lumley, 1971).

Tadjfar *et al.* (1985) created distributed roughness using arrays of spheres attached to a smooth surface and measured the velocity fluctuation between individual spheres and observed no evidence of T/S waves. They suggested that the transition mechanism described in §2.3, i.e., the mechanism driven by horseshoe and hairpin vortices generated by the roughness element. The contribution of the downstream element increases the strength of the upstream-generated vortices towards eventual transition. Disturbances grow while being carried downstream above the next sphere, where the mean flow has an inflection point. The most amplified disturbance eventually reaches the wake behind the next sphere and induces a global response to a frequency governed by the streamwise spacing between the spheres.

Corke *et al.* (1986) conducted experiments using sand paper to represent distributed roughness. They observe significantly enhanced T/S amplitudes in the presence of roughness. They reported that it is the low-inertial fluid in the valleys between the grains that respond to freestream disturbances; that once T/S waves appear they grow faster as compared to the smooth-wall case, and there is evidence of roughness-induced three-dimensionalisation of the wavefronts leading to secondary instabilities. Whether this is due to the destabilisation of the boundary layer or to a continuous input of environmental energy is unclear.

Chapter 3

Computational Model

A brief description of our direct numerical simulation scheme (DNS) to model boundary-layer disturbances over rigid, and more especially, compliant surfaces is described here. A novel *velocity-vorticity* formulation is applied. This is briefly described in §3.1. The modelling strategy is described in §3.2. The method is especially suitable for investigating three-dimensional transition in a spatially growing boundary-layer. The inclusion of a compliant surface requires certain modifications to ensure numerical and physical efficiency, accuracy and stability. These changes are briefly described. We will also demonstrate the integrity of the code for the case where a finite roughness element is used to generate Tollmien-Schlichting (T/S) waves.

3.1 Velocity-Vorticity (DNS) Formulation

A modified version of a novel velocity-vorticity formulation is used to investigate the particle- and surface-imperfection-induced receptivity phenomena. Our code is a modified version of the Navier-Stokes solver formulated by Davies & Carpenter (1997, 2001). The method is efficient at calculating perturbations to a flow field. In addition, no restrictions are placed on the form of the disturbance prescribed. The formulation only uses three governing equations for three primary dependent variables, namely perturbations to the wall-normal velocity component and the two vorticity components in the plane of the wall. The secondary variables are the perturbations to the remaining velocity and vorticity components and for some applications the pressure. These are defined in terms of the primary variables. Provided the primary variables satisfy certain weak conditions as the wall-normal coordinate, z, tends to infinity, (which would be satisfied on almost any conceivable practical application), our formulation is fully equivalent to the Navier-Stokes equations in primitive-variables form. Another important advantage offered by the approach lies in the treatment of the constraints placed on vorticity. No artifical boundary conditions are imposed on the vorticity. Instead, the wall boundary conditions placed on velocity are linked to the vorticity field through rigorously defined integral constraints based on the definition of vorticity. This approach ensures solenoidal velocity and vorticity fields.

A mixed spectral/finite difference scheme is adopted. Spectral expansions are used in the z (wall-normal) and y (spanwise) directions and finite discretisations in the x (streamwise) directions (Figure 3.1). Time discretisation is based on a three-point backward difference scheme. A predictor-corrector scheme is used for the convective terms. Note that most of the viscous terms can be treated implicitly. The resulting matrices are banded and pentadiagonal. This ensures that the advantages of spectral convergence can be combined with the use of efficient line iteration schemes.

The reader is referred to Davies & Carpenter (1997, 2001) for a full description of the method. A brief overview is presented here.

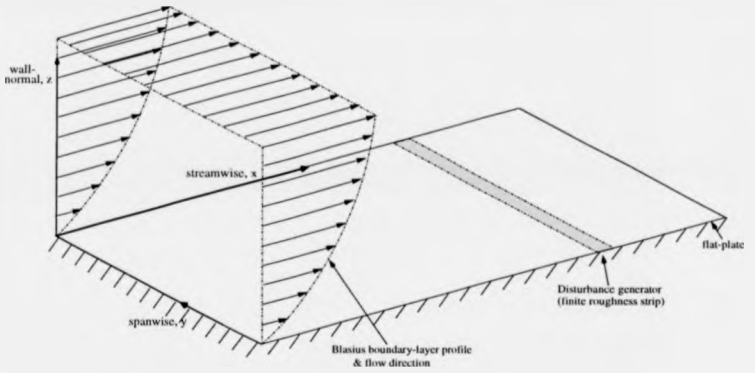

Figure 3.1: Adopted co-ordinate system.

3.1.1 Governing Equations

In two dimensions velocity-vorticity methods are attractive as the number of variables can be reduced from three (u,v,p) to two $(\omega,\ \psi)$. However, in three dimensions the number of variables increases from four (u,v,w,p) to six $(\omega_x,\omega_y,\omega_z,\ u,\ v,\ w)$! This poses no problem with our method as we reduce the number of governing equations from six to three! The Cartesian co-ordinate system described in Figure 3.1 is adopted. A constant-thickness, incompressible, boundary-layer flow is modelled as the basic undisturbed shear flow. Note that this undisturbed flow field is not a true solution of the Navier-Stokes equations, but is assumed here for simplicity. The Blasius profile is prescribed as the actual undisturbed boundary-layer profile (see §3.3).

The undisturbed flow solution is represented by the velocity and vorticity fields:

$$\boldsymbol{U}^B = (\boldsymbol{U}^B, 0, 0); \qquad \boldsymbol{\Omega}^B = (0, \boldsymbol{\Omega}^B_y, 0). \tag{3.1}$$

The total velocity and vorticity fields are decomposed into the undisturbed flow solution and a perturbation:

$$\boldsymbol{U} = \boldsymbol{U}^B + \boldsymbol{u}; \qquad \boldsymbol{\Omega} = \boldsymbol{\Omega}^B + \boldsymbol{\omega} \tag{3.2}$$

and perturbations from the prescribed undisturbed flow are represented as:

$$\boldsymbol{u} = (u, v, w); \qquad \boldsymbol{\omega} = (\omega_x, \omega_y, \omega_z). \tag{3.3}$$

The governing equations for the perturbations rather than the total flow variables are considered. The components of the perturbation flow fields are divided into *primary*, (ω_x, ω_y, w) and *secondary*, (u, v, ω_w) variables. The primary variables are obtained by projecting the velocity field along the wall-normal direction and projecting the vorticity field onto the orthogonal plane parallel to the wall. The secondary variables are obtained in the same manner, but the order of projections are reversed. The secondary variables are defined in terms of the primary variables and *vice versa*. As a result, one set can be eliminated and computed when required.

The evolution of the *dimensionless* primary variables is determined using only *three* equations:

$$\frac{\partial \omega_x}{\partial t} + \frac{\partial N_z}{\partial y} - \frac{\partial N_y}{\partial z} = \frac{1}{R}\nabla^2 \omega_x \tag{3.4}$$

$$\frac{\partial \omega_y}{\partial t} + \frac{\partial N_x}{\partial z} - \frac{\partial N_z}{\partial x} = \frac{1}{R}\nabla^2 \omega_y \tag{3.5}$$

$$\nabla^2 w = \frac{\partial \omega_x}{\partial y} - \frac{\partial \omega_y}{\partial x} \tag{3.6}$$

where, the Reynolds number is defined as $R{=}U_\infty \delta^*/\nu$, with the appropriate velocity, (U_∞), and displacement thickness, (δ^*), chosen for non-dimensionalisation. Equations (3.4) and (3.5) are the vorticity transport equations for the streamwise and spanwise components of the vorticity. Equation (3.6) is the Poisson equation for z. This can also be obtained by taking the wall-normal component of the relationship ($\nabla^2 \boldsymbol{u} = -\nabla \times \boldsymbol{\omega}$). The convective quantity, $\mathbf{N}{=}(N_x,\ N_y,\ N_z)$, is defined as:

$$\mathbf{N} = \boldsymbol{\Omega}^B \times \boldsymbol{u} + \boldsymbol{\omega} \times \boldsymbol{U}^B + \boldsymbol{\omega} \times \boldsymbol{u}. \tag{3.7}$$

The current definition for $\mathbf{N}$ includes the full non-linear aspects for the transport equations. As we will be initially concentrating on *linear* computations the final term in equation (3.7) is discarded. This is a valid assumption as we are studying perturbations

of small amplitude. This term is retained for the non-linear computations.

The secondary variables are defined explicitly in terms of the primary variables:

$$u = -\int_z^\infty \left(\omega_y + \frac{\partial w}{\partial x}\right) dz \tag{3.8}$$

$$v = \int_z^\infty \left(\omega_x - \frac{\partial w}{\partial y}\right) dz \tag{3.9}$$

$$\omega_z = \int_z^\infty \left(\frac{\partial \omega_x}{\partial x} + \frac{\partial \omega_y}{\partial y}\right) dz, \tag{3.10}$$

to allow calculation of $\mathbf{N}$, and u and v are assumed to vanish as $z \to \infty$. (3.8) and (3.9) are derived through integration of the appropriate components of the vorticity field with respect to z, and (3.10) follows from the integration of the condition that the vorticity is solenoidal. These definitions allow $\mathbf{N}$ to explicitly defined in terms of the primary variables.

To summarise, the transport equations (3.4) and (3.5) and the Poisson equation (3.6) can be viewed as a system of three governing equations for the three unknown primary variables. As a result, all reference to the secondary variables have been *eliminated*, (thus improving the efficiency of computation). Davies & Carpenter (2001) demonstrate how the N/S equations can be recovered in primary variables format provided the incompressibility condition is enforced and the u and v components of the perturbation velocity vanish as $z \to \infty$.

3.1.2 Boundary Conditions

The motion of the fluid must be matched to the wall. For a rigid impermeable wall at $z=0$, the boundary conditions are prescribed to ensure no-slip:

$$u(x, y, 0, t) = u_w(0, 0, 0, t) = 0 \tag{3.11}$$

$$v(x, y, 0, t) = v_w(0, 0, 0, t) = 0 \tag{3.12}$$

$$w(x, y, 0, t) = w_w(0, 0, 0, t) = 0 \tag{3.13}$$

where, u_w=v_w=w_w=0. These replace the wall boundary conditions for vorticity with the integral constraints obtained from (3.8) and (3.9) for the secondary variables into (3.11) and (3.12):

$$\int_0^\infty \omega_y dz = -u_w - \int_\eta^\infty \frac{\partial w}{\partial x} dz \tag{3.14}$$

$$\int_0^\infty \omega_x dz = -v_w + \int_\eta^\infty \frac{\partial w}{\partial y} dz. \tag{3.15}$$

These equations are fully equivalent to the wall-motion boundary conditions for u and v, and can be viewed as constraints on the evolution of the primary variables ω_y and ω_x respectively. Each constraint can be associated with the vorticity transport equations (3.4) and (3.5) to satisfy the no-slip condition. (Although non-parallel and non-linear terms are neglected, this method still ensures the approach remains well-posed.)

The inlet (x=0), the boundary conditions are supplied by the real part of the appropriate Orr-Sommerfeld, (O/S), eigensolution for the velocity and vorticity fields, i.e. they take the form of the undisturbed flow so that the perturbations are null.

A broad review regarding the difficulty in the choice of a suitable downstream boundary condition may be found in Kloker, Konzelmann & Fasel (1993). The outlet condition should allow the disturbance to propagate out of the domain, without distorting the upstream flow through unphysical boundary reflections. The flow variables are required to be wave-like:

$$\frac{\partial^2 v}{\partial x^2} + \alpha_r^2 v = 0 \tag{3.16}$$

$$\frac{\partial^2 \omega}{\partial x^2} + \alpha_r^2 \omega = 0. \tag{3.17}$$

to ensure small-amplitude, two-dimensional, Tollmien-Schlichting (T/S) waves are able to pass smoothly out of the computational domain. This is encouraged by ensuring the computational domain is sufficiently large to ensure flow perturbations at the downstream boundary are negligible. This follows work by Fasel (1976, 1980) and his coworkers. They found that wavelike boundary conditions would allow two-dimensional, small-amplitude, T/S waves to pass smoothly out of the domain, even when α_r was poorly selected. We choose α_r as the appropriate Orr-Sommerfeld (O/S) eigenvalue.

(This value is required to specify the upstream disturbance profiles.) In general, no problems were encountered when the rigid outlet portion of the wall was varied in length, and also for the case where the wall was compliant at the outlet. A description of the effect of α_r on the solution may be found in Kloker *et al.* (1993). For the compliant-wall case a damping function at the downstream boundary may be utilised.

3.1.3 Wall-normal co-ordinate mapping

A co-ordinate transformation is imposed on w in the limit $z \to \infty$. This facilitates the solution for the Poisson equation. ω_x and ω_y must also be considered in the same limit. However, as the secondary variables u and v cannot be used to obtain any additional constraint on ω_x and ω_y, the constraints need to be obtained by some other means. We apply conditions that ensure that both ω_x and ω_y vanish for $z \to \infty$. This is easier to implement and represents stronger boundary conditions than those required in Davies & Carpenter (2001). We impose the same sort of limiting behaviour for all three of the primary variables. The co-ordinate transformation:

$$\zeta = \frac{l}{z + l} \tag{3.18}$$

is made use of to obtain satisfactory solutions. This maps the semi-infinite physical domain $z \in [0,\infty)$ onto the finite computational domain $\zeta \in (0,1]$, where l is a stretching factor. The physical limit, $z \to \infty$, corresponds to the transformed co-ordinate limit, $\zeta \to 0$.

Derivatives with respect to z, are related to those with respect to ζ by:

$$\frac{\partial f}{\partial z} = -\frac{\zeta^2}{l}\frac{\partial f}{\partial \zeta}. \tag{3.19}$$

It can be deduced that the z derivative will vanish for $z \to \infty$, provided the ζ derivative remains bounded as ζ approaches zero. Provided our numerical simulations yield solutions for the primary variables which remain smooth functions of ζ when $\zeta \to 0$, the incompressibility condition ($\nabla \cdot \boldsymbol{U} = 0$) and the wall-normal vorticity will be automatically satisfied.

3.1.4 Compliant Surface

The effects of wall compliance are studied by modifying the code to include a finite panel in a similar manner to Davies & Carpenter (1997, 2001). The motion of the surface is modelled using the plate-spring model of Carpenter & Garrad (1995). This is essentially an elastic plate supported above a rigid surface with an array of springs (Figure 3.2).

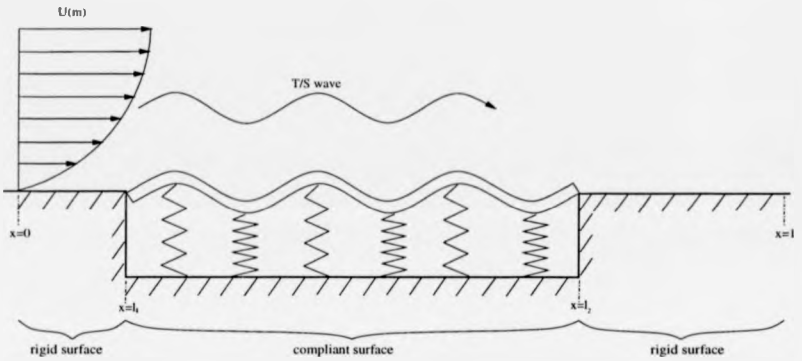

Figure 3.2: Compliant surface modelled as plate-spring model

Displacement of the surface is restricted to the vertical direction only. The dynamics of the model is described by the equation:

$$m\frac{\partial^2\eta}{\partial t^2} + \frac{d}{R}\frac{\partial\eta}{\partial t} + \frac{1}{R^2}\left(B\frac{\partial^4}{\partial x^4} - T\frac{\partial^2}{\partial x^2} + K\right)\eta = p_{wall} \tag{3.20}$$

where, η is the dimensionless vertical wall displacement and p_w is the dimensionless hydrodynamic fluid pressure disturbance acting on the wall. The non-dimensional wall-parameter components are: the areal density, m; the damping coefficient, d; the flexural rigidity, B; the applied streamwise tension, T, per unit span; and, the spring stiffness, K, per unit area of the compliant surface. These parameters are made dimensionless using the kinematic viscosity, ν, as opposed to the mean flow speed as this introduces the factors involving the Reynolds number in equation (3.20). They remain fixed when

the velocity and Reynolds number changes.[1]

With regards to the boundary conditions, the motion of the wall must be matched to that of the fluid. As the wall is constrained to only move in the z-direction, we set:

$$u_w(x,y,t) = -U^B(x,y,\eta,t) \tag{3.21}$$

$$v_w(x,y,t) = -V^B(x,y,\eta,t) \tag{3.22}$$

$$w_w(x,y,t) = \frac{\partial \eta}{\partial t}(x,y,t) - W^B(x,y,\eta,t) \tag{3.23}$$

where,u_w,v_w,w_w, are functions determined by the wall motion. (Recall that for a rigid wall η=0, $u_w = v_w = w_w$=0 at z=0.) We will demonstrate that these conditions allow explicit coupling between the fluid and compliant codes.

For the case where a compliant panel is embedded over a rigid surface, hinged boundary conditions are employed:

$$\eta = \frac{\partial^2 \eta}{\partial x^2} = 0 \qquad \text{at} \qquad x = l_1, \qquad \text{and} \qquad x = l_2. \tag{3.24}$$

These conditions tend to be more computationally demanding than other conditions, such as clamped conditions at the join.

Wave-like downstream boundary conditions, similar to those described in §3.1.2, are applied. The constraints on the wall motion at the downstream boundary are accordingly:

$$\frac{\partial^2 \eta}{\partial x^2} + 2\alpha_i \frac{\partial \eta}{\partial x} + |\alpha|^2 \eta = 0, \quad \text{and} \tag{3.25}$$

[1] For completeness, the non-dimensional wall-properties obtained are:

$$m \equiv \frac{m^*}{\rho h}; \quad \frac{d^*}{\rho U_{ref}} = \frac{1}{R} \underbrace{\frac{d^* \rho h}{\nu}}_{d}; \quad \frac{B^*}{\rho h^3 U_{ref}^2} = \frac{1}{R^2} \underbrace{\frac{B^*}{\rho h \nu^2}}_{B};$$

$$\frac{T^*}{\rho h U_{ref}^2} = \frac{1}{R^2} \underbrace{\frac{T^* h}{\rho \nu^2}}_{T}; \quad \frac{K^* h}{\rho U_{ref}^2} = \frac{1}{R^2} \underbrace{\frac{K^* h^3}{\rho \nu^2}}_{K}$$

Quantities marked by an asterix denote dimensional quantities. Note that these quantities remain fixed when the velocity and Reynolds number changes. See Carpenter & Garrad (1985) and Davies & Carpenter (1997, 2001) for full details.

$$\frac{\partial}{\partial x^2}\left(\frac{\partial^2 \eta}{\partial x^2} + 2\alpha_i \frac{\partial \eta}{\partial x} + |\alpha|^2 \eta\right) = 0. \tag{3.26}$$

Provided the growth or decay rate are small, the derivatives multiplied by α_i are be neglected and $|\alpha|$ may be replaced by α_r. No conditions need to be applied at the outflow when a finite-length compliant panel embedded in a rigid surface is modelled. Instead, conditions for a rigid-compliant wall join at a second x-location within the domain are applied.

3.2 Numerical Methods

3.2.1 Spatial & Spectral Discretisation

A hybrid spectral, finite-difference, discretisation scheme is applied. Streamwise, (x), components are discretised using a second-order, centered, finite-difference scheme. Spanwise, (y), components are discretised using Fourier expansions. Wall-normal, (z), components are discretised using Chebyshev polynomials.

The advantages of using a spectral scheme in the z-direction is that it can accurately resolve the disturbance profile and evaluate the pressure integral which is crucial for fluid-structure interaction computations. As described in §3.1.3, the wall-normal domain is semi-infinite. We utilise a co-ordinate transformation, ζ, (3.18) which maps the semi-infinite physical domain to the finite computational domain. First, the vorticity and wall-normal velocity disturbances are expanded in odd Chebyshev polynomials. (Note that integral operators lead to a more convenient form of spectral expansion than differential operators, as shown by Bridges & Morris (1984).) We then integrate the vorticity transport and Poisson equations twice with respect to ζ. This replaces them with ζ-integral operators. The expanded Chebyshev polynomials are substituted into the integrated vorticity transport and Poisson equations to yield two systems of equations. These are in a pentadiagonal form which can be efficiently and accurately solved using the line iteration scheme described by Davies (1995).

3.2.2 Temporal Discretisation

Implicit time discretisation is usually essential to ensure numerical stability when resolving unsteady disturbances over both rigid and compliant surfaces. Time discretisation is based on a robust three-point, backward-difference scheme. A predictor-corrector scheme is employed to explicitly calculate the convective terms in the governing equations. It is possible to use an Adams-Bashforth time-stepping treatment for the predictor stage, and a Crank-Nicolson time-stepping treatment for the corrector stage. For the rigid wall, the latter scheme is more efficient than the three-point backward-difference scheme. Note that in order to calculate the convective terms, it is necessary to calculate the secondary variables; hence the wall-normal integration of the primary variables is necessary. A tri-diagonal set of equations are formed through the integration of the Chebyshev polynomials which can be efficiently solved with a modified TDMA solver (see Davies (1995) for more detail).

A FFT is used to convert the primary perturbations into the spectral domain in order to calculate the product terms in equation (3.7). After the efficient multiplication of the mean flow has been applied an FFT is used to transform back to the spectral domain. The wall-normal viscous components in the transport equations are solved implicitly, and the streamwise and spanwise viscous terms solved explicitly.

The updated velocity field is calculated between the predictor and corrector stages with the Poisson equation (3.6). The viscous terms of the Poisson equation are solved implicitly with values of vorticity from the predictor stage being used to calculate the velocity field at the new time-step.

3.2.3 Numerical Treatment of Compliant Wall

Over a compliant panel, values of the vertical displacement, η, must be supplied in order to achieve the boundary conditions for the fluid motion. Also, in order to achieve stability, it is essential to implement a robust interactive scheme between the fluid and wall solvers, (the fluid flow generates forces that drive the wall, whilst the resulting wall

motion strongly influences the flow field). The wall motion is driven by the forces or pressure perturbations, p_w, acting on the wall. Coupling the fluid and wall solvers has been the source of major difficulty in the past, but was resolved by Lucey & Carpenter (1992) and later Belanger *et al.* (1994). They combine the hydrodynamic and wall inertia terms together, avoiding the dominance of one term over the other, i.e. if the inertia terms are treated separately, so that they lie on opposite sides of the equations used in the iterative scheme, there is always the likelihood that one of the terms will dominate the other causing the scheme to diverge.[2] The exact details of how the governing equation is employed to achieve stability is described in Davies (1995). In the interests of brevity, only the important features will be described here.

The total, non-dimensional, normal momentum over a flat plate is defined as:

$$\mu = mw_w + \int_0^1 w dz. \tag{3.27}$$

The original equation of motion for the wall (3.20) is combined with the equation for the pressure perturbation at the wall:[3]

$$p_w = -\int_0^z \Big(\frac{\partial w}{\partial t} + U\frac{\partial w}{\partial z} + \frac{1}{R}\frac{\partial \omega}{\partial z}\Big)dz \tag{3.28}$$

to give:

$$\frac{\partial \mu}{\partial t} + \frac{1}{R^2}\Big(B\frac{\partial^4}{\partial x^4} - T\frac{\partial^2}{\partial x^2} + K\Big)\eta + \frac{d}{R}\frac{\partial \eta}{\partial t} = -\frac{\partial}{\partial z}\int_0^z \Big(Uw + \frac{1}{R}\omega\Big)dz. \tag{3.29}$$

Recall the boundary conditions on the wall:

$$u_w = -U'_w\eta, \tag{3.30}$$

$$v_w = V'_w\eta, \tag{3.31}$$

$$\text{and } w_w = \frac{\partial \eta}{\partial t} \text{ at } z = 0. \tag{3.32}$$

[2] It is also possible to achieve a stable system if the wall inertias are neglected (Luo & Pedley, 1996) or if it is assumed that solutions are periodic in time. In general, such assumptions are not acceptable in view of the nature of our objectives.

[3] The spanwise vorticity transport equation, (3.5), is integrated to determine the pressure perturbation at the wall.

The latter is substituted into equation (3.29) to give:

$$\frac{\partial}{\partial t}\Big(mw_w + \int_0^1 w.dz\Big) + \frac{1}{R^2}\Big(B\frac{\partial^4}{\partial x^4} - T\frac{\partial^2}{\partial x^2} + K\Big) + \frac{d}{R}w_w = -\frac{\partial}{\partial z}\int_0^z \Big(Uw + \frac{1}{R}\omega\Big)dz. \tag{3.33}$$

The boundary condition (3.32) needs to be tranformed by applying the same three-point backward difference scheme for the fluid solver to discretise the time derivative. We apply the same to discretise the time derivative of μ appearing in equation (3.33):

$$\eta^l = \frac{1}{3}\Big(4\eta^{l-1} - \eta^{l-2}\Big) + \frac{2\Delta t}{3}w_w^l \tag{3.34}$$

$$\mu^l = \frac{1}{3}\Big(4\mu^{l-1} - \mu^{l-2}\Big) - \frac{2\Delta t}{3}\Big\{\frac{d}{R}w_w^l + \kappa\eta^l + \frac{\partial}{\partial z}\int_0^1 \Big(Uw^l + \frac{1}{R}\omega^l\Big)dz\Big\} \tag{3.35}$$

$$\text{where, } \kappa = \frac{1}{R^2}\Big(B\frac{\partial^4}{\partial x^4} - T\frac{\partial^2}{\partial x^2} + K\Big).$$

We arrive at the fully-discretised version of equation (3.33) by the elimination of η^l from equation (3.35) using equation (3.34):

$$\mu^l = \Big(\frac{2d\Delta t}{3R} + \frac{4(\Delta)^2}{9}\kappa\Big)w_w^l = \frac{1}{3}\Big(4\mu^{l-1} - \mu^{l-2}\Big) - \frac{2\Delta t}{9}\kappa\Big(4\eta^{l-1} - \eta^{l-2}\Big) - \frac{2\Delta t}{3}\frac{\partial}{\partial x}\int_0^z \Big(Uw^l + \frac{1}{R}\omega^l\Big)dz. \tag{3.36}$$

The streamwise derivatives are discretised using second-order finite differences. Chebyshev expansions are used for W and ω. The reference to η can then be eliminated by writing it on the right-hand side of (3.36). As a result, the new boundary condition imposed on v can be rewritten as:

$$\tilde{r}_k w_k = \tilde{v} \tag{3.37}$$

$$\text{where, } \tilde{r}_k = \Big(m + \frac{2d\Delta t}{3R} + \frac{4(\Delta t)^2}{9}K_o\Big)r_k + q_k,$$

$$\tilde{v} = \frac{1}{3}(mr_k + q_k)(4v_{k,n}^{l-1} - v_{k,n}^{l-2}) - \frac{2\Delta t}{9}\Big(4(\kappa\eta)_n^{l-1} - (\kappa\eta)_n^{l-2}\Big) - \frac{\Delta t}{3\Delta x}\Big(s_k(v_{k,n+1}^l - v_{k,n-1}^l) + \frac{1}{R}q_k(\omega_{k,n+1}^l - \omega_{k,n+1}^l)\Big) + \frac{4(\Delta t)^2}{9}r_k\Big(K_1(v_{k,n+1}^l - v_{k,n-1}^l) + K_2(va_{k,n+2}^l - v_{k,n+2}^l)\Big)$$

where, $K_o = \frac{1}{R^2}\left(\frac{6B}{(\Delta x)^4} - \frac{2T}{(\Delta x)^2} + K\right)$, $K_1 = \frac{1}{R^2}\left(\frac{4B}{(\Delta x)^4} - \frac{2T}{(\Delta x)^2}\right)$, and $K_2 = \frac{1}{R^2}\frac{B}{(\Delta x)^4}$. The values of $\tilde{v}$ at successive streamwise positions are recalculated with estimates for v and ω. See Davies (1995) for full details of the derivation. This boundary condition replaces (3.32).

There are two ways in which η can be calculated and inserted into the boundary condition to compute u_w and v_w. The first technique employs the recast governing equation (3.29) to obtain a block-tridiagonal system of equations which can be solved for η^l when v and ω are supplied. The second approach uses the boundary condition (3.34) to determine η directly. Closer examination of (3.37) reveals that all reference to η^l is removed. As a result, the latter is adopted as it is easier to implement and more readily converges to a solution.

3.3 Prescribed Velocity Profiles

3.3.1 Blasius Profile

A Blasius velocity profile is prescribed as the undisturbed flow profile for the majority of the computations. For a semi-infinite flat plate, $\partial U/\partial x$ is of the order 1/R, where R is the Reynolds number based on the freestream velocity and the thickness of the boundary layer. In view of this, the flow is assumed to be nearly-parallel. On the basis of this approximation, the basic velocity distribution is given as:

$$U(z) = f'(z) \tag{3.38}$$

$$\text{where,} \quad z = \left(\frac{U^*}{2\mu x^*}\right)^{\frac{1}{2}} z^* = \frac{1.2168 z^*}{\delta^*} \tag{3.39}$$

where, δ^* is the displacement thickness of the boundary layer, and $f(z)$ is the Blasius function, which satisfies:

$$f''' + ff'' = 0. \tag{3.40}$$

This equation is solved numerically, with the boundary conditions:

$$f(0) = f'(0) = 0 \text{ and } f(\infty) = 1 \tag{3.41}$$

set. Equation (3.40) is written with respect to the Blasius co-ordinate η. This is transformed to the physical z coordinate by straightforward factorisation. Figure 3.3 shows plots of the meanflow profile as generated from the Blaisus solver as a function of z, and its first two z-derivatives.

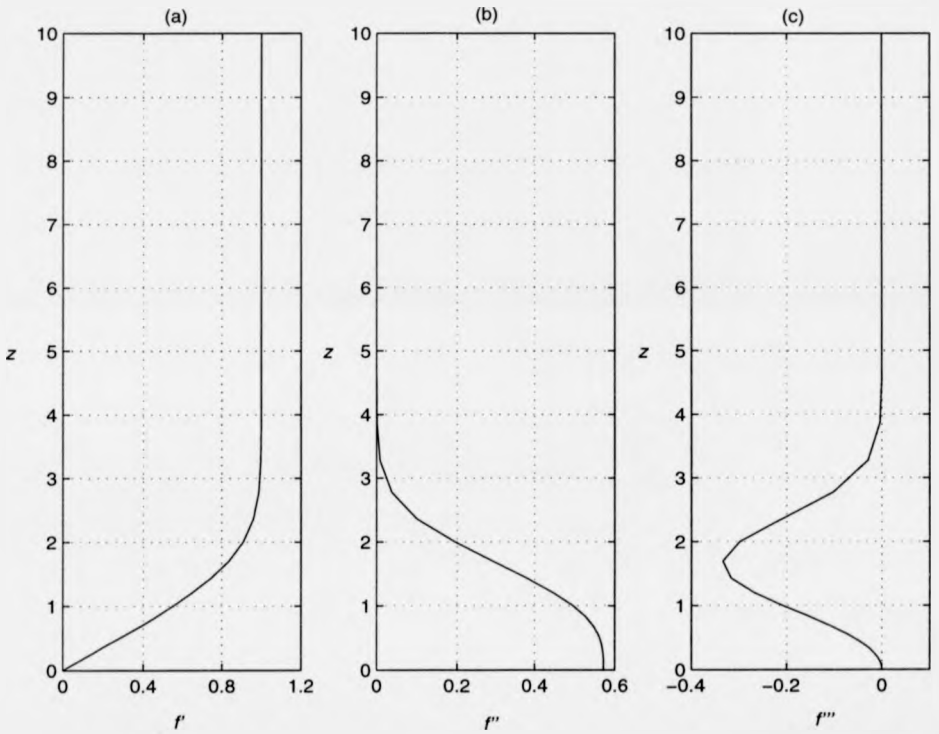

Figure 3.3: Mean flow profile as generated by the Blasius solver. (a). mean flow profile with respect to wall-normal height, z; (b)-(c). mean flow profile as a function of its first two z-derivatives. Non-dimensional with respect to δ^*, and velocity with respect to U_∞.

3.3.2 Turbulent Velocity Profile

Whilst the majority of our simulations are focused on the behaviour using the laminar (Blasius) profile as the undisturbed profile, we will also describe results where we have prescribed a turbulent velocity profile. The effects of a compliant surface in a turbulent boundary layer have not been widely studied theoretically and computationally. A preliminary investigation is undertaken here, with the aim of obtaining information regarding the streak like flow structures and the qualitative behaviour of particulates in the near-wall region of the boundary layer over compliant surfaces. (It is generally agreed that this region has the greatest influence on turbulence.)

The inner regions of the turbulent boundary layer are modelled with the analytical approximate formula for the 'law of the wall' (Spalding, 1961). This is a semi-empirically determined relationship which effectively describes the influence of a number of factors, such as past flow history, wall curvature, external potential flow character, by a single parameter, u^+, the streamwise velocity in wall units. The range for which the law is accurate is given in terms of the distance from the wall, z^+. This is termed the domain of the flow, and appears to extend from z^+=0 to 50, unless the flow is under transition or separating from the wall. The viscous, buffer and log layers can be modelled using this method by employing the semi-emprical formula:

$$z^+ = u^+ + e^{-\kappa B}\left[e^{\kappa u^+} - 1 - \kappa u^+ - \frac{(\kappa u^+)^2}{2} - \frac{(\kappa u^+)^3}{6}\right]. \tag{3.42}$$

The von Kármán constant, κ(=0.4), and B(=5.5) are near-wall universal constants for turbulent flow past smooth walls. The variables marked with '+' have been non-dimensionalised in terms of friction velocity, v^*, and the viscous length scale (the wall unit), ν/v^*. The wall layers (or inner regions) of the velocity profile are illustrated in Figure 3.4.

The outer layer is modelled using the 'law of the wake' (Coles, 1956). This has the form:

$$\frac{U - U_e}{u^*} = \frac{1}{\kappa}\left\{ln\left(\frac{y}{\delta}\right) + 2\Pi\left[sin\left(\frac{\pi y}{2\delta} - l\right)\right]\right\} \tag{3.43}$$

where, II is the wake component of the profile. It is affected by mild and slowly

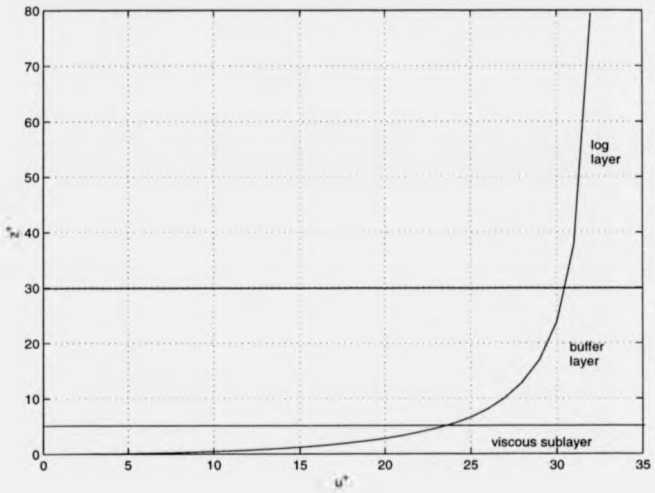

Figure 3.4: The inner regions of the turbulent boundary layer, generated by 'law of the wall' (Spalding, 1961).

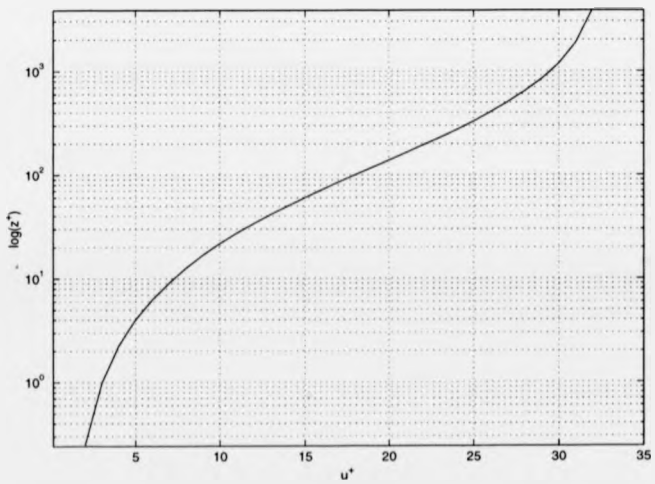

Figure 3.5: The full turbulent boundary layer.

varying pressure gradients. A logarithmic plot of the entire profile is shown on the previous page in Figure 3.5.

3.4 Code Validation

A number of simulations were run and compared with existing data to check the integrity of the code. The simulations involved prescribing an oscillating bump on the surface of a rigid and compliant flat plate in the absence of a wall join. The bump introduces time-periodic forcing, (effectively localised blowing and suction), which generates a Tollmien-Schlichting (T/S) wavepacket, (into a previously undisturbed flow). The disturbance is introduced a short distance from the inflow boundary appropriate to the expected T/S eigenmode at the inlet.[4]

The leading front of this disturbance is allowed to leave the domain as a check to ensure no reflections at the outlet are present. In practice this is not a problem, and as a result it was deemed unnecessary to introduce a buffer domain to damp out any disturbances (for the majority of the scenarios run). It was found that there was a high degree of insensitivity to the precise value of α_r chosen for the outlet boundary condition. Minor disturbances can be ignored or easily removed by either extending the length of the computational domain and/or increasing the number of Chebyshev polynomials. For the majority of our simulations, 32 Chebyshev polynomials are used, although 16 is more than adequate for resolving the features. We generally chose a step size, Δx of 0.8 for finite discretisation in the x direction. The value of Δx depends on the smallest wavelength present. Long domains are more demanding than shorter domains owing to the large accumulation of phase error, hence Δx must be smaller. For stability and convergence, the time step, Δt, is generally set at $0.5\Delta x$.

Figure 3.6 charts the evolution of a T/S wavepacket over a surface in the absence of compliance. An oscillating disturbance creates this response. The (non-dimensional)

[4]For most cases a body force is used as the disturbance driver. Please §4.1.2 for a description of the different categories employed.

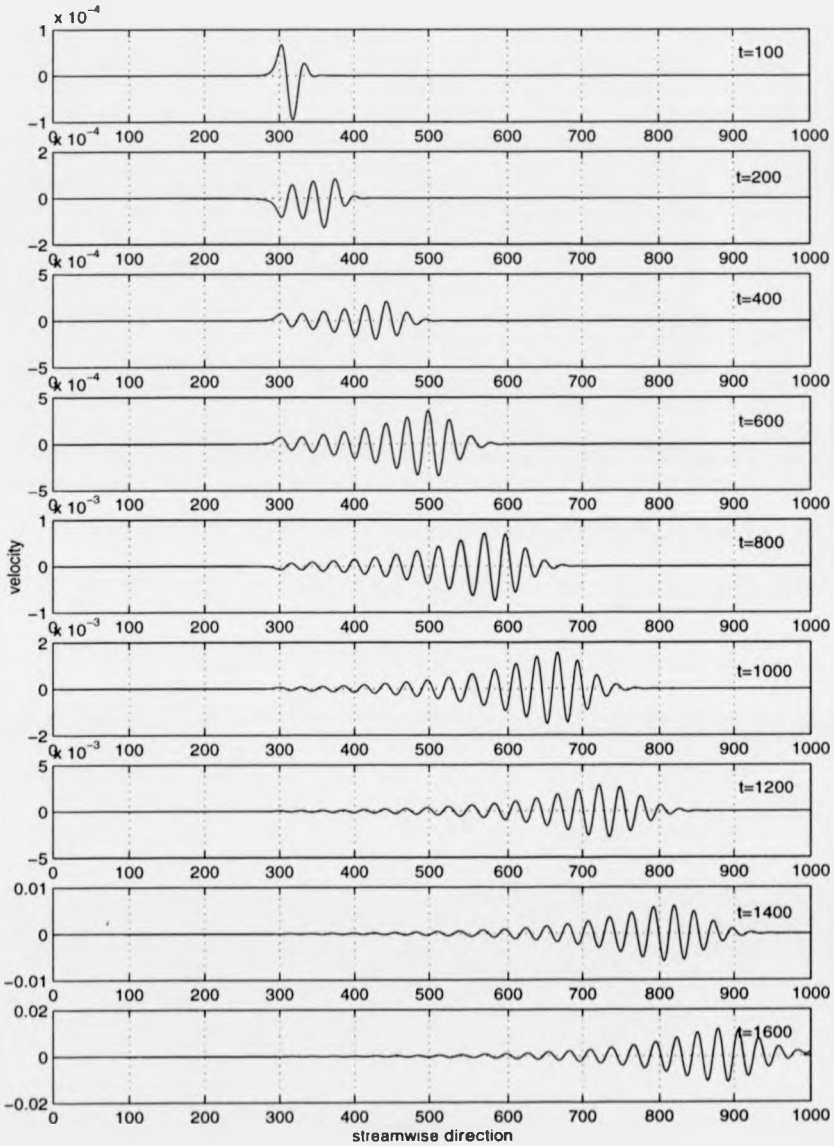

Figure 3.6: Evolution of a 2D Tollmien-Schlichting (T/S) wavepacket with time. The T/S wave is produced by an oscillating bump located at x=297.5 R=1400; W=72.46×10^{-6}; β=0; bump height=11μm).

forcing frequency is set to an appropriate value (W=72.46×10^6), depending on the freestream speed, U_∞. A bump of height, 11μm (0.011δ^*), and length of 15mm (15δ^*), placed at a streamwise location of x=203δ^*. Figure 3.6 illustrates the clean T/S waves present, a short distance downstream and falls to a value close to the mean. If the amplitude were to rise to a sufficiently high level, three-dimensional non-linear effects would be observed.

Inspection of the T/S wave over the rigid surface, reveals that apart from the behaviour in the immediate vicinity of the inlet and outlet, there are virtually no reflections and no streamwise variation of α. Excellent agreement was found between linear theory and our simulations (Figures 3.7 & 3.8).

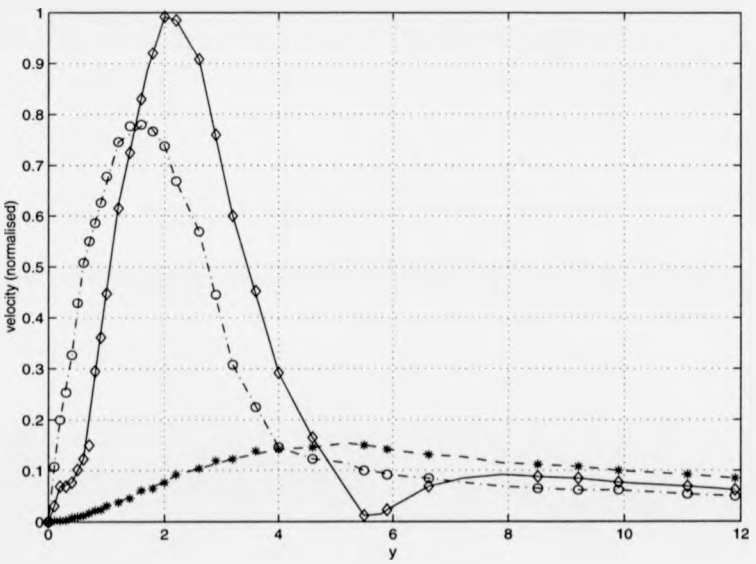

Figure 3.7: Comparison of normalised velocity profiles for a three-dimensional T/S wave calculated by linear theory and with our code over rigid surface. Linear stability theory for streamwise (-), spanwise (-.), and normal (-), compared with simulations (◇,○,∗). R=790; β=0.4. Velocities normalised with respect to streamwise velocity.

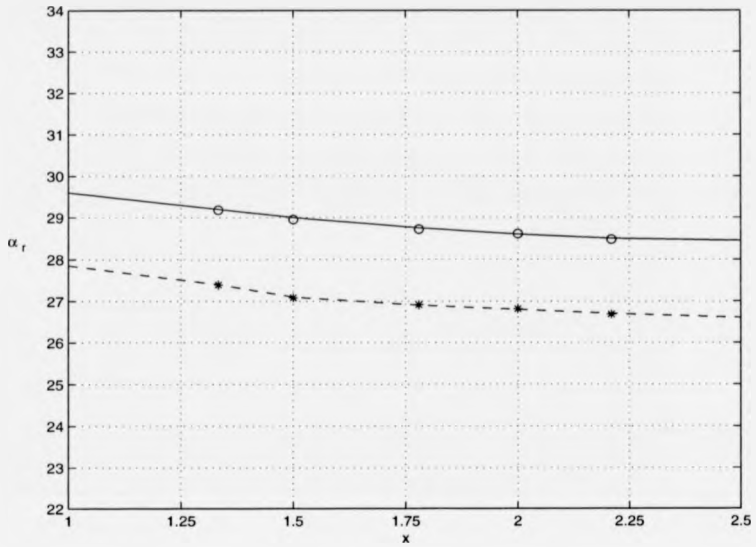

Figure 3.8: Variation of streamwise wavenumber α_r with streamwise location. Linear stability theory for two-, (∘−), and three-dimensional (∗−) simulations. (The wavenumbers are zero and 0.133 for the respective simulations.) Comparison made with data from Fasel *et al.* (1990).

To check the integrity of the compliant code a similar procedure to that adopted by Davies (1995) is employed, namely the motion of the wall is verified and then the integrity of the coupling method.

As mentioned earlier, the T/S wave is generated by forcing the wall and fluid upstream with properties corresponding to a solution of the Orr-Sommerfeld (O/S) equation. The conditions on the fluid are identical to the two-dimensional rigid-walled case:

$$w = \mathcal{R}\Big(w_{o/s}(z)e^{-i\beta t}\Big),\ \omega_z = \mathcal{R}\Big(\omega_{o/s}(z)e^{-i\beta t}\Big) \tag{3.44}$$

where, $w_{o/s}$ and $\omega_{o/s}$ are complex eigenfunction profiles derived from the O/S equation for spatially evolving waves with a temporal frequency, β. The streamfunction pro-

file, $\phi(z)$ and complex spatial wavenumber, α, can be determined with the standard expression:

$$w_{o/s} = i\alpha\phi;\ \omega_{o/s} = (D^2 - \alpha^2)\phi \tag{3.45}$$
$$\text{where, } D = \frac{d}{dz}.$$

The streamfunction profile, $\phi(z)$ is used to define w and ω_z is calculated using the compliant-wall boundary conditions to solve the O/S equation. The upstream wall motion is matched to the fluid motion by setting:

$$\eta = \mathcal{R}\left(\eta_{o/s} e^{-i\beta t}\right), \tag{3.46}$$

where the displacement amplitude is defined as:

$$\eta_{o/s} = -\frac{D\phi_w}{U'_w}. \tag{3.47}$$

Equation (3.47) can be used to mimic the response of compliant walls at other streamwise locations. Therefore the displacement can be written as:

$$\eta = \mathcal{R}\left(\eta_{o/s} e^{i(\alpha x - \beta t)}\right). \tag{3.48}$$

The complex wavenumber, α, is determined from the O/S equation. The prescription of the wall velocity is determined by pre-multiplying η by $-i\beta$ before taking the real part of the solution. Under these conditions, the fluid is time periodically forced at all wall locations as well as at the upstream boundary. We observed identical growth rates, wavenumbers and velocity profiles with the two-dimensional simulations conducted by Joslin *et al.* (1992) where the wall motion had been solely determined by the fluid pressure. We show that the profiles match those expected from linear stability theory (Figure 3.9).

The second test focuses on the integrity of the interactive coupling scheme adopted. To determine the wall motion when the walls are compliant, the upstream wall forcing function is supplemented by:

$$\frac{\partial^2 \eta}{\partial x^2} = -\mathcal{R}\left(\alpha^2 \eta_{o/s} e^{-i\beta t}\right). \tag{3.49}$$

Now, the two-component equation:

$$\begin{bmatrix} \eta \\ \frac{\partial^2 \eta}{\partial x^2} \end{bmatrix} = \mathcal{R}\left\{ \begin{bmatrix} 1 \\ -\alpha^2 \end{bmatrix} \eta_{o/s} e^{-i\beta t} \right\}, \tag{3.50}$$

needs to be solved. This can be easily implemented and replaces the condition that η=0 would apply at the vicinity of the rigid-compliant join.

Similar simulations to that over a rigid surface were conducted. The number of Chebyshev polynomials, and the values of Δx, Δt, bump height and location, and W were similar to those used in the rigid simulations. For a wholly compliant surface, with Kramer-type properties, i.e.:

$$m = \frac{1}{3};\ T = 0;\ d = 0;\ B = 1.92 \times 10^7;\ K = 4B,$$

T/S waves evolve in a similar manner to those over rigid surfaces. There is initially exact agreement with linear stability theory; the locally computed growth rates and wave profiles agreed with values calculated from the O/S equation made by Joslin *et al* (1992) (Figure 3.9). The eigenfunction imposed at the upstream boundary, which incorporated the inclusion of the wall motion was replicated in the form taken by the profile as the disturbances propagated downstream. No streamwise variation of α was observed as the T/S wave travelled downstream and left the domain without any detrimental behaviour.

Similar results are observed for the case where a compliant panel is introduced. Away from the immediate vicinity of the joins, the waves take the same character as they would if no joins were present. This agrees with simulations conducted by Davies & Carpenter (1995) and later Wiplier & Ehrenstein (2000) (see Figure 3.10).

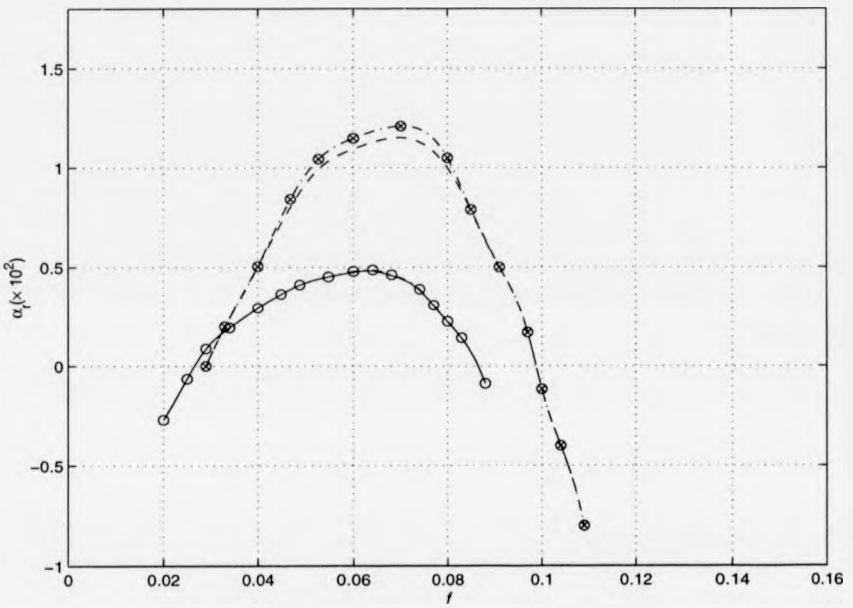

Figure 3.9: Variation of two-dimensional growth rate, α_i, as a function of frequency-comparison with Joslin *et al.* (1991). Our results for the rigid- ($\otimes-\cdot$) and compliant-($\circ-\cdot$) surfaces are compared with calculations, (rigid surface:$(--)$; compliant surface:$(-)$), performed by Joslin *et al.* (1991). Compliant wall properties: K=0.354 GN/m^3; E=1.385 MN/^{2}; b=0.735 mm; R=2240.

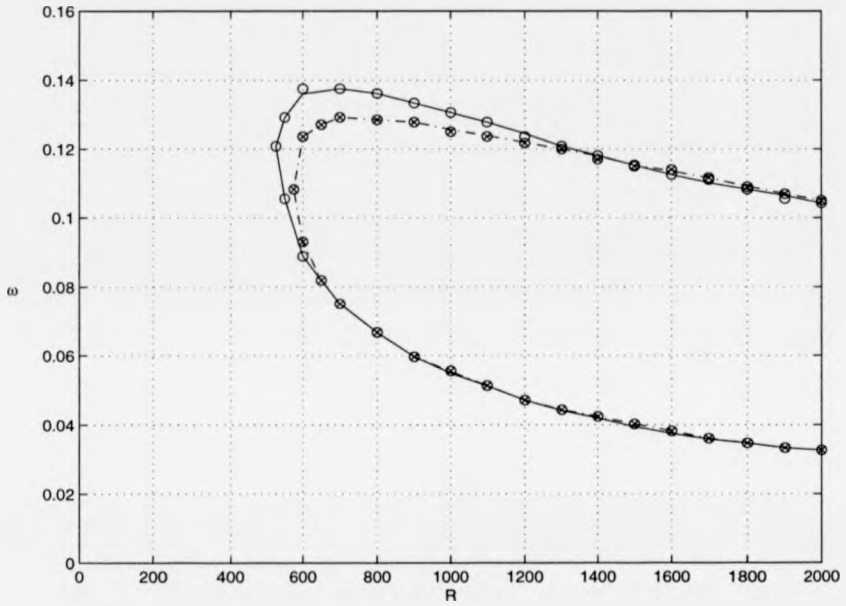

Figure 3.10: Neutral stability curve for a Blasius boundary-layer (local parallel flow assumption). (o) indicates our rigid wall data compared to Wiplier & Ehrenstein (2000) rigid-wall data (-). Similarly (⊗) indicates our compliant-wall data compared to Wiplier & Ehrenstein (2000) compliant-wall data (-.-). (Compliant-wall properties: b=0.1mm; E=0.5 MN/m^2; κ^*=10^4 MN/m^4; d=T=0; Re$_\delta$=2000.)

Chapter 4

Klebanoff Mode Receptivity over Rigid & Compliant Surfaces

Whilst it is already well known how compliant surfaces can be optimised to suppress or even eliminate Tollmien-Schlichting (T/S) waves, relatively little is understood regarding the effects when such a surface is subject to freestream turbulence. Such concerns are pertinent for the development of practical devices for use in marine applications. (In marine environments, the main source of freestream turbulence is likely to be particulate matter.) This is addressed through an investigation of *minute* particle-induced receptivity over wholly compliant and rigid surfaces, and also the case where a compliant panel is embedded in a rigid surface.

4.1 Particulate-Induced Receptivity

The importance of T/S waves for transition initiated by freestream turbulence is unclear. At high levels of freestream turbulence, T/S waves are difficult to identify and are not the route to transition. At low levels, wavepackets can be identified travelling at the same speed as T/S waves, with their amplitude scaling non-linearly with the turbulence level. If one introduces T/S waves with a boundary layer subjected to freestream turbulence, their amplification rate would be smaller than in an undisturbed boundary layer (Boiko *et al.*, 1994).

Our interest lies with the investigation of the effects that freestream turbulence generated by minute particle(s) has on the excitation and evolution of disturbances within the boundary layer. Despite there being no confirmation yet, it appears that the formation of *streaks* may play a rôle in bypass transition. Streaks are associated with the Klebanoff mode, (first identified by Klebanoff (1971), although his original study was unpublished). They are generated by a periodic, spanwise modulation of the streamwise velocity. Note that Klebanoff modes are an ensemble-averaged view of the instantaneous streaks. They are not modes in the sense of being eigenfunctions. They are vortical disturbances, forced by low-frequency, freestream turbulence to which the boundary layer responds in the form of a large-scale motion, generating streak-like structures. These grow and extend downstream. This phenomenon has been widely studied over flat-plate rigid surfaces, (reviewed in Chapter 2), but not over compliant surfaces, which will be addressed here.

4.1.1 Excitation by Body Forces

A freestream spanwise body force is used to generate streamwise vorticity, and hence, as a result streaks develop. Figure 4.1 illustrates the computational model. The body force models the effect a minute particle would have in the boundary layer. This is similar to a study of Klebanoff modes over rigid surfaces performed by Fasel and his coworkers (Meitz,1996; Meitz & Fasel, 2000; Fasel, 2002). They model the interaction of

freestream turbulence, (by generating two-dimensional T/S waves by suction/blowing), on the Klebanoff mode, whereas our interest lies with, in the first instance, simulating the streaky structures. Meitz and Fasel run a linear code to generate the streaks and then use the appropriate wavenumber-frequency parameters as input data for non-linear simulations, (where the interaction of two-dimensional wavepackets are investigated), and were able to look at steady and unsteady, linear and weakly non-linear disturbances. Our simulations are less complicated to run.

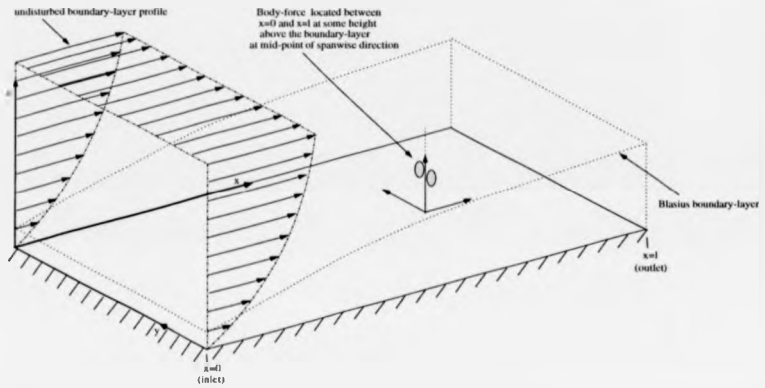

Figure 4.1: Body force simulation schematic.

It is necessary to modify the velocity-vorticity formulation by introducing a body force directly into the N/S equations. To include it in the vorticity transport equations we take the curl of the forcing components. For solely spanwise forcing, this is relatively simple and leaves the transport equations in the following form:

$$\frac{\partial \omega_x}{\partial t} + \frac{\partial N_z}{\partial y} - \frac{\partial N_y}{\partial z} = \frac{1}{R}\nabla^2 \omega_x - \frac{\partial F_y}{\partial z} \tag{4.1}$$

$$\frac{\partial \omega_y}{\partial t} + \frac{\partial N_x}{\partial z} - \frac{\partial N_z}{\partial x} = \frac{1}{R}\nabla^2 \omega_y \tag{4.2}$$

$$\frac{\partial \omega_z}{\partial t} + \frac{\partial N_y}{\partial x} - \frac{\partial N_x}{\partial y} = \frac{1}{R}\nabla^2 \omega_x + \frac{\partial F_y}{\partial x} \tag{4.3}$$

where: $\mathbf{N} = \boldsymbol{\Omega}^B \times \boldsymbol{u} + \boldsymbol{\omega} \times \mathbf{U}^B + \boldsymbol{\omega} \times \boldsymbol{u}$. Equation (4.3) is not directly calculated! This does not leave one component of the body-force unaccounted for. It can be shown that

the augmented wall-normal transport equation (4.3) can be derived explicitly from the *primary* transport equations: Equations (4.1) and (4.2) are differentiated with respect to x and y respectively and then summed together:

$$\frac{\partial}{\partial t}\left(\frac{\partial \omega_x}{\partial x}+\frac{\partial \omega_y}{\partial y}\right)+\frac{\partial^2 N_x}{\partial y \partial z}-\frac{\partial^2 N_y}{\partial x \partial z}=\frac{1}{R}\nabla^2\left(\frac{\partial \omega_x}{\partial x}+\frac{\partial \omega_y}{\partial y}\right)-\frac{\partial^2 F_y}{\partial x \partial z}; \tag{4.4}$$

Bearing in mind that the solenodial property of the vorticity perturbation field requires:

$$\frac{\partial \omega_x}{\partial x}+\frac{\partial \omega_y}{\partial y}=-\frac{\partial \omega_z}{\partial z}, \tag{4.5}$$

this is substituted into equation (4.4) to give:

$$\frac{\partial^2 \omega_z}{\partial t \partial z}-\frac{\partial^2 N_x}{\partial y \partial z}+\frac{\partial^2 N_y}{\partial x}\partial z=\frac{1}{R}\nabla^2\frac{\partial \omega_x}{\partial z}+\frac{\partial^2 F_y}{\partial x \partial z}; \tag{4.6}$$

and, the wall-normal vorticity transport equation is obtained with the additional body-force component after integration with respect to z:

$$\frac{\partial \omega_x}{\partial t}+\frac{\partial N_y}{\partial x}-\frac{\partial N_x}{\partial y}=\frac{1}{R}\nabla^2\omega_z+\frac{\partial F_y}{\partial x}. \tag{4.7}$$

4.1.2 Form of the Body Force

The body forcing is either continuous and over a specified time period only spatial variation is described by the forcing function. The forcing function is much simpler in form to that employed by Meitz (1996) and produces a spanwise array of counter-rotating streamwise vortices downstream and upstream of the disturbance. Meitz employs the unsteady form of the function. Cleaner streaks are produced with our type of forcing. (A single-point body-force would create counter-rotating vortices in the streamwise and wall-normal directions.)

The function is in the form:

$$F_y=\int Gexp\{-a(x-x_f)^2+i\beta y-b(z-z_f)^2\}dz \tag{4.8}$$

where, G is the magnitude, x_f the streamwise position of the body force, z_f the normal position of the body force and β the spanwise wavenumber. a and b determine the

sharpness of the, (numerically approximate), streamwise and wall-normal delta functions respectively. A body-force in the form of (4.8) results in a delta-type streamwise vorticity production:

$$\frac{\partial F_y}{\partial z} = Gexp\{-a(x-x_f)^2 + i\beta y - b(z-z_f)^2\}. \tag{4.9}$$

Disturbance Driver Categorisation

A number of types of body-force drivers are employed in this and the following chapters. A classification scheme is described here to avoid ambiguity and for future reference.

- Type $FC(c)$: A continuous, (fixed in space), constant body force that, in general, varies sinusoidally in the spanwise direction, with spatial variation of the form:

$$F_y = \int Gexp\{-a(x-x_f)^2 + i\beta y - b(z-z_f)^2\}dz.$$

- Type 2D$FC(c)$: As above, but does not vary in the spanwise direction.

- Type $FC(fd)$: As Type $FC(c)$, but the body force is applied for a fixed duration only.

- Type $MC(fd)$: As Type $FC(c)$ but moves downstream at the freestream flow speed, so spatial variation takes the form:

$$F_y = \int Gexp\{-a(x-x_f-U_f t)^2 + i\beta y - b(z-z_f-U_f t)^2\}dz.$$

- Type FO: A fixed body force that oscillates harmonically with time and, in general varies sinusoidally in the spanwise direction, so has spatial and temporal variation of the form:

$$F_y = \int Gexp\{i\mathcal{F}t - a(x-x_f)^2 + i\beta y - b(z-z_f)^2\}dz.$$

- Type 2DFO: As above, but does not vary in the spanwise direction.

- Type MO: As Type FO but moving downstream at the freestream flow speed, so has spatial and temporal variation of the form:

$$F_y = \int Gexp\{i\mathcal{F}t - a(x - x_f - U_f t)^2 + i\beta y - b(z - z_f - U_f t)^2\}dz.$$

- Type IP: A 'pseudo-particle', (two-dimensional), body force that interacts dynamically with the boundary layer. The body force represents the force that the particle exerts on the fluid flow. The trajectory of the 'pseudo-particle' is governed by the equation of motion for the particle.

- Type Im: A true impulsive body force with a spatial and temporal variation that approximates a delta function:

$$F_y = \int Gexp\{-c(t - t_f) - a(x - x_f)^2 + i\beta y - b(z - z_f)^2\}dz.$$

4.1.3 Streaky Structures over Rigid Surfaces (Code Validation)

Computations over a rigid surface were performed to check the integrity of the method. The Klebanoff mode is generated by prescribing a body force of the form described by equation (4.8) at a fixed streamwise position (x_f=203) just outside a constant-thickness, parallel, Blasius boundary-layer (Figure 4.1). The body force is placed downstream of the leading edge as we are only considering how simple vortical freestream disturbances interact with a laminar boundary layer; (the effect of the leading edge would continuously force disturbances in the boundary layer). The body force is stationary and non-oscillating, (i.e., type $FC(c)$). After some time, the perturbations reach a steady state. Figure 4.2 illustrates a 'typical' streamwise velocity streak. Figure 4.3 describes the evolution of such a streak with time. Low-velocity streaks are believed to be produced by the lift-up of low-velocity fluid near the wall. Similarly, high-velocity streaks are produced by the introduction of high-velocity fluid pulled down from the freestream.

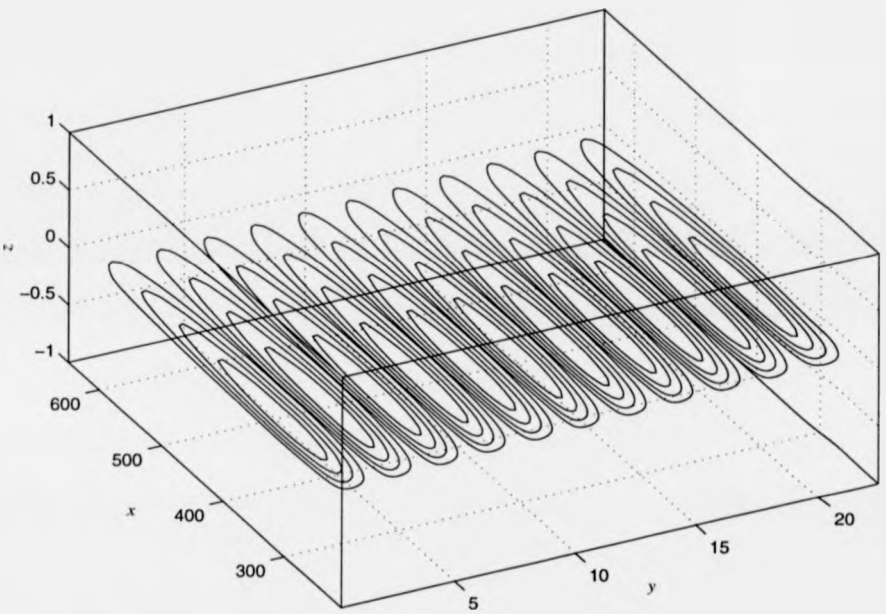

Figure 4.2: Spanwise perturbation velocity contours at t=1000 over a rigid surface. Spanwise wavenumber, β=0.07; R=1000; stationary and non-impulsive body force at a fixed location of x_f=303,z_f=2.314. Body force type $FC(c)$.

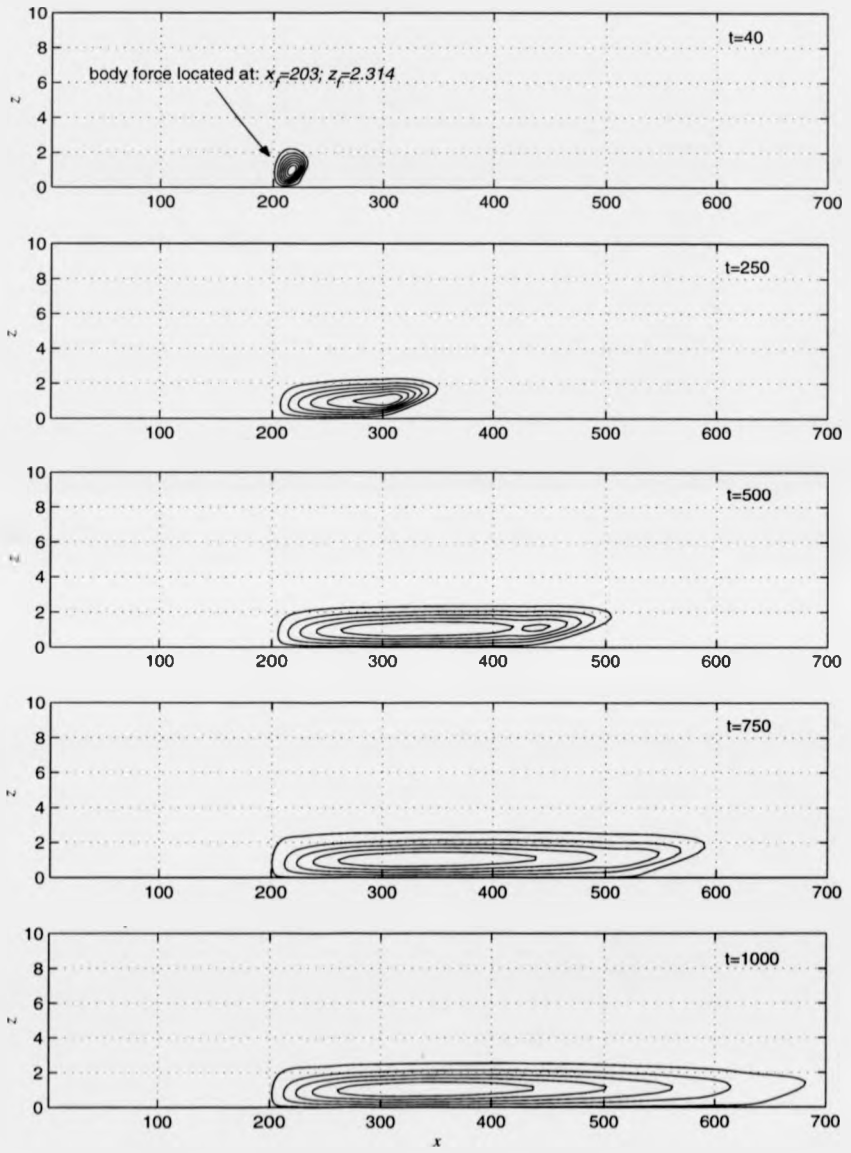

Figure 4.3: Streamwise velocity contours: Evolution of 'streaky structures' with time, t over a rigid surface. Spanwise wavenumber, β=0.07; R=1000; stationary and non-impulsive body force at a fixed location of x_f=203,z_f=2.314. Body force type $FC(c)$.

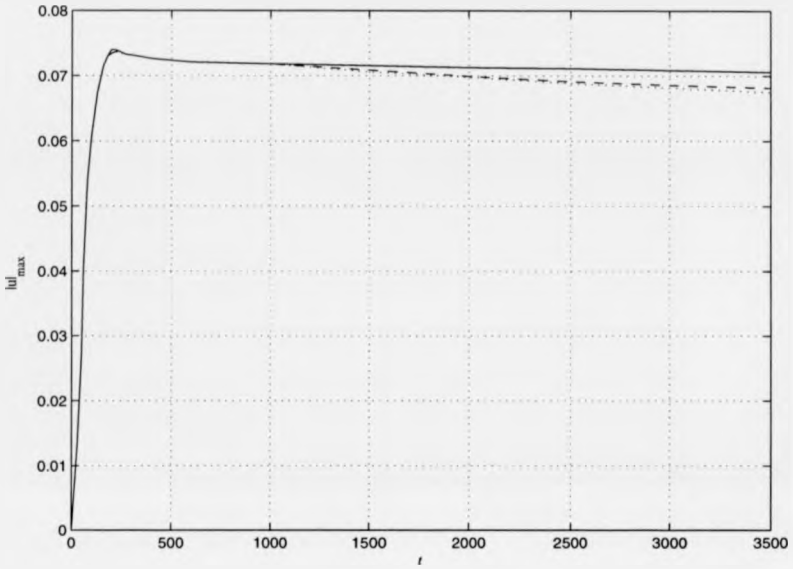

Figure 4.4: Amplitude, maximum streak velocity, $|u|_{max}$, as a function time, t for R=1000. Spanwise wavenumber, β=0.07; R=1000; stationary and non-impulsive body force at a fixed location of x_f=203, z_f=2.314. The long-term development of the streak with the linear viscous (−), linear inviscid (−−) and psuedo non-linear viscous (···) are shown. Body force type $FC(c)$.

The dominant, spanwise, vortical, Klebanoff mode observed in the Blasius boundary layer has been calculated. A trace of the variation of the maximum streak velocity, $|u|_{max}$ with time, t, indicates that after an initial rapid rise in amplitude, a maximum velocity is reached after which there is slow decay (Figure 4.4). Figure 4.4 suggests that the decay, whilst very slow is exponential. Comparison is made with the linear inviscid and linear viscous and psuedo non-linear viscous versions of the code. The latter retains the non-linear components from the convective quantity, **N**, (equation (3.7), and is discussed in greater detail in Chapter 5. The trace indicates that the inviscid results decay more rapidly than the viscous results. Due to the location of the

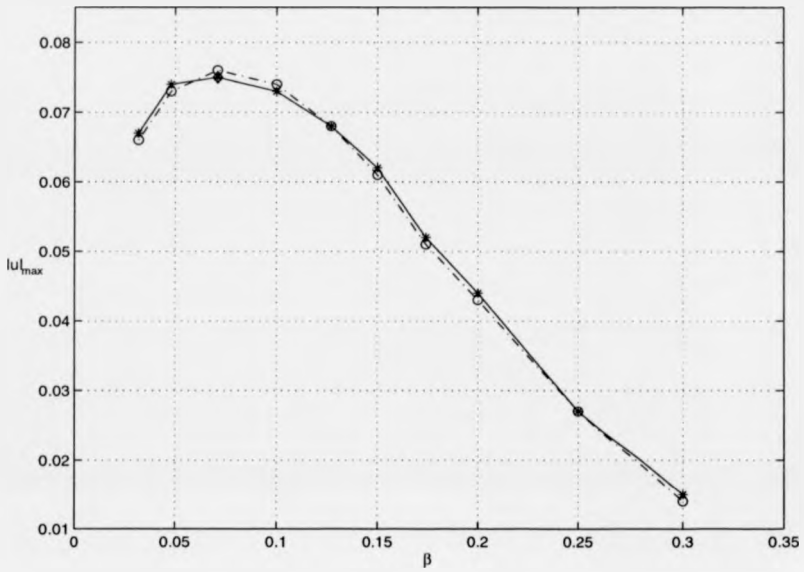

Figure 4.5: Amplitude, maximum streak velocity, $|u|_{max}$, as a function of the spanwise wavenumber, β, for R=1000. Our results for the maximum streak velocity, (-o-) are compared with simulations performed by Bertolotti (1997),(-$*$-). The maximum streak velocity for the Klebanoff mode at β=0.071 is observed experimentally by Klebanoff ($\diamond$). Body force type $FC(c)$.

streaks, one would expect the mechanism to be viscous and this is what is observed for the case where we use our code to simulate the near-wall structures in a turbulent boundary layer. Figure 5.3, in Chapter 5, shows, as expected that the viscous results decay more rapidly than the inviscid results.

Figure 4.5 illustrates the variation of $|u|_{max}$ with the spanwise wavenumber, β. Close agreement to the dominant spanwise wavenumber observed experimentally by Klebanoff, (reported by Westin *et al.* (1994) as β=0.071), and the series of simulations performed by Bertolotti (1997) was found.

The observation of streaks over rigid surfaces has been widely reported. Klebanoff

modes are not associated with exponential instabilities, like T/S waves, but instead grow and extend downstream in a manner such that the growth rate reduces as frequency increases. Note also, based on the low values of the streamwise vorticity, compared to wall normal and spanwise directions, it is believed that the low-frequency fluctuations associated with the Klebanoff mode are not streamwise vortices, but spanwise variations of the boundary layer thickness (Fasel, 2002).

It is important to note that a *linear* code is used to generate streaks in a parallel, Blasius boundary-layer. Although others have previously modelled Klebanoff modes linearly, at present there is some debate as to the validity of this. Most studies, (reviewed in §2.4 and §2.5), assume that the streak production is a non-linear phenomenon and is thought to give rise to bypass transition. The methodology adopted where the forcing of a single disturbance outside the (Blasius) boundary layer is sufficient to produce streaks with properties with characteristics that agree with experiments. Fasel (2002) suggests that it is intrinsically inadequate to model the streaks using a linear code, based on a linear perturbation of the boundary layer, as high amplitude disturbances cause non-linear effects that qualitatively change the scaling on the disturbances in the wall normal and streamwise directions. He advocates using a non-linear code where weakly non-linear perturbations are prescribed. From a practical view point, we are interested in the (prevention and) control of the streaks and as a result we are not concerned with the 'non-linear' developments. Our aim is, in the first instance, to determine whether streaks can develop over a compliant surface, and on the basis of this, it is a reasonable assumption to adopt a linear code to model the initial stages of streaks development. Studies by Henningson and his co-workers have concluded that streak production is subject to two receptivity mechanisms: A linear mechanism which is only efficient for freestream vortices, and a secondary non-linear mechanism, where the amplitude of the streaks grow sufficiently large for instabilities to develop and provoke early breakdown and transition (Berlin & Henningson, 1999). In Chapter

5 we describe the non-linear development of streaks (in a turbulent boundary layer)[1]. Finally, it is worth noting that a complete simulation of the evolution of freestream turbulence and its influence on the streak-like and other structures in a boundary layer would be beyond the limits of the most powerful computers available owing to the incredibly fine grid resolution and thousands of time steps required. A simplified model, containing sufficient physics to capture the relevant mechanisms and faciliate comparison with experiments is a more sensible approach.

4.2 Streaky Structures over Compliant Surfaces

We will now show that streaks are generated over a compliant surfaces in the same manner, albeit with much lower maximum amplitudes within a fixed Reynolds number range. To our knowledge, this appears to be the first such study of its kind. Of prime interest is how quickly and easily the streak can grow, and over an embedded panel, how easily it can adapt to the presence of compliance. The results indicate that with increasing freestream turbulence, streaks develop which may eventually form behaviour synonymous with bypass transition. In general, however, both wholly and embedded compliant panels appear to be remarkably resilient to disturbance growth when subject to relatively low levels of freestream turbulence.

4.2.1 A brief note on the selection of compliant wall properties

Bearing in mind that our ultimate aim is to provide information to aid the development of compliant surfaces for practical, (marine-type), applications, a short note on

[1]Non-linear terms would redistribute energy amongst disturbance frequencies but have no effect on the instantaneous growth rate of the energy. This implies that there must be a linear growth mechanism for the energy of a disturbance of any amplitude to increase. As the linearised N/S operator is non-modal for many (shear) flow cases, a significant transient growth of a given perturbation may occur before any subsequent exponential behaviour. In light of this, it is thought that such algebraic growth involves non-modal perturbations and can exist for subcritical values of the governing parameters

the selection of relevant non-dimensional, compliant-wall parameters, (m, T, d, B, K) is required.

The selection of non-dimensional wall parameters is based on those surfaces that have previously been found to delay transition in water at temperatures typical of marine environments. In view of this, the length of the domain can be carefully chosen to avoid any deterimental behaviour, such as growing T/S waves, and exclude the introduction of flow-induced, wall-based, surface instabilities. (This would have defeated the purpose of our study, unless caused by the development of the streaks themselves.) These limits are widely quoted for wholly and embedded compliant surfaces (Carpenter, Lucey & Davies, 2001). Using the information from the study of the generation of streaks over a rigid surface, (§4.1.3), it is reasonably straightforward to estimate the ideal wall and optimum spanwise forcing parameters and the critical Reynolds number ranges for streak production. A semi-heuristic approach is adopted, where wall properties of increasing flexibility are investigated.

There is a considerable degree of freedom in the selection of the wall parameters, bearing in mind the above selection criteria, and the method with which the wall parameters are non-dimensionalised. (As stated in §3.0, the wall properties, in the Blasius flow case are non-dimensionalised to ensure the dimensional variables remain fixed when the Reynolds number varies as a result of the flow behaviour in the streamwise direction.) Following Carpenter & Garrad (1985) the wall tension, T, is assumed negligible.

4.2.2 Development of Streaks over Compliant Surfaces

Figure 4.6 charts the temporal development of streaks over a surface without wall joins, with the wall properties:

$$m=\tfrac{1}{4};\ T=0;\ d=0;\ B=1.92\times10^{7};\ K=4B.$$

These properties are similar to the Kramer-type coatings, for the case where water flows over a flat plate studied by Carpenter & Garrad (1985). The surface is relatively

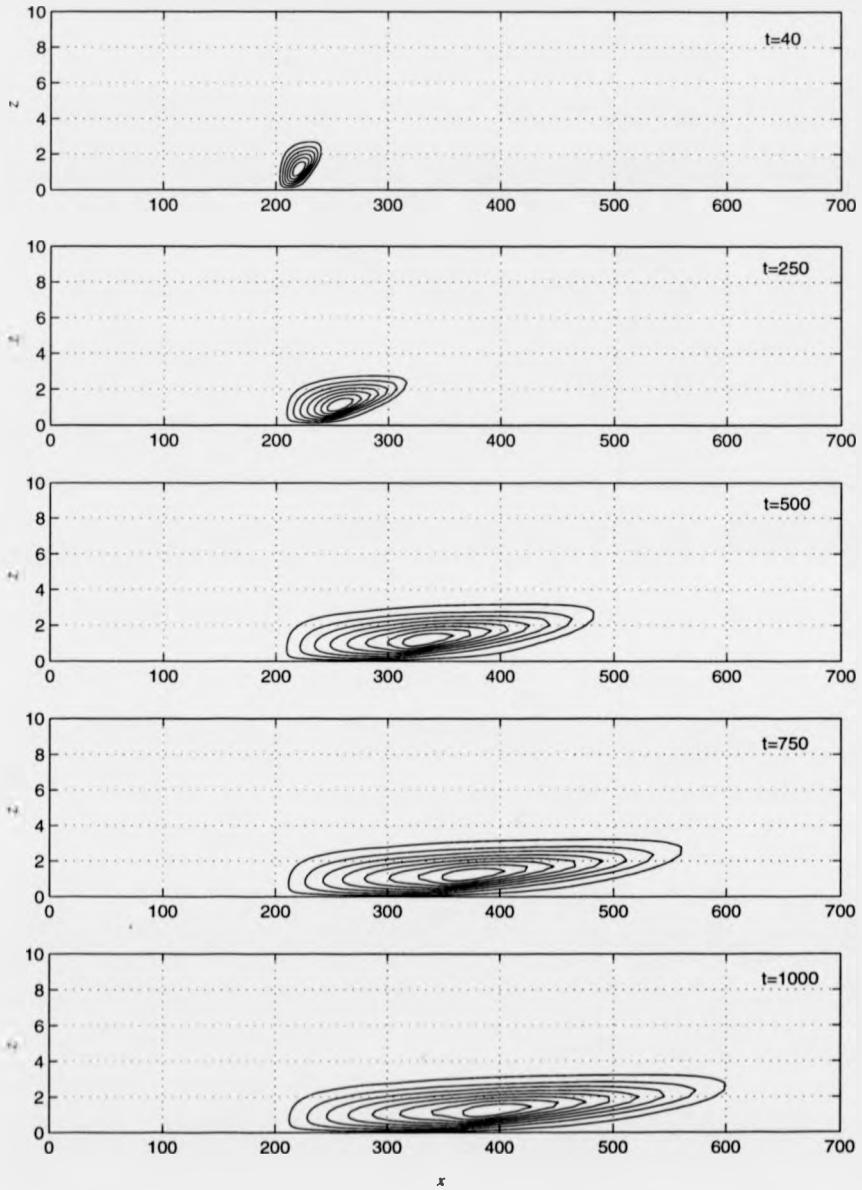

Figure 4.6: Streamwise velocity contours: Evolution of 'streaky structure' with time over a Kramer-type, compliant surface.(R=1000; β=0.083, Body force type $FC(c)$.)

stiff, primarily to avoid flow-induced surface instabilities.[2] The 'compliant streaks' were found to scale with the Reynolds number and evolve in an identical manner to those over a rigid surface. The major difference is that they appear to be narrower, shorter and weaker than their rigid counterparts, as seen in Figure 4.7 for R=1000. This behaviour is typical of other more flexible surfaces, within limits. A trace of $|u|_{max}$ with t, confirms that compared to those over a rigid surface, the compliant streaks develop at a much slower rate. Figure 4.8 shows how $|u|_{max}$ varies as a function of β between R=700-1500. As expected, $|u|_{max}$ falls as β varies over compliant surfaces. Comparison with rigid surface reveals a 40% reduction in $|u|_{max}$ for the 'best' case.

The results described thus far have been for a Kramer-type surface. It was found that the effect of increasing the flexibility altered the likelihood of streaks developing, and their reduced strength, (in terms of growth rate and $|u|_{max}$), downstream. In general, the stiffer the surface, the greater the likelihood that streaks develop. Over 'softer' surfaces, streaks develop, but grow at a much slower rate downstream. Accompanying this change, the streaks become increasingly narrow as they are prevented from growing.

Figure 4.9 illustrates how $|u|_{max}$ reduces with increasing flexibility for R=1000. Clearly, increasingly softer surfaces significantly reduce $|u|_{max}$ and shift the value of β at which streaks are most likely to grow. The massive reduction in $|u|_{max}$ with increasing flexibility is seen in Figure 4.9. Compared to the rigid wall, the most flexible streak-bearing surface, in this case a surface with wall properties which are a fifth the stiffness of the Kramer surface, yields a 81% (maximum) reduction of $|u|_{max}$! More flexible surfaces would be 'unstable' as they are capable of generating and supporting their own waves. Figure 4.10 plots the Reynolds number limits within which streaks can develop as a function of β. The graph seems to suggest that the more compliant the wall the wider the range of (R,β) in which streaks are seen. It is likely that the (frequency of) motion of the wall may prove beneficial at reducing the velocity per-

[2]We have demonstrated in Chapter 3 that if a T/S wave were to be generated over this surface, it would decay in a similar fashion to that over a rigid wall.

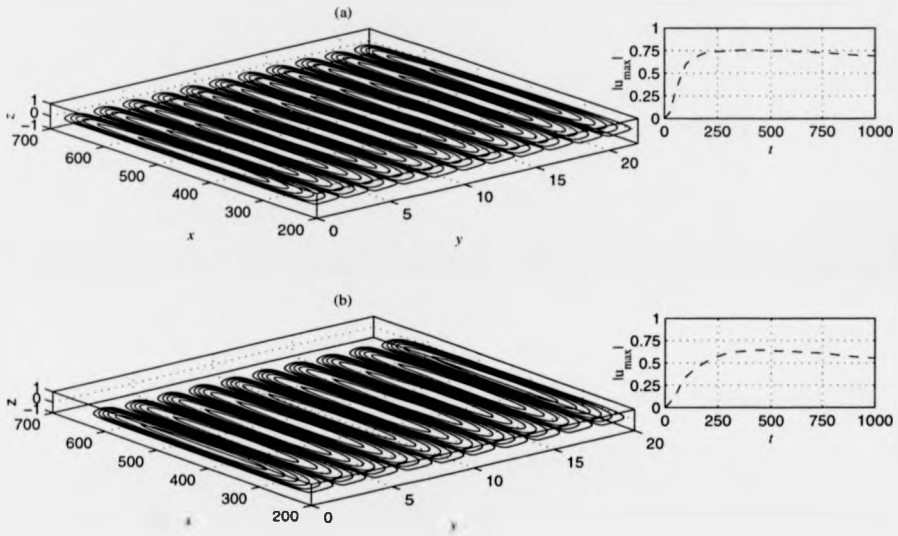

Figure 4.7: Spanwise perturbation velocity contours and variation of u at t=1000 over (a) rigid surface, and a Kramer type (b) compliant surface. The inset boxes chart how the maximum streamwise velocity varies with time, (t). Spanwise wavenumber, β=0.07; R=1000; stationary and non-impulsive body force at a fixed location of x_f=203, z_f=2.314. Body force type $FC(c)$.

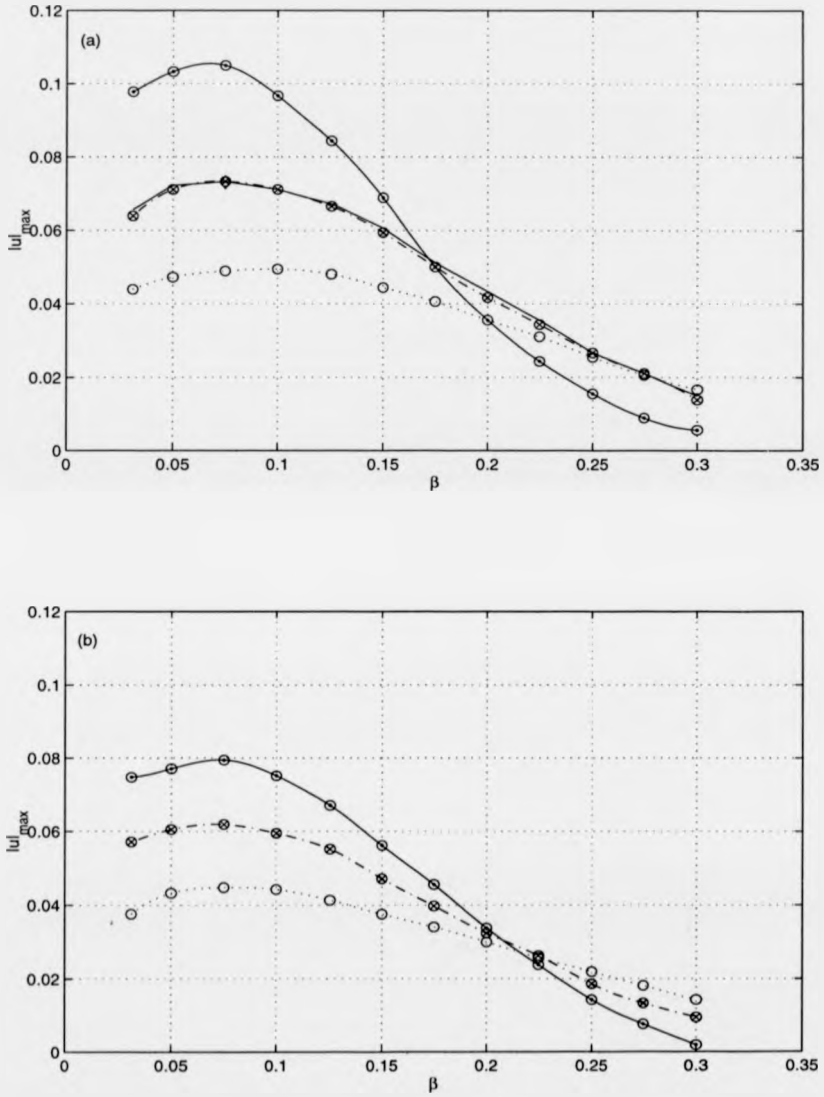

Figure 4.8: Amplitude, maximum streak velocity, $|u|_{max}$, as a function of the spanwise wavenumber, β, over a rigid (a) & compliant surface (b). Results are presented for the following Reynolds numbers: R=1414, (⊙-); R=1000 (⊗-·); R=707 (∘···); Bertolotti (1997) simulations denoted by the solid line. The maximum streak velocity for the Klebanoff mode is oberved experimentally at β=0.071 (⋄). The compliant surface appears to be more resiliant to streak growth. Body force type $FC(c)$.

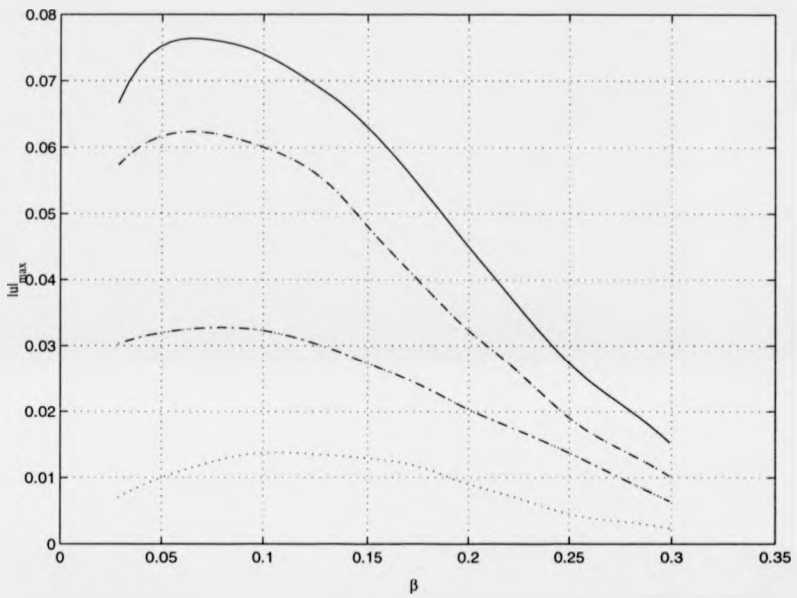

Figure 4.9: Amplitude, maximum streak velocity, $|u|_{max}$, as a function of the spanwise wavenumber, β, over compliant surfaces of increasing flexibility at R=1000. The maximum reduction in $|u|_{max}$, for the Kramer-type surface $(--)$ is 16.5%, and surfaces which have stiffness which are half, $(-\cdot)$, 57.1%; and third,$(\cdots)$, 80.5% of the Kramer surface. The solid line denotes results over a flat plate rigid surface. Increasing the flexibility of the surface, increases the resiliance to streak growth. Note, the massive reduction of amplitude with only a modest increase in surface flexibility. In general, the more flexible the surface the less the likelihood of streaks developing and extending downstream.

turbations associated with the streaks. As a result, the surface maintains a favourable environment to deter and slow streak growth. Consequently, the streaks are maintained for longer over the surface, delaying bypass and/or other associated transition scenarios. The wide range of (R,β) observed is a reflection of the ability of the motion of the wall to accommodate the velocity perturbations. A similar conclusion is made in Chapter 5, where the near-wall streak-like structures in a turbulent boundary-layer are investigated.

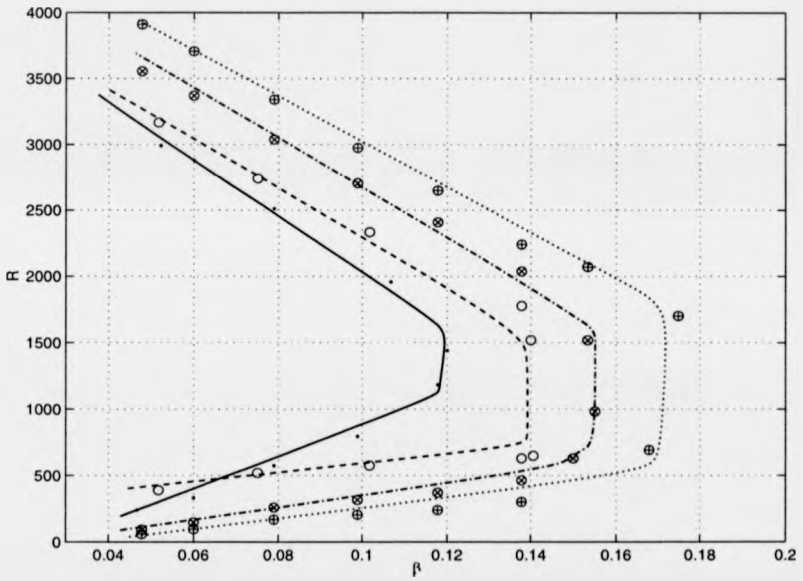

Figure 4.10: Spanwise wavenumber streak bearing limits, (β), as a function of the Reynolds number, R, for a rigid (-) and compliant surfaces. The lines indicate the boundary of streak production for a rigid ($-$) and Kramer-type compliant ($--$, $\circ$) surface and surfaces with a 1/2 and a 1/3 the level of the stiffness of a Kramer-type surface ($-\cdot$, $\otimes$) and ($\cdots$, $\oplus$) respectively.

It is not clear how to formulate a measure of how 'receptive' the boundary layer is to streak generation. Any measure, in terms of a coefficient, ReC needs to take into account the strength of the forcing produced by the body force and the subsequent response of the boundary layer some distance downstream. Initially we defined ReC as ratio between the vorticity gradient (multiplied by the total time, $\mathcal{T}$), divided by the strength of the forcing, G. This is a rather simplistic approach to adopt. The influence of the compliant wall through the form of its motion in order to sustain streak development is an additional factor which we have assumed is included in our equation (as a result of the vorticity gradient downstream). Close examination of our crude definition for ReC reveals that it is faulty, as G, the strength of the forcing, actually has dimensions of ((vorticity/time)×length^2)! This can be demonstrated. The definition for ReC, in this form, is:

$$\frac{|\frac{\partial \omega_x}{\partial z}|\mathcal{T}_{max}}{G}.$$

Now, an approximate form for Equation (4.9) may be taken as:

$$\frac{\partial F_y}{\partial z} = Ge^{i\beta y}\delta(x - x_f)\delta(z - z_f),$$

which only has meaning when integrated with respect to x and z. As a result, the total amount of vorticity generated by the body force is:

$$\frac{\partial}{\partial t}\int\int \omega_x dzdx = \int\int \frac{\partial F_y}{\partial z} dzdx = Ge^{i\beta y} \text{ or } G\cos\beta y.$$

Hence, G has the dimensions of (vorticity/time)×length^2, rendering our definition for ReC incorrect. Although not an inadequate measure, an alternative definition for ReC can be proposed which takes into the length of the streak at the time of its maximum strength, l_{max}. For this, first we assume that the rate of creation of streamwise vorticity at the source, (i.e. the body force), integrated over space is:

$$\int\int \frac{\partial F_y}{\partial z} dzdx = G\cos\beta y.$$

Assuming that the delta function has been modelled exactly, the above averages to zero in the spanwise direction. As a result, the root mean square value of the strength

of the forcing is used, $G/\sqrt{2}$, which could be compared with the maximum reached in the streak for $(\omega_x^2)^{1/2}$ integrated over the streak, or at least over the perturbation lying between one spanwise wavelength. *ReC* is now:

$$ReC = \frac{\left[\int\int\left(\int_0^{2\pi/\beta}\omega_x^2 dy\right)^{1/2} dxdy\right]_{max}}{\frac{G}{\sqrt{2}}t_{max}},$$

where the numerator is the maximum strength of the perturbation which is reached at t_{max}. This can be roughly approximated with:

$$ReC = \frac{|\frac{\partial\omega_x}{\partial z}|_{max} \times \delta^* \times l_{max}}{\frac{G}{\sqrt{2}}t_{max}}. \tag{4.10}$$

Figure 4.11 compares how *ReC* varies as a function of β for a rigid wall with a series of Kramer-type surfaces of increasing flexibility. A low *ReC* denotes a low receptivity to streak development, (and hence slow streak development), and *vice versa*. The curves become shallower with increasing surface flexibility, and the spanwise wavenumber, β, increases as *ReC* falls. As a result, it can be deduced that the compliant surface appears to be very resilient to streak formulation. The value of *ReC* indicates that, compared to the rigid case, a relatively high degree of forcing, (or freestream turbulence), needs to be applied to generate consistent streaks.

A better measure to reveal the behaviour of the streaks and surface is the energy flux and enstrophy. This is especially pertinent for the case where a compliant panel is embedded in a rigid surface and will be described in the next section.

4.2.3 The Evolution of Streaks over Compliant Panels

The idea of using compliant panels derives from work by Carpenter and his co-workers. A series of panels, as opposed to a single, long panel, spanning a fixed finite length to delay transition has a number of practical advantages. Besides the obvious ease of manufacture, it would be possible to achieve T/S supression more effectively by tailoring the wall properties of individual or sets of panels to specific local Reynolds number ranges. In addition, Lucey & Carpenter (1993a) have shown that shorter panels are less

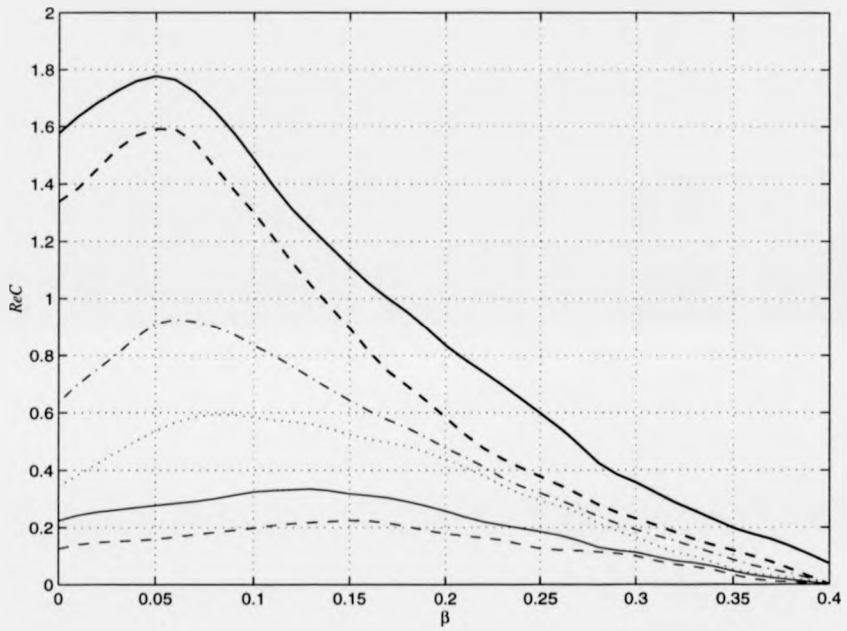

Figure 4.11: Receptivity Coefficient (ReC) as a function of spanwise wavenumber, β, over compliant surfaces of increasing flexibility. Each curve corresponds to walls of reducing stiffness: (The bold $-$) line corresponds to a rigid surface and $(--)$ a Kramer-type surface. $(-\cdot)$,$(\cdots)$,$(-)$ and $(--)$ denotes surfaces which have 1/2, 1/3, 1/4 and a 1/5th of the stiffness of the Kramer surface. A low ReC indicates a low receptivity to streak development and *vice versa*.

prone to hydroelastic instability compared to longer panels. Recent work has shown that, at least in theory, the use of only two panels can lead to a substantial rise in transition delay, compared to a compliant wall whose properties are invariant in the streamwise direction (Carpenter, 1993; 1998).

The present study was carried out with the same ethos as Davies & Carpenter (1997). They showed that short embedded panels, with lengths comparable to a T/S wavelength or less are capable of suppression, and investigated the effect of the leading-edge, (rigid-compliant) and trailing-edge, (compliant-rigid), joins. The length of the panel needed to sustain streaks is not our main interest. Instead, the prime focus resides with whether the panel can bear streaks and, the effect of the leading- and trailing-edge joins (Figure 4.12).

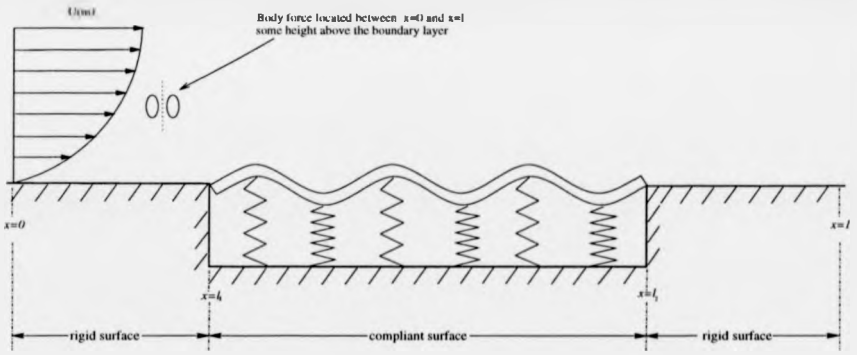

Figure 4.12: Embedded Compliant Panel

Identical results to those obtained in §4.2.2 are obtained when the body force is placed *over* the compliant panel. The body force is located downstream from the leading-edge of the panel, typically 150 streamwise wall-units downstream of the join. The panel is an appropriate length for the relevant material properties and Reynolds number range. This allows the streaks to develop in the same way as over a wholly compliant surface before passing over the trailing-edge join. Poor implementation of the body force leads to detrimental effects arising over the panel, especially at the trail-

ing edge. This results in the creation of unphysical disturbances, such as reflections interfering with the streaks and forcing other wall- and/or fluid-based instabilities to form. These simulations serve to show that the character of the streak is largely unaffected at the trailing-edge join over Kramer-type surfaces.

Figure 4.14 shows that as the streak evolves, it appears to grow and leave the panel unchanged. Note the qualitative difference in the streaks. The growth of the streak rapidly adjusts once it has left the compliant surface until it attains the characteristics observed over a rigid surface. As expected, a trace of the variation of $|u|_{max}$ over the compliant panel reveals a small, but discernible disturbance at the trailing-edge (Figure 4.14(b)).

Increasing the level of forcing, (to values within the threshold range defined in §4.2.2), had no undesirable effect on the streaks passing over the trailing-edge. In light of this, the disturbance generated is likely to be the effect of the adjustment of the compliant surface to a rigid surface and is also likely to be composed of numerical errors associated when resolving the flow at the trailing-edge. Other additional disturbances due to scattering at the trailing-edge are generated which may promote the growth of the streak. The disturbance could be viewed as a tiny trip-element which provides an additional packet or kick of energy to maintain streak growth, whilst the characteristic properties of the surface changes. However, this is unlikely at low Reynolds numbers for such relatively stiff compliant surfaces, bearing in mind the level of forcing required and stable nature of the streak. In addition, for further confirmation, no evidence of the generation of T/S waves or large reflections were observed as a result. (Improvements to minimise the numerical errors with a buffer domain, or the trailing-edge boundary conditions made no worthwhile improvement.)

Therefore, to conclude: the trailing-edge join has no detrimental effect on the development of streaks downstream over Kramer-type surfaces. The streaks extend far downstream onto the rigid surface, and would break down in the conventional manner. The join does not play a destructive rôle, except over very flexible compliant surfaces, in which case the material is capable of supporting its own waves in the way described

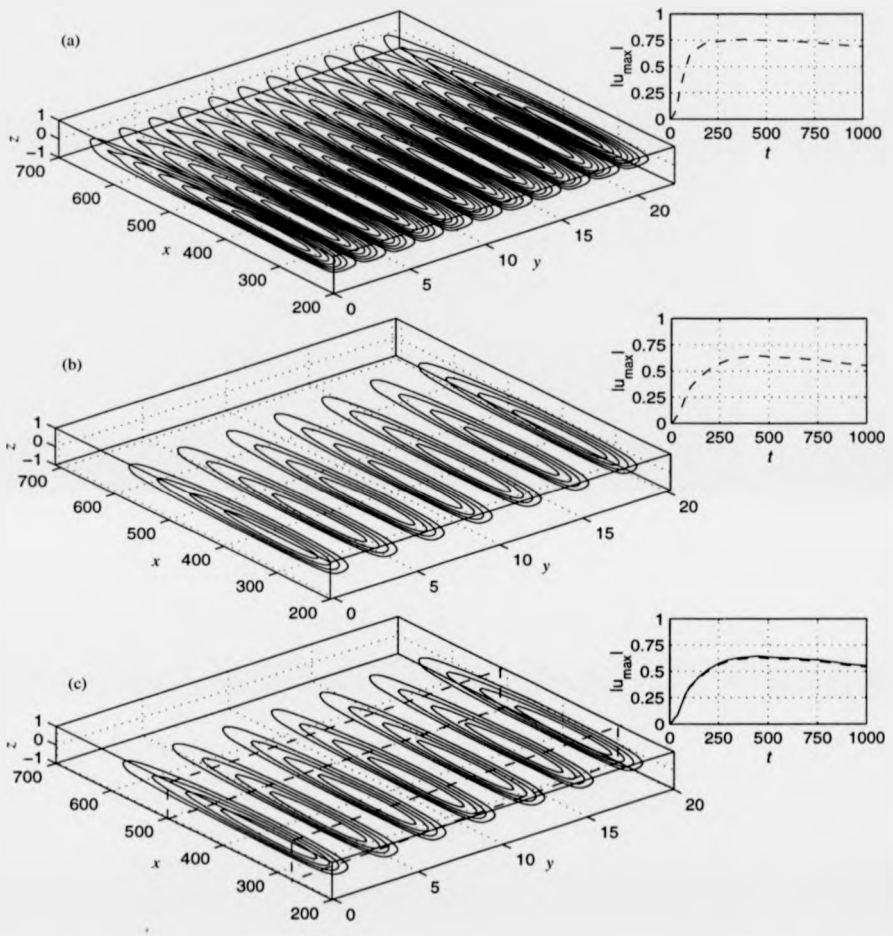

Figure 4.13: Spanwise perturbation velocity contours at t=1000 over (a) rigid surface, and Kramer type (b) wholly and (c) embedded compliant surfaces. The inset boxes chart how the velocity varies with time, t. (c) refers to the case where the body-force is placed over the compliant surface sufficiently far away from the L/E join, but at a comparable location to (a) and (c). The location of the panel is clearly marked in (c). (The following parameters are set: Spanwise wavenumber, β=0.071; R=1000; stationary and non-impulsive body force at a fixed location of x_f=203, z_f=2.314. The location of the leading and trailing edges of the panel are marked by (−−) in (c). Body force Type $FC(c)$.

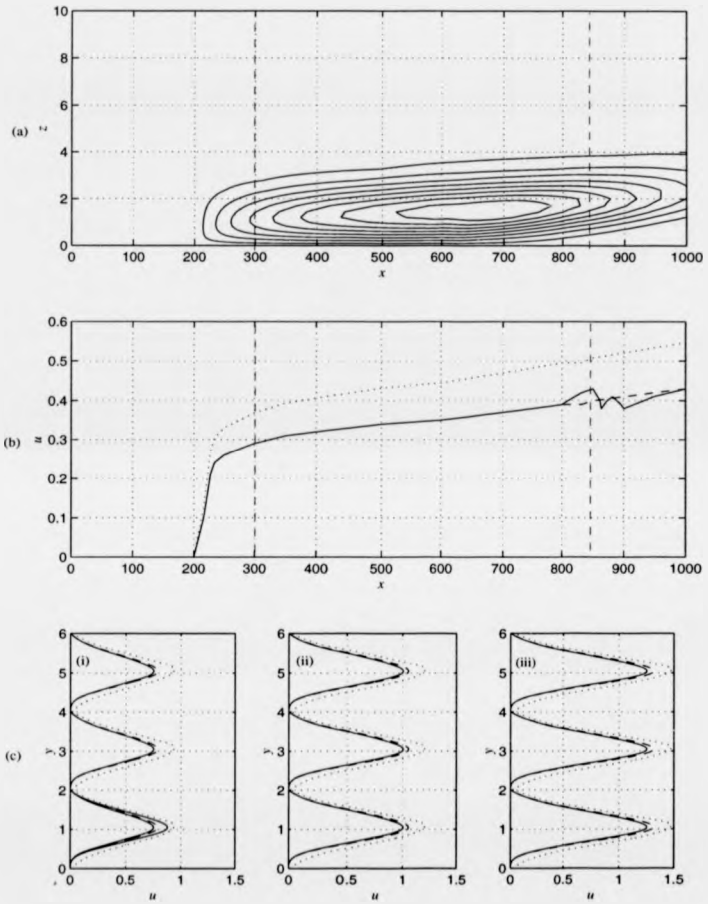

Figure 4.14: Streamwise perturbation velocity contours, (a), and variation of u in the streamwise (b), and spanwise (c), directions for a streak generated over an embedded, Kramer-type, compliant panel at t=1000. L/E and T/E denote the panel ends. Note that a stationary and non-impulsive body force is positioned *on* the compliant panel at a fixed location of z_f=2.314. (β=0.07; R=1000). Body force Type $FC(c)$.

earlier. The most flexible embedded compliant surface that can sustain streaks generated in this way, is one which has only a stiffness of 25% of the Kramer surface (Figure 4.15).

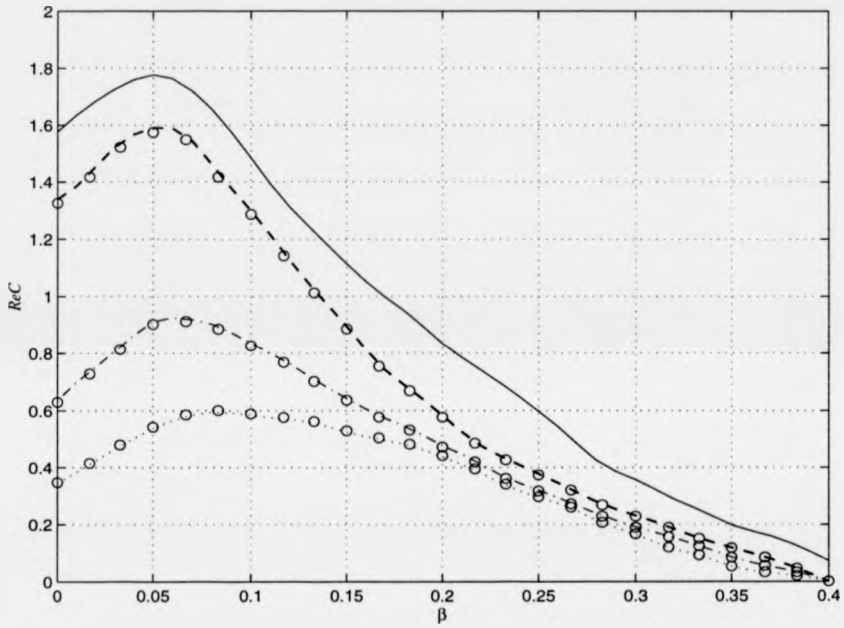

Figure 4.15: Receptivity Coefficient (ReC) as a function spanwise wavenumber, β, for embedded and wholly compliant surfaces of increasing flexibility. Each curve corresponds to walls of reducing stiffness- the $(-\cdot)$ and $(\cdots)$, denote surfaces which have a half and a third of the stiffness of the Kramer surface $(--)$ respectively. The coefficients for the case where a streak is generated on and allowed to leave a compliant panel are denoted by $(\circ)$. The solid line indicates a flat-plate rigid surface.

We will revisit the effect of the trailing edge in more detail for the more important case where the streak is allowed to develop onto and out of the panel.

Local and global behaviour of compliant panel

Our focus has, so far centred on the case where the streaks were generated on the panel, and allowed to leave. This revealed features of the trailing edge. This section will concentrate on the more pertinent case where streaks are generated over the rigid surface and then allowed to develop over the panel. This will illustrate the global effectiveness of the panel, and the behaviour in the vicinity of the leading and trailing edges.

In general, the same basic trend reported in §4.2.2 is followed, i.e. the more flexible the surface, the slower the growth of the streak and *vice versa*. Previously, the trailing-edge join introduced an additional disturbance, which may have contributed to the adjustment of the streak and the subsequent maintenance of its growth over the rigid surface. This effect, within the Reynolds number and material ranges, did not qualitatively alter the streaks appearance, except in cases where very flexible panels were implemented. A similar result may be expected where streaks are initiated over the rigid surface, i.e. the leading edge can adjust easily to the streak. This was true for only a narrow range of Reynolds numbers. The leading edge appeared to introduce locally detrimental effects. Now, the join has to rapidly adjust to and sustain a relatively high-strength streak and hence needs to be resilient to any additional disturbances. In other words, the leading edge has to aid the streak to effectively 're-tune' itself as it passes onto the compliant surface.

Davies & Carpenter (1997) noted that the panel can exert powerful upstream effects when T/S waves propagate over its surface. These disturbances originate locally in the vicinity of the trailing edge join, or over a greater distance, take the form of an (upstream) flow-induced wave. With regards to streak production, the simulations described here suggest a combination of competing mechanisms and/or disturbances are present, which have a strong dependence on the material and flow parameters. These include: the development and strength of the streak by the body force; and the amplification of disturbance at the join. The latter manifest themselves as scattered perturbations and additional numerical errors at the leading edge. Whilst these effects

are locally confined, they can be dangerous if unchecked, especially over insufficiently long panels. We show that by choosing the correct material properties it is possible to reduce the locally detrimental impact of the leading edge. Our initial description will focus on this disturbance, and how it affects streak production and flow/surface stability.

For these computations, the body force is placed on the rigid surface sufficiently far away from the inlet, to avoid any reflections affecting the streaks (Figure 4.12). The body force is positioned such that streaks are allowed to develop sufficiently fully before passing over the leading-edge join. (Typically, 200 streamwise wall-units upstream of the inlet, and 200 streamwise wall-units downstream of the leading-edge.) The panel length is appropriately fixed for each particular Reynolds number and material type to account for any local end effects and instabilities to decrease in magnitude and therafter promote streak growth and avoid other instabilities. Behaviour over a Kramer-type surface, with the properties described in §4.2.2 will be considered.

Figure 4.16 charts the temporal evolution of a 'stable' streak at R=1000. A 'stable' streak is defined as one which develops over the length of the domain unaffected by effects at the leading and trailing edges. Figure 4.17 shows the amplitude of the streaks have reduced. Qualitative comparison with streaks developed over wholly compliant (Figure 4.6) and rigid (Figure 4.3) surfaces reveals that the streaks are slightly 'weaker', and significantly narrower. Figure 4.18 illustrates how the Reynolds number ranges have narrowed. Accompanying this it can be deduced that a greater degree of spanwise forcing is required to force and maintain the growth of streaks over the panel. This is an indication of the difficulty with which it is possible to sustain streaks over the panel without the detrimental influence of the leading-edge. Figure 4.18 defines the narrower Reynolds number range with the increased spanwise forcing now required, compared to the wholly compliant surface.

Figure 4.19 shows the effect of streak production on progressively flexible surfaces. As the flexibility increases, the value of $|u|_{max}$ falls substantially. There is an even narrower range over which streaks can be generated. Figure 4.20 shows how ReC varies as

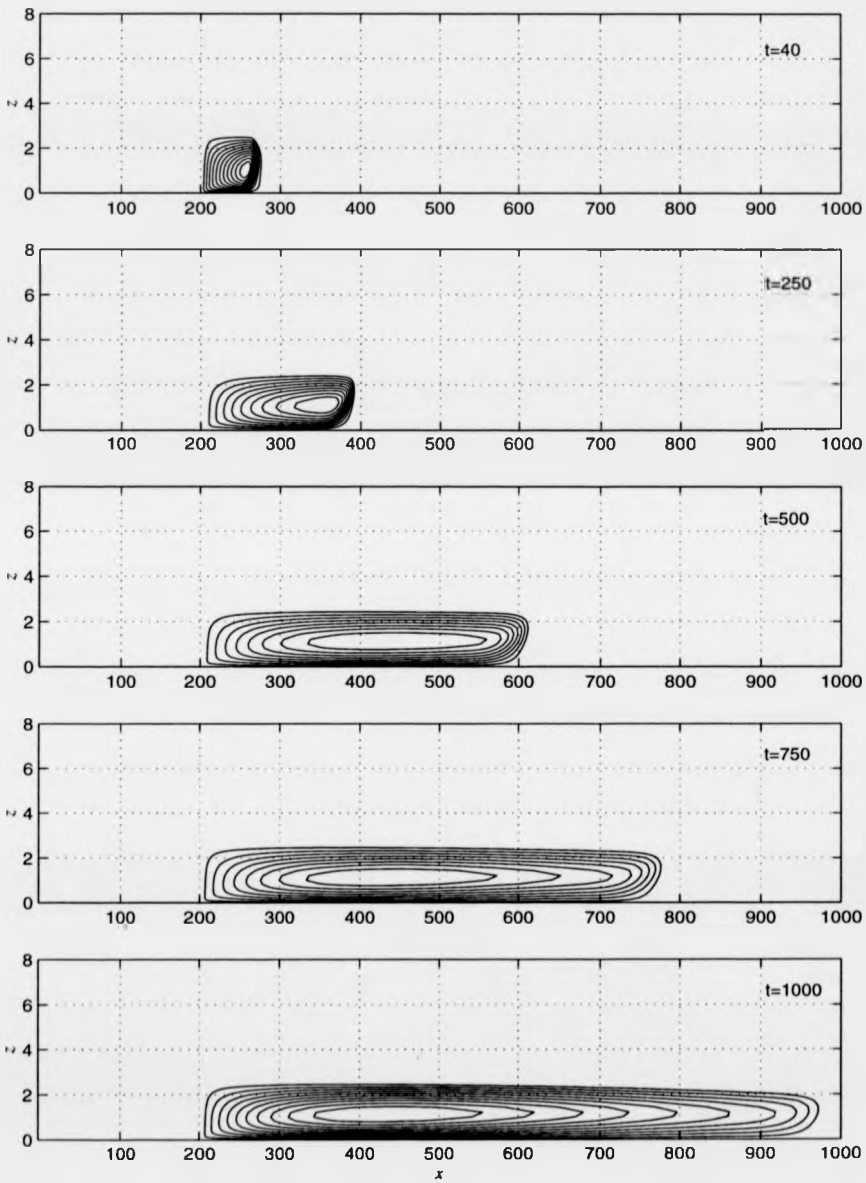

Figure 4.16: Streamwise velocity contours: Evolution of 'streaky structure' with time over a Kramer-type, wholly compliant surface. (R=1000; β=0.04. Panel situated between x=203, to x=800. Body force type $FC(c)$.

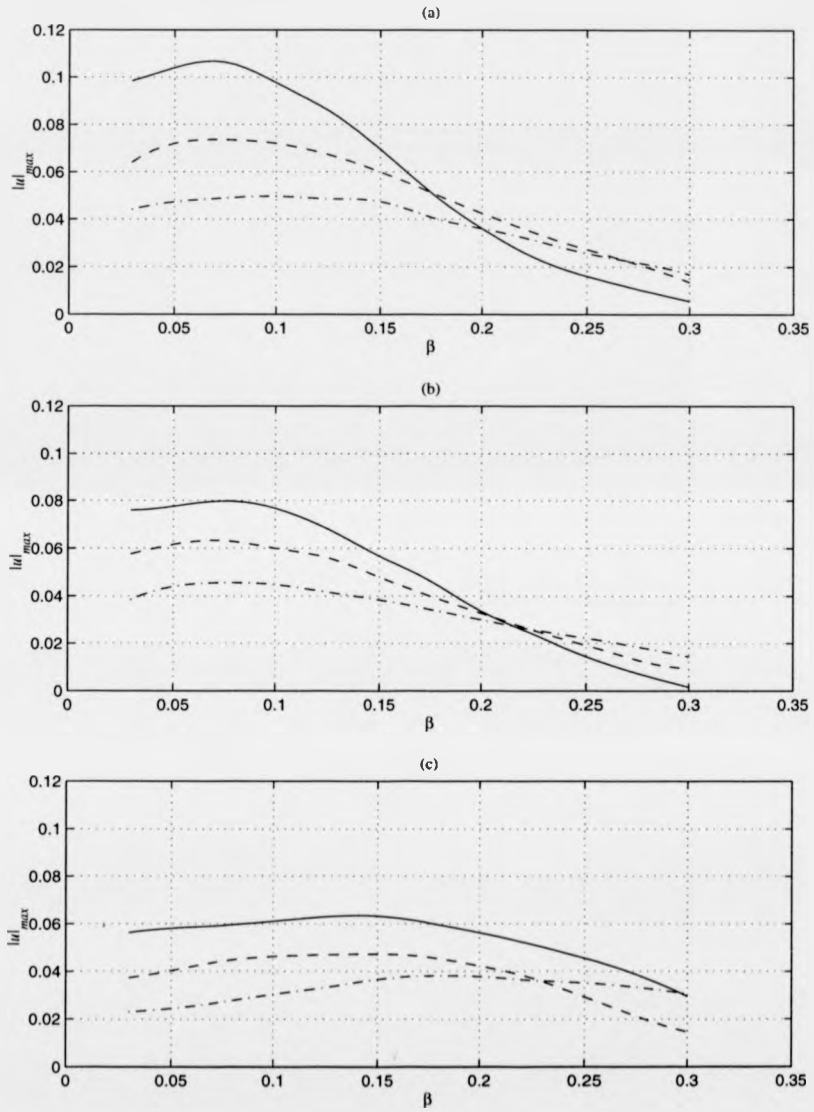

Figure 4.17: Amplitude, maximum streak velocity, $|u|_{max}$, as a function of the spanwise wavenumber, β, over a rigid (a) and compliant surface, (b), and panel (c) respectively. Results are presented for the following Reynolds numbers: R=1414, (−); R=1000 (−−) and R=707 (−·). The compliant surface appears to be more resilient to streak growth.

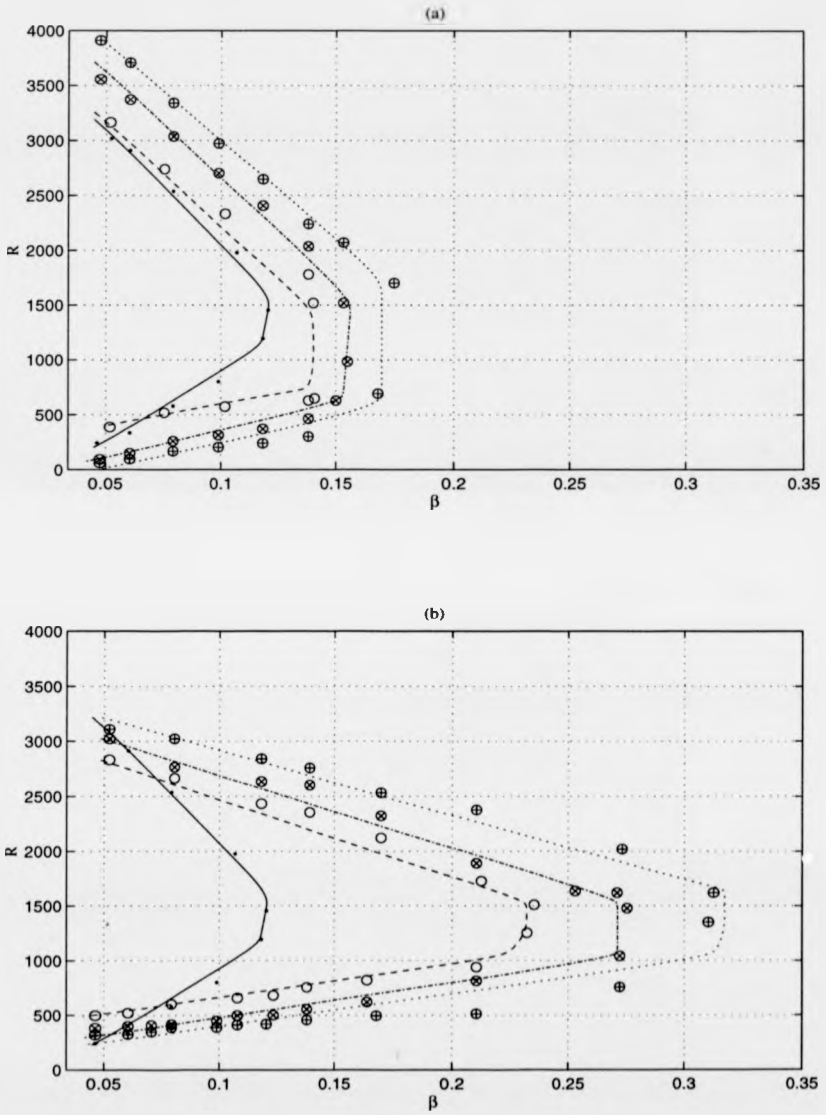

Figure 4.18: Spanwise number streak bearing limits, (β), as a function of the Reynolds number, R, for compliant (a) surfaces and (b) panels. The lines indicate the boundary of streak production for a rigid ($-$,$\cdot$) and Kramer-type compliant ($--$,$\circ$) surface and, a surface with 1/2, ($-\cdot$,$\otimes$), and 1/3, ($\cdots$,$\oplus$), the stiffness of a Kramer-type surface.

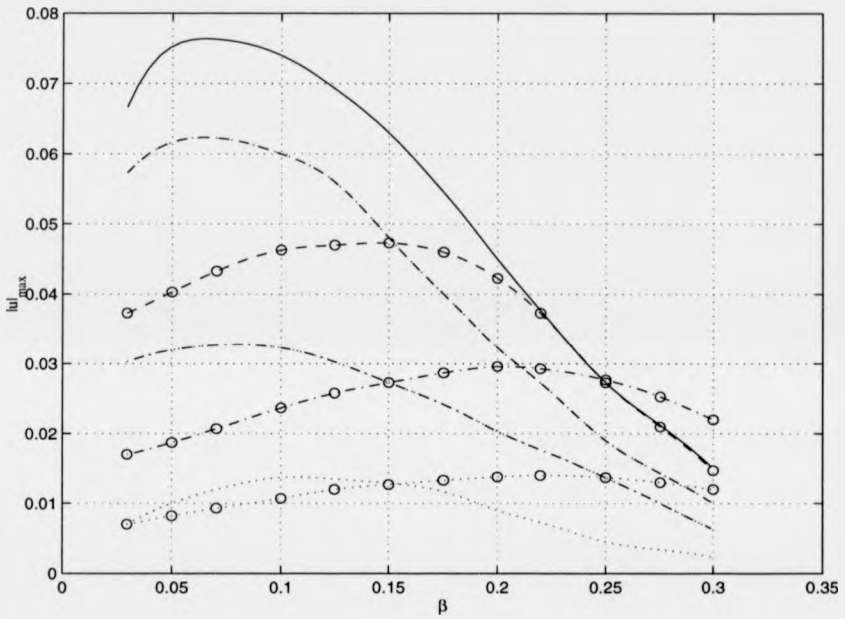

Figure 4.19: Amplitude, maximum streak velocity, $|u|_{max}$, as a function of the spanwise wavenumber, β, over wholly and embedded compliant surface of increasing flexibility. The maximum reduction in $|u|_{max}$, for the Kramer-type surface $(--)$, and surfaces which have stiffness which are half, $(-\cdot)$ and third,$(\cdots)$ of the Kramer surface are compared to compliant panels with identical material stiffness $((-\circ-)$, $(-\circ\cdot)$ and $(\cdot\circ\cdot)$ respectively). The solid line denotes results over a flat-plate rigid surface. The body force is located upstream of the leading edge of the panel.

a function of β for a range of streak-bearing surfaces. Surfaces more flexible than one with one-third the stiffness of the Kramer surface cannot effectively bear streaks. The definition for ReC has been modified to only include the effect of the body-forcing. This is achieved by running simulations without the body force, noting the effect of the leading edge and subtracting this away from those with the body force. Although not strictly rigorous, this is a reasonable first approximation as a measure of streak receptivity.

As expected, a trace of the variation of $|u|_{max}$ over the domain revealed that there were no significant disturbances at the trailing edge. This is largely due to the relatively weak nature of the streaks. Thus, the streak passes over to the rigid surface unaffected and then rapidly attains a growth rate characteristic of a rigid surface. It is unlikely that the disturbances at the trailing edge promote the growth of the streak over the rigid surface for the reasons outlined earlier. (Any 'glitches' at the trailing edge can be minimised with the introduction of a suitable buffer domain.)

The local disturbance observed at the leading edge can be examined by tracing the variation of the disturbance enstrophy and kinetic energy of the streak propagating in its vicinity. These two quantities are defined as:

$$E_d = \frac{1}{2}\int_0^z \left(u^2 + v^2\right) dz \text{ and} \tag{4.11}$$

$$E_n = \int_0^z \omega^2 dz. \tag{4.12}$$

It was found that there was an increase of the two quantities in the vicinity of the leading edge is followed by a smaller decrease as the streak propagates over to the trailing edge. The growth of the streak over the bulk of the panel is similar to a comparable one over a surface without the influence of joins. The behaviour appears to be the reversed to that at the trailing edge. After passing the trailing edge the streak magnitude is slightly increased. The disturbance at the leading edge appears to be representative within the limits described earlier. Note that the panel joins can generate locally detrimental effects which can have a significant global effect, such as to produce a T/S wave, (or others that can occur in the presence of wall roughness).

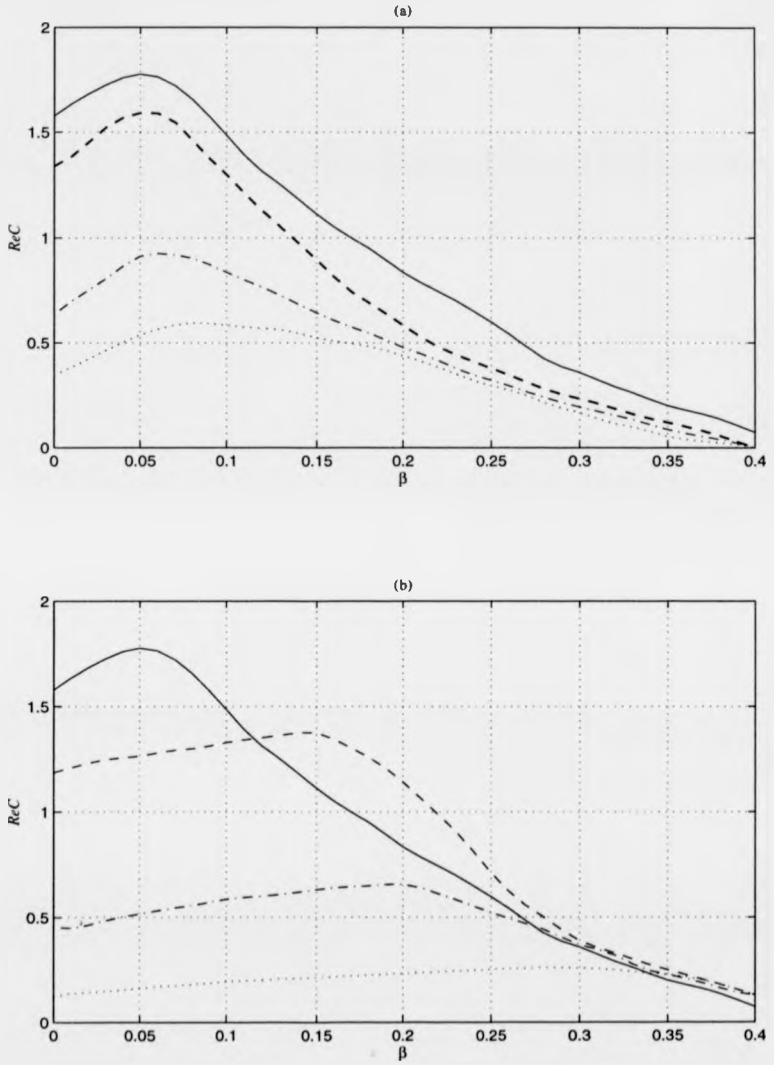

Figure 4.20: Receptivity Coefficient (ReC) as a function of spanwise wavenumber, β, over compliant surfaces (a), and panels (b) of increasing flexibility. Each curve corresponds to walls of reducing stiffness: $(-)$ corresponds to a rigid surface and $(--)$ a Kramer-type surface. $(-\cdot)$ and $(\cdots)$ denotes surfaces which have 1/2 and a 1/3rd of the stiffness of the Kramer surface respectively. A low ReC indicates a low receptivity to streak development and *vice versa*. The solid line corresponds to a rigid surface.

This behaviour is observed in Figure 4.21, which plots the terms in the expression for the kinetic energy. This allows the relative importance of the various physical processes to be gauged. The expression can be derived by multiplying the governing u-, v- and w-momentum equations by u, v and w respectively. The incompressibility condition and definition for ω is employed. In the first instance this yields:

$$\Big(\frac{\partial}{\partial t}+U\frac{\partial}{\partial x}\Big)\Big[\frac{1}{2}\Big(u^2+v^2\Big)\Big]+uv\frac{dU}{dy}+\frac{\partial(up)}{\partial x}+\frac{\partial(vp)}{\partial y}=\frac{1}{R}\Big(\frac{\partial(u\omega)}{\partial y}-\frac{\partial(v\omega)}{\partial x}-\omega^2\Big). \quad (4.13)$$

The time derivative in this expression is eliminated by averaging over a the time of maximum growth of the streak (referred to as the period herein) and integrated with respect to the height of the boundary layer to give:

$$\begin{aligned}&\frac{d}{dx}\Big[\overbrace{U\frac{1}{2}\int_0^z(\overline{u^2}+\overline{v^2})dz}^{(A)}+\overbrace{\int_0^z\overline{up}dz}^{(B)}+\overbrace{\frac{1}{R}\int_0^z\overline{v\omega}dz}^{(C)}\Big]\\&=\underbrace{\int_0^z(-\overline{uv})U'dz}_{(a)}-\underbrace{\frac{1}{R}\int_0^z\overline{\omega^2}dz}_{(b)}-\underbrace{\overline{v_wp_w}}_{(c)}+\underbrace{\frac{1}{R}\overline{u_w\omega_w}}_{(d)}\end{aligned} \quad (4.14)$$

where, the quantities with an overbar are those which have been averaged over a period. (A) denotes the average disturbance kinetic energy convected past a streamwise location. (B) and (C) describe the rate of work done by the fluid disturbance against the perturbation stresses at a known streamwise location. Term (C) is negligible in magnitude. Collectively, the first two terms on the right hand side of Equation (4.14) describe the energy balance between energy production and removal. (a) defines the rate of Reynolds stress production and (b) the rate of viscous dissipation. Term (c) defines the rate of irreversible work done to the wall by the disturbance pressure. (d) cannot easily be attributed to energy transfer processes between the fluid and wall. Carpenter (1990) and later Davies (1995) define (d) as an extra energy-removal term equivalent to additional viscous dissipation. It is worth adding a note of caution here. We do not claim our calculations for the energy terms to be strictly correct. This is because it is difficult to determine as to what time period to choose to perform the calculation. It may be probable that our runs are too short, which is a valid criticism

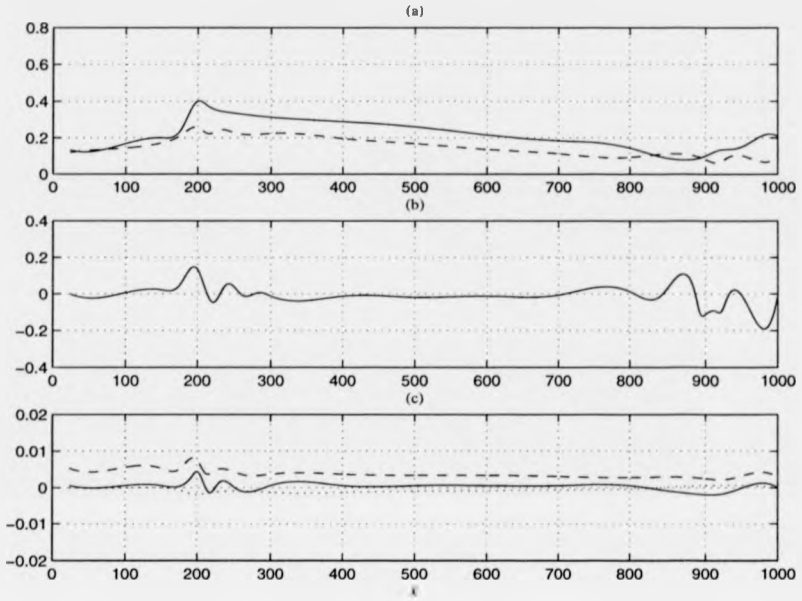

Figure 4.21: Streamwise variation of energy components over a compliant panel. (a) shows variation of terms A $(-)$, and B, $(--)$, (b). shows variation of Reynolds Stress term, a, and (c) shows variation of terms b, $(--)$, c, $(-)$, and d $(\cdots)$. (R=1000; β=0.04, body force type $FC(c)$, Panel situated between x=203, to x=800.)

which is acknowledged here. A similar criticism can be made in Chapter 5.

Examination of the variation of these quantities in Figure 4.21(b) reveals that all the quantities are the same order of magnitude, except that the Reynolds Stress dominates the other quantities over the panel-edges. Much in the same way as found for the T/S disturbances at the edges, the large abrupt change in the Reynolds Stress production is responsible for sharp changes in the disturbance enstrophy and kinetic energy. Accompanying this change is a smaller change in the pressure work. The size of Reynolds Stress at the leading and trailing edges are determined by subtle differences between the streamwise and wall normal velocities in the vicinity of the joins. The

leading-edge exerts a considerable upstream influence as the Reynolds Stress production begins to rise steeply well before the wave reaches the join. A similar destructive interference occurs at the trailing-edge.

It appears that, in this case, the disturbance at the leading edge can either prove detrimental by introducing a T/S wave, or some other fluid or wall-based disturbance, or it can prove benefical by providing an extra boost to maintain the streak over the join downstream. The amplitude of the disturbance at the join is crucial in determining the subsquent behaviour downstream. Effectively, two receptivity sources exist- the body-force and join. However, any analysis linking the magnitude of the wall motion and velocity at the leading-edge, to the amplitude of the body force as a function of the Reynolds number proved to be inconclusive in highlighting the different components. Similarily a plot of the ratio of the total disturbance vorticity to the disturbance vorticity produced by the body force as a function of the Reynolds number proved inconclusive. (In this case if the ratio exceeded unity, some additional vorticity is generated by the mismatch at the join destroying the streak.) A Fourier analysis of the disturbance at the joins was performed, but the results proved to be inconclusive.

4.2.4 Orthotropic Surfaces

Orthotropic surfaces are those where the flexibility of the panel is different in the spanwise and streamwise directions. Our motivation is to determine whether the streak properties are attenuated or enhanced under this situation. There is a limited body of work describing the passive control of boundary-layer disturbances with plate orthotropicity. See, for example the work by Yeo (1986, 1990, 1992), Joslin, Morris & Carpenter (1991) and Carpenter & Morris (1990). The latter model the anisotropic material used in a series of experiments on turbulent flow by Grosskreutz (1971, 1975). The anisotropic plate-spring model developed by Carpenter & Morris can be viewed as an approximation to a flexible plate supported by fibre-composite sheets or a thin-plate supported by spanwise ribs. The model is essentially a series of hinged and sprung rigid

members, the angle of which can be varied to allow horizontal and vertical movement. Thus, the flexibility can be easily controlled in the spanwise direction. The plate motion is treated such that each element of the plate can oscillate in a pendulum-like motion about its rigid member. We do not fully adopt this model. Instead, a number of modifications were made to our existing plate-spring model.

Consider the plate-spring governing equation:

$$m\frac{\partial^2\eta}{\partial t^2} + \frac{d}{R}\frac{\partial\eta}{\partial t} + \frac{1}{R^2}\left(\mathcal{B} - T\frac{\partial^2}{\partial x^2} + K\right)\eta = p_{wall}. \tag{4.15}$$

The differential operator for the orthotropic plate, ($\mathcal{B}$) can be written as:

$$\mathcal{B}\eta = \left(B_x\frac{\partial^4}{\partial x^4} + 2B_{xy}\frac{\partial^4}{\partial x^2\partial y^2} + B_y\frac{\partial^4}{\partial y^4}\right)\eta, \tag{4.16}$$

and the coefficients of flexural rigidity are defined as:

$$B_x = \frac{E_x h^3}{12(1-\nu_x\nu_y)}, \quad B_{xy} = \nu_y B_x + \frac{Gh^3}{6} \quad \text{and } B_y = \frac{E_y h^3}{12(1-\nu_x\nu_y)}.$$

The suffices define the direction and the elastic moduli, Possion ratio and the shear modulus of plate material are denoted by E, ν and G respectively. G is defined as:

$$G = \frac{E}{2(1+\nu)}.$$

We follow Lucey & Carpenter (1993) by introducing an 'orthotropicity parameter', f_o, and assume the relationship: $E_x\nu_y{=}E_y\nu_x$ holds. In doing so, the differential operator is transformed to the biharmonic operator:

$$B_x\left(\frac{\partial^2}{\partial x^2} + \sqrt{f}_o\frac{\partial^2}{\partial y^2}\right)^2\eta \qquad \text{where,} \quad f_o = \frac{B_y}{B_x}. \tag{4.17}$$

Therefore, when $f_o{<}1$, the wall is more flexible in the spanwise direction.

Validation

As a check on the integrity of the code, T/S waves were generated using a single body force and their growth and decay rates calculated and compared to those by Joslin, Morris & Carpenter (1991). The freestream velocity, density and kinematic viscosity

chosen are: U_∞=20m/s, ρ=1000kg/m^3 and ν_k=1×10^{-6}m^2/s respectively. The (local) Reynolds number chosen was R$_\delta$=2240. This value corresponds to the case where T/S growth rates are minimised. The wall properties are fixed as K=0.059GN/m^3 (and E_x=0.509MN/m^3). Figure 4.22 illustrates the growth rates as a function of frequency for the most extreme orthotropic case, i.e. when f_o=0. Excellent agreement with Joslin *et al.* is observed.

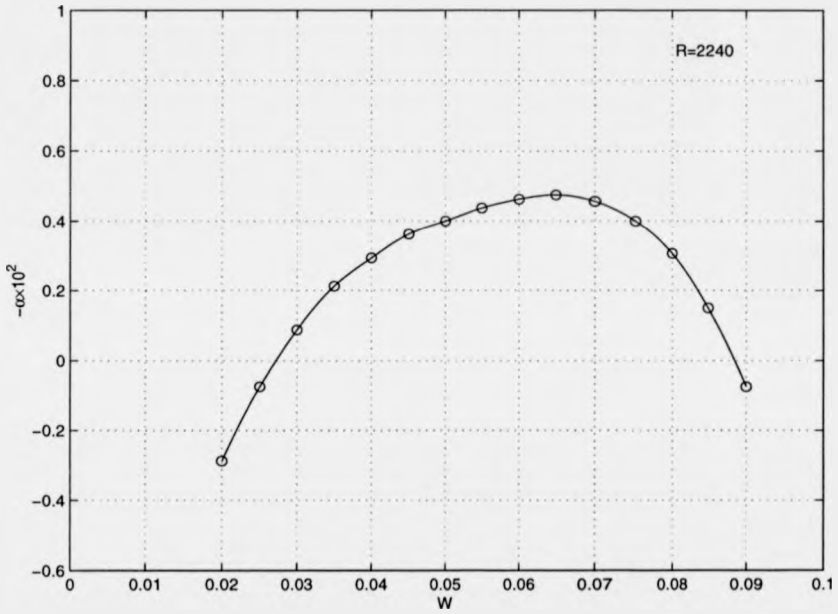

Figure 4.22: Growth rates, $(-\alpha_i)$ as a function of frequency, (W) for T/S waves generated over an orthotropic compliant surface. The solid line denotes the result from Joslin *et al.* (1991) and (o) our results. Excellent agreement is obtained. Computation variables: R$_\delta$=2240, f=0, E_x=0.509MN/m^3 and K=0.059GN/m^3.

Effect of orthotropicity on streaks over compliant surfaces

The effect of orthotropicity is reasonably well understood for the case where two- and three-dimensional T/S disturbances are generated, but its effect on streak growth is unknown, (until now). The introduction of orthotropicity improves transition delay by removing the possibility of extraneous wall disturbances due to the fluid forcing. Lucey & Carpenter (1993b) show that the hydroelastic stability of a compliant panel is not radically altered. They found that since the hydroelastic mode of instability is two-dimensional, the critical flow speed and growth rates did not radically alter. The main advantage of 'anisotropic' surfaces is the control of three-dimensional rapidly growing, linear (oblique) T/S waves which if unchecked can spark additional instabilities. Anisotropic surfaces are known to have much better transition-delaying properties than isotropic ones. Consider the Grosskreutz model. This is arranged so that rather than being displaced up and down by the fluctuating pressure, it is displaced in a direction making a substantial angle to the vertical generating a negative Reynolds stress at a compliant surface. This is a very benefical mechanism in nature. As we will describe in Chapter 6, the dermal papillae found in dolphin skin makes an angle to the vertical which varies over the body from 10° to 80°. Combined with tiny cutaneous ridges running circumferentially and perpendicular to the flow, it is likely that dolphin skin can vary its properties to increase transition delay as a result.

The effect of orthotropicity has positive effects on suppressing streak growth. Recall that the streaks are generated by the spanwise forcing of the streamwise velocity. As the flexibility is effectively altered in the spanwise direction, intutition suggests this may prove significant. The scenario observed is that it has a stabilising effect on streak growth, hence delaying (bypass) transition. The degree of spanwise forcing for fixed, β would be required to be significantly higher to produce the same growth when orthotropicity is not present. We concur with Lucey & Carpenter (1993) that additional T/S or wall-based disturbances that would form at higher frequency are not observed.

Figure 4.23 shows a series of snapshots of the compliant panel at identical times

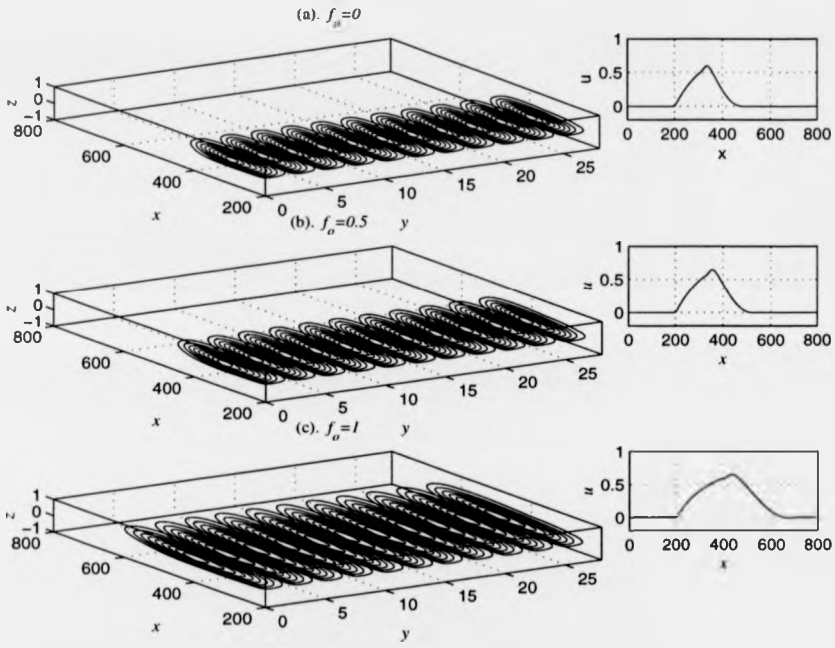

Figure 4.23: Trace of near-wall structures and growth rate over a Kramer-type compliant surface with varying orthotropicity: f=0 (limiting case), f_o=0.5 and f_o=1 (isotropic case). β=0.07, R=1200, t=800

for the isotropic (f_o=1) and orthotropic cases, f_o=0.5 and f_o=0. The later models the limited case (which is unrealistic in practice). The value of β is fixed for each case. The contour and velocity traces reveal that a modest increase in orthotropicity results in a reduction in growth. This is a result of the reduced stiffness of the surface in the spanwise direction sufficiently altering the spanwise modulation of the streamwise velocity. This is evidenced by the increase of Reynolds stress and rate of irreversible work done to the wall. The effect is similar to the case over an isotropic panel with reduced flexibility. However, in this case the suppressive effect of the wall with increased flexibility is greater, but it is subject to other instabilities. Figure 4.24 shows how $|u_{max}|$ falls as a function of β over surfaces with increasing orthotropicity

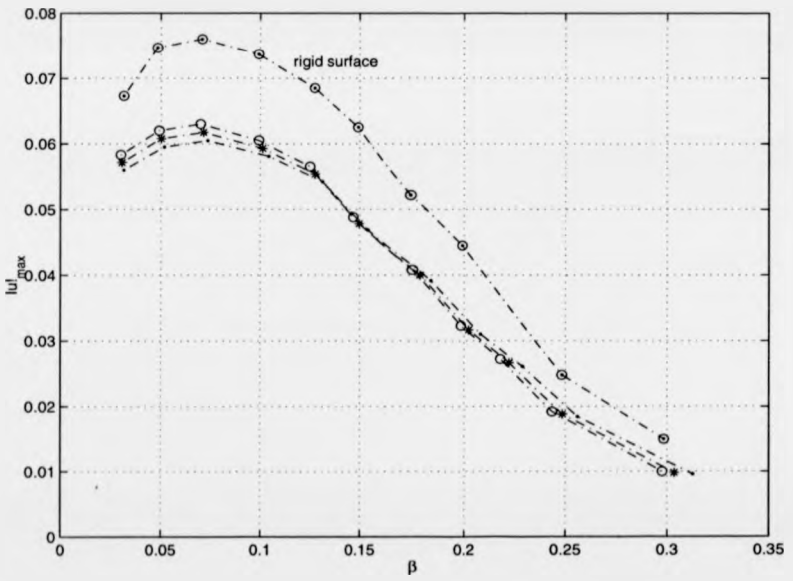

Figure 4.24: Amplitude, maximum streak velocity, $|u|_{max}$, as a function of the spanwise wavenumber, β, over wholly Kramer-type orthotropic and isotropic compliant surfaces Rigid surface data is denoted by ($\odot$–·), isotropic compliant surface by ($\circ$–·), and orthotropic compliant surface of, f_o=0.5 and 0.25 by ($*$–·) and (·–·) respectively.

to confirm this. Only a small change in the flexibility of the surface in the spanwise direction is sufficient to cause the small reduction observed. Where T/S instabilities are generated, the effect of orthotropicity is noted to have some effect on the wave. For this case, anisotropic surfaces, where the angle of fibres can be varied have a much more powerful effect. For the most extreme conditions our simulations did not reveal any flow-induced surface instabilities (FISI) occurring. In fact, the limits appeared to be slightly extended. Inspection of the energy components in Equation (4.13) revealed that the Reynolds stress appeared to be the largest (negative) component, and the rate of irreversible work done to the wall was also greater.

For the practically important case of a compliant panel, almost identical results are obtained in so far as the effect of orthotropicity reduces the streak growth. (The effect of othotropicity in this scenario may play a greater rôle in the suppression of FISI due to scattering at the panel edges, which is encouraging for the development of multi-panel walls in 'real' environments.)

4.2.5 A Brief Note on the Effects of Wall Damping

To conclude, we shall briefly comment on the effect that the introduction of wall damping has on streak production.

The use of damping to control wall- and fluid-based instabilities/disturbances is well understood. Benjamin (1960, 1963) and Landhal (1962) demonstrated that wall damping could actually *promote* T/S wave growth, i.e. waves grew at a faster rate for a higher level of damping than for lower levels. This contradicted Kramer's theory. He believed that the silicone oil in his compliant coatings, (which he thought was analogous to the fatty tissue in the upper dermal layer of the dolphin[3]), damped out and suppressed the growth of the waves. Benjamin's discovery prompted him to categorise the resulting waves, based on how they responded to irreversible energy transfer, into two main groups: Class A (or negative energy waves, NEW, e.g. T/S waves), and

[3]See Chapter 6

Class B (or positive energy waves, PEW, e.g. travelling wave flutter).[4]

To illustrate the benefical effects of wall damping, consider the experimental observation of travelling wave flutter (TWF). Gaster (1987) experimentally observed that for the most compliant of the panels, transition occured suddenly when a critical speed was attained, as opposed to the expected linear growth of T/S waves. Analysis by Lucey & Carpenter (1995) showed that this was due to TWF, which set in at the observed transition speed. TWF is a flow-induced surface instability, which is convective in nature and categorised as PEW. TWF is more sensitive to wall damping than T/S waves. Furthermore, as TWF is stabilised by energy transfer *out of* the wall, damping can easily control it. In light of this, it appears that the true rôle of damping in Kramer's surface was to control TWF. (Sen & Arora (1988) noted that the excessive use of wall damping to control TWF can give rise to an instability termed 'transitional mode'. This is a Class C instability and occurs when NEW and PEW T/S waves coalesce. However, although this sets an upper limit on the level of damping that can be used to control TWF, wall damping is not essential for its existence.)

We find that small levels of damping have little effect on streak production, even in the case where we have an embedded compliant panel. A Kramer-type surface was be considered, where the values for m, B and K were retained, and a wall damping coefficient set as d=1000. We have already highlighted the positive effect of orthotropicity in supressing extraneous waves over the compliant surface. The aim here was to observe whether the appearance of such disturbances could be suppressed or reduced with a positive effect on the streak phenonemon. The rôle of damping was to stabilise any disturbances that still existed and ensure that they did not hinder the adaptation of streaks in the presence of compliance.

[4]At about the same time, Briggs (1964) independently adopted the same system of classification to describe instabilities in plasma physics. NEW waves are destabilised (stabilised) by irreversible energy tranfer out of (into) the system due to, for example, wall damping. A typical example are T/S waves. Class B (PEW) waves are stabilised (destabilised) to energy processes having the opposite effect.

We have already demonstrated that the streaks can easily and rapidly adjust their spatial growth rate when generated over an embedded panel. At the trailing edge, no significant detrimental effects were observed as opposed to the leading edge. This behaviour was typical within a range of forcing frequencies and wavenumbers and Reynolds numbers for various sets of compliant wall parameters. We found that small levels of damping in compliant walls only had a small effect in reducing such disturbances and hence any detrimental rôle that could be played by any resulting (flow-induced surface) waves. This did not significantly extend the range over which streak production was found.

Comparison between the variation of the disturbance energy for a damped and undamped compliant wall reveals that large peaks in the vicinity of the leading-edge join are slightly reduced, compared to the undamped case. These are followed by a smooth, rapid, decline over the length of the compliant wall. The presence of the disturbance at the trailing-edge join cannot be easily distinguished as it could be for the undamped walls.

4.3 Chapter Summary

(i). **Rigid Surface**

We have simulated the Klebanoff mode with a linear version of the velocity-vorticity code in a laminar boundary layer and showed excellent agreement with Bertolotti (1997).

(ii). **Compliant Walls**

We have simulated the Klebanoff mode with a linear code in a laminar boundary layer over a Kramer-type compliant surface. This appears to be the first such study of its kind. The Kramer type surface has a Youngs Modulus of 1.53MPa and its stiffness varied by altering its spring stiffness. The general trend observed is that the more flexible the surface the less likelihood of streaks developing and *vice versa*. We have established the boundaries in (R,β) space where streaks may be generated. We found that streaks can be generated provided the surface stiffness is not less than or equal to a fifth of that of the Kramer-type surface, after which the surface is prone to generating a range of other disturbances. We have formulated a measure of the receptivity for streak production, *ReC*. The definition takes into account the 'forcing' produced by the body force and response of the boundary layer. Our results indicate that compliant surfaces appear to be very resilient to bypass transition. The effect of anisotropic/orthotropic compliant walls where flexural rigidity may be different in streamwise and spanwise directions appears to have had marginal effects on the phenonmenon.

(iii) **Compliant Panels**

We have simulated the Klebanoff mode occuring over embedded compliant surfaces in the same way as for rigid and wholly compliant surfaces. For the case where we initiate the streaks on the compliant surface, sufficiently far from the join, the results appear to be identical to those over wholly compliant surface; the downstream join has very little effect on the streak. If we initate our streaks on the rigid surface, the rigid-compliant join has an effect on the streaks. They appear to be weak in comparison to the wholly compliant surface. We have identified the Reynolds number range for streak

production to be narrower. We have investigated the effect of the join and identified two mechanisms- the body force and the effect of the leading edge where the streaks are broken down. The beneficial effects of orthotropicity was shown to reduce the streak growth rate. In practice, a compliant surface resilience to disturbance growth may be achieved if the surface properties (i.e. frequency of motion of the surface) are tuned to minimise disturbances at the join.

Chapter 5

Effect of Wall Compliance on Near-Wall (Streaky) Structures in Turbulent Flow

In this chapter, the favourable effects of wall compliance on the growth of near-wall structures, (streaks), in a turbulent boundary layer will be described. To do this, an analogy between the streaks observed in a transitional boundary layer with the near-wall structures observed in a fully turbulent boundary layer is adopted. It is important to note that the streamwise streaks associated with the Klebanoff mode are fundamentally different from the structures observed in a turbulent boundary layer. §5.1 will briefly describe the current (mostly experimental) work in the field. §5.2 will outline the modifications made to the code and demonstrate the integrity of the results. The remaining section is devoted to a description of the effects of compliance for this scenario.

5.1 Effects of Wall Compliance on Turbulence

The effect of compliance on a turbulent boundary layer is not fully understood. A preliminary investigation is conducted here with the aim of obtaining information regarding the qualitative behaviour of streaks in the near-wall region of the boundary layer in the presence of wall compliance. A brief review of current work will be given here. Refer to Gad-el-Hak (2002) for a comprehensive review.

Whilst the relevant computational studies are still of a preliminary nature, and existing experimental studies appear to be inconclusive, there is a general consensus on the (conceptual) behaviour of the near-wall structures in the turbulent boundary layer. Over a rigid surface, the near-wall region of the turbulent boundary layer is characterised by coherent structures in the form of steady 'rolls', i.e. counter-rotating streamwise vortices. Low-speed fluid is swept between these rolls into a low-speed streak. The rolls undergo a series of changes from their initial (steady) state: They oscillate and 'burst', ejecting low-momentum fluid out into the flow, thereby generating high levels of stress and leading to large levels of drag (Figure 5.1). If the growth of these streaks, and hence the bursting process can be reduced, it would be possible to reduce the turbulent (skin-friction) drag.

Figure 5.2 shows streaks over a compliant surface. The photographs compare the near-wall flow structures in a flat-plate turbulent boundary layer with and without wall compliance. The flow visualisations were performed by Lee, Fisher and Schwarz (1993) in the same manner as the seminal study over a flat-plate by Kline *et al.* (1967), using the hydrogen-bubble technique. The photographs clearly reveal the structure of the 'streaks' over each surface. These become less visible as one moves away from the viscous sublayer close to the wall, to the buffer, log and wake regions. In the latter region no streaks are visible. Lee and his co-workers found that the streaks appeared to be characterised by a wider spanwise spacing in the presence of compliance. They believed that this was due to a local reduction in the wall (shear) Reynolds stress, resulting in a reduction of the skin-friction drag. They observed slightly broadened viscous sublayer

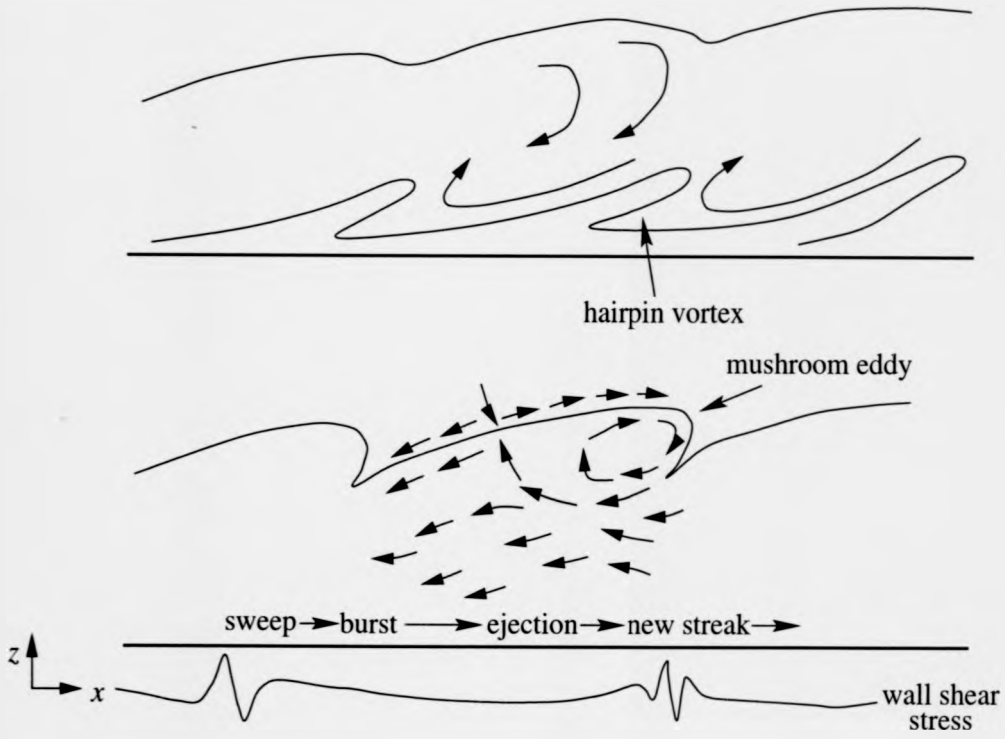

Figure 5.1: Illustration of physical mechanism of near-wall structures in the turbulent boundary layer. The streaks undergo a process whereby they grow, oscillate and then burst or eject.

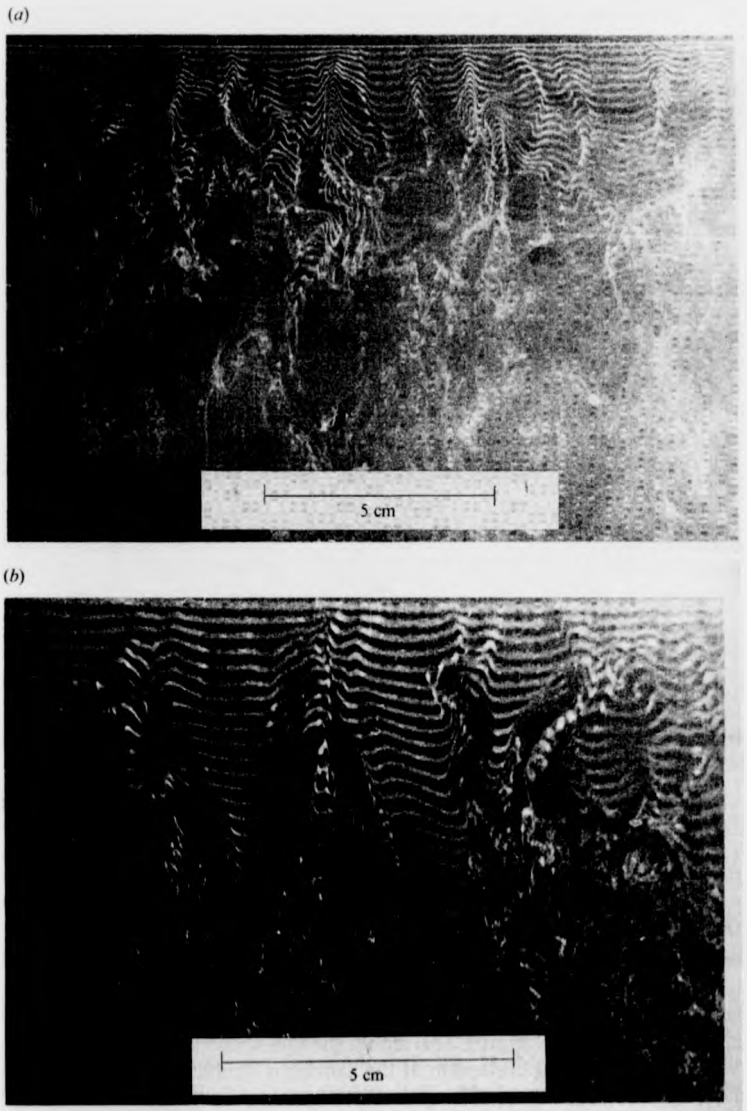

Figure 5.2: Low-speed streaks in (*a*) rigid surface (z^+=51) and (*b*) compliant surface flat-plate turbulent boundary layer (z^+=49). R=1348, pulse (disturbance-wire) frequency, f=40. The compliant surface has a shear modulus of 227 Pa and a damping ratio of 1.64. The flow visualisations were made using a hydrogen-bubble technique by Lee, Fisher & Schwarz (1993).

and buffer regions and a greater degree of laminarisation at lower Reynolds numbers. Although, it is difficult to determine the exact properties of the compliant surface used, there has been no direct qualitative validation of their results. Note that Lee *et al.* only inferred local skin-friction drag reductions, but did not actually measure the drag. Based on this Lee's results appear to be inconclusive. Gad-el-Hak, Blackwelder and Riley (1984) also conducted a series of experiments with a compliant surface with longitudinal grooves scaled with the low-speed streaks in the turbulent boundary layer. They observed a hydroelastic instability in the form of a spanwise wave structure, but did not measure the local drag reduction.

Direct numerical simulations (DNS) by Metcalfe *et al.* (1991) suggests that compliant surfaces, that possess properties effective in the linear transition regime, remain extremely effective in the non-linear regime where the flow structures become highly three-dimensional. Although this sounds rather promising, it is noted that the scale and form of the near-wall structures in the turbulent boundary layer are *completely different* from those found in a linear and weakly non-linear transition regime. Recent experimental investigations by Choi *et al.* (1997, 2001, 2003) reported favourable, but small drag reductions, (typically 5 to 10%), over single-layer viscoelastic compliant surfaces. The wall compliance in these experiments were relatively high, (approximately two orders of magnitude higher than in the Gaster (1987) experiments), and confirm earlier results obtained in Russia by Kulik, Poguda & Semenov (1991).

These results suggest that the surface response to turbulent 'pressure pulses' during the burst events in the near-wall region depends on the natural frequency of the coating. When the wall compliance is very low, local wall displacements are generated that are attributable to turbulent pressure fluctuations driving the wall. The effect of these displacements on the near-wall structures is much greater than the direct interaction between the near-wall structures and the compliant wall. Random phase changes to the near-wall structures are believed to interfere with the bursting process thereby causing substantial drag reductions. Choi and his co-workers have experimentally demonstrated that a local surface displacement is obtained when the

natural frequency of the compliant coating is selected to match the pressure pulses in the turbulent near-wall region (Choi, 2003; Tamilarasan & Choi, 2001). They show that sweep events in the near-wall region, (which are believed to be major contributors to the pressure pulses), have a characteristic frequency which compares well with the range of non-dimensional natural frequency of successful coatings.

At present there appears to be little information obtained by numerical simulation for the development of streaks over compliant surfaces in the avaliable literature. Recent studies by a team led by Lumley and Rempfer at Cornell University claim to have shown the essential features of near-wall structures over compliant coatings through DNS and other novel theoretical techniques (Rempfer, Xu, Parsons & Lumley, 2003). Recent DNS by Endo & Himeno (2001a,b) also show the development of streaks. However, it is unclear as how to make a comparison as both studies are preliminary in nature and limited in detail.

5.2 Code Validation

5.2.1 A brief note on the modelling approach

To aid our modelling, it is useful to recap on the mechanisms believed to be responsible for generating turbulent streaks. Bypass transition is generally agreed to be caused by transient or algebraic growth mechanisms (Bertolotti, 1997; Landhal, 1990). Algebraic growth is characterised by the so-called 'lift-up' effect, which promotes longitudinal streaky structures similar to those associated with the Klebanoff mode. Butler & Farrell (1992, 1993) demonstrated the link between the streaks associated with a fully turbulent boundary-layer and algebraic growth. There is also some information regarding the equivalence of the Klebanoff mode in the transitional boundary layer, to streamwise vortices in the fully turbulent boundary layer. Also, recall that freestream turbulence induces streaks in the transitional case, whereas for the developed turbulent case, the inner boundary-layer appears to be responsible. In view of this, it is possible

to use a similar method to that adopted in Chapter 4 to model the streaks.

A freestream spanwise body force is used to generate streamwise vorticity in the same way as described in §4.1.1-2. The velocity-vorticity code is modified in the same manner, except that now, the convective quantity, **N** includes the non-linear aspects for the transport equations, i.e.:

$$\mathbf{N} = \mathbf{\Omega}^B \times \boldsymbol{u} + \boldsymbol{\omega} \times \mathbf{U}^B + \boldsymbol{\omega} \times \boldsymbol{u}. \tag{5.1}$$

The forcing function is defined by equation (4.8) and the streaks are generated in the semi-empirical turbulent velocity profile described in §3.3.2. We deviate somewhat from the approach described in Chapter 4. Here, a prime concern is to determine the optimum normal position within the turbulent mean-flow profile in which to position the streak-generating body-force. Previously, freestream forcing was implemented and the body force fixed some distance away from the wall. Also, whereas previously the form of the body force was continuous, now the body force acts for a discrete time period of t^+=15 (in non-dimensional wall units). This matches the non-dimensional period of suction used by Gad-el-Hak & Hussain (1986) to artifically generate streaks.

By determining the optimum perturbation location, we follow the same approach as Lockerby (2001). The 'optimum' streak is defined as the one with the largest streamwise velocity at any time during its evolution. Butler & Farrell (1992) apply a somewhat similar method, but restrict the growth to a pre-determined period. They define the optimum as the disturbance with the maximum energy growth over a fixed period of $t^+ \approx 100$. However, this approximation appears to be incorrect. The results of our simulation over a rigid surface reveals that the 'optimum' streak reaches a maximum at around t^+=60, in agreement with Lockerby (2001) and Kim & Lim (2000). This value is significantly shorter than that claimed by Butler & Farrell.

5.2.2 Streaky Structures over Rigid Surfaces

It is important to bear in mind that our model essentially uses an analogy between the streaks observed in a transitional boundary layer and the near-wall structures observed in a fully turbulent boundary layer. (Note that the streamwise streaks associated with the Klebanoff mode are fundamentally different from the structures observed in a turbulent boundary layer.) Additionally, *a 'pseudo' non-linear code is adopted; but strictly full non-linear simulations are not run as our methodology involved only a single mode in the spanwise direction.* The integrity of our approximation was verified by generating streaks over a rigid surface. The body force is positioned away from the inlet to avoid the generation of extraneous disturbances. A stationary and non-oscillating body force is located at various wall-normal and streamwise positions within the mean flow profile. The streaks generated grow algebraically and, at later times, display the onset of viscous-induced decay. Figure 5.3 shows a comparison of the long term development of the streak with our linear viscous, linear inviscid and non-linear viscous calculations. The trace shows that the viscous results decay more rapidly than the inviscid ones.

Figure 5.4 shows how the optimum wavelength, λ^+_{opt}, varies linearly with the wall-normal position, z^+_f. This agrees with simulations by Lockerby (2001). An identical body force to that used in Chapter 4 is used to generate the streaks here. The results presented have been generated using our pseudo non-linear code, although almost identical results are observed with the linear version. (However note that the capture of the lift-up effect is much better revealed with the psuedo non-linear code.) Figure 5.5 describes how the maximum streak velocity, $|u|_{max}$, varies with λ^+. An optimum streak spacing was found to occur at approximately 100 non-dimensional wall units, (ν/v^*). This compares well with the simulations by Lockerby (2001) and the average streak spacing observed experimentally by Kline *et al.* (1967). Note that the body force was normalised in order to generate the same strength of vorticity at each wall-normal position in order to find the optimum spanwise spacing. Note also that the linearity observed in our computations has been widely observed experimentally thereby verify-

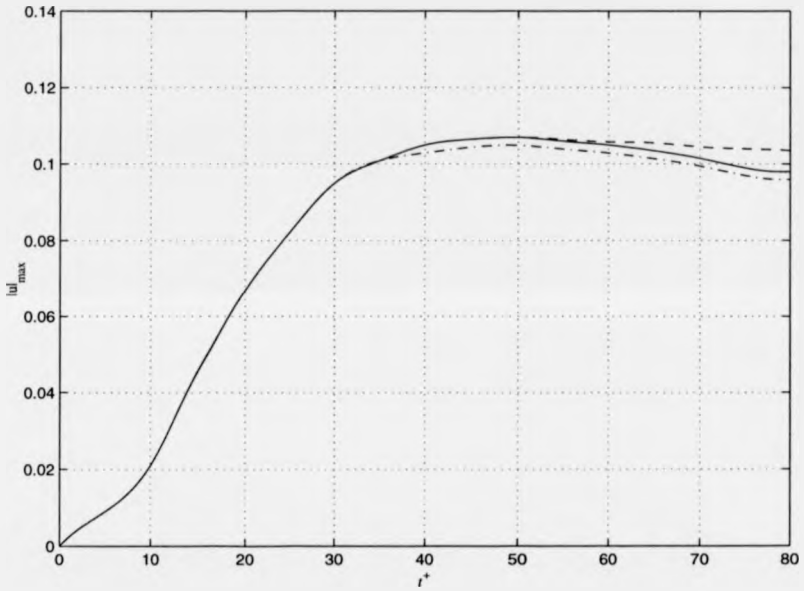

Figure 5.3: Amplitude, maximum streak velocity, $|u|_{max}$, as a function time, t^+ for R=1000. Spanwise wavenumber, β=0.04; R=1000; stationary body force at a fixed location of x_f^+=203, z_f^+=18.4. The long term development of the streak with the linear viscous (−), linear inviscid (−−) and psuedo non-linear viscous (−·) codes are shown. Note the effect of adding non-linear terms.

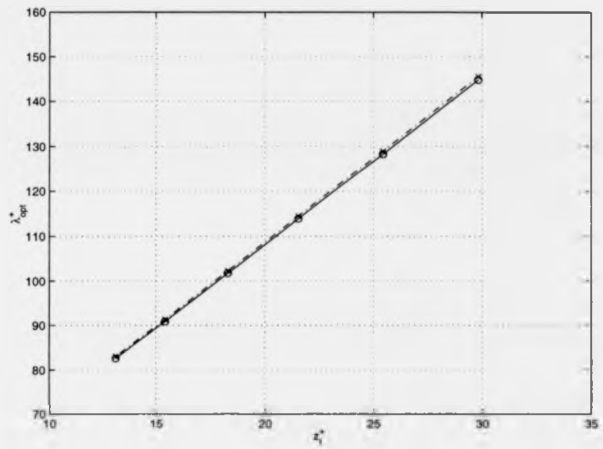

Figure 5.4: Optimum spanwise wavelength, λ^+_{opt} as a function of the normal distance from the wall, z^+_f.Results (-×-) show excellent agreement with Lockerby (2001) (-○).

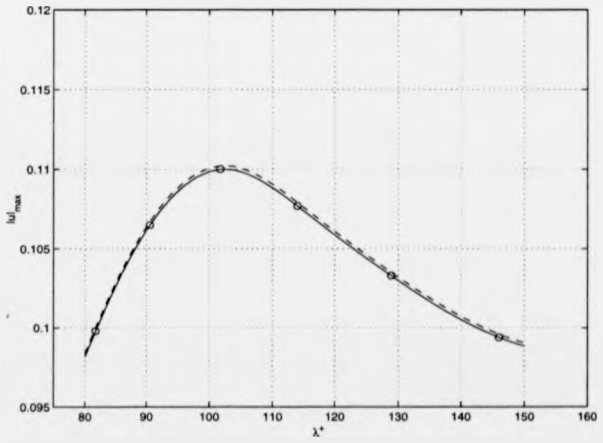

Figure 5.5: Maximum streak velocity, $|u|_{max}$, as a function of the spanwise wavelength of the body force, λ^+. Results (−−) agreement with Lockerby (2001) (-○). Body force located at z^+_f=18.4.

ing the approach adopted here.

Figures 5.6 and 5.7 show the spatial and temporal development of a typical turbulent streak. Note that low-speed streaks are generated. As explained earlier, these have an important active roll in turbulence generation. The streak continues to grow after the maximum streamwise velocity is reached. This agrees with the experimental observations by Johansson *et al.* (1991). Note how the streak appears to lift.

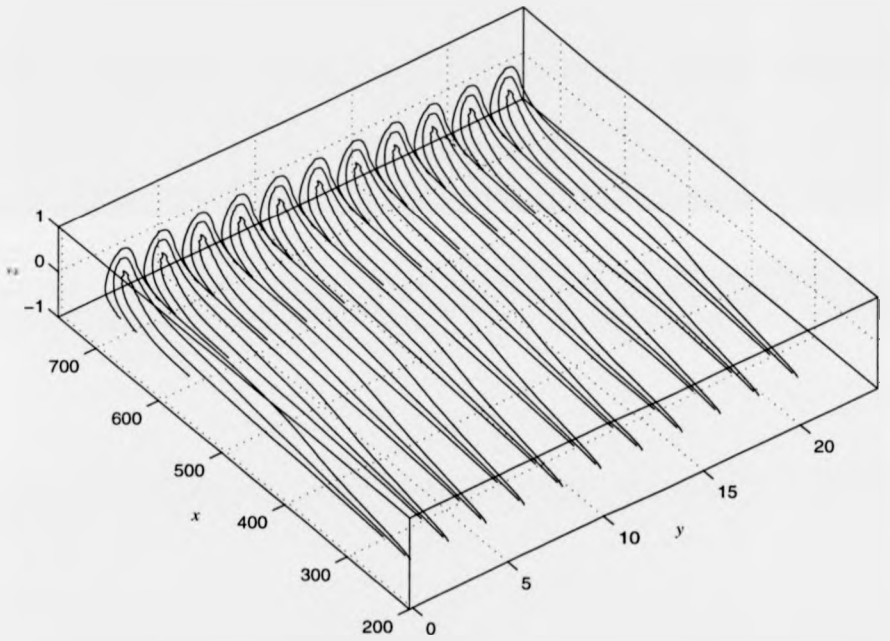

Figure 5.6: Spanwise perturbation velocity contours at t^+=50 over a rigid surface. Spanwise wavenumber, β=0.04; R=1000; stationary body force at a fixed location of x_f=203, z_f=2.314 (in domain). Pseudo non-linear simulation.

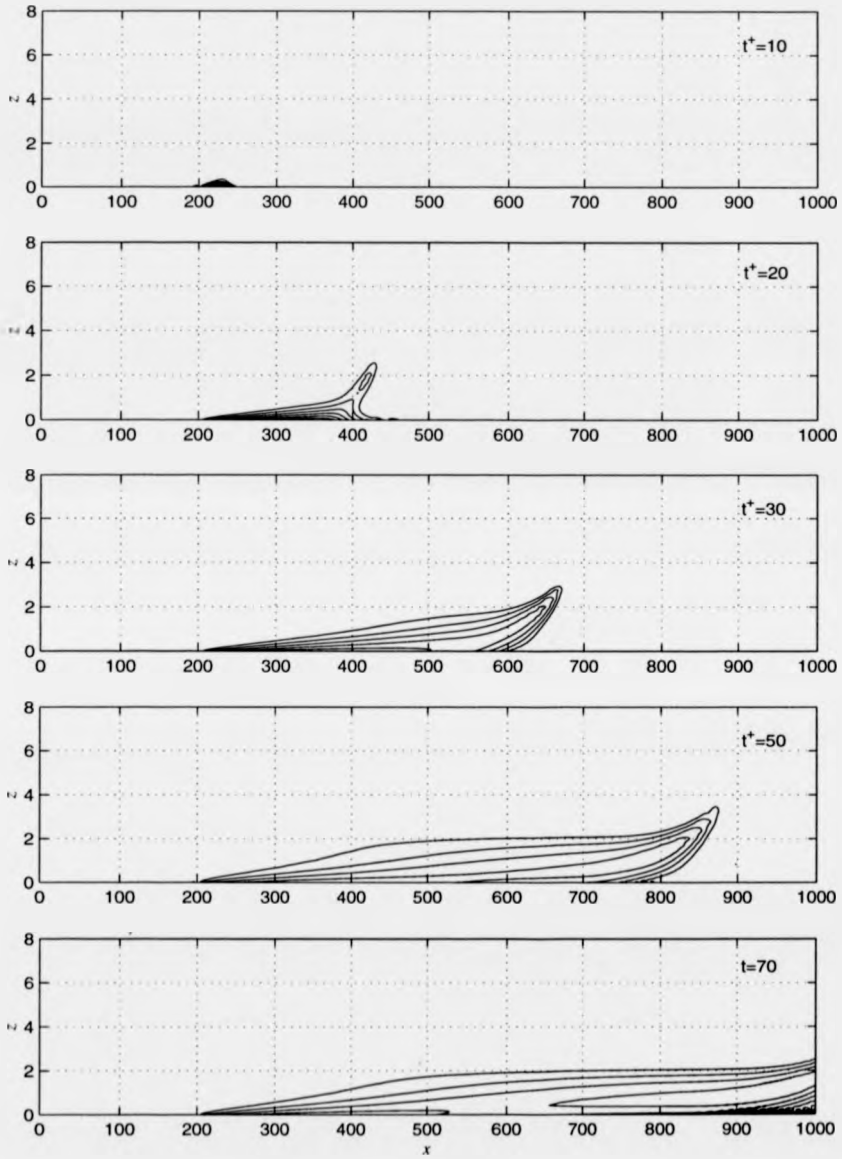

Figure 5.7: Streamwise velocity contours: Evolution of 'streaky structures' with time, t^+ over a rigid surface. Spanwise wavenumber, β=0.04; R=1000; stationary body force at a fixed location of x_f=203, z_f=2.314 (in domain). Pseudo non-linear simulation.

5.3 Streaky Structures over Compliant Surfaces

The effect of wall compliance on turbulent streaks will now be described. As in Chapter 4, our interest resides with the streak growth over both a wholly compliant surface and a finite-length panel. With regards to the latter, the ability of the streak to adapt to the presence of the leading and trailing edges is of particular interest. The streaks are generated in an identical manner to §5.2, with the psuedo non-linear code.

5.3.1 Development of Near-Wall Structures over Compliant Surfaces

The selection of wall parameters is based on the same criteria and assumptions described in §4.2.1. A semi-heuristic approach is adopted to estimate the ideal wall parameters and optimum spanwise forcing and critical Reynolds number ranges based on the previous chapter. In accordance with Yeo *et al.* (2001), care is taken to avoid the generation of static divergence and other instabilities that are detrimental to streak production.

It was noted in §5.2 that a number of experiments had been conducted where turbulent streaks had been examined. However, although there is some consensus as to the form and behaviour of the near-wall structures, there is no evidence of any rigorous demonstration of either qualitative or quantitative agreement between research groups. This is, in part, a result of the wide variation in experimental conditions and wall properties chosen. There is also a distinct lack of theoretical and computational work with which to make any comparison. Apart from a stability analysis by Yeo *et al.* (2001), most computational studies are preliminary in nature and have not been explicitly set up to compare with the existing experimental data. Yeo *et al.* remark that the study of the development of near-wall structures has been hampered by a lack of a theoretical model to describe the fine-scale interaction observed by Lee *et al.* (1993).

For our purposes, validation is made against the study of Lee *et al.*. Our streaks are generated with a stationary, non-oscillating body force positioned in the same manner

as over a rigid surface. It is important to reiterate that fully non-linear simulations have not been run, as only a single mode in the spanwise direction was considered. Additionally, only qualitative agreement can be provided as it is not clear how the properties of the compliant surface could be translated to our model. Lee *et al.* used a single-layer, isotropic, viscoelastic wall that had a shear modulus of 227 Pa and a damping ratio of 1.64. This is a very soft surface, and its choice was based on the numerical study by Duncan (1986), and made to ensure the existence of small-amplitude, stable, compliant-surface displacements 'which represent the footprints of the flow structure in the shear layer'. The surface is composed of 10.1:1 ratio of inert 100 cSt silicone oil, (with a specific gravity of 0.97), to a silicone elastomer (of specific gravity 1.05). This indicates that the surface is extremely soft (and is largely composed of oil). (It is highly debatable whether such a surface is of practical use.) In order to model this surface it is necessary to calculate the non-dimensional flexural rigidity, B, defined as:

$$B = \frac{Eb^3}{12(1-nu^2)}\frac{1}{\rho h \nu_s^2}$$

where, for a a plate of thickness, b, 3.8mm, assuming a Poisson ratio, ν, as 0.5 and taking the density, ρ and viscosity, nu_s of sea water to be 1025kg/m^3 and 1.37×10^{-6}m^2/s returns B=480×10^3. Using the same method as Carpenter & Garrad (1985) this is scaled to K=$4B$=1.92×10^6. The original Kramer-type surface described in §4.2.2 has a stiffness of K=7.68×10^7 was also investigated.

The streaks generated grow algebraically and display the onset of viscous-induced decay. Figures 5.8 and 5.9 show the spatial and temporal development of a typical turbulent streak. The growth of the streak is significantly reduced and weaker in strength as a result. This is almost certainly due to the effects of wall compliance. Figure 5.10 shows the variation of the optimum wavelength, λ^+_{opt}, as a function of the Reynolds number, R. The graph shows that the streaks are wider apart and, as a result the ranges of the Reynolds number and spanwise wavelength of the forcing are considerably narrower. Comparison with the experimental results of Lee *et al* reveals a remarkable similarity, although based on our assumption regarding the properties of the surface,

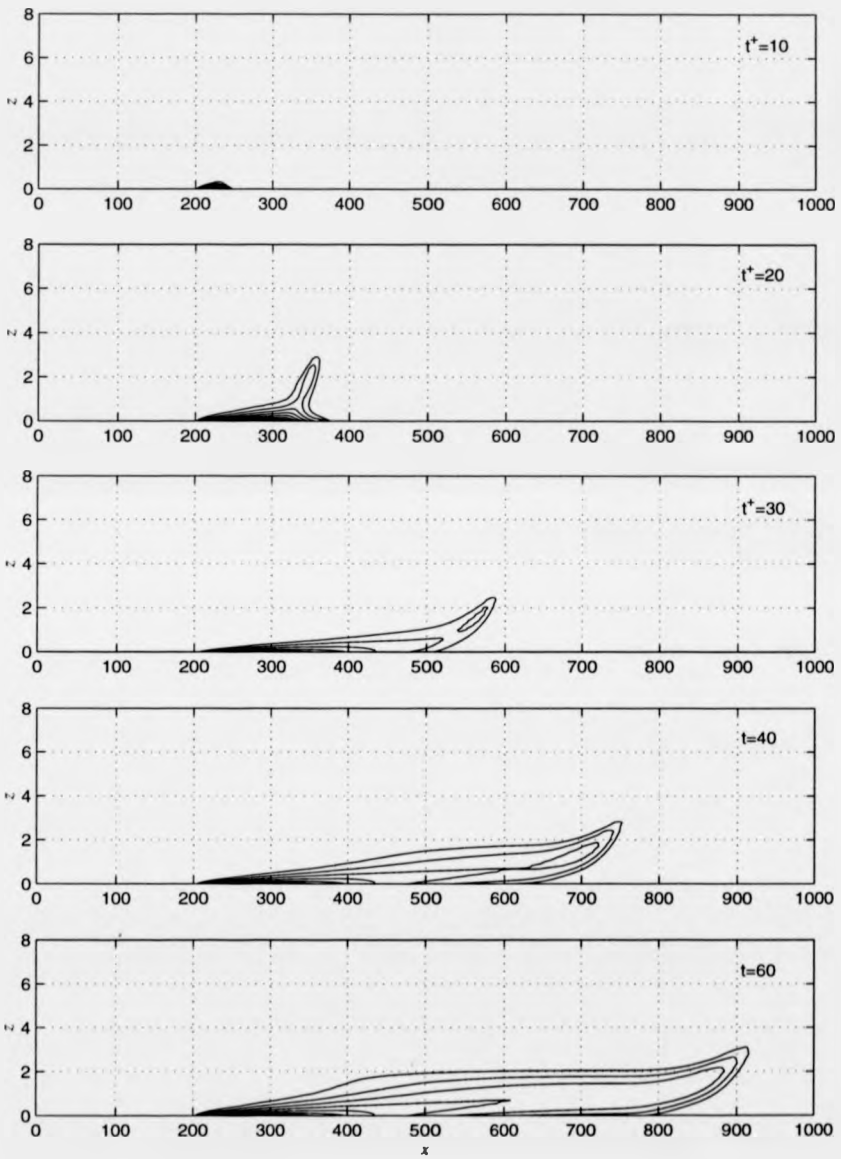

Figure 5.8: Streamwise velocity contours: Evolution of 'streaky structures' with time, t^+ over a compliant surface with Lee-type properties. Spanwise wavenumber, β=0.04; R=1000; stationary body force at a fixed location of x_f=203, z_f=2.314 (in domain).

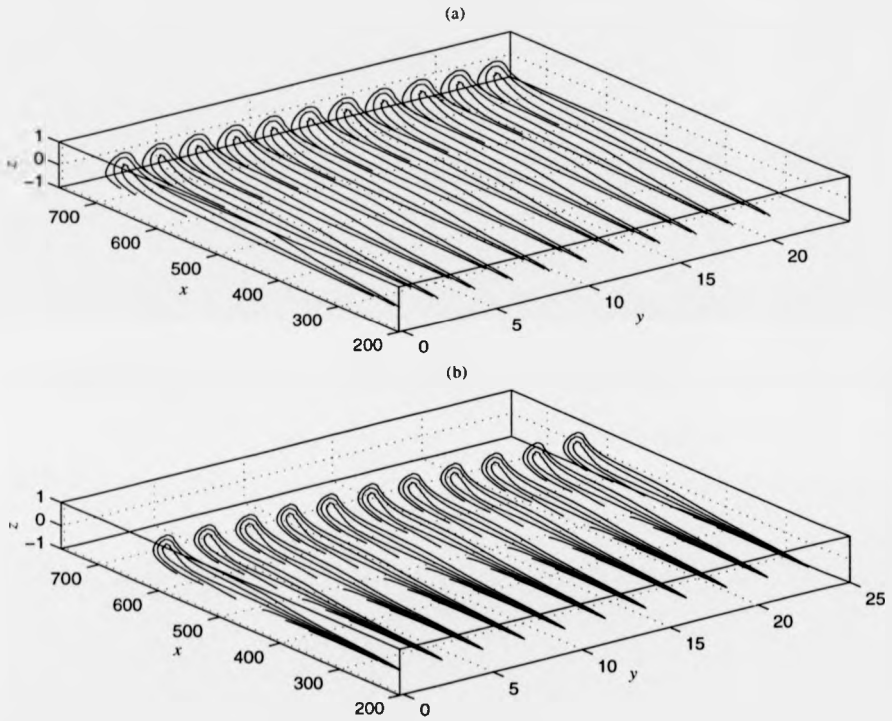

Figure 5.9: Spanwise perturbation velocity contours at t^+=50 over (a) rigid surface and (b) compliant surface with Lee *et al.* type properties. Spanwise wavenumber, β=0.04; R=1000; stationary body force at a fixed location of x_f=203,z_f=2.314.

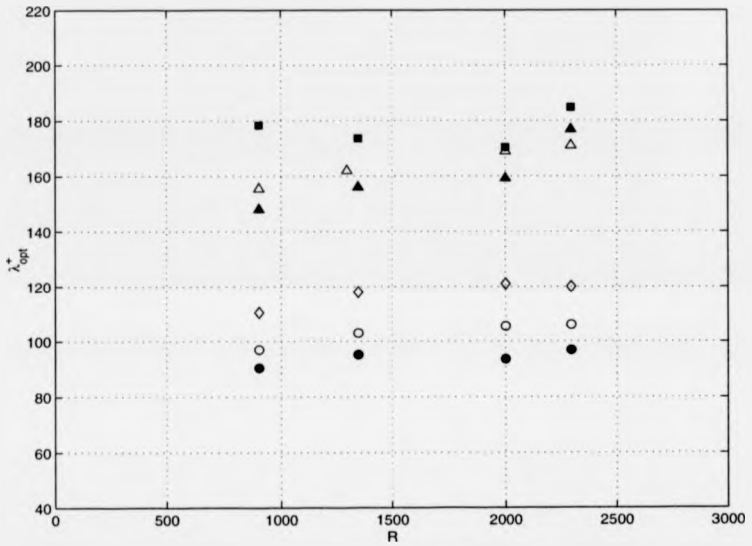

Figure 5.10: Optimum streamwise streak spacing, λ^+_{opt} as a function of Reynolds number, R for Lee and Kramer-type surfaces. (•), (▲) and (■) denotes measurements for the rigid, and compliant surfaces respectively made by Lee *et al.*. (The (▲) and (■) data are non-dimensionalised by the friction velocity from the rigid- and compliant-surface cases respectively.) (∘) and (△) represent results from our rigid and wholly compliant simulations respectively, and (◊) denotes results where we have considered a Kramer type surface.

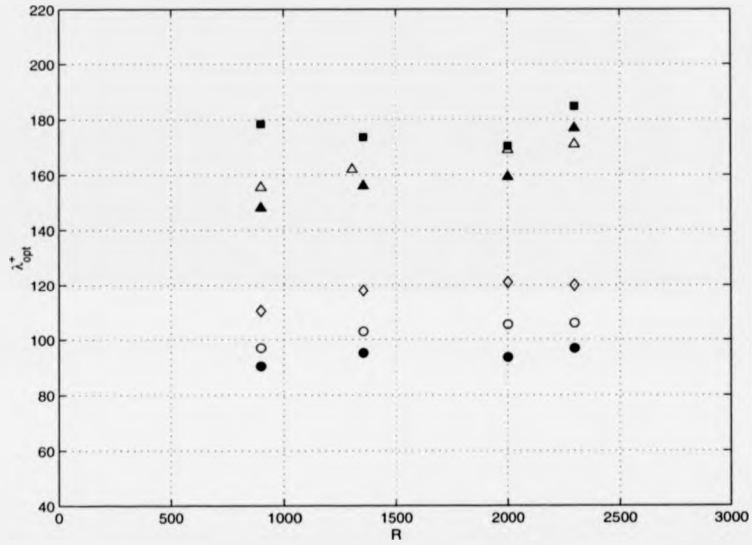

Figure 5.10: Optimum streamwise streak spacing, λ^+_{opt} as a function of Reynolds number, R for Lee and Kramer-type surfaces. (•), (▲) and (■) denotes measurements for the rigid, and compliant surfaces respectively made by Lee *et al.*. (The (▲) and (■) data are non-dimensionalised by the friction velocity from the rigid- and compliant-surface cases respectively.) (○) and (△) represent results from our rigid and wholly compliant simulations respectively, and (◇) denotes results where we have considered a Kramer type surface.

it would be incorrect to claim that this shows quantitative agreement.

Figure 5.11 shows how the maximum streak velocity varies as a function of the spanwise spacing. This and the previous graph shows that the optimum spanwise spacing, λ^+_{opt} of 100 non-dimensional units is increased by as much as 80% in the presence of a compliant wall! As before, the body force was normalised in order to generate the same strength of vorticity at each wall-normal position in order to find the optimum spanwise spacing.

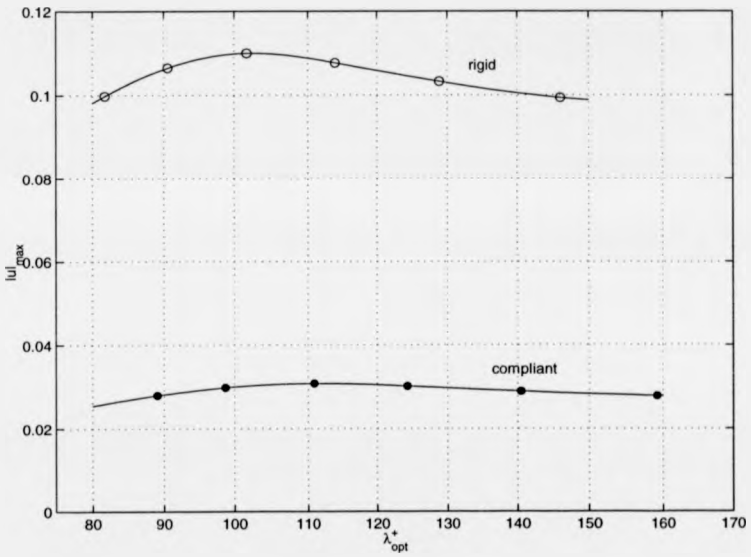

Figure 5.11: Maximum streak velocity, $|u|_{max}$, as a function of the optimum spanwise wavelength of the body force, λ^+_{opt} for rigid (-o) and Lee-type compliant surface (-•).

Figures 5.12 and 5.13 demonstrate how λ_{opt} increases and $|u|_{max}$ falls with only relatively small increases in flexibility. The general trend followed is similar to that described in Chapter 4- the more compliant the surface the greater the spanwise streak spacing. As a consequence, the streaks are considerably weaker and, by implication, the average skin friction is reduced. The data describe the characteristics of the streak

production for the various surfaces, resulting in the shift of λ_{opt} and reduction in $|u|_{max}$.

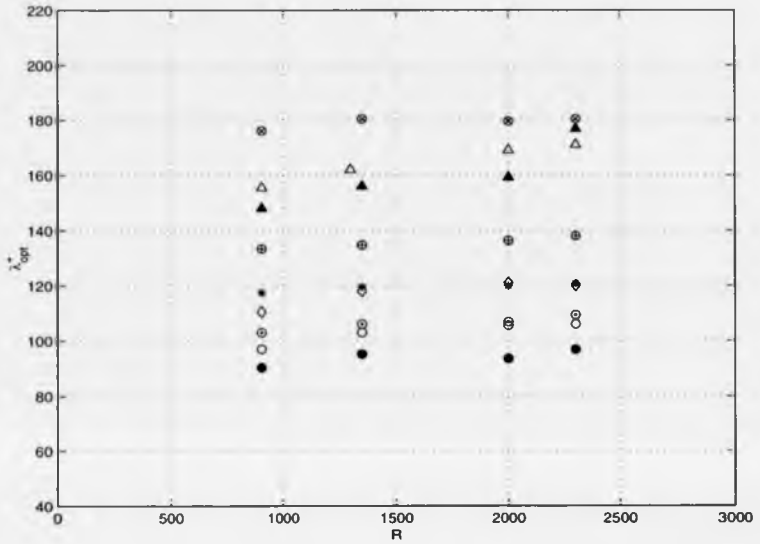

Figure 5.12: Optimum streamwise streak spacing, λ^+_{opt} as a function of Reynolds number, R. (•) and (∘) denotes experimental and numerical rigid data respectively, (▲) and (△) denote experimental and computational data for the Lee *et al.* surface respectively, (⊗) denotes spanwise spacing for a surface which has a third of the stiffness of the Lee surface, (◊) and (⊕) refers respectively to to spanwise spacing over the original Kramer surface and one with a third the stiffness. (⊙) and (∗) denotes surfaces with E_1=2.81×10^{6}Pa and E_2=1.70×10^{6}Pa respectively, considered by Choi *et al.*.

Note that if the surface is too flexible, a full laminar-to-turbulent simulation may show that the fast-moving surface waves generated act as large roughness elements sparking early transition, i.e. the streaks develop much more rapidly and presumably promoting lift-up almost instantaneously. Highly unstable surfaces are known to be prone to flow-induced surface instabilities and two- and three-dimensional waves sparking transition earlier. In a turbulent boundary layer it is much more difficult to generate streaks as

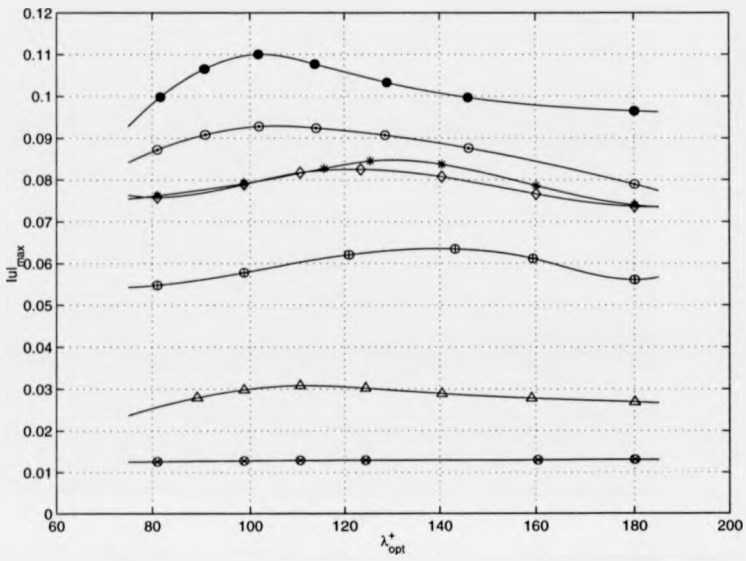

Figure 5.13: Maximum streak velocity, $|u|_{max}$, as a function of the optimum streamwise streak spacing, λ^+_{opt}. See Figure 5.12 for legend.

other detrimental flow- and surface-induced phenomenon rapidly tend to dominate.

At this juncture it is necessary to consider the Choi *et al.* (1997, 2001) experiments. Choi and his co-workers observed a drag reduction of up to 7% with compliant materials that were approximately 7mm thick, covering a body of revolution (of 0.175m diameter). The compliant surfaces tested were very stiff, (at least two orders of magnitude stiffer than the coatings used by Gaster (1987)). The first and second coating both have a density of ρ=2140kg/m^3, and elastic moduli of E_1=2.81$\times$10^{6}Pa and E_2=1.70$\times$10^{6}Pa respectively. Asssuming a value for the Poisson ratio of 0.5, the wall parameters in our code were altered in order to ascertain how the streaks develop over such surfaces. The flow parameters were scaled to the working speeds of 2 to 6m/s, which according to Choi *et al.* achieved the best drag reductions. Therefore, using the same procedure as for the Lee surface, the corresponding (non-dimensional)

stiffnesses are K_1=9.78×10^7 and K_2=3.71×10^{10}. Figure 5.12 shows how the spanwise spacing varies with the Reynolds number for both these surfaces. A crude comparison with a rigid surface reveals that the streak spacing increased slightly for both surfaces. Furthermore, the optimum streak velocity (Figure 5.13) is also less compared to that for a rigid surface. This supports their claim that drag reduction is achieveable with their (stiffer) surfaces. The Choi *et al.* experiments were performed in order to provide confirmation of whether the drag reductions previously obtained by Kulik *et al.* (1991) could be achieved in a controlled environment. Although the same test bodies where used, it is not clear whether newly prepared coatings were employed. If the original coatings were used, it might be expected that the properties of the material would have changed. However, Choi *et al.* report that Kulik and Semenov (1996) show that the viscoelastic properties of the surface have *not* significantly aged, so should not have affected the drag-reduction properties of the original samples.[1]

So far, the turbulent streaks have been generated with a pseudo non-linear code. This is acceptable, as the rôle of linear (and weakly non-linear) mechanisms have been well documented (see Chapters 2 and 4). The results show agreement with Lee *et al.* verifying the approach undertaken. The results suggest that within the narrow band defined, the streaks appear to be consistent and stable. Outside of these limits the streaks are more prone to spanwise instabilities and non-linear effects. These are characterised by the rapid enhancement of the streaks near the wall, resulting in lift-up and subsequent bursting mechanisms. Closer examination of Figure 5.9 revealed that the code could predict the onset of the lift-up effect.

The initial stages of streak development involve the slow elongation of the streaky structure. The onset of lift-up is marked by a more rapid growth. The process is much less pronounced over a compliant wall, and can be reduced further with surfaces of progressively increased compliance, up to predefined limits, (after which the surface is capable of sustaining its own waves, altering the route to turbulence). This is encourag-

[1] A crude estimate of the drag reduction may be made using the observation found for polymer solutions, that the streak spacing is an increasing function of the drag reduction. See Page 118.

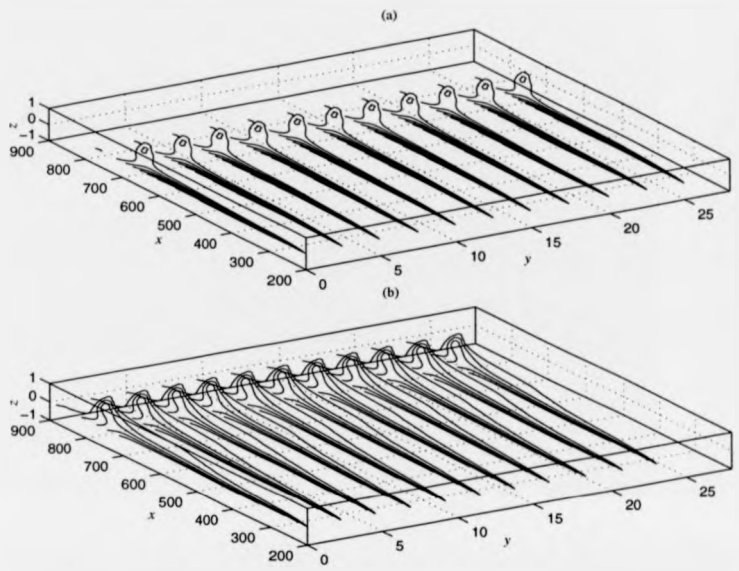

Figure 5.14: Streamwise velocity contours: 'streaky structures' at t^+=50 over (a) Lee *et al.*-type and (b) Kramer-type surface. Spanwise wavenumber, β=0.04; R=1000; stationary and non-impulsive body force at a fixed location of x_f=203, z_f=2.314 in domain).

ing as it supports the hypothesis that, despite the narrow range and close dependency on the local flow conditions, turbulent streak development and lift-up can be effectively controlled through a series of compliant panels, as opposed to a single finite coating (Figure 5.14). This is the subject of the following section.

Although it has been shown that streak growth can be suppressed by wall compliance, little attempt has been made to show why this is the case. It is believed that the motion of the surface plays a significant role. Lee *et al* (1993) show evidence of slightly broadened viscous sublayer and buffer regions. This is accompanied by a shift in the local log-law velocity profile. Choi *et al.* and Gad-el-Hak *et al.* (1984) observe a similar shift of the profile. This behaviour is indicative of the fine-scale, near-wall interaction and has also been observed in flows with drag-reducing polymer additives (Lumley,

1973) and also over riblet surfaces (Choi *et al.*, 1994).[2] Its effect is to locally reduce the skin-friction. The thickening of the viscous sublayer and buffer region strongly suggests that the turbulence energy produced in the near-wall region is reduced by the motion of the surface.

Our primitive simulations support the reasoning outlined above. Figure 5.15 plots the components of the energy balance defined in §4.2.3 for the surfaces under consid-

[2]With regards to polymer additives, it has been well known for a number of years that the addition of small amounts, as little as 100 parts per million, to the flow can provide substantial drag reductions. The classic experimental studies perfomed by Tiederman and his co-workers, (Donohue, Tiederman, Reischman, 1972; Oldaker & Tiederman, 1977; Tiederman, Luchik & Bogard, 1985), were based on the hydrogen bubble technique used by Kline *et al.* (1967) to view the near-wall structures of the boundary-layer in a channel flow. Tiederman and his co-workers observed that the spanwise spacing of the low-speed streaks in the viscous sublayer increased, confirming earlier work by Eckelman, Fortuna & Hanratty (1972), and that the polymer directly affected the subsequent lift-up and bursting process that occured in the buffer region. However, if a thin region of polymer solution only existed in the viscous sublayer, the bursting rate of the near-wall structures and spanwise spacing of the streaks would *not* alter. Therefore, for effective drag reduction, (i.e. control of the bursting process), polymer additives need to be dispersed in the viscous sublayer and buffer regions of the flow. Consequently, spanwise spacing of the wall layer streaks increases as the bursting rate falls, as a result yielding an increase in the drag reduction. Recently, direct numerical simulations by Sureshkumar, Beris & Handler (1997) confirm these findings and highlight new information on the physical mechanism.

Tiederman and his co-workers show that there is an approximately linear correlation between the streak spacing and streamwise velocity, and percentage drag reduction. The same result may apply to compliant walls, as Figure 5.13, shown earlier demonstrates a similar effect. For example, using the maximum values for the streak spacing in Figure 5.13, and the data provided by Tiederman *et al.* (1985) and Sureshkumar *et al.* (1997), a very crude estimate for the drag reduction of the Choi surfaces is 6-12%. This compares favourably with that found experimentally by Choi *et al.* (1997). However, it is important to make clear that the attenuation of the streaks by wall compliance is due to the modification of the flow by the motion of the wall. Depending on the frequency of the wall perturbations, this effect can have far-reaching effects in the buffer region. The effect of polymer additives can have similar effects. In this case, the physical mechansism by which suppression is achieved is highly complex, and due to the interaction and stretching of the individual or concentrated suspensions of polymer molecules with the flow.

eration. Figure 5.15(a) shows how the flow-work-type terms: the average disturbance kinetic energy (A) and the rate of work done by the disturbance against the perturbation stresses, (B) fall downstream. Figure 5.15(b) and (c) show the variation of the energy production terms. Figure 5.15(b) shows a substantial reduction of the production of turbulence energy by Reynolds stress downstream in the near-wall region. The reduction of quantities (a), (b) and (c) are very small. The Reynolds stress production shows the largest reduction in the magnitude in the presence of compliance compared to the viscous dissipation term (b) and the extra-energy-removal term (viscous dissipative) term (d). (The latter is negative in value.) The rate of irreversible work done to the wall by the disturbance pressure is lower compared to the rigid surface and maintains a reasonably constant negative value over the panel (Figure 5.15(c)).

Figure 5.16-18 shows the variation of the Reynolds stress term, $(-\rho u'v')$ for a variety of compliant surfaces. An important note of caution must be added. First we clarify that the calculation of the Reynolds stress is due to the streaks only. Secondly, due to the nature of our (psuedo non-linear) simulations we do not in any way claim our calculations for this term to be strictly correct. It was decided to choose the time period over which the streaks just begin to show the onset of lift-up to perform the calculation (for the time averaging). This may not be a reasonable measure. In practice, it is difficult to determine what time period to chose, particularly as the simulations we perform are very short. This is a valid criticism which is acknowledged here. In order to remedy this, a full non-linear simulation is required, where a much longer time period is employed.

The effect of the motion of the wall under the influence of the fluid are revealed in Figures 5.15-17. Firstly, with a progressively softer surface, the Reynolds stress production appears to have dropped significantly. Secondly, the graphs appear to suggest that maximum reductions are obtained when the natural frequency of the motion of the compliant coatings fall within a narrow range that allows interaction with the near-wall events; i.e. frequency or rate of growth and lift-up of the streak. (This was suggested by Choi (1989) and Choi *et al.* (1994) as a possible mechanism.) The displacement of

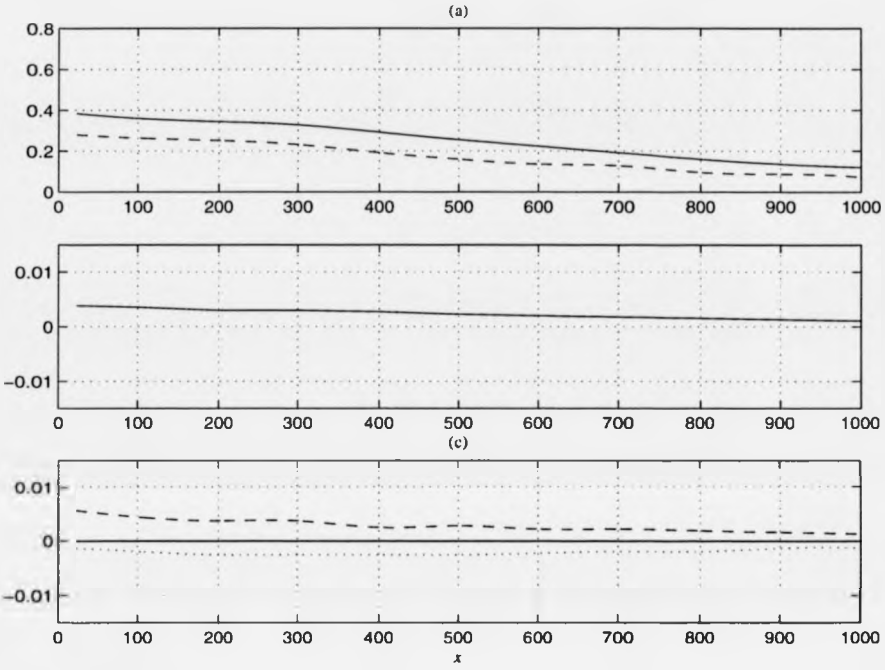

Figure 5.15: Streamwise variation of energy components over a compliant surface. (a) shows variation of terms A $(-)$, and B, $(--)$, (b). shows variation of Reynolds stress term, a, and (c) shows variation of terms b, $(--)$, c, $(-)$, and d $(\cdots)$.

the compliant surface would interact to weaken the growth of the streak and lift-up, and may be responsible for the increase in growth of the viscous sublayer observed by Lee *et al.* and Choi and his co-workers. The growth of the streak is slower, as a result the streaks tend to be more stable and the lift-up effect extends further before bursting occurs. In order, for confirmation of this mechanism, a fully non-linear run is required where the complete process is simulated. However, we can conclude that the flow field is modulated by the effects at the wall, resulting in the reduction of the shear stress. Our results tend to suggest that an overall global skin-friction and Reynolds

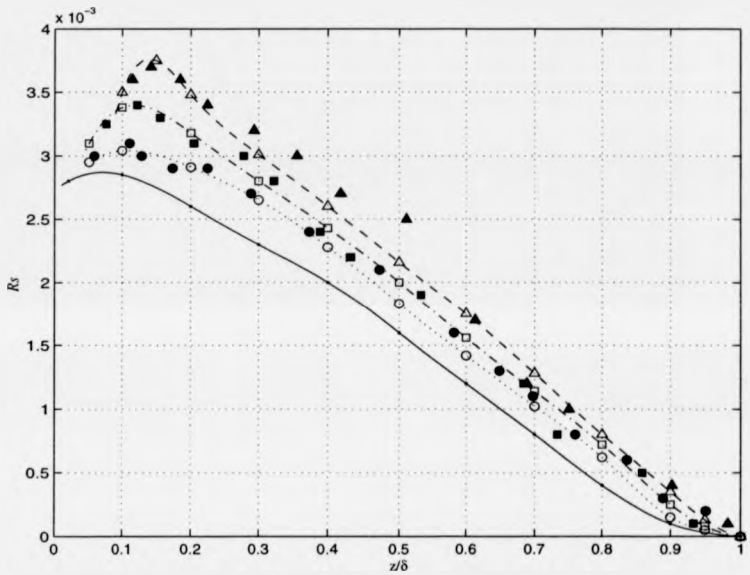

Figure 5.16: Reynolds stress, (Rs) as a function of wall-height, z/δ for different Reynolds numbers, R over a rigid surface. Comparison is made with the experimental measurements made by Lee *et al.*, these are denoted by the solid symbols. The following Reynolds numbers are considered: R=1348, ((▲), (△−−)); R=1952 ((■), (□−·)); R=2347 ((•), (○···)). Klebanoff's (1953) measurements at high Reynolds number, taken from Lee *et al.* are also plotted, and denoted by the solid line.

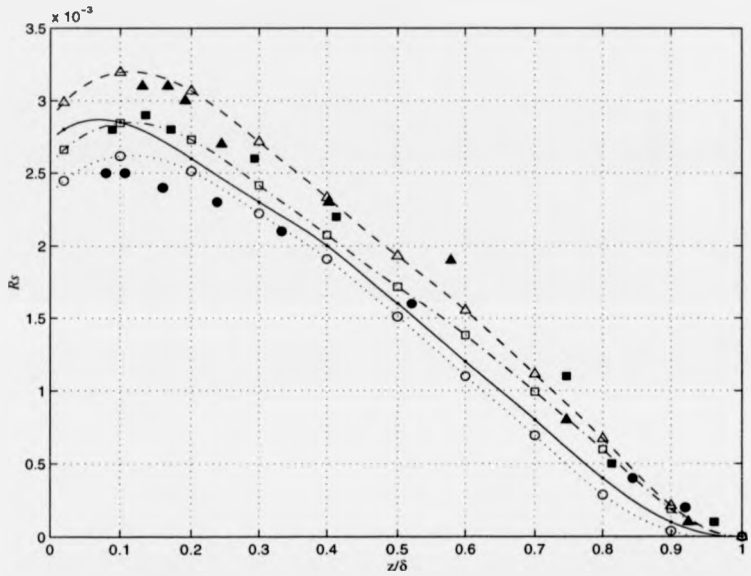

Figure 5.17: Reynolds stress, (Rs) as a function of wall-height, z/δ for different Reynolds numbers, R over a compliant surface. Comparison is made with the experimental measurements made by Lee *et al.*, these are denoted by the solid symbols. The following Reynolds numbers are considered: R=1348, ((▲), (△−−)); R=1952 ((■), (□−·)); R=2347 ((●), (○···)). Klebanoff's (1953) measurements at high Reynolds number, taken from Lee *et al.* are also plotted, and denoted by the solid line.

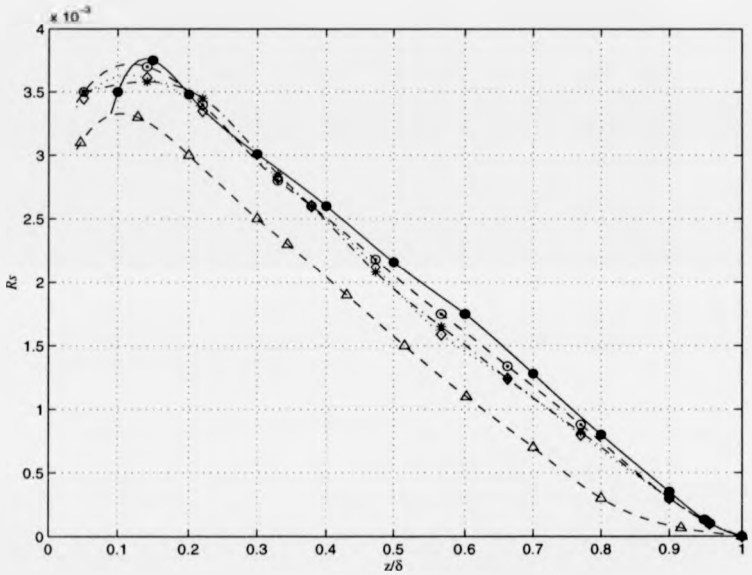

Figure 5.18: Reynolds stress, (Rs) as a function of wall-height, z/δ for different Reynolds numbers, R. with Choi properties at R=1348. Comparison is made with the experimental measurements made by Lee *et al.*, these are denoted by the $(\triangle)-\cdot$. $(\diamond\cdots)$, $(\circledast--)$, $(\odot--)$, $(\bullet)$ denote the Kramer-type, both Choi surfaces and a rigid surface respectively.

stress reduction can occur (depending on the length of the panel). This cannot be confirmed, as at present it is not possible to fully gauge the cyclic behaviour of the growth, oscillation, bursting ejection process of the streaks with our model.[3] The Lee *et al.* study observes intermittency and only local Reynolds Stress and skin-friction reductions. Bearing in mind the oscillatory nature of the flow, this may not be as unexpected as one may imagine, even though the surface is very soft. However, Choi *et al.* suggests a global reduction is achieveable.

5.3.2 Development of Near-Wall Structures over Compliant Panels

In light of the above, the practically important case of a compliant panel is investigated. The simulations are run in a similar manner to §4.2.3. Care is taken to ensure that the panel length was the appropriate length for the relevant material properties and Reynolds number range. The body force is positioned sufficiently far away from the inlet and panel leading edge to avoid reflections and allow the streak to develop before reaching the panel. Bearing in mind the increased sensitivity of the surface in a turbulent environment, both the leading and trailing edges are of prime concern. A compliant surface with properties identical to those used in the previous section is chosen.

In general, it appears as if the streaks are not significantly affected by the presence of the join. This is similar to the findings made in Chapter 4. Figure 5.19 shows the spatial and temporal development of a typical turbulent streak over the Lee *et al.* type

[3]Recent results from an ambitious DNS computation by Endo & Himeno (2001a,b) try to capture near-wall behaviour of the streaks in a turbulent channel. They show show qualitative differences between the vortical and streaky structures over a compliant wall. They do not observe the spacing of the streaky structures are reduced, but instead report that the width of the high- and low-speed streaks are slightly reduced and claim a 2 to 3% drag reduction as a result. Their simulations are limited as their solution is not fully optimised, and the surfaces chosen are very stiff. The latter is probably a reflection of the difficulty of obtaining a stable solution with their numerical scheme.

surface. Although it appears as if the leading-edge join marks the onset of the lift-up

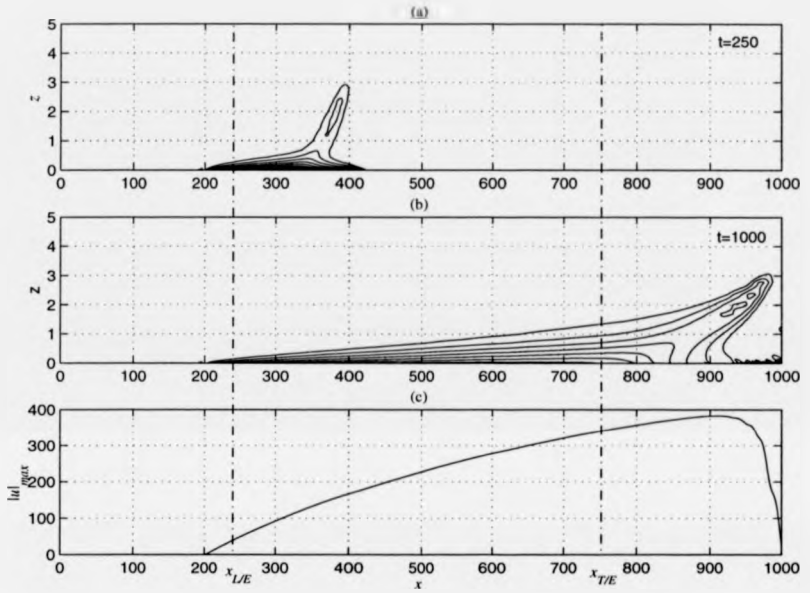

Figure 5.19: Development of near-wall structure in a turbulent boundary layer over a Lee *et al*-type compliant panel. (a)-(b) charts the development of the streak at t^+=20 and 50 respectively. (c) charts the velocity over the surface close at z_f^+=2.314.

effect, (especially for the Lee *et al.* model), the growth of the streak appears to have been substantially reduced over a compliant wall. Comparison with the development of a streak over a rigid surface reveals that the spatial and temporal location at which lift-up is induced appears to occur much later. This indicates that the effect of the mismatch between the rigid and compliant wall in the vicinity of the leading edge is sufficient to initiate lift-up, although the subsequent growth is considerably reduced. As the streak grows and gains momentum, the surface displaces accordingly to absorb any disturbance due to the mismatch of the surfaces at the join. Figure 5.19 traces the velocity across the domain. Note how the displacement at the join rapidly decays to a

much lower value which then remains invariant with time.

The trailing edge has little effect on the streak. The velocity traces reveal a smaller acceleration on the panel in the vicinity of the trailing edge. On the rigid surface, the lift-up of the streak rapidly attains an acceleration typical of the surface. In general, similar behaviour is observed in §4.2.3; The streak can pass freely, without significant distortion over the panel.

As described previously, the viscous and buffer regions would have thickened owing to the postponement of the bursting and sweep events of the streak and extension of lift-up. Figures 5.20-21 shows that the turbulence energy produced in the near-wall region is reduced (by the motion of the surface). The reduction of the production of turbulence energy by the Reynolds stress downstream in the near-wall region shows a massive steady reduction over compliant walls.[4] The effect of the leading-edge join adds an additional input of energy to the system, which ensures that its magnitude is large and its effects are felt over a reasonably short distance downstream. As before, a steady reduction of the viscous dissipation (b) and energy removal-term (d) is observed. The rate of irreversible work done to the wall by the disturbance pressure is reasonably high in the vicinity of the join, but rapidly decreases thereafter. Whereas the effect of the join, probably initiates the onset of lift-up, the effect of compliance delays the oscillatory and bursting and ejection effects. This is due to the remarkable ability of the panel to tune its wall response to the disturbance.

It was observed earlier that the maximum reduction of the growth of the streak was obtained when the natural frequency of the motion of the compliant coating fell within a narrow range that allows the interaction of the near-wall events. The displacement of the compliant surface would interact to weaken the growth of the lift-up of the streak, postponing the bursting events. For the case where a panel is sandwiched between two rigid surfaces, it is not suprising that the onset of lift-up occurs almost instanteously as

[4] As noted on Page 119, our choice of time period in which to calculate the Reynolds stress term corresponded to the period over which the streaks just began to exhibit lift-up. This may not be an adequate measure, and as such Figure 5.20-21 should be treated with caution.

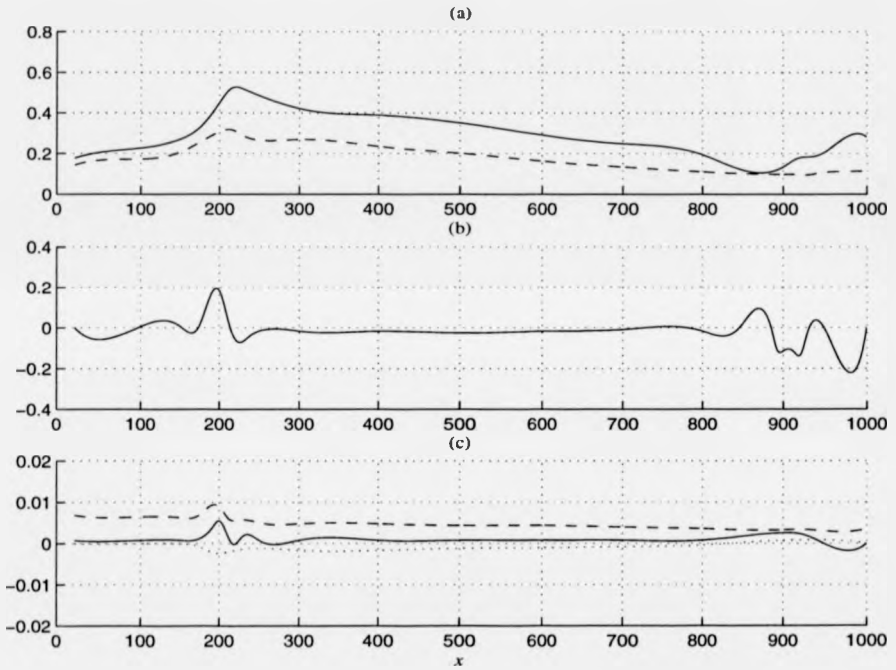

Figure 5.20: Streamwise variation of energy components over a compliant panel. (a) shows variation of terms A $(-)$, and B, $(--)$, (b). shows variation of Reynolds Stress term, a, and (c) shows variation of terms b, $(--)$, c, $(-)$, and d $(\cdots)$.

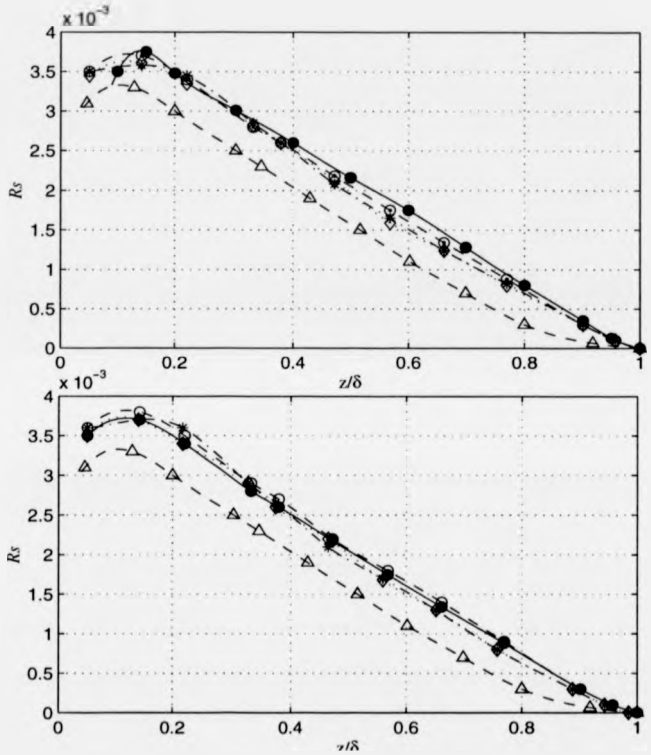

Figure 5.21: Reynolds Stress, (Rs) as a function of wall-height, z/δ for different Reynolds numbers, R=1348 over (a) compliant surfaces and (b) compliant panel. ($\triangle--$), ($\Diamond\cdots$), ($*--$), ($\odot--$), ($\bullet$) denote the Lee *et al.*, Kramer-type, both Choi *et al.* surfaces and rigid surface respectively.

the displacement of the surface increases from zero. This is sufficient to initiate lift-up and, if excessive, other flow- and surface-induced instabilities. If the disturbance is high enough and the panel too short its effects can be realised far downstream as if the large inflection effectively acts as a large roughness element. The ability of the compliant surface to react rapidly to reduce this effect at the join and downstream is therefore important. Our results indicate that the motion of the surface can readily adapt to this (although the limits are slightly narrower). In order to further reduce this, small levels of damping were introduced. This had little effect on the phenomenon: only marginal reductions of the growth rate were observed and almost no effect was observed at the leading edge.

Figure 5.22 shows how the spanwise spacing of the streaks increases as a function of the maximum streak velocity. The streaks are slightly less spaced out in comparison to that over a wholly compliant surface as a result of the additional forcing effect of the join. Nevertheless, the effect of compliance acts to suppress streak growth, although this is less than over a wholly compliant surface for the reasons described earlier. The graph also shows how progressively increasing the flexibility reduces the optimum streak velocity and increases the streak spacing. However, it must be borne in mind that softer surfaces are much more susceptible to flow-induced and surface-induced instabilities at the join. Turbulence may well be instantaneously initiated, as the join may act as a large roughness element, breaking down the streak altogether (i.e., the fast-moving surface waves act as large roughness elements sparking earlier transition). This is particularly the case for weaker streaks which are susceptible to rapid changes in boundary-layer and compliant wall motion.

As before, an attempt was made to quantify the ratio of the amplitude of the disturbance at the leading-edge join to the amplitude of the body forcing. If the amplitude of the disturbance at the join was sufficiently low, or only marginally greater than the body forcing, it was assumed that streak growth would either be sustained and/or promoted. If the disturbance was excessive, it was assumed that it could break down. This is a reasonable approximation, (although flow- and surface-induced instabilities

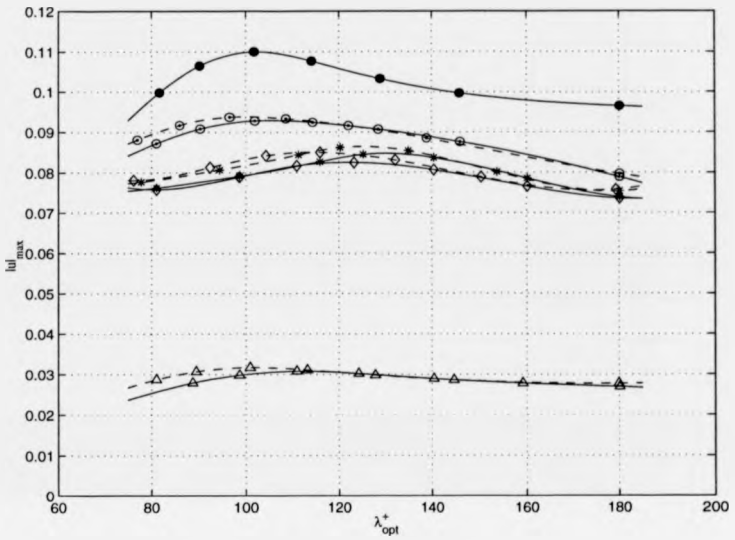

Figure 5.22: Maximum streak velocity, $|u|_{max}$, as a function of the optimum streamwise streak spacing, λ^+_{opt}. (•) denotes rigid surface, (△) denotes the Lee surface, (◇) refers to spanwise spacing over the the Kramer surface. (⊙) and (∗) denotes both surfaces considered by Choi *et al.* the solid lines represent variation over a wholly compliant surface, and the broken lines the variation over the panel.

also play a role). However, a plot of the amplitude ratio proved inconclusive. A Fourier analysis of the disturbance also proved inconclusive.

It can be concluded that despite the narrow range, it is likely that streak production can be successfully controlled using a series of locally tailored panels, particularly as the trailing-edge appears to successfully allow the streaks to pass over it almost unchanged. Care has to be taken at the leading edge, in the present configuration. If the wall properties are correctly chosen, such that the growth of the streak can be rapidly reduced in magnitude over a short space locally, then turbulence generation can be effectively reduced over the surface.

5.3.3 Effect of Orthotropicity

Previously, it was found that orthotropicity had a beneficial effect on the 'laminar streaks', through stabilising the streak growth. A similar effect occurs here, albeit to a lesser degree.

The orthotropic code used is based on that described in Chapter 4 with the some minor changes to ensure robustness in the presence of a turbulent boundary layer. Few attempts have been made to model the interaction of a turbulent boundary layer with orthotropic or anisotropic coatings. An early numerical study by Duncan (1986) was extended to study anisotropic surfaces in the early nineties (Duncan & Sirkis, 1992). Their model approximated the turbulent flow with a superimposed pressure-pulse convecting downstream to mimic the pressure disturbance of a single bursting event. The pressure pulse characteristics were taken from experimental measurements. The potential flow was also modified to incorporate experimental data. Duncan & Sirkis reported that anisotropy effectively controlled the amplitude and produced a more stable response pattern than with isotropic surfaces. (The amplitudes generated were larger than those over an isotropic surface, providing greater potential for modifying the turbulence.)

The outcome of a crude simulation over a wholly compliant surface for three cases: f_o=0 (limiting case), f_o=0.5 and f_o=1 (isotropic case) revealed that the growth rates were only slightly increased (as the compliance is increased in the spanwise direction). Figure 5.23 shows how the optimum spanwise spacing, λ^+_{opt}, varies as a function of the $|u|_{max}$. It is clear that orthotropicity generates much slower-convecting streaks. (Which may be helpful in controlling the motion (frequency) of wall responding to the streak production, as a result altering the limits to production and delaying lift up, thereby extending the viscous sublayer/buffer region.)

The effect of embedded panels is much the same, although the leading- and trailing-edge disturbances are more susceptible to the generation of extraneous disturbances. Only a marginal effect is observed.

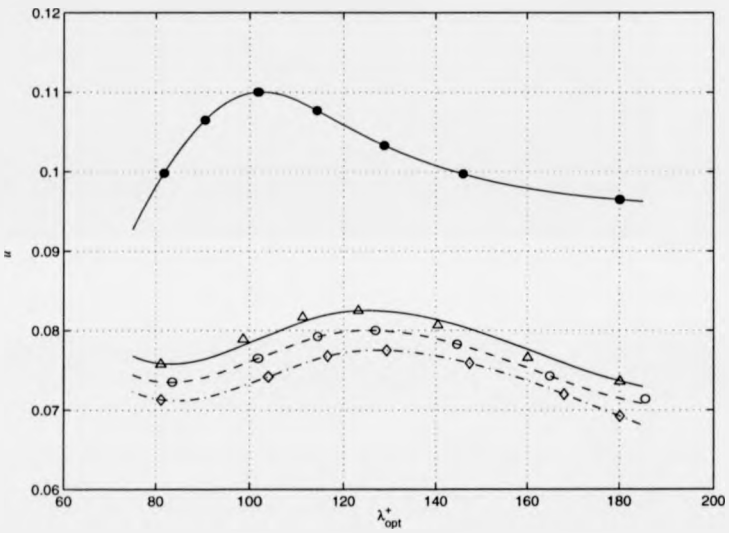

Figure 5.23: Maximum streak velocity, $|u|_{max}$, as a function of the optimum streamwise streak spacing, λ^+_{opt} over a Kramer-type compliant surface with varying orthotropicity. (•) denotes rigid surface, (△−) denotes the isotropic surface f=1, (◇−−·) the limiting orthotropic case, f_o=0, and (○−−) an intermediate surface,f_o=0.5.

5.4 Chapter Summary

(i). **Rigid Surface**

Streaks have been simulated over a rigid surface in a semi-empirical turbulent boundary layer and successfully validated by comparison with the experimental data provided by Kline *et al.* (1967), and Johansson *et al.* (1991), and the numerical simulation by Lockerby (2001). A freestream spanwise body force was used to generate the streaks. The velocity-vorticity model was extended to include the non-linear terms of the transport equations in order to to do this. It is important to note that fully non-linear simulations were not run as only a single mode in the spanwise direction was considered. Note that we are essentially using an analogy between the streaks observed in a transitional boundary layer with the near wall structures observed in the fully turbulent boundary layer. The streamwise streaks associated with the Klebanoff mode is fundamentally different from the structures observed in a turbulent boundary layer.

(ii). **Compliant Surface**

Streaks have been simulated over a range of compliant surfaces in a turbulent boundary layer demonstrated up to an 80% increase in the optimum spanwise spacing, compared with the rigid case. This is in agreement with the experimental study by Lee *et al.* (1993). The Lee surface has a Youngs Modulus, E, of 277Pa which is considerably more flexible that the Kramer-type (E=1.53MPa) and Choi-type (E=2.81MPa and 1.70MPa) surfaces that were also investigated. The general trend appears to be similar to that shown by the 'linear' streaks: The more flexible the surface the less likelihood of streaks developing and *vice versa*, (although a much greater dependency on the local flow conditions exists). This trend eventually breaks down as the surface is capable of generating its own waves and disturbances. The effect of damping and orthotropicity extended these limits slightly. The streak appeared to lift-up, which may be thought to herald the onset of a similar mechanism in a real turbulent boundary layer. It is likely that the behaviour observed may be due to the numerical scheme as well as changes in the mean velocity profile. Similar trends are observed for the case where streaks are

generated over a compliant panel. In general, they pass without distortion over the trailing edge. Where streaks pass over the leading edge, (rigid-compliant join), a local disturbance is induced, which can be detrimental if uncontrolled.

Chapter 6

Effect of Surface Roughness over Rigid & Compliant Surfaces

This chapter describes the effects that minute surface imperfections, in the form of waviness, has on the boundary layer over compliant surfaces. This is similar to a study of the effects of surface roughness and is important for a variety of applications. Although this phenomenon has been studied over rigid surfaces, our investigation over compliant surfaces appears to be the first such of its kind. The key findings are discussed in §6.3. A feature of dolphin skin is the existence of cutaneous ridges or microscales which run approximately normal to the direction of flow. We describe the hydrodynamic effect of these ridges.

6.1 Surface Roughness Receptivity

The study of surface roughness over rigid and compliant surfaces is challenging. Transition can be easily initiated by the roughness of different amplitude, geometry, distribution and flow conditions. Observation of the effects over compliant surfaces are unavailable, despite its importance for the development of marine drag-reduction devices. Effects over rigid walls, especially in turbulent flows are well known. Schlichting & Gersten (2000) describe the well-known experiments by J. Nikuradse where rough pipe walls were investigated. They also describe the concept of 'equivalent sand-grain (or standard) roughness'. This assumes that a specific roughness geometry, of height k, can be approximated as a wall covered with a layer of closely packed spheres, the diameter of which is termed the sand roughness height, k_e. An equivalent sand-grain roughness can be determined for specific roughness elements, such as ribs, cones, hemispheres, *etc.* However, whilst there are many possible forms of roughness elements, little attempt has been made by experimentalists, to choose of a 'standard' laboratory or equivalent geometry with which to study roughness. This has made it almost impossible to make any meaningful, quantitative comparison. Nevertheless, it is agreed that roughness favours transition, the transitional Reynolds number over a rough wall would be *lower* than for a smooth wall.

Figure 6.1 describes what is thought to occur over a rough surface. It is not unreasonable to assume that the effects caused by transition may have similarities to the structures over a smooth surface. Note, however, that for this scenario, no single predominant feature has yet been attributed (Morkovin, 1990).

The distribution and density of the imperfections has a significant effect on transition. If the imperfections are closely packed, there will be little upstream fetch to generate strong 'loop-like' vortices (shown in Figure 6.1). With increasing density, partially dead fluid may form between the elements. Consequently, the fluid in the troughs will have a low inertia and can be easily influenced by the freestream vorticity and pressure disturbances. The crests will have considerably higher streamwise (iner-

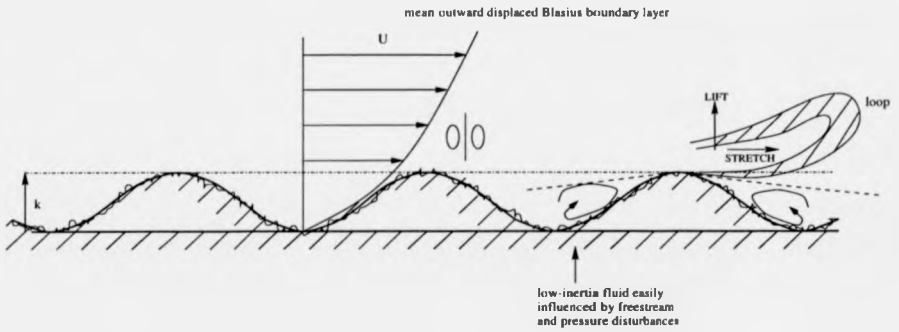

Figure 6.1: Schematic of flow over a rough (wavy) wall.

tia) velocity, (with spanwise scales of order, k, but minute relative to the boundary layer thickness, δ). Manufacturing imperfections, i.e. wall waviness, may create larger spanwise scales which could promote the amalgamation of smaller streamwise structures.

The value of the roughness height, k also has an effect. Small values of k, have almost no effect on transition and such walls are termed 'hydraulically smooth'. When k is sufficiently large, transition occurs at the roughness element. For intermediate values of k, transition occurs a certain distance downstream from the location of the roughness, (with the distance falling with increasing k).[1] Schlichting & Gersten (2000) describe this process in the form of experimentally derived correlations between k, the flow conditions and the critical Reynolds number for certain roughness geometries. The accuracy of this for the design applications to which they are commonly applied is unclear, as their correlations are based on limited experimental data determined from artifically created roughness forms, (typically single two- or three-dimensional elements).

[1] The roughness Reynolds number, R_k is defined as: $R_k = \frac{U_k k}{\mu}$, where, k is the roughness height, U_k is the undisturbed velocity at k, and μ is the kinematic viscosity. The effects are divided into three regimes: $0 \leqslant k \leqslant 5$ hydraulically smooth, $5 < k < 70$ transitional region, and $70 \leqslant k$ fully rough.

Experimental difficulties can be attributed to the isolation and quantification of the distributed receptivity. As roughness acts as a *steady passive device*, the unsteadiness has to be forced by sound or freestream turbulence. Some facets are known, but not fully understood. At low Reynolds numbers, the geometry alters the steady continuous distribution of vorticity in the boundary layer (Kendall, 1981; Reshotko & Leventhal, 1981; Corke *et al.*, 1986). The existing experiments conclude that there is a 'violent, almost instantaneous transition' from laminar conditions, the cause for which is unknown (Reshotko, 1984; Morkovin, 1990). Corke *et al.* (1981) reported that roughness increases the receptivity to bypass modes. They observed enhanced Tollmien-Schlichting, (T/S), wave amplitudes in the presence of (sandpaper) roughness, and suggested that low-inertia fluid in the valleys between the grains respond to freestream disturbances; once T/S waves appear, they grow faster than over a smooth wall. Reshotko (1984) suggested the disturbances amplified with frequencies lower than the T/S waves are driven by the local wake profile at the crest of the distributed roughness elements.

There is a lack of theoretical, numerical and experimental work to substantiate these claims. Recent DNS studies for flow over a series of spheres indicates that it is likely that the most amplified disturbances appeared to be located behind the following sphere. This induces a large response which is linked to the frequency governed by the streamwise spacing between the spheres. It may be that a combination of roughness and freestream turbulence causes this phenomenon, bypassing normal transition scenarios, and increasing boundary-layer thickness, δ. Kendall (1981) observed K-modes under these conditions. As we described earlier, this is a motion closely attributed to distributed roughness and has narrow, but stronger, scales.

Contrary to intutition, it has been shown that the distortion of the meanflow profile by roughness does *not* enhance instability. Instead, the thickening of the undeformed boundary layer drives the profile outward (Reshotko & Leventhal, 1981). Waviness introduces a continuous input of environmental energy to the system which, if excessive, may account for the experimental observations of Corke *et al.* (1981) that the

three-dimensionalisation of wavefronts leads to secondary instabilities. (The possibility that this is due to the destabilisation of the boundary layer is unlikely.)

Theoretical and numerical analysis appears to be more straightforward than experimentation. In the light of this, a series of crude simulations, in a laminar boundary layer, with a body force acting as the T/S driver over a *wavy* surface was undertaken. *Waviness implies minute, regular spaced, surface imperfections, as opposed to the random geometry of a (real) rough surface.* Our motivation resides with a basic understanding of the physical behaviour and stability of the T/S wave over compliant surfaces. Most geometrical forms of roughness can be modelled if represented spectrally, on a mode-by-mode basis for small roughness amplitudes. This allows easy exploration of the interactions amongst various modes of 'wall waviness'. This method is employed here, a description of which now follows.

6.2 Wavy-wall formulation

The roughness is modelled spectrally as a Fourier series. The flow over a wavy wall, and the possible interactions amongst various modes of wall waviness are modelled. Figure 6.2 illustrates the computational model. As the amplitude of the waviness is minute, each mode is considered separately. This is assumed to be a reasonable representation of a rough surface.

The waviness is modelled as a stationary sine wave. This avoids uncertainties associated with modelling boundary conditions on an irregular boundary, and allows easy control and investigation of the effects of k, and the density and distribution through the wavenumber, α. This reasoning is based on the assumption that the mechanisms governing transition are qualitatively similar. Note, however, that there is no evidence of the equivalence of our model to a 'real' rough surface. However, the roughness on a real surface could be decomposed into a Fourier series and each mode separately analysed, (where k and α are the investigating parameters). Floryan (1997) has shown this methodology to be physically meaningful. He demonstrated that, for suction-modified

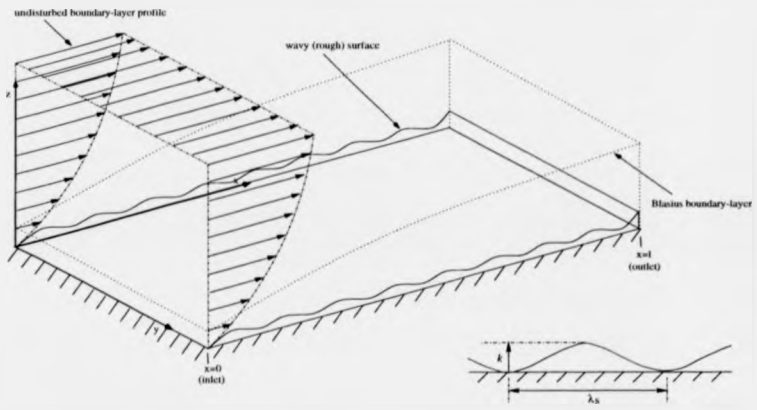

Figure 6.2: Rough (wavy) wall simulation schematic. d is the spacing between the peaks; λ_S is the wavelength; and k, the roughness amplitude.

flow, if the amplitude is small enough, the model accurately described how the flow modifications could induce an instability. (If the flow modifications were too weak, non-linear distortion of the velocity flow field would need to be induced before any effect occurred. If this were the case, the wall would be 'hydraulically smooth', and each particular roughness would need to be separately studied.) Note that Floryan (1997) does not impose a 'physical' wavy surface. Instead he introduces wall suction at regular intervals to simulate surface roughness.

Modelling surface roughness as a wavy surface is common amongst researchers modelling large-scale geometries and turbulence and heat-transfer effects. Other methods include 'immersed boundary' methods, where an array of body forces are used to model the surface. A recent paper by Cui, Patel & Lin (2003) demonstrate all three methods. Unfortunately, apart from Floryan (1997), and this research, there are hardly any studies which investigate the receptivity problem, as most concentrate on turbulence and heat transfer effects.

The wavy wall can be simply implemented as a simple, fixed, sine-wave distribution. The wavy surface is two-dimensional, (as shown in Figure 6.2 there is no spanwise

variation). The body force, which is used as the disturbance source, is varied in the spanwise direction as described in Chapters 4 and 5, but oscillates with time in order to generate a T/S wave. (According to the notation devised in §4.1.2, the body force is defined as Type *FO*.) It is necessary to match the amplitude of the compliant wall with that of the wavy surface. It was found that coupling of the fluid and wall-motion components to the wavy distribution did not pose a problem.

The system can be thought of as two components: a 'fixed' component with a displacement, η_f, and displacement of the compliant, or 'moving' wall, η_m. Using the co-ordinate system outlined and adopted in Chapter 3, consider the total velocity field composed into the undisturbed flow solution and a perturbation:

$$u = U + u'. \tag{6.1}$$

The exact boundary conditions require that:

$$u(z) = 0 \quad \text{at} \quad z = \eta; \tag{6.2}$$

$$w(z) = \frac{\partial \eta_m}{\partial t} \quad \text{at} \quad \eta = \eta_f + \eta_m, (\text{note that}, \eta_f = k_w sun(\lambda_w x)) \tag{6.3}$$

where $\eta \ll 1$. Expanding u(η) in a Taylor series about y=0, and neglecting terms of $\mathcal{O}(\eta^2)$, we get:

$$w(\eta) = w'(o) + \mathcal{O}(\eta^2) \tag{6.4}$$

$$u(\eta) = u'(0) + DU(0)\eta + \mathcal{O}(\eta^2) \tag{6.5}$$

Combining the two previous sets of results we obtain:

$$u'(0) + DU(0)\eta = 0 \Rightarrow u'(0) = -DU(0)\{\eta_m + k_w sin(\lambda_w x)\} \tag{6.6}$$

$$\text{and,} \quad w'(o) = \frac{\partial \eta_m}{\partial t}. \tag{6.7}$$

where, k_w and λ_w are the waviness amplitude and wavelength respectively. In order to maintain stability, two provisos must be ensured: Firstly, the speed of the travelling wave in the surface must match that of the flow and; Secondly, the amplitude and more importantly the wavelength of the waviness must match the motion of the surface. It

was found that the code behaved well. The compliant surface was able to respond adequately over a relatively wide k range, even for the case where a compliant panel was modelled. This will be demonstrated in the following section, over rigid and compliant walls.

6.3 Effect of Surface Roughness over Rigid Surfaces

6.3.1 Validation

T/S waves were generated over a wavy-rigid surface. A stationary body force, which was varied in the spanwise direction, was implemented as the T/S driver. This is necessary as waviness is a passive device, i.e. roughness alone is not sufficient to result in destabilisation. The unsteadiness introduced by the driver and the behaviour of the T/S wave, under the influence of waviness is examined. In the first instance, this serves to establish whether the code can produce satisfactory results. (The implementation and spanwise variation of the body force is described in §4.1.2.)

Figure 6.3(a) shows neutral stability curves for three, (non-dimensional), roughness heights, k^*: a hydraulically smooth surface, k^*=0.718; a moderate roughness, k^*=18.9; and a large roughness height, k^*=55.7.[2] Comparison is made to a smooth surface, k=0. Compared to the smooth case, transition occurs earlier in the presence of roughness. Figure 6.3(b) demonstrates the integrity of the methodology adopted through comparison with the experimental study in air by Reshotko (1984). Whilst no definite claim is made to the equivalence of our model to 'real' roughness, and taking into account the uncertainties in the available experimental data, the results of the simulations appear to show general agreement.

Figure 6.4 shows how the growth of the T/S wave is enhanced in the presence of waviness. Figure 6.4(d) shows how the growth rate of the T/S wave increases with

[2]These have been non-dimensionalised with using kU_∞/ν, where k is the dimensional roughness height and U_∞ is the freestream speed. The density of sea water, ρ is about 1025kg/m^3 and ν is the kinematic viscosity 1.0026×10^{-6}m^2/s.

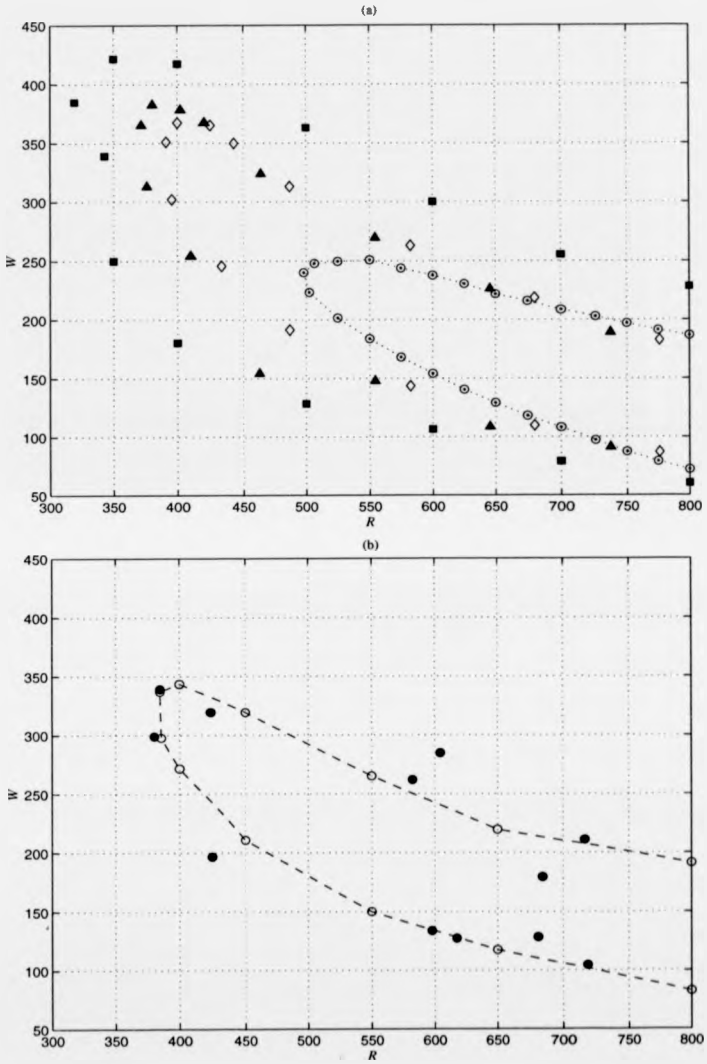

Figure 6.3: Neutral Stability Curves for surfaces of varying roughness over a rigid wall. (a). (⊙−−) refers to the smooth, (k^*=0), surface. (◇), (▲) and (■) denotes surfaces with roughness heights of, k^*≈0.718, 18.9 and 55.7 respectively. (b). (•) denotes experimental results for k^*≈0.718 by Reshotko (1984), and (∘) results from our simulation. W is the non-dimensional frequency.

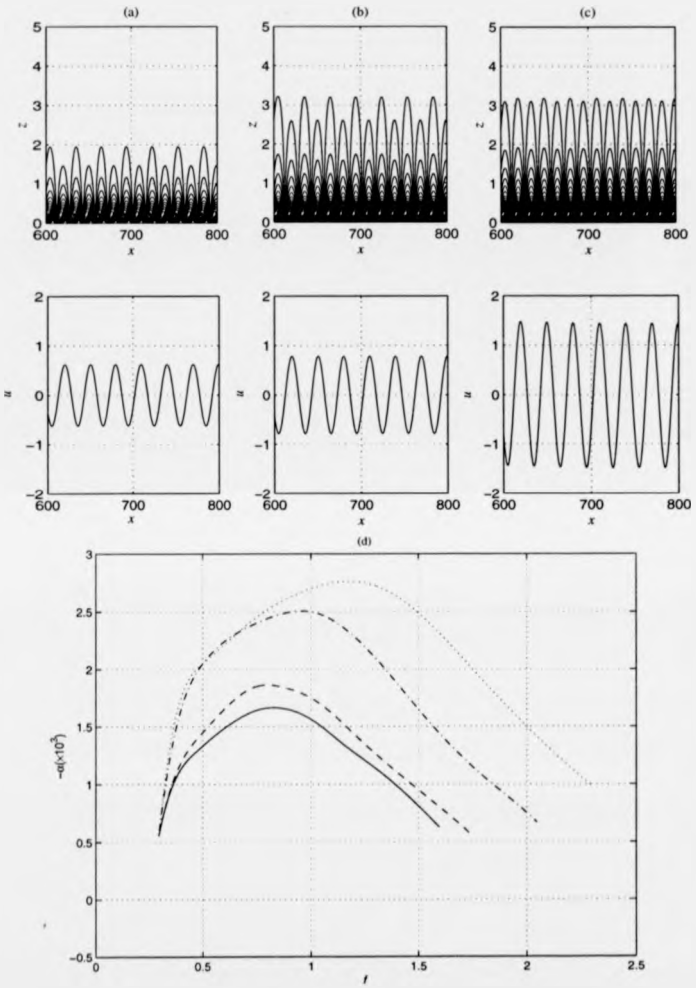

Figure 6.4: T/S wave development over smooth, (a). k=0; and wavy: (b). k^*=18.9, (c). k^*=55.7, surfaces at R=750. The growth rate of the T/S wave as a function of frequency, f for a the three surfaces is shown in (d). A contour plot of the vortices and trace of the streamwise velocity at z=2.34 is shown in (a)-(c). Note the change in the character of the T/S wave with increasing k. (d) shows how the growth rate of the T/S wave varies with f. $(-)$ corresponds to k=0, and $(--)$, $(-\cdot)$ and $(\cdots)$ correspond to k^*=0.72, 18.9, and 55.7 respectively. λ_S is fixed at 125μ. According to Figure 6.3, for R=750, W is chosen as 155.

an increase in k^*. The optimum for each k^* refers to the case where T/S waves are likely to grow the most rapidly. At first glance, it may be thought that the contour plots, (a)-(c) show that the T/S wave is slightly 'tilted back' in nature. However, this is probably not the case, even though the contours appear to be that way. Nor should they be confused with oblique waves, which are associated with the initial development of three-dimensional effects. 'Oblique' in this context refers to the orientation of the wavefronts in the horizontal plane, and such effects are often the result of an interaction between a two-dimensional disturbance and a pair of oblique instability waves with equal but opposite spanwise wavenumbers. This occurs at a particular resonant frequency and/or location, and can cause the oblique waves to amplify sufficiently to interact with themselves so that the dominant non-linear activity becomes the self-interaction between a pair of oblique T/S waves. Certain flow structures, such as streamwise vortices, are believed crucial for the generation of small-scale turbulence, and is attributed to such an interaction. In general, the presence of oblique waves cannot be disregarded. Slightly oblique waves, for example may occur. These have been shown to have almost the same amplification as two-dimensional waves by Wu, Leib & Goldstein (1997) and probably also occur in this scenario, as in practice, any slight asymmetries in the flow can make such waves a dominant feature, (leading to early secondary instabilities).

For the completeness, a note may be made regarding the effect of altering the roughness wavelength, λ_S, i.e. the spacing between the crests and troughs, for rigid walls. Figure 6.5 shows the behaviour of a T/S wave where k is fixed and λ_S is varied. The plot summarises the general trend observed. As the height is effectively fixed and the spacing between each surface wave increased, the growth of a well-defined two-dimensional T/S wave is promoted, and the fluid then allowed to sufficiently recover its momentum between the next change in curvature. This is expected as, in nature, the increase of λ_S is associated with a substantial reduction of k- i.e. the surface approaches the scenario where the wall is hydraulically smooth. When λ_S is of the order of k, a two-dimensional T/S wave is observed which remains well-defined. When λ_S

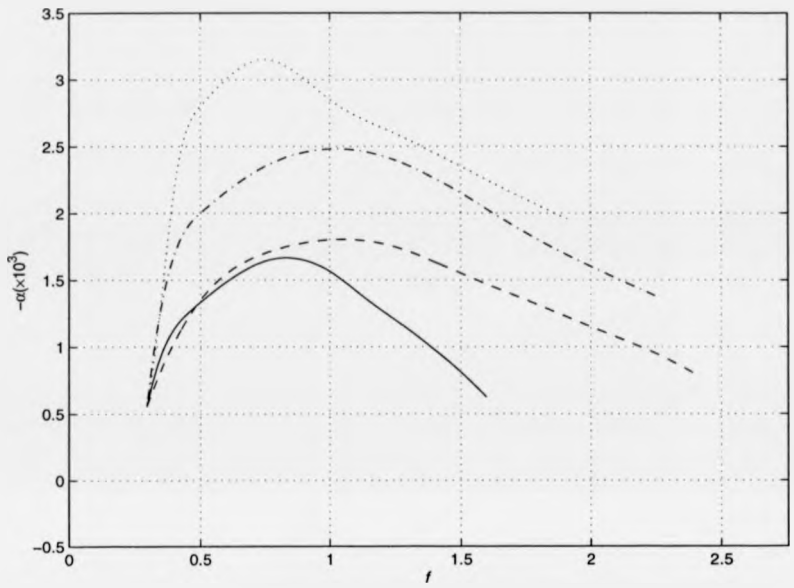

Figure 6.5: Growth rate of a T/S as a function of frequency, f, over a surface with a fixed roughness height, k^*=18.8 and varying wavelength, λ_S. $(\cdots)$, $(-\cdot)$ and $(--)$ correspond to λ_S=50, 125, 170μ. $(-)$ approaches a smooth surface. According to Figure 6.3, for R=750, W is chosen as 155.

is very small and k is large the T/S wave has the highest amplitude and grows most rapidly.

In conclusion, we concur with the findings in the available literature: there appears to be a basic relationship between the geometry of the waviness and the character of the T/S wave. When the height of the geometry increases (λ_S fixed), the character of the T/S wave is changes and the growth rate increases. When λ_S is increased, (k is fixed), the growth rate of the T/S wave is reduced and subsequent non-linear effects are postponed. In nature, a general trend is exhibited where λ increases as k falls and *vice versa*. In this case: when λ_S approaches k, a well-defined two-dimensional T/S wave

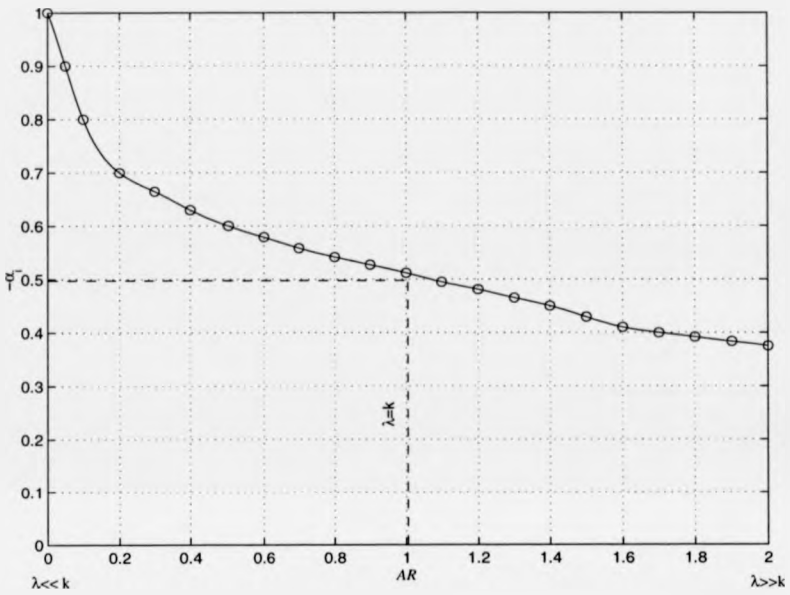

Figure 6.6: Growth rate as a function of the roughness aspect ratio, AR, over surfaces in the absence of compliance. The aspect ratio of the wavy surface is defined as λ_S/k. At the extremes, when the wavelength, λ_S, is very long and coincides with very low roughness amplitude, k, T/S waves grow as if roughness did not exist. If λ_S is very short (or close to zero), and k is very high, T/S growth is accelerated.

can be maintained; When k is much greater than λ_S, a rapidly growing T/S wave is prompted and, When λ_S is longer than k the behaviour is almost identical to that over a 'smooth' surface. This is summarised in Figure 6.6. Although not shown, the effect of increasing the Reynolds number would shift the curve upwards as three-dimensional effects would set in earlier.

6.4 Hydrodynamic Effects of Roughness over Compliant Walls

This section is devoted to a description of the hydrodynamic effects of roughness over a compliant surface. Our prime interest is to show the effect that the dolphin's cutaneous ridges have, which is currently unknown. §6.4.1 describes these ridges in the context of their perceived function. §6.4.2 describes the general effects of wall waviness over compliant walls. §6.4.3 describes results where cutaneous ridges are modelled. For the majority of the simulations reported a simple scaling of the flow parameters and careful choice of wall properties was required. The T/S driver was implemented in the same manner as in §6.3.

6.4.1 The Structure of Dolphin Skin

Figure 6.7 illustrates the main structural features of the dolphin epidermis and upper dermal layer based on work by several authors. Close examination of a (live) dolphin clearly reveals the existence of these ridges. Figure 6.8(a) shows the location of the cutaneous ridges (or microscales). They run approximately normal to the direction of flow, as opposed to the ridges found on shark scales, which run in the direction of flow. Cutaneous ridges are spaced approximately 250μm apart with the roughness height, k_d, of the order of a few microns. They are not found on the snout, melon and lower jaw, but become prominent at the level of the blowhole and eyes (Figure 6.8(a)). Although the existence of these ridges is reasonably well known, most studies refer to the skin surface as 'smooth' implying that they have little hydrodynamic effect. Ridgway & Carder (1993) suggest that they may have an important rôle.

Babenko & Surkina (1969) postulate that the skin is subject to considerable levels of active control by the nervous system. Pressure fluctuations are transmitted to an underlying layer composed of dermal papillae by an elastic membrane (upper epidermal layer). Dermal papillae and their matrix are composed of a suspension of fat cells and

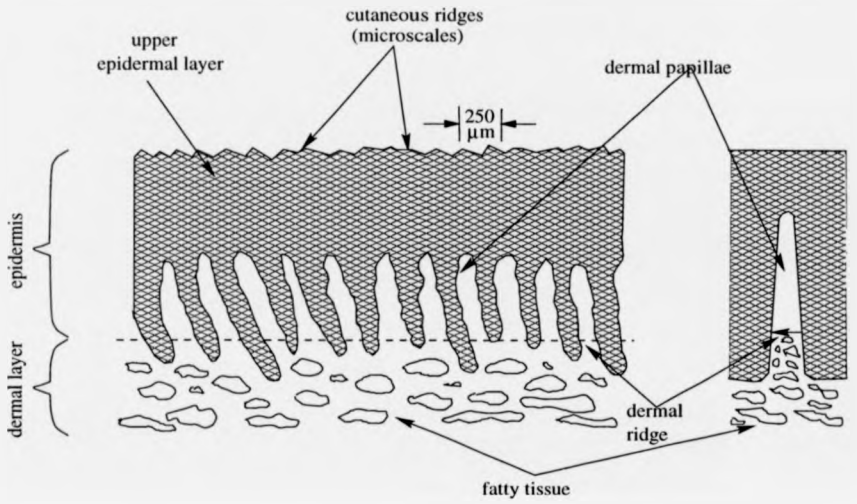

Figure 6.7: Cross-sectional view of dolphin skin. (Carpenter, Davies & Lucey, 2000) Babenko & Surkina (1969) notes errors in Kramer's original model of the epidermis. Kramer's coatings were manufactured from soft natural rubber with voids containing highly viscous silicone oil to model the effect of hydrated fatty tissue. The grade of these components were varied to obtain the maximum drag reduction. Kramer based his model on misleading photographs of sections of dolphin epidermis, which, although they appear to be similar, in particular with respect to dimensions, are incorrect.

hydrated tissue. Depending on their location, the dermal papillae make an angle of 10° to 80° to the vertical and extend upwards from dermal ridges running in the streamwise direction. It is likely that the viscoelastic properties of the papillary layers and skin are regulated by the variation of blood through the dermal papillae (Babenko & Surkina, 1969; Babenko & Carpenter, 2003).

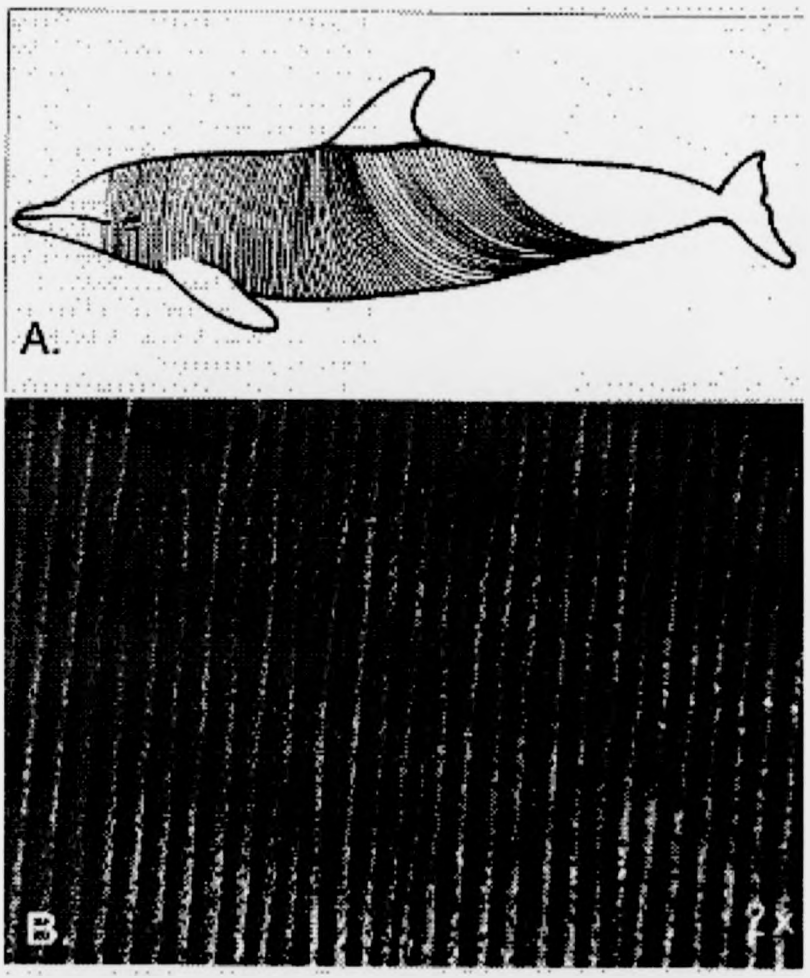

Figure 6.8: Dolphin Skin Structure. (a). Sketch showing orientation of cutaneous ridges on a bottlenose dolphin; (b). 2× photograph of skin 250mm posterior to the blowhole and 100mm lateral to the dorsal midline where the ridges run perpendicular to the length of the body. (Ridgway & Carder, 1993).

6.4.2 Hydrodynamic Effects

For the first time, our simulations reveal the possible beneficial effects of roughness in the form of fixed surface waves over a compliant wall. As a result, the possible effect of cutaneous ridges may have been identified. We show that roughness can trip the boundary layer under 'real' conditions if k is large enough. The growth rate of T/S waves are significantly reduced compared to a surface without compliance. Within a certain range of spanwise forcing, surface geometries and Reynolds numbers, streamwise vortices can be induced. As described in §4.0 and §5.0, these are believed to be indicative of the onset of bypass transition and can be easily avoided by tailoring the panel to the appropriate flow conditions.

Kramer-type coatings are adopted with surface properties similar to those described in Chapters 4 and 5, (i.e. they can be realised for water flowing over a flat plate and ensure that divergence and travelling-wave-flutter are marginally stable at a given flow speed). The majority of the simulations are conducted at a speed of 9m/s. This corresponds to a Reynolds number of approximately R=20×10^6 for flow over a 2m long flat plate (based on the body length of *Tursiops truncatus*). Carpenter, Davies & Lucey (2001) report that calculations have been made from photographs which reveal the wavelength of divergence was close to that predicted for optimum compliant surfaces designed for 9m/s. Measurements of the free wave speed on live dolphins by Madigosky *et al.* (1986) over a limited number of locations generally agreed with an estimate of $0.7U_\infty$ for an optmised surface (if U_∞ is taken as 9 m/s).

T/S waves were generated in an identical manner to §6.3.1. The body force is situated at x_f=203 and z_f=2.314 (non-dimensional) wall units to introduce a T/S wave over a wholly compliant surface (Figure 6.2). A T/S wave is generated over a progressively wavy surface until the height and wavelength of the intended waviness is reached. This was necessary to avoid start-up problems. (Checks over a rigid wavy surface showed that the short gradual increase of the roughness until the desired value is met did not affect the solution.) Each simulation was conducted using null values to

initialise the disturbance field. The downstream boundary conditions were strengthened to ensure no reflections of the disturbance occurred. Similar checks to those described in Chapter 3 were made in order to confirm the code behaved satisfactorily.

The effect of waviness for compliant walls can be appreciated through examination of the neutral stability curves shown in Figure 6.9. Stability curves for a variety of roughness heights are shown. As expected, instability occurs earlier in the presence of roughness- the curve is shifted to the left, and as a consequence, the critical Reynolds number, (R_{crit}) is reduced. For example, for a moderately wavy surface, where $k^*\approx18.9$, T/S waves are stabilised when $R_{crit}\lessapprox438$. When R exceeds this value, the disturbances rapidly propagate downstream. This compares to the corresponding case in the absence of compliance, where $R_{crit}\approx375$. In general, comparison with identical geometries for rigid walls reveals that instability occurs sooner and at lower disturbance levels. Compliant walls can readily tune their motion to the geometry of the waviness at certain disturbance levels. (In addition, it is worth noting that at low Reynolds numbers there is little difference between *smooth* walls, whether compliant or rigid.)

Figure 6.10 shows a selection of velocity and contour traces at three different Reynolds numbers for the case where the roughness prescribed is of the form $k^*=18.9$. The traces demonstrate how the T/S wave is modified. The character (amplitude) of the T/S waves differ in each case. Figure 6.11 compares the growth rates of the T/S waves. The curves clearly show that the T/S waves propagate more rapidly over a compliant surface, compared to the rigid-wavy surface.

Closer examination of Figure 6.10 reveals that when R exceeds 375, the contours appear to be slightly tilted back. As described earlier, this should not be confused with oblique waves. 'Oblique' in this context refers to the orientation of the wavefronts in the horizontal plane. As described earlier, such waves are associated with the initial development of three-dimensional effects. However, slightly oblique waves which have almost the same amplification as two-dimensional waves may occur in practice due to any slight asymmetries in the flow, as a result of unsteadiness from the T/S wave. (Wu *et al.* (1997) noted that the inclined or oblique streamwise vortices are believed to

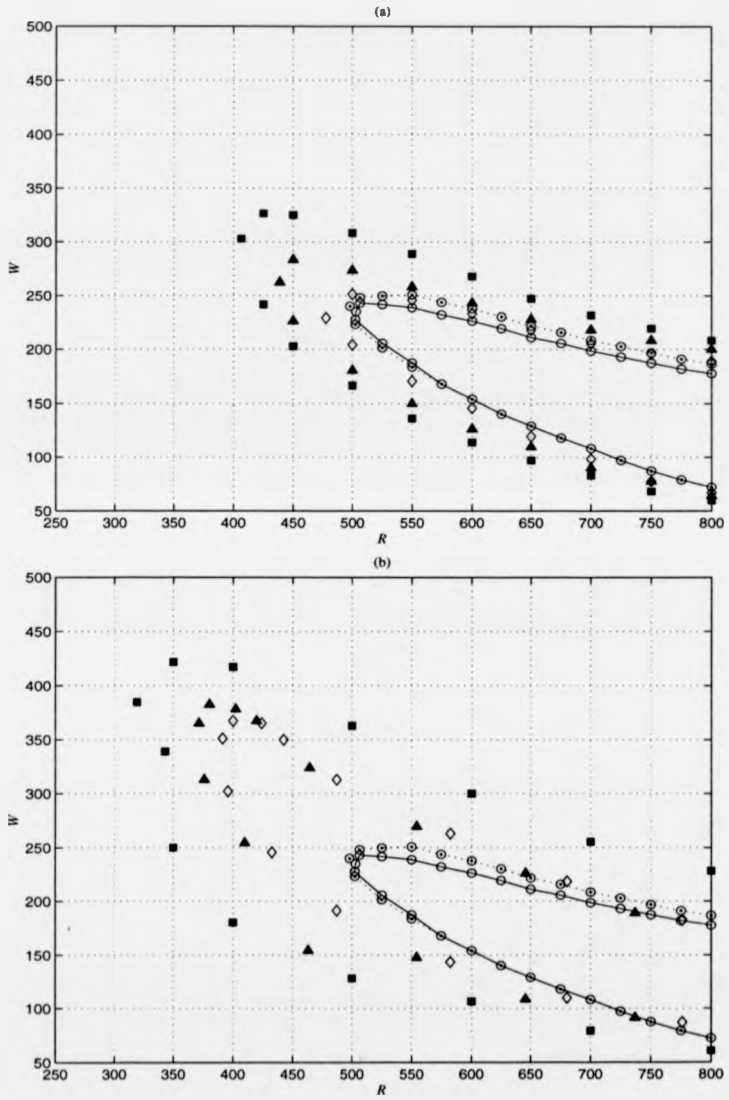

Figure 6.9: Neutral Stability Curves for surfaces of varying roughness over (a) compliant, (Kramer type) and (b) rigid walls. ($\odot\cdots$) and ($\circ-$) indicate the numerical solution over smooth rigid and compliant (Kramer-type) surfaces respectively. ($\Diamond$), ($\blacktriangle$) and ($\blacksquare$) denotes surfaces with roughness heights of, $k^*\approx$0.718, 18 9 and 55.7 respectively. Note how increasing k increases the region of instability in both cases.

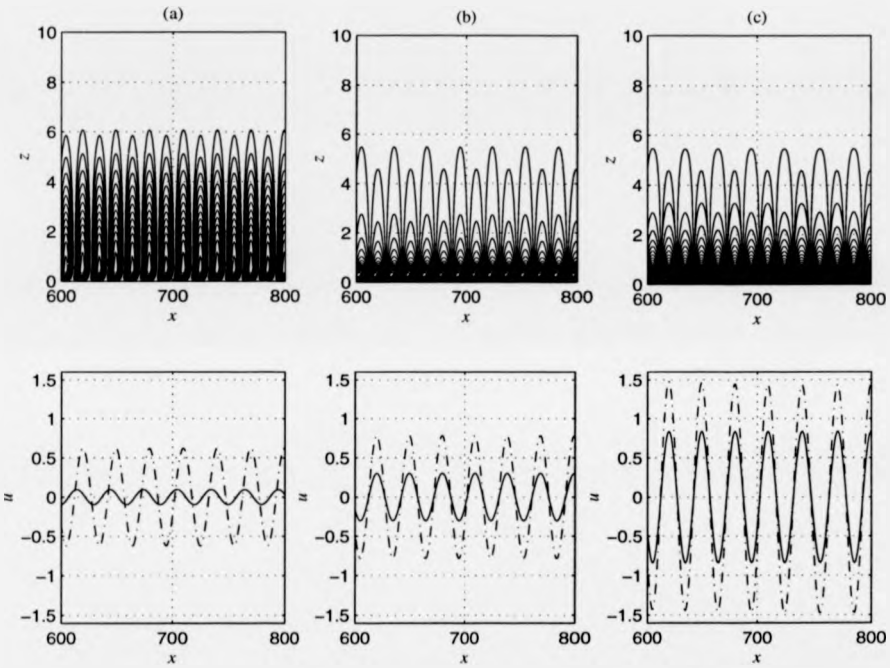

Figure 6.10: Contour and velocity traces of T/S wave over a compliant surface with an imposed waviness of k^*=18.9 for (a) R=750, (b) R=904 and (c) R=1100.(i). Contour plot of the vorticity and (ii) a trace of the streamwise velocity at z=2.34 is shown. The $(-\cdots)$ trace corresponds to velocity over a rigid wall. Note the reduction of amplitude and character of the T/S wave. λ_S is fixed at 125μm. According to Figure 6.9, W is chosen for R=750, 904, 1100 as W=140, 130 and 95 respectively.

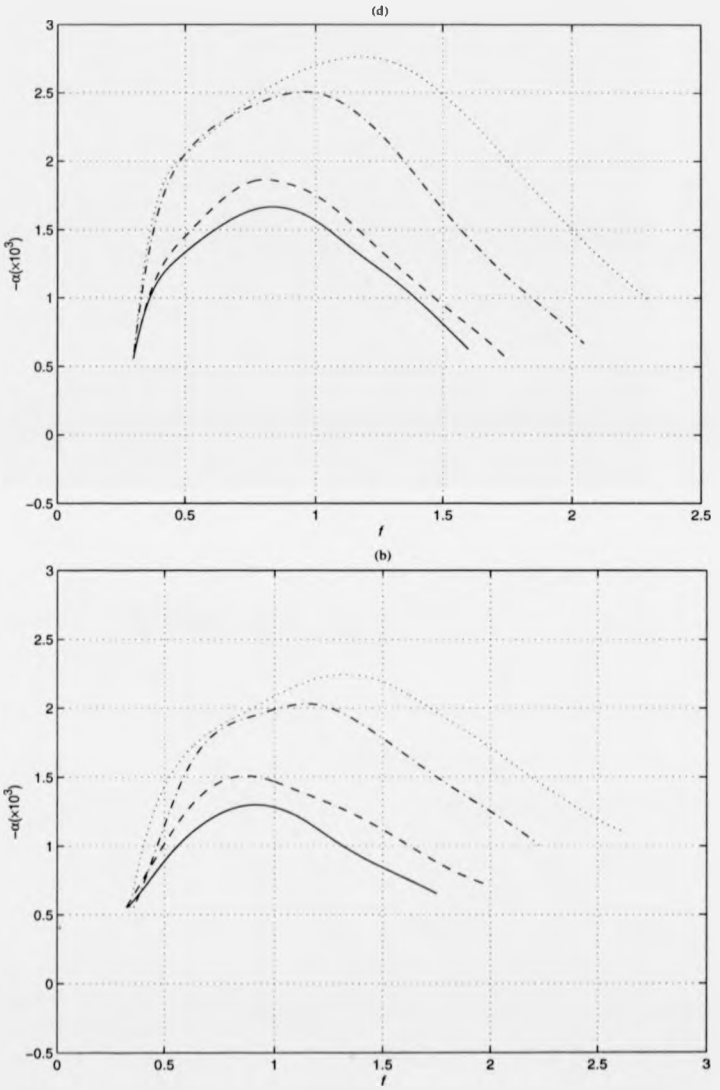

Figure 6.11: Growth of T/S wave over smooth and wavy surfaces over a rigid, (a), and compliance, (b), wall as a function of frequency.(−), (− −), (−· · ·) and (· · ·) denote k^*=0, 0.719, 18.9 and 55.7 respectively. λ_S is fixed at 125μm. For R=750, W is chosen as 155.

be crucial for the generation of small-scale turbulence are attributed to such a mode. Oblique waves are equivalent to such an interaction, i.e. they are equivalent to disturbances that vary sinsodially with the spanwise direction in a symmetric and periodic nature. Additionally, it is known that oblique T/S waves have been observed growing at a faster rate than two-dimensional ones over smooth compliant walls (k=0) (Yeo, 1992; Yeo, Zhao & Khoo, 2001).) Note also that, compared to the rigid wavy surface, the effect of compliance shifts the optimum frequency, f, at which the maximum growth occurs. This indicates a higher threshold must be reached before the onset of instability is triggered over compliant walls (i.e. compliant walls are less effected than rigid walls where roughness is present).

Examination of the velocity profile showed that whilst the nature of the T/S waves have changed, i.e. amplification rates are reduced, compared to that in the absence of compliance, the actual global character of the flow field has not drastically altered. This concurs with similar studies over a rigid-wavy/rough surface. Also the character of the flow field only changes very weakly as a function of the Reynolds number. Our simulations for rigid walls qualitatively supported the general findings from existing experimental (Reshotko, 1984; Corke *et al.*, 1986) and computational work (Floryan, 1997), and were found to also hold true over compliant walls. As the boundary layer was only marginally affected, within the limits of stability, flow modifications do not create significant local inflection points in the velocity profile observed. Traces of the local and global velocity profiles in either case confirm this: the boundary layer, or more precisely the nature of the surface is relatively accomodating.

An additional brief note may be added regarding the wavelength and roughness height. Figure 6.9(a) showed a selection of neutral stability curves for wavy-compliant surfaces, where k varies from hydrodynamically smooth, (k^*=0), to rough (k^*=55.7). Closer examination reveals that R_{crit} is reduced by as much as 10-15% compared to an identical geometry over a surface in the absence of roughness. It is clear that instability occurs earlier in the presence of roughness. Increasing k reduces R_{crit} further, until in theory, instability and transition occur almost instantaneously. The effect of

increasing the spacing between the crests, (i.e. increasing λ_S), generally delays the onset of instability. This suggests that there is a certain geometry for each particular flow condition in which the T/S wave can be sufficiently attenuated such that its growth rate is comparable to that over a smooth surface. On the basis of this, and the structure of actual dolphin skin described in §6.4.1, it is likely that the dolphin can alter the spacing between the ridges too by flexing their skin. (Photographs showing the rippling of skin of dolphins leaping out of the water, (i.e. porpoising), suggests that this is likely, although as yet there is no experimental or computational work which supports this view.)

Although, it is possible to mark the limits to where the roughness level acts as hydrodynamically smooth, transitional or rough surface, it is unclear as to whether there is a clear quantitative relationship between the amplification rate, and hence character of the T/S wave and k and/or λ_S. A trace of the reduction of the growth rate as a function of k shows no consistent mathematical trend where the reduction of growth is proportional to k. Figure 6.12 plots the growth rates of the T/S wave as a function of the ratio of k to λ_S. The graph shows that the compliant surface is relatively more accommodating to disturbances without significant destabilisation. Those disturbances that are most likely susceptible to trigger transition are those which generate the most 'amplified' vortices. To avoid this and maintain stability, it is reasonably straightforward to tailor the panel by varying k and λ and the level of compliance to suit the disturbance level, (in this case to the spanwise wavenumber characterising the body forcing.)

The Effect of Wall Compliance

Figure 6.13 illustrates the effect of progressively increasing the compliance. The curves show how the growth of a T/S wave is modified, as a function of frequency for a moderately wavy surface of k^*=18.9. Each curve corresponds to surfaces which have properties giving stiffnesses that are half and a third the level of stiffness of the Kramer surface. Whilst the actual practical use of these surfaces is dubious, the graphs clearly

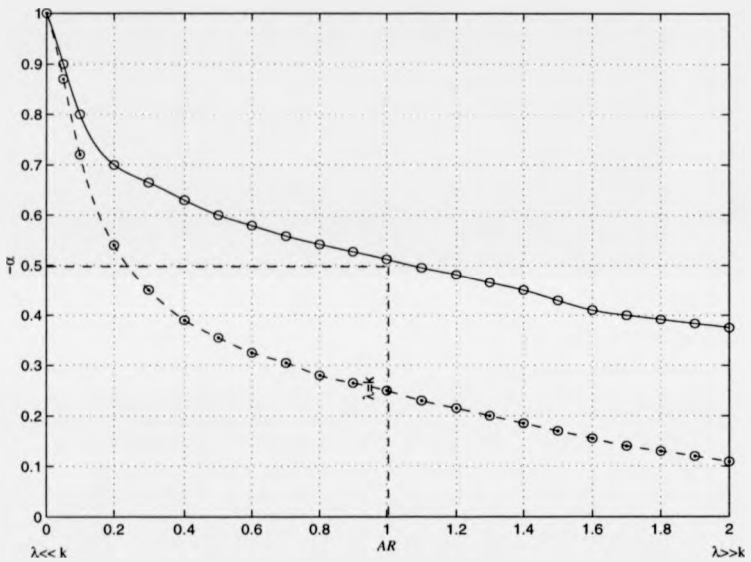

Figure 6.12: Growth rate as a function of the roughness aspect ratio, AR for compliant ($-\odot-$) and rigid ($-\circ$) surfaces. The aspect ratio of the wavy surface is defined as λ_S/k. At the extremes a long surface wavelength, λ_S, coinciding with very low roughness amplitude, k, promotes T/S growth as if roughness did not exist. If λ_S=0, and k is very high, T/S growth is accelerated.

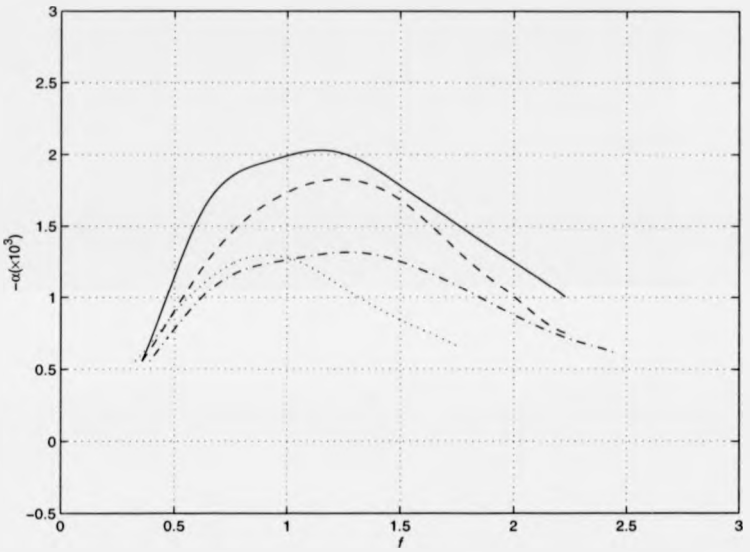

Figure 6.13: Growth rate as a function of frequency, f for surfaces of increasing compliance. $(-)$, $(--)$ and $(-\cdot)$ denote a Kramer surface, and surfaces which have half and a third of the Kramer surface stiffness respectively. k^* is fixed at 18.9, λ=125μm, R=1000. $(\cdots)$ denotes the growth rate for a smooth Kramer type surface. For R=750, W is chosen as 145.

demonstrate the benefical nature of increasing compliance: compared to an identical geometry in the absence of compliance, the amplitude of the T/S wave is reduced by as much as 15% and 46% for surfaces with a half and third of the stiffness of the Kramer surface. Associated with this, the maximum growth rate, (i.e. the most amplified or dangerous state), occurs at much higher spanwise wavenumbers. A selection of neutral stability curves are shown in Figure 6.14. These confirm that the critical Reynolds number, R_{crit} is considerably lower with increasing flexibility. Unfortunately, this behaviour breaks down if the compliance is increased beyond a third of the stiffness of the Kramer surface.

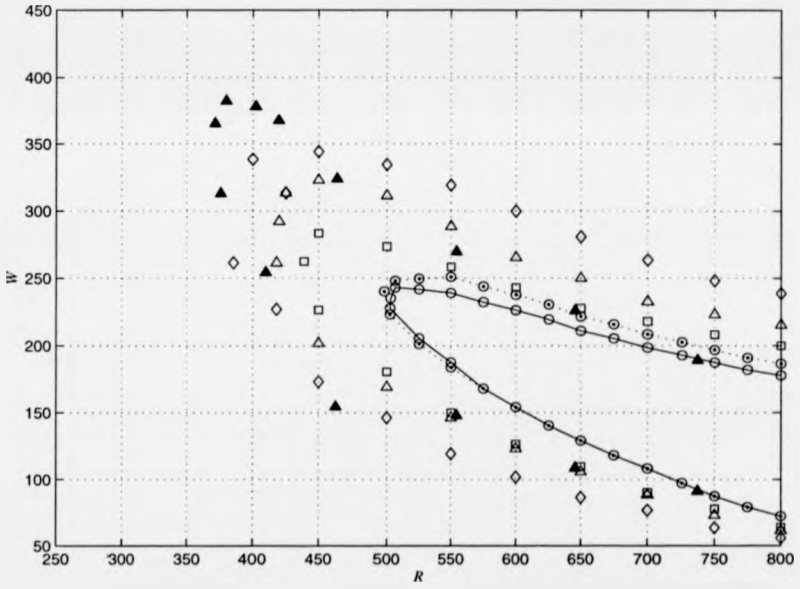

Figure 6.14: Neutral Stability Curves for surfaces of varying compliance with a waviness of k^*=18.9. ($\odot\cdots$) and ($\circ-$) indicate smooth rigid and compliant (Kramer-type) surfaces respectively. ($\square$), ($\triangle$), and ($\Diamond$) denotes Kramer and surfaces that have half and a third of the Kramer surface stiffness respectively. ($\blacktriangle$) denotes an identical geometry over a rigid surface. k^*=18.9 and λ_S=125μm.

demonstrate the benefical nature of increasing compliance: compared to an identical geometry in the absence of compliance, the amplitude of the T/S wave is reduced by as much as 15% and 46% for surfaces with a half and third of the stiffness of the Kramer surface. Associated with this, the maximum growth rate, (i.e. the most amplified or dangerous state), occurs at much higher spanwise wavenumbers. A selection of neutral stability curves are shown in Figure 6.14. These confirm that the critical Reynolds number, R_{crit} is considerably lower with increasing flexibility. Unfortunately, this behaviour breaks down if the compliance is increased beyond a third of the stiffness of the Kramer surface.

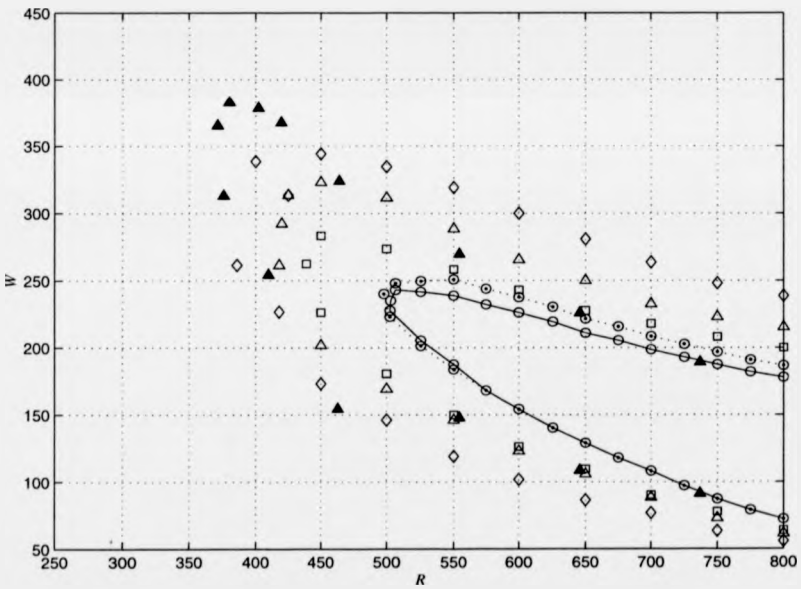

Figure 6.14: Neutral Stability Curves for surfaces of varying compliance with a waviness of k^*=18.9. ($\odot\cdots$) and ($\circ-$) indicate smooth rigid and compliant (Kramer-type) surfaces respectively. ($\square$), ($\triangle$), and ($\Diamond$) denotes Kramer and surfaces that have half and a third of the Kramer surface stiffness respectively. ($\blacktriangle$) denotes an identical geometry over a rigid surface. k^*=18.9 and λ_S=125μm.

The stability of the surface is dependent on its roughness geometry. Figure 6.15 plots the maximum growth rate of T/S waves as a function of the aspect ratio for surfaces of increasing compliance. A basic trend is shown between the variables, which is increased when the level of compliance is raised. Where the graph deviates sharply, resulting in a rapid rise in the T/S growth rate, this indicates the inability of the surface to adequately adjust its displacement to match that generated by the imposed waviness and the forced T/S waves. Under this condition, rapidly growing waves are formed which are likely to spark transition-to-turbulence earlier. In general, any asymmetry in the flow can force transition to occur earlier than otherwise expected. For this reason, unsuprisingly, smoother compliant surfaces appear to be more resiliant to such destabilisation than those in the presence of high levels of roughness.

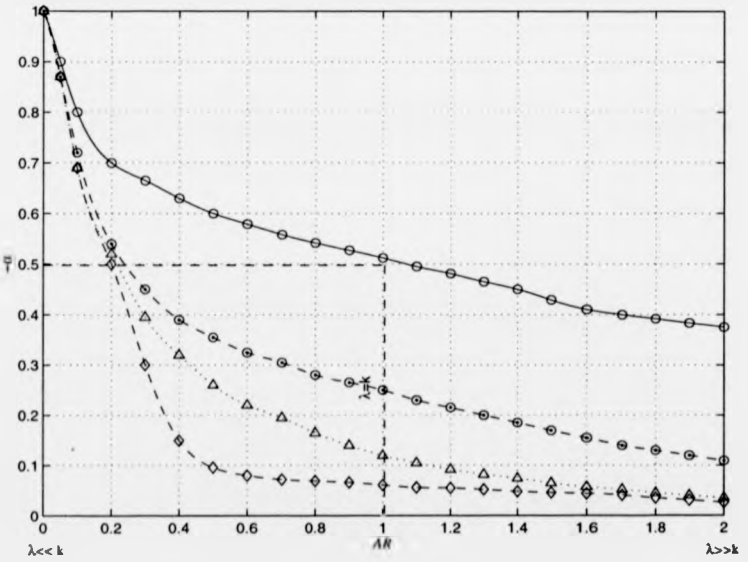

Figure 6.15: Growth rate as a function of the roughness aspect ratio, AR for surfaces of varying compliance. (⊙), (△) and (◇) denotes Kramer and surfaces that have half and a third of the Kramer surface stiffness respectively. (○) denotes a rigid wall.

6.4.3 A Brief Note on the Hydrodynamic Significance of Cutaneous Ridges

It is now possible to demonstrate the hydrodynamic effect of cutaneous ridge. The geometry of the imposed waviness is similar to that quoted in the literature: The cutaneous ridges are modelled aligned normal to the direction of flow and spaced 250μm apart with a roughness height, k, of less than 50μm. The ridges are assumed to be uniformly spaced. A flow speed of 9 m/s is assumed, and Kramer surface wall properties are chosen as described earlier.

Figure 6.16 compares a typical T/S wave generated over a smooth compliant surface (k=0) to that over our cutaneous-ridge model. It is immediately obvious that, under identical conditions the T/S waves have a lower amplitude, over a wavy wall. Figure 6.17 plots the growth rate as a function of the frequency for the cutaneous ridge wavelength, λ_S, varying from 50 to 1000μm. In general, the T/S waves, over this surface are noted to travel much slower than over a rigid surface. It is also worth noting that increasing the λ_S also reduces the growth rate and shifts the optimum spanwise wavenumber, such that it approaches the case for a smooth surface (when k is very small). The growth rate demonstrates that the wave is growing much slower with a reduced T/S amplitude. It may be noted that the motion of the wall can rapidly tune itself to the pressure perturbations under such geometries.

6.4.4 Compliant Panels

Now our attention will turn to the practically important case where a finite compliant panel is located within a rigid surface, as shown in Figure 6.18. As described earlier, Davies & Carpenter (1997) have shown that T/S suppression can be achieved with short panels with lengths comparable to T/S wavelengths of one or less. Particular interest resides with the effects where a T/S wave passes over the leading and trailing edges.

As before, Kramer-type coatings with the wall properties defined in §4.3.2 are cho-

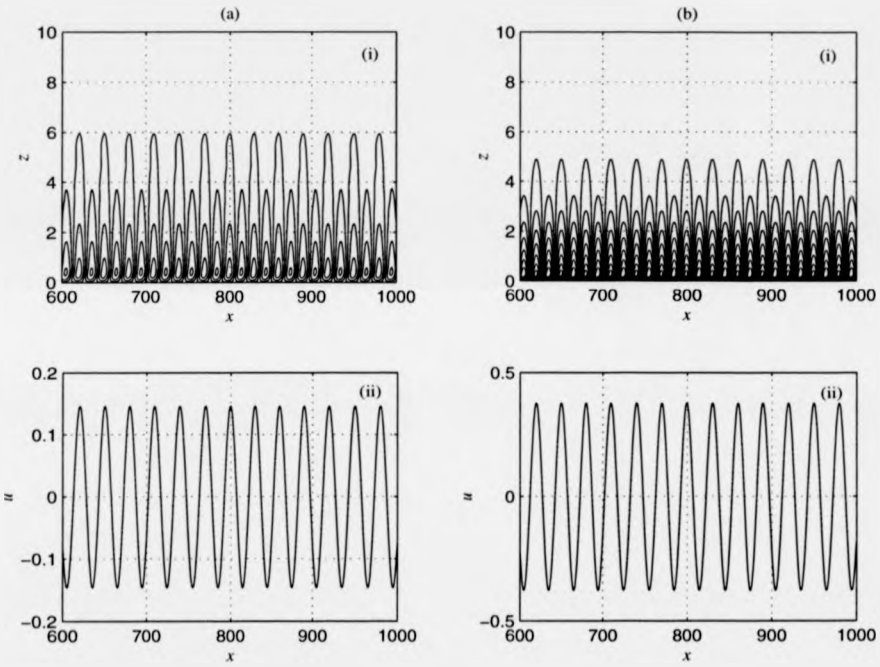

Figure 6.16: Development of T/S wave over a compliant surface with cutaneous ridge geometry. Contour and velocity trace over Kramer-type compliant (a) wavy, (k^*=50μm, λ=250mmm) and (b) smooth ($k = 0$) wall. R=750, W=155.

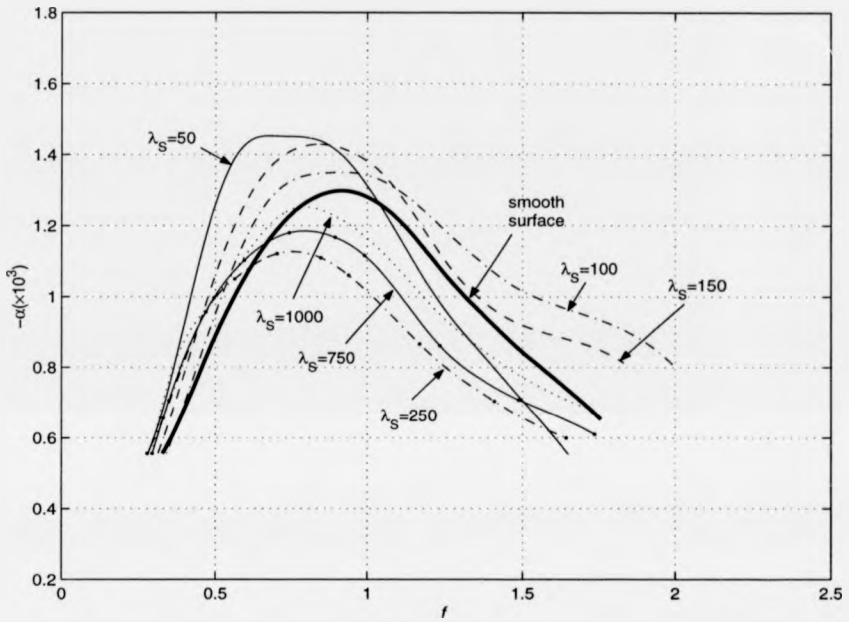

Figure 6.17: Growth rate as a function of frequency, f for surfaces of varying wavelength λ_S for fixed roughness height, k=50μm. In general, over a rigid surface, increasing the wavelength of the roughness promotes a reduction in amplitude until the surface is considered hydrodynamically smooth, *denoted by the bold solid line.* In general, over a compliant surface the same principle applies. It is noted that there is a small region of wavelengths which yields a lower growth rate and amplitude, bucking the general trend observed. This is observed here with our cutaneous ridge model. The compliant surface can successfully tune itself the wavelengths observed to cause a reduction in growth rate and amplitude. This is not so suprising as the relative roughness and height changes as a result of the displacement of the surface. For R=750, W is chosen as 155.

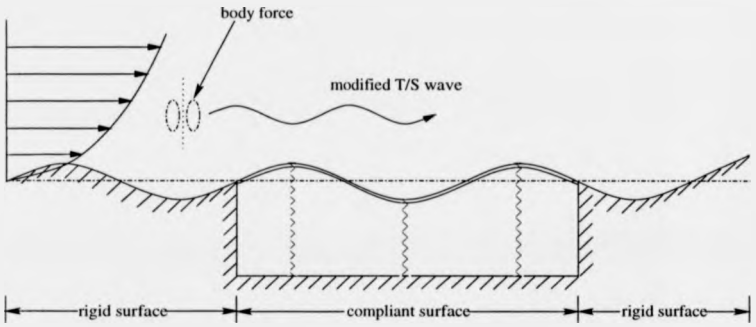

Figure 6.18: Waviness (roughness) imposed compliant panel test case under study.

sen and the majority of the simulations conducted at speeds of between 7 and 9 m/s. T/S waves are generated over the rigid surface and allowed to develop over the entire length of the compliant panel before passing onto the rigid surface. The waviness of the rigid surface increases steadily to the desired roughness height for the reasons outlined in §6.4.2. Each simulation was conducted using null values to initialise the disturbance field. The downstream boundary conditions were strengthened to ensure no reflections of the disturbance. The body force (i.e. the T/S driver) is positioned sufficiently far away from the inlet and panel leading edge to avoid unphysical/forced disturbances and allow the T/S wave to develop sufficiently. (Typically, 50-100 streamwise wall units downstream and 100-200 wall units upstream of the leading edge. The latter depends on the roughness geometry.)

As a check on the integrity of the code a T/S wave was allowed to develop over a hydrodynamically smooth geometry, and compared to a plane surface. The streamline variation of the locally defined wavenumber and spatial growth rate of the T/S wave is similar to the smooth case. The local disturbances at the leading and trailing edges are of the same order of magnitude as the smooth case and globally insignificant for this scenario.

In practice, as Chapter 4 showed, the leading edge could influence the system.

However, the situation is now complicated by the presence of roughness, as well as the leading-edge and the effects of compliance. For the surface to be effective, the wavelength of the modified wave should fall within a range to which the motion of the compliant surface can respond favourably. This has already been determined for a wholly compliant surface and henceforth will be used as a guide. Davies & Carpenter (1997) have specified the limits and behaviour of a two-dimensional T/S wave passing over a smooth compliant panel. They showed that the panel could influence the upstream flow through localised disturbances originating close to the leading edge, or over a greater disturbance in the form of an upstream propagating flow-induced wave.

The behaviour of the panel is also dependent on whether the T/S wave is above or below the panel cut-off frequency. Davies & Carpenter (1997) show that over a smooth surface the panel response is dominated by the T/S wave when the T/S frequency is below cut-off. The panel response is highly complicated above cut-off. In this case, the wall motion is described by three components: A damped, flow-induced surface wave which propagates upstream from the trailing-edge with a wavelength close to the T/S wave; A lightly damped, almost neutral, much longer, flow-induced surface wave that propagates downstream from the panel leading edge, and a local response at the panel edges that can be closely modelled by the solutions to the pressure-free equation of motion for the compliant wall. The introduction of the additional component of waviness, i.e. the effect of stationary free waves, complicates matters further! We shall avoid this by running simulations below cut-off, as under this condition the panel response is dominated by a T/S wave (modified by the presence of roughness and compliance).

Before we describe the local effects at the ends, it is useful to note the global nature of the boundary-layer profile was not drastically altered. The local changes in the boundary-layer profile brought about by the roughness alone is not sufficient to bring about excessive change. The displacement of the compliant surface is more than likely to be the cause of change in the character of T/S waves. Traces of the velocity and growth rates of a T/S wave modified by a roughness were found to have only slightly increased to the case without any joins. The panel appears to accept T/S waves propa-

gating across it without any significant detrimental effect, after any initial disturbances due to the leading-edge join have travelled out of the domain. As we will show later, traces of the T/S wave across the domain demonstrates that the T/S wave can readily and rapidly adjust its growth as if it were generated on a compliant surface without any joins. Once the T/S wave has left the trailing-edge it rapidly adjusts its growth rate. The rate at which these changes occurs is greater than over a smooth surface, and is due to the presence of the leading and trailing edges. Figure 6.19 shows curves of neutral stability for a variety of roughness geometries. The curves are similar to those shown earlier, although displaced.

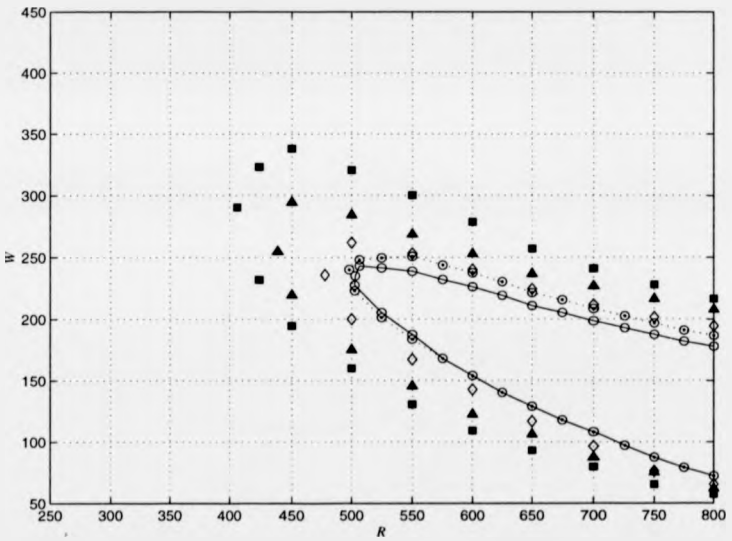

Figure 6.19: Neutral Stability Curves for surfaces of varying geometries over compliant panels. (⊙...) and (∘−) indicate over smooth rigid and compliant surfaces respectively. (◊), (▲) and (■) denotes surfaces with roughness heights of, $k^*\approx 0.719$, 18.9 and 55.7 respectively.

So, to conclude, the surface is relatively inert to detrimental destabilisation of the T/S wave, particularly as the wave can pass over the joins. The effect of varying the

geometry of the T/S wave, expecially at the joins can be benefical as local disturbances can be effectively controlled in this way.

Local Behaviour of the Panel Edges

Local disturbances occur at the leading and trailing edges, which if excessive, can cause other types of instabilities to form and dominate. The traces of the disturbance enstrophy and kinetic energy integrals for a T/S wave highlight the general behaviour (Figure 6.20) . The T/S wave is amplified and reaches a maximum in the vicinity of the leading edge. The local disturbance created is sustained for a short distance,

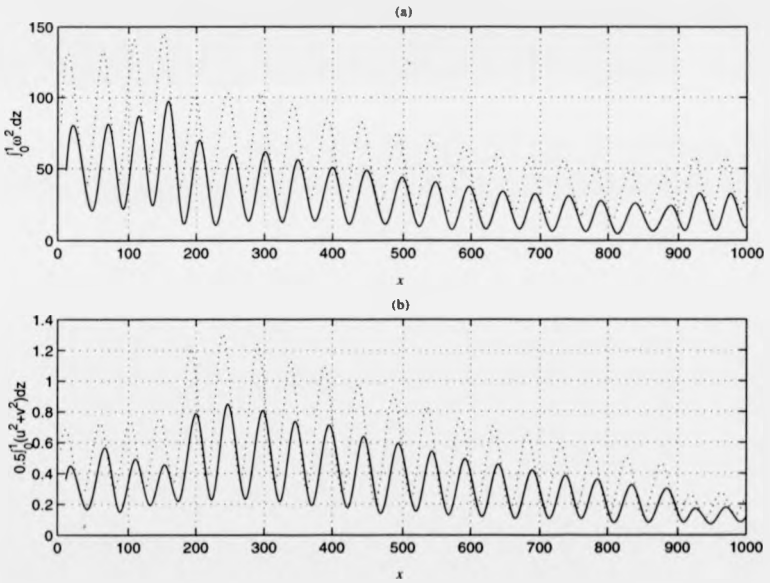

Figure 6.20: Trace of the disturbance enstrophy, (a), and kinetic energy, (b), for a T/S travelling over a compliant panel. $(\cdots)$ and $(-)$ denotes streamwise variation over a surface with k=0.21mm and k=0 respectively. The panel is situated between x=160 and 810. Note that the rigid and compliant walls are both wavy.

(typically 5-10 streamwise wall units) and then it rapidly decays to a well-defined state, and then leaves the domain. (The amplitude of the T/S wave is greater than over a smooth surface for this case.) The opposite occurs at the trailing-edge: the amplitude of the T/S wave rises at the trailing-edge and then immediately falls. The T/S wave is then allowed to attain a growth rate typical of that over a rigid-wavy surface. The amplification at the trailing-edge is of an order of magnitude lower than at the leading edge. Comparison with a smooth surface reveals considerably lower T/S amplitudes and growth and decay rates.

Figure 6.21 shows how the amplification rates vary as a function of surface geometry. The amplification rates appear to be consistently higher than corresponding case for a smooth compliant panel. The break from the linear nature of the line indicates the

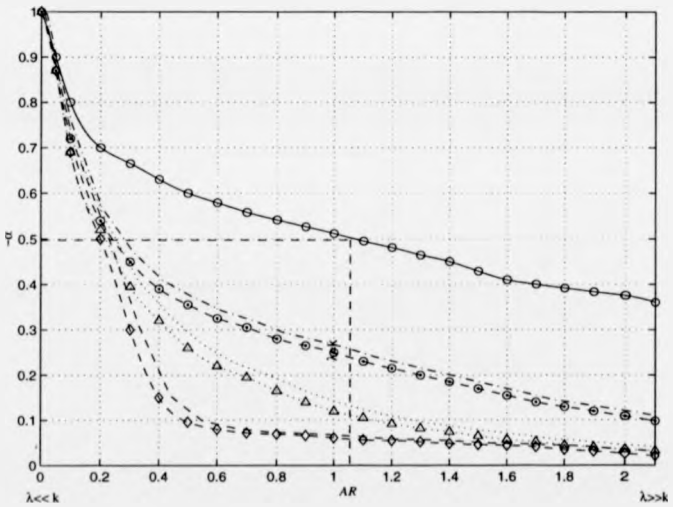

Figure 6.21: Growth rate as a function of the roughness aspect ratio, AR for surfaces of varying compliance. (⊙−·), (△···) and (◇−−) denotes Kramer and surfaces which have which are half and a third of the Kramer stiffness respectively. The lines without symbols denote growth rate of T/S wave over a panel. (∘) denotes a rigid surface.

position at which the beneficial effects of the panel begins to reduce and transition-to-turbulence sets in. This is associated with rapidly propagating oblique T/S waves. The amplitude spike of the disturbance at the leading edge may lead to premature transition if the amplitude of the incident T/S wave is sufficiently large. Smaller instabilities that travel in the opposite direction from the trailing-edge may also have a deterimental effect. However, apart from the obvious case where the amplitude of the disturbance at the join forces the panel to generate and sustain its own surface-based destabilising waves, no conclusive quantitative relationship can be found to link the amplitude at the panel edges to the panel response. The growth rate of the T/S wave where the compliance of the panel is increased is also shown in Figure 6.20. Careful choice of the geometry, Reynolds number and panel length must be made to achieve the most stabilised modified wave. An increase of compliance does not necessarily reduce the amplification rate as the mismatch between the rigid and compliant surfaces can generate enhanced T/S waves over shorter lengths. Within the realistic Reynolds number ranges and geometries studied, favourable effects were observed.

Analysis shows the panel ends, especially the trailing edge, is relatively inert with regards to forcing any detrimental destabilisation to the T/S wave. The T/S wave can pass relatively unaltered over the trailing edge. Any local disturbances, especially for very flexible surfaces can be controlled by altering the surface geometry. This maintains the suppressed T/S wave or forces further decay while suppressing other faster growing instabilities.

It is possible to conduct a more detailed analysis of the behaviour at the leading edge by studying the work done by the wall and fluid to ascertain the exact nature of behaviour. The equation for the kinetic energy derived in §4.2.3 will be employed. This equation can be viewed as a means to ascertain the importance of the energy production and removal terms involved in the growth and decay of the disturbances. To recap, the energy balance has the form:

$$\frac{d}{dx}\Big[\overbrace{U\frac{1}{2}\int_0^z(\overline{u^2}+\overline{v^2})dz}^{(A)}+\overbrace{\int_0^z\overline{up}dz}^{(B)}+\overbrace{\frac{1}{R}\int_0^z\overline{v\omega}dz}^{(C)}\Big]$$

$$= \underbrace{\int_0^z (-\overline{uv})U'dz}_{(a)} - \underbrace{\frac{1}{R}\int_0^z \overline{\omega^2}dz}_{(b)} - \underbrace{\overline{v_w p_w}}_{(c)} + \underbrace{\frac{1}{R}\overline{u_w \omega_w}}_{(d)} \tag{6.8}$$

where, (A) denotes the average disturbance kinetic energy convected past a streamwise location; (B) and (C) describe the rate of work done by the fluid disturbance against the perturbation stresses at a known streamwise location; (a) and (b) define the rate of Reynolds stress production and viscous dissipation respectively; and (c) denotes the rate of irreversible work done to the wall by the disturbance pressure. Term (d) is an additional viscous dissipation term.

Over the smooth, (k=0) surface, all the quantities are of the same order of magnitude except the Reynolds stress (a), which dominates the other quantities at the panel edges. This is a well-known result, and has been described by Davies (1995). The large abrupt change in this quantity is responsible for the change in the disturbance entrophy and kinetic energy plotted in Figure 6.22. The powerful influence of the leading-edge upstream is evidenced by the sharp rise in Reynolds stress production before the wave reaches the join. A similar effect is observed at the trailing edge, except that the magnitude is much smaller. Over a rough surface, things are less clear cut: the dashed lines indicate the variation of the same quantities. Reynolds stress production still dominates in magnitude over the other quantities and has somewhat of a slightly oscillatory nature downstream. This is observed over the smooth surface; the Reynolds stress rapidly decays to a negative value. At the leading edge, for the smooth case the fluid is brought into motion, and the process accelerated by the abrupt change of displacement. Now, the fluid at the wall exists as rolls of fluid due to the effect of roughness. This is further accelerated at the leading edge owing to the initial motion of the wall as it adjusts rapidly to the cope with the fluid and and roughness geometry. This causes a similar peak of the Reynolds stress. Over the rigid rough surface the Reynolds stress is largely positive, over the compliant surface it is negative. A state of energy production and removal is observed, whereas over a smooth surface there is energy removal. The magnitude of this quantity between the two cases illustrates the

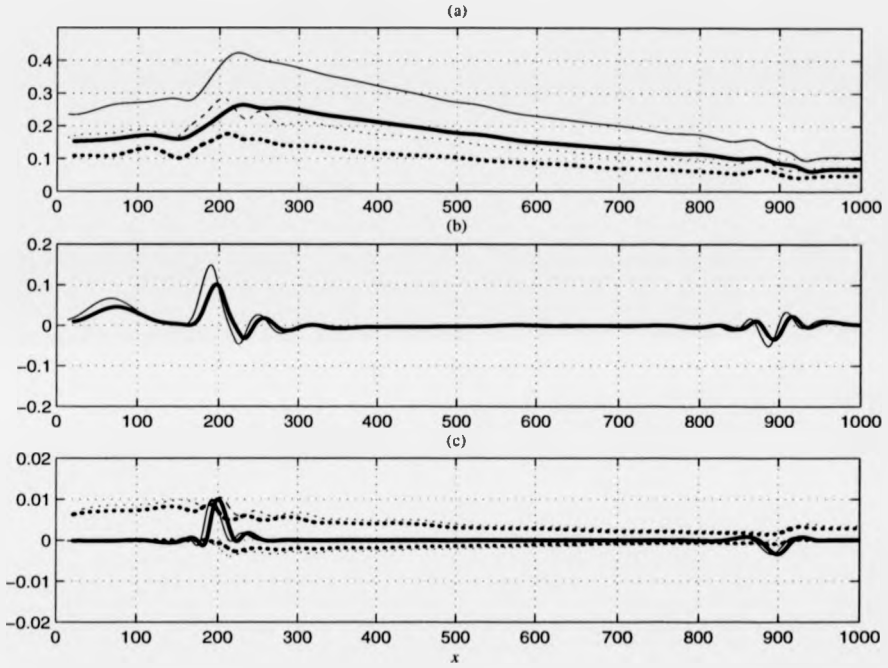

Figure 6.22: Streamwise variation of energy components over a wavy and smooth compliant panel. (a) shows the variation of terms (A) and (B). The bold solid and broken line indicates a surface where k=0.21, and the lighter lines indicates a smooth surface. (b) shows the variation of term (a). The bold line denotes k=0.21mm, and the lighter line, k=0. (c). shows the variation for terms (b), denoted by bold and normal $(\cdots)$ line, (c), denoted by solid bold and normal lines, and (d) denoted by bold and normal $(--)$ lines.

greater effectivness for the smooth case.

The other quantities differ for obvious reasons: the viscous dissipation is slightly greater and there is a greater change of the irreversible work done to the wall by the disturbance pressure. The latter is not unexpected and is responsible for improvements of reductions in three-dimensional growth rates and unstable frequencies. Reverse effects are observed at the trailing-edge.

If the roughness can match the wavelength of the motion of the wall a stable scenario is adopted. This only occurs much later on. The large phase difference between the velocities, caused by the mismatch results in the sharp changes of the Reynolds stress at the joins. As before (d) is stabilised across the panel.

6.4.5 A brief note on the effect of damping & orthotropicity

To counteract any detrimental effects at the joins, the careful use of damping and orthotropicity were used. §4.2.5 described in detail the effect that small levels of damping had on compliant surfaces where a T/S wave is introduced and also on the streak phenomenon. In the case of the former, it is now well known that wall damping can actually *promote* T/S growth. Small levels of damping are introduced here: the damping coefficient, d, is fixed as 1000 and the values for m, K and B are retained. Traces of the amplification rates of T/S waves, (not shown in the interests of brevity), for a variety of roughness heights, with and without damping revealed only slight improvements to the scenario. A slight stabilising effect on the T/S waves was observed, which extended the neutral-stability regime by a small amount. Although small amounts of damping is not detrimental, for the cases that were studied, no worthwhile extensive benefit was observed.

Orthotropicity was first encountered in §4.2.4. To recap briefly, this is where the flexibility of the panel is reduced in a spanwise (y) direction. Our investigation focuses on whether the properties of the T/S wave are amplified or attenuated under this condition. Again, only marginal improvements were observed. The hydroelastic stability

of the panel is not radically altered for two-dimensional disturbances. As for when damping was introduced, no extensive benefit was observed for the cases investigated. However, further investigation is necessary.

6.5 Chapter Summary

(i). **Rigid Surface**

Tollmien-Schlichting waves have been generated over a rigid-wavy surface. This is necessary as the minute roughness height of the wavy surface alone is not sufficient to result in any destabilisation, (the wavy-wall is a passive device). A body force is used as the disturbance driver to generate a Tollmien-Schlichting wave. The waviness is modelled spectrally as a Fourier series which allows the vaious modes of wall waviness were investigated. The wavy wall code was coupled to the velocity-vorticity solver without any difficulty. The stability limits have been determined and demonstrated agreement with Floryan (1997).

(ii). **(Kramer-type) Compliant Surfaces**

The first computational study of the effects of surface imperfections on the use of Kramer-type compliant walls for laminar flow has been successfully studies. No significant numerical problems were encountered during coupling. The compliant-wavy surface was capable of sustaining T/S waves, albeit with an amplitude and growth rate significantly lower than that over a rigid-wavy surface. The T/S wave appeared to be more sensitive to compliance in this scenario. This may be accounted for by the ability of the compliant surface to react to and tune its motion and geometry profile to that imposed by the wall waviness, (it is likely that a stable regime is possible when the frequency of the wall motion coincides with a range imposed by the simulated waviness).

For the more practically important case of an embedded surface, a similar principle applies. The stability limits are dependent on the length of the panel and compliance, in addition to the amplitude of the imposed waviness. The effects of the leading and trailing edges can introduce local disturbances, which can be detrimental if uncontrolled. The leading-edge disturbance is particularly susceptible, largely due to the mismatch between the wavy-rigid and wavy-compliant surface. This can be controlled by tuning the amplitude of the waviness over the compliant surface to that over the rigid surface at this location. A similar method can be applied to the trailing edge,

(although largely unnecessary as the T/S wave can pass relatively unaltered at this location). The effect of small amounts of damping and orthotropicity resulted in only slightly altering the stability threshold, but not to meaningfully significant levels. However, in light of this, local suppression can be achieved using a series of panels with various compliance and roughness levels.

(iii). **Hydrodynamic Effect of Cutaneous Ridges on the Dolphin Epidermis**
In general, a significant reduction in the growth of T/S waves were observed for a cutaneous ridge geometry. This highlighted for the first time the benefical nature of the ridges and a new drag mechanism.

Chapter 7

Conclusions & Recommendations for Future Work

A brief summary of the major conclusions from this thesis is outlined in §7.1. §7.2 will provide suggestions for future computational and experimental work.

7.1 Conclusions

This research has focused on the remaining practical issues of a fundamental nature regarding the use of compliant walls for laminar-flow-control. Research prior to this showed that transition could be postponed and drag reduction achieved with optimised compliant surfaces in low-disturbance environments. In real marine environments, disturbances due to freestream turbulence and particulate matter exist. Understanding the rôle of these disturbances is pertinent for the development of compliant walls for drag reduction in marine environments. The results presented here represent the first such study of the effects of either type of disturbance on the performance of compliant surfaces. The surface of marine vehicles would be subject to manufacturing imperfections and natural degradation due to particulates in sea-water impinging on its surface. How 'rough' or uneven compliant surfaces behave is of practical importance for marine applications. As a result, our investigation represents the first of its kind to study the

effects of imperfections/roughness in the form of regular surface undulations.

In brief, the following conclusions can be made:

1. The development of streaky structures, or Klebanoff modes, were observed over compliant walls. These are transient disturbances that are observed in disturbed flow environments. They are thought to be the mechanism for bypass transition seen when freestream turbulence reaches a threshold level. The development of these structures appears to be greatly affected by the properties of the surface. These structures were simulated with a linear version of the velocity-vorticity code in a laminar boundary layer. A stationary body force of the form described in §4.1.2 was used as the disturbance driver. The compliant walls are modelled using a plate-spring formulation and are of the Kramer type (with the properties defined in §4.2.2). The flexibility of the surface is altered by changing the spring stiffness. The general trend observed is that the more flexible the surface the less the likelihood of them being observed. This suggests that it is possible to optimise a compliant surface to suppress the streaks and hence prevent bypass transition. At any rate, the compliant walls are less susceptible to the growth of K-modes than rigid surfaces. (Freestream turbulence generates weaker disturbances over a compliant wall than a rigid one and hence boundary layers over compliant walls are less receptive.) The effect of generating streaks over a compliant panel revealed similar results. The leading and trailing edges had little effect on the development of the streaks. The effect of reducing the stiffness in the spanwise direction, as in so-called orthotropic compliant surfaces, proved beneficial, extending the limits of streak suppression. In general, it is noted that compliant surfaces are remarkably resilient to the growth of streaks.

2. The above velocity-vorticity model was extended to investigate the effects of compliance on the near-wall structures believed to generate the high skin-friction drag found in turbulent boundary layers. Essentially an analogy is used between the streaks observed in a transitional boundary layer with the near wall structures observed in a fully turbulent boundary layer. It is important to note that the streamwise streaks

associated with the Klebanoff mode are fundamentally different from the structures observed in a turbulent boundary layer. A freestream spanwise bodyforce is used to generate streamwise vorticity in the same way as for the Klebanoff mode streaks and the velocity-voticity code now includes the non-linear aspects for the transport equations. Regarding the latter, to be precise, fully non-linear simulations are not run as only a single mode in the spanwise direction was considered. The streaks were generated in a semi-empirical turbulent velocity profile. Kramer type compliant surfaces with identical properties to that used in the previous model were used. It was found that the optimum spanwise spacing of 100 wall units found for rigid walls is increased by wall compliance. Moreover, the growth of the streaks is substantially reduced. As the surface is made progressively more flexible, (achieved by altering the spring stiffness), the streaks weaken and their spanwise spacing increases. This may provide an explanation for the favourable effect of compliant walls on turbulent skin friction and could serve as a model for optimisation studies. Importantly, for the first time, we have also shown qualitative agreement with the experimental study by Lee *et al.* (1993), and showed that the compliant walls of Choi *et al.* (1997) are very much capable of drag reduction. These surfaces are modelled by varying the properties, most notably the spring stiffness of the materials. It is worth noting that the former surface (Lee-type) has a Youngs modulus, E, of 227Pa and is considerably sofer compared to the former (E=2.81MPa and 1.70MPa) and our Kramer type (E=1.53MPa) surfaces. It is likely that the 'lift-up' effect observed may be due to the numerical method and not only the effect of the mean velocity profile.

3. For the first time, the effect of roughness, modelled as a wavy surface has been investigated for flow over a Kramer-type compliant wall. This essentially models the effect of surface imperfections in the form of fixed waves in the compliant surface. Note that waviness implies minute, regular spaced surface imperfections, as opposed to the random geometry of a (real) rough surface. The waviness is modelled spectrally as a Fourier series and the possible interactions amongst the various modes of wall

waviness were investigated. The wavy wall is simply implemented as a fixed, sine-wave distribution with no spanwise variation. A body force is used as the disturbance source to generate a Tollmien-Schlichting wave. The wavy wall code was coupled to the velocity-vorticity (fluid) and compliant wall codes without any difficulty. Kramer-type compliant surfaces similar to that used in the streak invetsigations were chosen. It was observed that compliance had a stabilising effect on the Tollmien-Schlichting (T/S) waves generated. In general, as for over rigid walls, the effect of increasing the height of the waviness prompted earlier onset of transition. This is accounted for by the inability of the surface to tune its motion to the geometry and distribution of the imposed undulations. In general, if the wall properties are tailored to the local flow, so that the motion of the wall matches the geometry of the roughness, a stable regime can be achieved. Embedded compliant surfaces pose an additional problem as the leading and trailing edges can generate a rich diversity of additional (and sometimes detrimental) disturbances. However, within certain limits the same general principle applies.

4. There appears to be little understanding of the passive control features of dolphin skin and more specifically, the hydrodynamic effects of cutaneous ridges, which run approximately normal to the direction of flow. Our wavy model was used to investigate this, where the geometry of the ridges are uniformly spaced 250μm apart and less than 50μm high. Comparison with an identical geometry over a rigid wall revealed a substantial reduction of the amplitude of the T/S waves, for the first time highlighting the beneficial nature of the ridges and a possible new, (to mankind), laminar flow technique. Note that it may be possible that slightly oblique components of the T/S waves wavepacket may be generated over wavy-compliant surfaces. Such waves may grow much less rapidly when waviness, similar to the cutaneous ridges, is present.

5. At this juncture it is worth commenting on the results of a limited study of the effects of particulates, modelled as stationary and non-stationary body forces to simulate particle-induced receptivity in laminar boundary layers. This revealed a number

of unknown effects. Note, however that due to the preliminary and incomplete nature of this study, these conclusions should be treated with some caution! Full details regarding the model to describe the particle dynamics, the coupling procedure to the fluid and compliant-wall aspects of the code and analysis may be found in Appendix A. In brief, it was observed that:

(*a*). A (particle) body force moving with the freestream flow was found to generate a disturbance that broke into two components- one of which travelled with the body force and a second which was essentially a wavepacket of Tollmien-Schlichting waves. The latter grow as they travel downstream more slowly than the body force, and are the component that would initiate transition to turbulence. Compliant surfaces were found to be less receptive to such disturbances. When a compliant panel is investigated, the junction between the two surfaces had an effect whereby the behaviour at the wall has greater beneficial effect on the generation of T/S wavepackets over the compliant panel.

(*b*). Although not described here, as an aside to our study it was noted that over compliant (and rigid) surfaces, stationary, horizontal forcing appeared to be more powerful than vertical forcing for the generation of Tollmien-Schlichting waves.

(*c*). The development of a simple model, where the wall, fluid and particle dynamics were coupled together was conducted to track the behaviour of the 'particle' close to the wall. (The procedure for this is described in Appendix A.) Although the model for the particle dynamics was relatively simple, (containing only the basic hydrodynamic lift, drag and buoyancy forces acting on the particle), the influence of the motion of the wall on the particle was discernible. The effect of the particle on the development of perturbations at the wall appeared to be similar to that for a moving body force. The T/S wave generated is locally suppressed at the wall owing to the fact that the influence of the particle on the wall is reduced because the growing boundary layer ejects the particle rapidly away from the wall and out of the boundary layer. This has not been previously reported in the literature, and as a result we believe it may represent a new receptivity mechanism. In addition, a comparison between the trajectories

of the particle over a compliant and rigid surface indicates that a steeper trajectory is observed over a rigid surface. The more flexible the surface the less steep the trajectory. This is a complex phenomenon and requires much more detailed study.

7.2 Recommendations for Future Research

The results presented have demonstrated only a little of the rich diversity of the complexities of the flow. Other instabilities also exist which would need to be either exploited or suppressed depending on the local flow conditions. A number of immediate recommendations can be easily carried out.

7.2.1 Computational Study

1. It is clear that further study is required on the complex phenomenon concerning the influence of the particulates on the compliant surface and the associated instabilities generated. The preliminary findings were briefly mentioned in the previous section and in more detail in Appendix A. Our present work was based on a rather simple model. In order to advance current knowledge a more sophisticated code describing the particle dynamics is necessary. This would involve modelling individual or suspensions of particles of different size and density.

2. Further investigation is required to look at the effects of surface imperfections. In the first instance, a rigorous analysis of the results of our numerical simulations is necessary in order to fully understand the effects of scattering at the panel edges. Whilst the cause of the development of three-dimensional (linear) oblique waves over such surfaces is linked to the roughness, it is also likely that the asymmetry caused by the joins and motion of the wall is an important factor.

3. It was observed that orthotropicity had an effect whereby it tended to suppress T/S waves and other wall-based instabilities over wavy surfaces. The effects of anisotropic

surfaces, (where the fibres of the surface are angled in order to achieve optimum suppression), over smooth surfaces is well known. But does this play an important rôle over a wavy surface? It is believed that dolphin skin is subject to a considerable degree of active control, where the properties of the surface and also the spacing of its cutaneous ridges are altered. In order to study this effect, our current plate-spring model could be easily converted to the Grosskreutz-type model adopted by Carpenter & Morris (1990). As the surface deforms, how does the spacing of the ridges alter? And what effect does this have on three-dimensional waves? Answers to these questions would be extremely helpful.

4. So far, our fluid-solver has largely been used in linear and psuedo non-linear mode. In order to run a more complete simulation of the near-wall streaks in laminar and more especially turbulent boundary layers, a fully non-linear simulation would need to be run. For this, further development of the code would be necessary to capture the fine-scale interactions between the near-wall flow simulations and the boundary. Although time consuming, this would model the further stages of streak growth and bypass transition. This is not a priority for the wavy-wall and particulate models as the methodology has not yet matured.

7.2.2 Experimental Study

So far our recommendations have dealt with the requirements for additional computations. These are relatively easy to perform and less expensive than experiments. However, experiments are necessary in order to provide validation and enhance the credibility of the computations. Experiments are difficult to do. A low-noise environment is needed and suitable measurement techniques would need to be adopted. On a very basic level, a series of water-tunnel experiments, similar to those conducted by Lee *et al.* (1993) are necessary to provide more information regarding the development of streaks over a compliant surface. A hydrogen-bubble flow-visualisation technique

may be employed in the same manner as Lee *et al.* to capture the streaks.

More accurate hot-film/wire measurements would be needed where the effects of particulates are investigated. The same would also be true for the study of the effects of surface imperfections. In both these cases, flow-visualisation techniques would not be accurate enough to capture the tiny disturbances generated. With regards to the former, a low-noise water tunnel or towing tank would be required in order to ensure that the only noise generated would be due to the suspension of particles introduced to the flow. With regards to the latter, not only is a low-noise environment required, but also a suitable manufacturing process would be required to generate a 'rough' compliant surface and measure its roughness. This could involve either creating the undulations by setting the surface in appropriately machined moulds, or permanently fixing sand of known height to a smooth compliant surface, (creating a sandpaper type configuration). This is similar to cutaneous ridges.

(As an aside, it is useful to note the recent and ongoing experimental work performed at Warwick on the rotating-disc facility. The main advantage of a rotating-disc study is that it represents an easily accessible, low-noise environment in which to make detailed boundary-layer measurements to study the transitional features exhibited by a fully three-dimensional boundary layer. Earlier experimental work has already highlighted the ability of compliant discs to stabilise the cross-flow instability leading to substantially higher transitional Reynolds numbers, compared to a rigid disc (Colley, *et al.* (1999), and Colley *et al.* (2000) as reported in Carpenter *et al.* (2003)). A set of successful experiments exploring surface roughness over rigid rotating discs by Dr. Farzam Zoueshtiagh and the author (Zoueshtiagh *et al.*, 2003) are to be extended to investigate 'rough' compliant discs. In this case, the rough surfaces would be created with the use of appropriately machined moulds, as suggested above. In addition to this, a means by which a minute disturbance, in the form of a small particle suspended above the surface in the disc boundary layer has been devised to shed light on particle-induced phenomena. In both cases a combination of hot-film anemometry and (kalliroscope) flow visualisation will be used to make measurements.)

The suggestions given above are intended for the exploration of the basic science of the behaviour of the surface with the fluid and particles. The experiments largely involve the study of single panels, as opposed to multi-panelled walls. Of course, an important aim would be to conduct a series of trials in a towing tank for a series of optimised surfaces for use on marine vehicles. Moreover, an ultimate aim would be to test these surfaces on actual vehicles in sea water! This could only be effectively realised if the more fundamental experiments (and computations) were conducted.

Appendix A

Effect of Particulates on Receptivity over Rigid & Compliant Surfaces

The major source of freestream turbulence in marine environments is likely to be minute particulate matter. In this appendix, the effects that tiny particles, (modelled as body forces), have in a boundary layer over a compliant wall will be explored. To our knowledge, there is no literature avaliable where the effect of either a single particle or suspension of particles over a compliant surface is studied. §A.1 will briefly outline the terms employed to describe particle dynamics. A simple model containing only the basic hydrodynamic lift, drag and buoyancy forces acting on the particle is employed, which is sufficient to trace the trajectory of the particle. The effects of compliance on the behaviour of the particle and flow field will be described in §A.2 and §A.3. *Note that this is a preliminary study and as a result the code development and analysis is very much in its infancy. Therefore, the results should be viewed with some caution.* However, our findings appear to highlight what we believe is a new receptivity mechanism.

A.1 Particle Dynamics

Previously, the effect of a stationary particle was studied. The model is now extended to include the basic dynamics of a (real) particle in motion, where the size of the particle is minute compared to the boundary-layer thickness, δ. This methodology, whilst crude, has been shown by Loth (2000) to be an acceptable approximation to the behaviour of a real particle.

It is not strictly correct to describe such a flow as a (two-phase), multi-phase flow, even though two distinct phases are present. Such flows have been widely studied and are important for a variety of applications. However, in both cases an understanding of the complex flow behaviour, and in particular the transfer mechanisms, are important. Comprehensive reviews may be found in Clift, Grace & Weber (1978), Crowe, Sommerfeld & Tsuji (1998) and more recently Loth (2000).

In general, the particles and fluid are subject to the influence of a variety of convective and gravitational forces. In our case, the behaviour is further complicated by the motion of the compliant walls and the effect of the panel ends. A study of the behaviour of a *single*, minute, particle under the influence of the surrounding fluid and the wall in the presence of compliance is the main motivation behind this chapter. As described in §2.3, there are no studies that have looked at the effect of tiny particles, or suspensions of particles in the flow. Most studies focus on the bypass mechanism and particle interaction during the turbulent phase with regard to bodies moving through heavily laden particulate environments. A set of experimental studies, focusing on moving and stationary isolated particles in a laminar boundary layer revealed the predominate mechanism was a form of bypass transition (Hall, 1967, Blackwelder *et al*, 1993, Vincent & Petrie, 1993). However, the size of the particle in these studies was one third of the boundary-layer thickness, which is far from the case in our study. However, recent experiments in low-concentration particle-laden environments (Lauche *et al.*, 1995), and computations (Saiki & Biringen, 1997, Jacobs & Durbin, 2001) agree with our tentative observations of 'isolated disturbances' that are linked to the route

to transition. This will be discussed in §A.2 and §A.3. Our primitive investigation represents the first of its kind over rigid and compliant surfaces.

A brief description of the numerical methods used to solve the governing flow and particle equations, in particular the particle forces involved, namely momentum and gravity will be outlined. As our emphasis is concentrated on the effect of a single, minute, moving particle, the numerical scheme and subsequent analysis is considerably simplified.

For the remainder of this chapter, the body force will be termed a minute pseudo-particle, denoted by subscript p, (and formally defined as an unattached body whose motion is controlled by convection, viscous and gravity forces). The fluid surrounding the particle will be denoted by subscript, f. The particle and fluid will be called the 'mixed-fluid' and denoted by subscript, m. The fluid is assumed to act as a continuum, (i.e. a defined continuous distribution of matter with no empty space), with respect to particle interaction, and the particle size assumed to be minute compared to the system- in this case the plate length and width.

It is already well known how fluids influence the motion of a particle. Stokes Law is an expression for the force exerted by the fluid on a sphere based on the assumption that the inertial forces, required to accelerate or decelerate the particle, are negligible in comparison to the viscous forces, i.e. the Reynolds number is very low. It is also assumed that no other boundary surface is close enough to affect the flow around the sphere, the motion is steady and there is no slip between the fluid and sphere. On the basis of this, the force opposing the motion, the drag force, is equal to $3\pi\mu u_r d$ where, u_r is the relative velocity (u_p-u_f). This only applies if the sphere is microscopic in size. For a small solid sphere falling through a fluid under its own weight, the particle accelerates until the net downward force on it is zero, i.e. no further acceleration is possible and the particle is said to have reached its terminal velocity. This can be calculated using the equation:

$$0 = \frac{\pi}{6} d^3 \rho_p g - \frac{\pi}{6} d^3 \rho_f g - 3\pi\mu u_r d \tag{A.1}$$

where,

$$u_r = \frac{d^2(\rho_p - \rho_f)g}{18\mu}. \tag{A.2}$$

Flow around small bodies at very low Reynolds numbers is known as 'creeping' motion. The total drag force is given by $3\pi\mu u_r d$. The Stokes drag coefficient, C_d, is defined as:

$$C_d = \frac{24}{R_p} \tag{A.3}$$

where, the particle Reynolds number, R_p, is defined as:

$$R_p = \frac{\rho u_r d}{\mu_f}. \tag{A.4}$$

An improved solution (Schlichting & Gersten, 2000), taking account of the omitted inertia terms for R<1 is:

$$C_d = \frac{24}{R_p}\Big(1 + \frac{3}{16}R_p\Big), \tag{A.5}$$

and an empirical relation,(Schlichting & Gersten, 2000), acceptable to about R_p=100 is given as:

$$C_d = \frac{24}{R_p}\Big(1 + \frac{3}{16}R_p\Big)^{\frac{1}{2}}. \tag{A.6}$$

Figure A.1 shows how C_d varies as a function of the Reynolds number. The curves shown on the graph correspond to drag predictions from Stokes and other theoreticians. The curve corresponding to equation (A.3) is chosen as our estimate of C_d. The Stokes Number, St, determines how readily a particle can follow the fluctuations of an eddy, and is defined as:

$$St = \frac{\tau_A}{\tau_B} \tag{A.7}$$

where, τ_A is the particle reponse time and τ_B is the time scale associated with the fluid (turbulent) motion. For St much less than unity, the particle will act as a passive tracer as it can rapidly respond to fluid fluctuations. For St much greater than unity, the particle trajectory will be unable to respond to the fluctuations yielding a path which will be primarily controlled by mean convection and gravity. For intermediate Stokes numbers, a heavy particle can centrifuge out of the eddy cores. For a buoyant particle, attraction to the eddy cores can have the opposite effect.

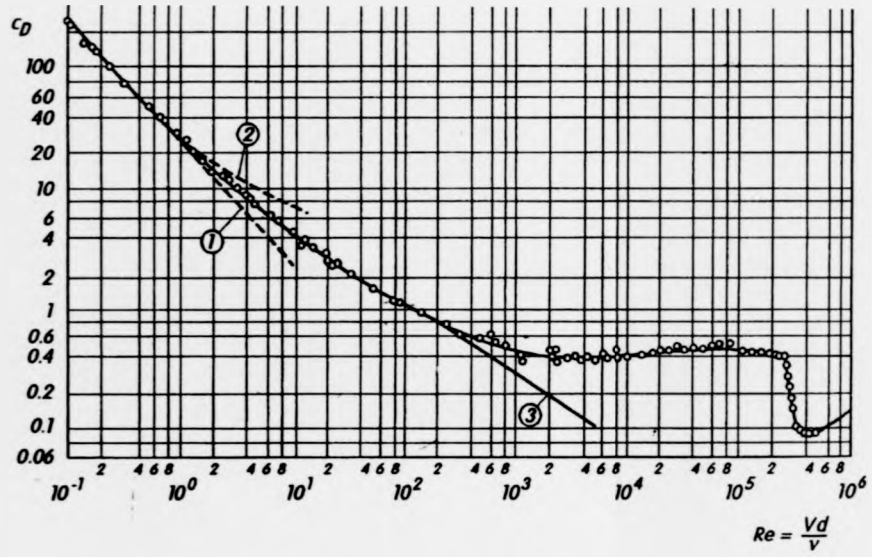

Curve 1: theory, after G.G. Stokes (1856), $c_D = 24/\mathrm{Re}$
Curve 2: theory, after C.W. Oseen (1911), $c_D = 24/\mathrm{Re}[1 + 3\mathrm{Re}/16]$
For the extension of this theory for higher Reynolds numbers, cf. M. Van Dyke (1964b)
Curve 3: numerical results, after B. Fornberg (1988)
Onset of unsteady flow at Re = 200, cf. U. Dallmann et al. (1993)

Figure A.1: Drag coefficient of sphere as a function of the Reynolds Number (Schlichting & Gersten, 2000)

There are various ways in which a particle can influence the fluid flow. Where the particle loading is low, the effects of the particle on the fluid flow is often ignored. As only the particles feel the effects of the fluid, the fluid equations can be easily solved to ensure conservation of mass and fluid momentum, and the particle equations solved after the converged solution of the continuous phase (i.e. fluid and wall motion) has been obtained. This is the approach taken here.[1]

The basic dynamics of a single particle can be modelled by Newton's Second Law of Motion:

$$F_p = \frac{d}{dt}(m_p u_p) \tag{A.8}$$

where, m_p is the mass of the particle, u_p is the particle velocity and F_p is the force on the particle. Bear in mind that the 'particles' we are considering are tiny and, as a result, d and m_p can be considered negligible. Therefore, we would expect that when the particles come under the influence of the boundary layer, at least over a rigid surface, they would be flicked away from the wall. The approach we have taken is to model the particle as a body force, which in light of the above assumption is valid. The new position of the particle at each time instant, dt, can be obtained from:

$$u_p = \frac{d\vec{x_p}}{dt} \tag{A.9}$$

where, $\vec{x_p}$ is the position vector of the particle. However, when a suspended particle is moving relative to a surrounding fluid, its response depends on the several hydrodynamic forces acting on it. Its complete momentum equation relates to the acceleration of the particle to the sum of the various forces, F_p, acting on the particle:

$$F_p = F_d + F_g + F_L + F_s + F_h + F_w \tag{A.10}$$

where, F_d, F_g, F_L, F_s, F_h and F_w, refers to the drag, buoyancy, lift, virtual-mass (i.e. the fluid stress), Basset-history and wall-interaction forces respectively. Whereas, the

[1] If the particle loading is heavy, particle effects due to the transfer of mass, momentum or energy can no longer be ignored. The fluid equations need to be solved, (with additional sources or sinks), accounting for the interactions between the particles (i.e. two-phase coupling). In this way, both the fluid and particles feel the effects of each other.

particle trajectories calculated for heavy moving particles neglect unsteady forces due to the high particle-to-fluid density ratio. For nearly buoyant particles, a complete model is required to take into account all of the hydrodynamic forces acting on the particle to determine its our motion. Our model is incomplete as it only takes into account the buoyancy, drag and lift forces, and as such should only be viewed as a preliminary starting point for further work.

The **buoyancy** force, F_g, is the simplest force and does not require any sophisticated modelling. It is defined as:

$$F_g = V_p(\rho_p - \rho_f)g = V_p\rho_r g \tag{A.11}$$

where, V_p is the volume of the particle. ρ_p and ρ_f are the density of the particle and surrounding fluid respectively, and ρ_r is the difference between these quantities. g is the gravitational acceleration, (9.81m/s^2).

The **drag** force, F_d, can be calculated using:

$$F_d = \frac{1}{2}C_d\rho_f u_r^2 A_p \tag{A.12}$$

where A_p is the projected area of the particle in the direction of flow. The particle Reynolds Number, R_p, has been previously defined and the drag coefficient, C_d, depends on it. The latter is defined using equation (A.3) and is obtained from Figure A.1 for our purposes. As described earlier, the Stokesian drag is often used as a base for other conditions by including factor f, which is the ratio of the particle drag coefficient to the Stokesian drag coefficient,

$$\text{i.e.} \quad C_d = f\left(\frac{24}{R_p}\right).$$

The **lift** force, F_L, is perpendicular to the drag and given by:

$$F_L = C_L\frac{\pi}{8}d^2\rho_f u_r^2. \tag{A.13}$$

C_L is the lift coefficient. For inviscid flows around a sphere, C_L=0.5 and for viscous flows, C_L varies from 0.01 to 0.5. The lift force can be complicated by numerous factors,

such as turbulence, and in our case the displacement of the wall. At low Reynolds Numbers, two lift effects occur: shear (Saffman)- and spin (Magnus)-induced lift. In both cases the lift force of a spherical particle is a result of the local or particle Reynolds Number and an additional, non-dimensional, rotational parameter. Lift is proportional to the rotational rate, the relative velocity and the continuous-fluid density. Hence, the lift is negligible for very heavy particles whose gravitational force and drag are proportional to the particle density.

The other components of equation (A.10) are highly complicated and have been eliminated from our model in the first instance. These include the Basset-history forces, F_h, which arise due to the temporal development of the particle wake and are important where strong fluid accelerations evolve at time-scales of the order of convection over the particle surface. F_h is highly complicated and described in more detail by Loth (2000). The virtual-mass force, F_s has been included in our model. It is defined as the force caused by the inertia of the fluid surrounding the particle, (and is merely equivalent to altering the particle density, ρ_p to $\rho_p+(\rho_f/3)$). F_s is strongly dependent on the particle shape (and concentration). Some authors relate this term to the acceleration of the fluid in the vicinity of the particle, in which case it is termed the fluid-stress-gradient force, F_{sg}.

The flow field around a particle is modified in the vicinity of a wall, which gives rise to a wall, (or viscous), lubrication force, F_w, which tends to push the particles away from the wall. This term is especially important where high concentrations of particles, (or bubbles), are found very close to the wall resulting in particle and wall collisions. This is been ignored in our model for simplicity, and futhermore, as we are not so much interested in the direct action of the wall on a single particle, but rather in the effect of the modified boundary layer created by the motion of the wall on the particle. Full details about wall effects may be found in Clift *et al.* (1978).

The equation of motion for a single particle in the flow is obtained by adding the forces together. In a still fluid, the particle dynamics for a single particle starting from

rest, at low Reynolds Numbers, is:

$$\frac{\pi}{6}d^3\rho_p\frac{du_p}{dt} = -\frac{\pi}{4}\rho_f d^3$$
$$\left\{ \underbrace{\frac{1}{3}\frac{du_p}{dt}}_{\text{virtual mass, } F_a} + \underbrace{\frac{12\nu u_p}{d^2}}_{\text{viscous drag, } F_d} + \underbrace{\frac{6}{d}\left(\frac{\nu}{\pi}\right)^{\frac{1}{2}}\int_0^t \frac{du_p}{dt}\frac{d}{(t-\tau)^{\frac{1}{2}}}}_{\text{Basset force, } F_h} + \underbrace{\frac{2}{3}\left(1-\frac{\rho_p}{\rho_f}\right)g}_{\text{buoyancy, } F_g} \right\}. \quad \text{(A.14)}$$

This can be rewritten for a moving fluid by taking into account the acceleration terms. For an inviscid moving sphere this is:

$$\overline{F} = \frac{\pi}{6}d^2\rho_f\frac{D\overline{u}_f}{Dt} + \frac{\pi}{12}d^3\rho_f\left[\frac{D\overline{u}_f}{Dt} - \frac{d\overline{u}_p}{dt}\right] \quad \text{(A.15)}$$

where,

$$\frac{D}{Dt} = \frac{\partial}{\partial t} + (\overline{u}_f.\nabla) \qquad \text{and} \qquad \frac{d}{dt} = \frac{\partial}{\partial t} + (\overline{u}_p.\nabla)$$

are the time rates of change along a streamline and particle trajectory respectively. The first term on the right-hand side is due to the pressure gradient in the fluid surrounding the particle. The second term is the force required to accelerate the virtual mass of the particle relative to the ambient fluid. The drag force has been extended beyond the Stokes flow regime, (as the Reynolds Number based on the relative motion could be of the order of unity or larger). The equation of motion for the particle in the flow field is thus:

$$\frac{\pi}{6}d^3\rho_p\frac{d\overline{u}_p}{dt} = \frac{\pi}{6}d^3\rho_f\frac{d\overline{u}_f}{dt} +$$
$$\frac{\pi}{4}d^3\rho_f\left\{\underbrace{\frac{1}{3}\left(\frac{D\overline{u}_f}{Dt} - \frac{d\overline{u}_p}{dt}\right)}_{\text{virtual mass, } F_a} + \underbrace{\frac{C_d}{2d}|\overline{u}_f - \overline{u}_p|(\overline{u}_f - \overline{u}_p)}_{\text{viscous drag, } F_d} +\right.$$
$$\left.\underbrace{\frac{6}{d}\left(\frac{\nu}{\pi}\right)^{\frac{1}{2}}\int_0^t \left(\frac{D\overline{u}_f}{Dt} - \frac{d\overline{u}_p}{dt}\right)\frac{d\tau}{(t-\tau)^{\frac{1}{2}}}}_{\text{Basset force, } F_h} + \underbrace{\frac{2}{3}\left(1-\frac{\rho_p}{\rho_f}\right)\hat{g}}_{\text{buoyancy, } F_g}\right\} \quad \text{(A.16)}$$

where, the size of the particle is assumed to be much smaller than the length scale of the flowfield. This equation is written in terms of the assumption that the particle is tiny, and modelled as a body force, and can be solved to obtain the particle trajectory and velocity, when placed in a growing Blasius boundary layer over a wall. The terms

crossed out have been neglected in order to achieve this. The equation is implemented in the code and easily solved after the converged solution for the fluid and wall motion are obtained. This represents a simple approximation to a 'real', but tiny particle in the flow. (Modelling a real particle would be much more involved as there is a need to take into account its geometry as well as the neglected forces. A significant amount of computing time is required to solve for such a scenario.) The drag coefficient, C_d is taken from the relations in Figure A.1 and inserted into the equation of motion for each specific Reynolds Number. As a check on the integrity of the code, we have compared the trajectory of our pseudo-particle with that calculated by Morsi & Alexander (1972), for a tiny particle of 100μm in diameter, travelling in air and observe good agreement.

A.2 Effect of a Moving Particle

The effect of a moving, psuedo-particle (body force), travelling downstream over the domain was investigated. The dynamics of such a particle can be simply implemented by linking its movement with time at a uniform speed, i.e.:

$$x = \frac{U_\infty}{t}.$$

In this way the particle, moves with the freestream speed, U_∞. Note that none of the hydrodynamic force terms have been included. The pseudo-particle is essentially, according to the notation in §4.1.2, a moving body force of Type MC or MO, depending on whether it is stationary or oscillating. All the computations in this and the following section are two-dimensional. The focus of interest is not the influence of the boundary layer on the particle, but the disturbance induced by the particle. To this end, a body force is placed just outside the boundary layer developed over the rigid and compliant walls and allowed to move, unaffected, downstream. This is similar to the method adopted by Hall (1967). He towed a sphere in a tubular smoke tunnel using fine wire and studied the resulting wake. Hall's conclusions are probably not applicable to this study as the sphere was a third of the size of the boundary layer.

The effect of oscillating particles are important for many engineering applications and occur in nature, as fluctuations of the fluid velocity usually increases the mean drag and transfer rate of the particles. Clift *et al.* (1978) reports that modification of the drag by flow oscillations have been investigated for insect flight. Chapter 5 demonstrated the beneficial effects of wall compliance in a turbulent boundary layer and Chapter 6 the effects of roughness. In this case the tiny disturbances produced are known to produce any of three distinct flow perturbations: streaky structures (Klebanoff mode); a weak, streamwise, outer, Tollmien-Schlichting wave; or the conventional Tollmien-Schlichting wave with higher growth rates.

Figure A.2 traces the disturbances generated by an oscillating pseudo-particle moving with the freestream speed, (i.e. Type MO). The computation is two-dimensional. The Reynolds number of the flow is approximately 1000, and the body force oscillated at a non-dimensional frequency of 88.0. This combination of Reynolds number and non-dimensional frequency would correspond to unstable Tollmien-Schlichting waves. The pseudo-particle is located just outside the boundary layer at z=2.314, over a rigid surface. The pseudo-particle and its associated disturbance waves were found to leave the computational domain without inducing any reflections. As expected, the particle generates vorticity in its wake. The resulting (freestream) disturbances are believed to contribute to the three-dimensional aspects of the breakdown process (Kendall, 1998), whereas the irrotational components (i.e. noise) are understood to contribute to the initial amplitudes of the quasi-two-dimensional, Tollmien-Schlichting, (T/S), waves (Saric, Reed & Kerschen, 2002).

At about $t^+ \approx 15$, the disturbance breaks into two parts. One part continues to travel downstream with the particle. The other part is a T/S wavepacket which grows at a substantially slower rate downstream compared to the particle wavepacket. This is evident from a trace of both disturbances (Figure A.3). The T/S wavepacket is the one that will eventually initiate transition to turbulence. The wake left by the pseudo-particle travels much faster than the T/S wavepacket and leaves the domain much earlier, leaving no remnant of its presence in the flow (i.e. the wake decays

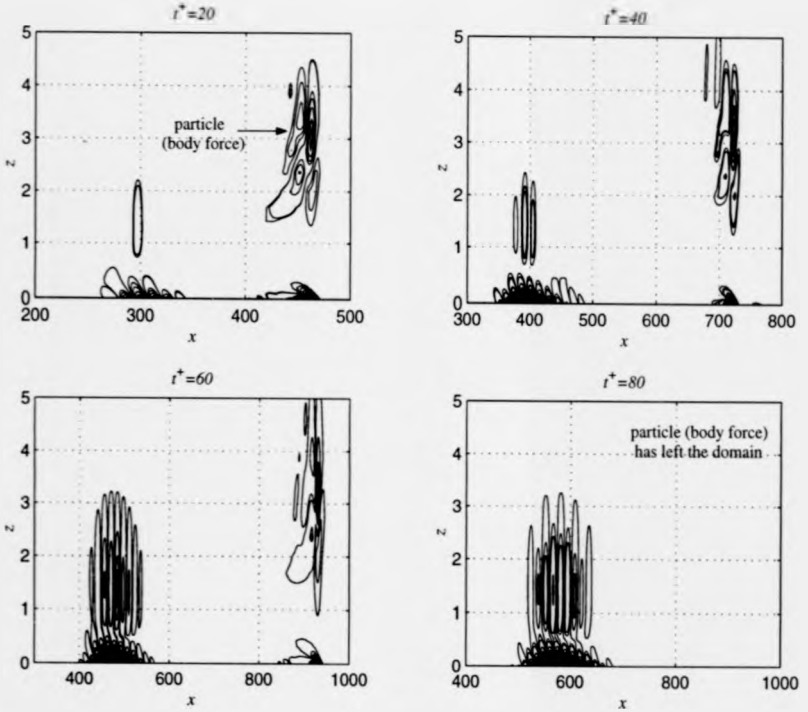

Figure A.2: Temporal evolution of disturbances generated by a travelling, oscillating, particle unaffected by the boundary layer over a rigid wall. The body force is Type *MO*, R=1000, W=88.0 and positioned at z=2.314 (non-dimensional units). The computation is two-dimensional.

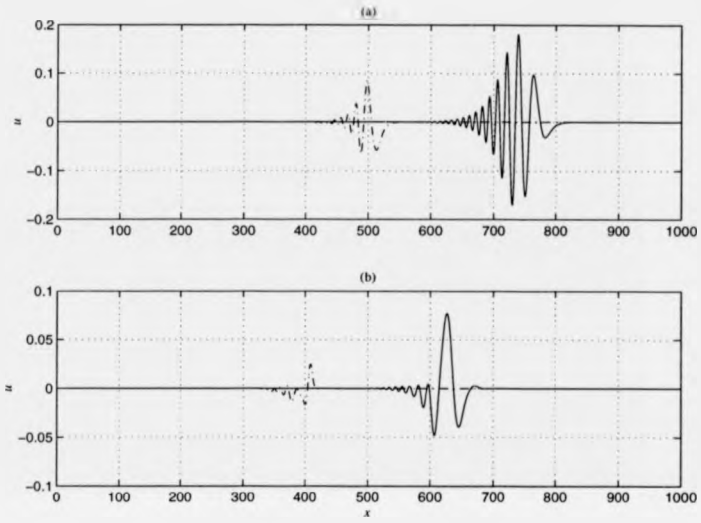

Figure A.3: Evolution of T/S (−·) and particle wavepackets (−) over a (a) rigid, and (b) compliant wall t^+=80 at z=1.9. The body force is Type *MO*, R=1000, W=88.0, and positioned at z=2.314 (non-dimensional units). The computation is two-dimensional.

rapidly). As a result it has no influence on the induced T/S wavepacket. As mentioned earlier, recent computations by Saiki & Biringen (1997) observed isolated disturbances that are believed to be linked to transition caused by three-dimensional disturbances. However, these studies model large particles, and the disturbances are directly linked to the wake disturbances and not those induced at the wall by the particle. Our model shows the wake wavepacket is relatively stable, and the disturbance near the wall is two-dimensional in nature. At some point, the T/S wavepacket will trigger transition in the conventional manner. Our simulations agree with receptivity experiments showing that the freestream disturbance decays rapidly towards the wall, and that T/S disturbances are dominant near the wall and convect downstream. The phenomenon we observe is similar to that observed by Kendall (1998), although he used a wall with a blunt leading-edge rather than a moving particle in order to study the wavepackets

produced, with the aim of relating the T/S wave amplitudes to the amplitude of the freestream turbulence. The wavepackets Kendall observed are of lower amplitude compared to other modes of behaviour. This led him to conclude that internally generated wavepackets behave differently than externally generated ones. The same conclusion can be applied to our observations- the amplitude of the T/S wavepacket is lower than the particle wavepacket, and they behave differently. However, at present there is no evidence from similar simulations, experiments or other indirect evidence in the available literature to support our results, (although in principle, there is no reason why such low-frequency-induced disturbances should not occur and behave in the way observed here). An investigation into how the T/S wavepacket is induced by the particle, and how it is sustained is necessary. The particle whilst active in generating the disturbance does not play a role in sustaining its growth. Further modelling of the initiation stage is required.

Figure A.4 traces the disturbances generated by an oscillating pseudo-particle moving with the freestream speed at the same Reynolds number over a compliant wall, with the Kramer-type properties described in §4.2.2. The frequency of oscillation is identical to the rigid-wall case, and the body force of type MO. Much the same behaviour occurs compared to the rigid surface, except that the growth of the T/S waves are considerably reduced. This clearly demonstrates that a similar transition mechanism occurs, (within limits, after which the compliant surface is capable of sustaining its own fluid and/or wall-based waves). Furthermore, the compliant wall is much less receptive to disturbances generated by such a travelling particle. It is possible to measure the receptivity of this behaviour as a ratio of the vorticity of the psuedo-particle to the total vorticity contained in the T/S wavepacket at the point where the disturbance splits, (which occurs at a slightly earlier time step). Whilst adequate, it is not a strictly correct measure, and instead we propose the trace of the wall enstrophy of the perturbation produced by the particle with time (Figure A.5). The calculation of the wall enstrophy only requires a simple line integration, as our simulations are two-dimensional. Interpretation of the behaviour of the enstrophy indicates that the

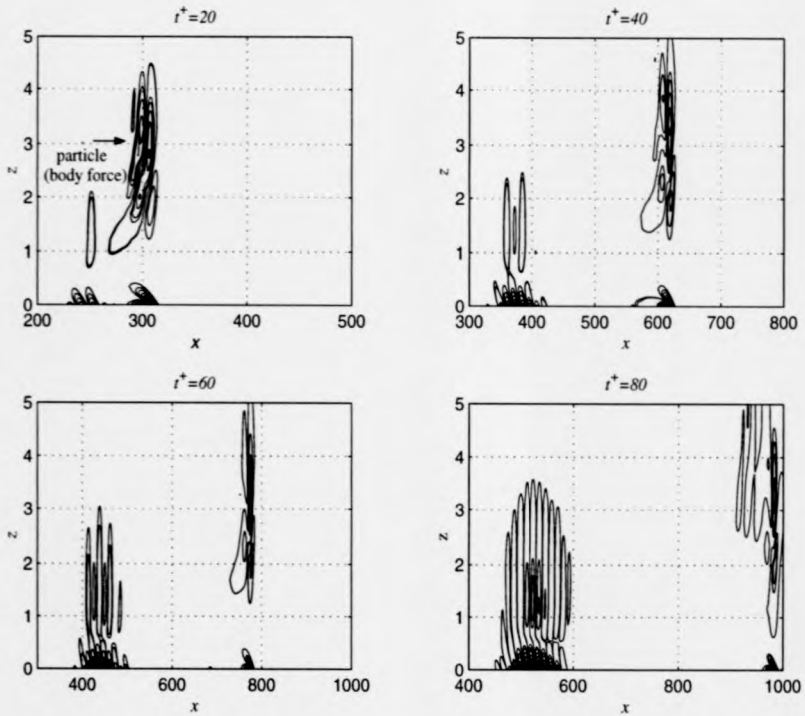

Figure A.4: Temporal evolution of disturbances generated by a travelling, oscillating, particle unaffected by the boundary layer over a compliant wall. The body force is Type MO, R=1000, W=90.0 and positioned at z=2.314 (non-dimensional units). The computation is two-dimensional.

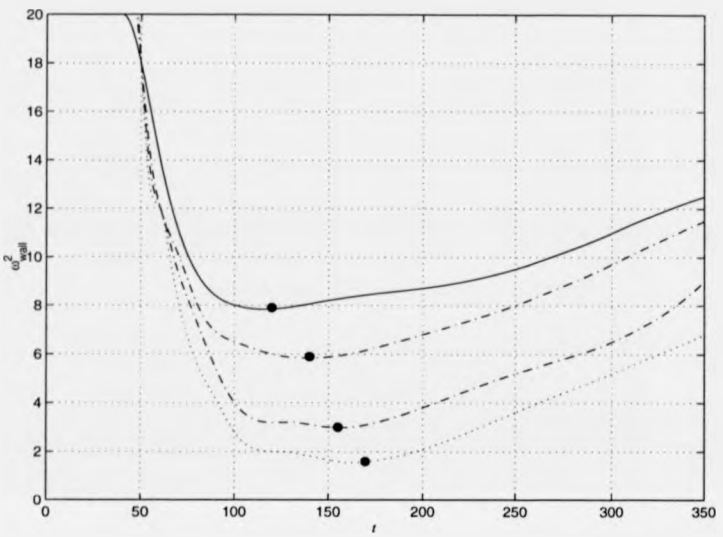

Figure A.5: Variation of wall enstrophy, (ω_w^2), with time, (t), for the particle-induced T/S disturbance over rigid and compliant surfaces. $(-)$, $(--)$, $(-\cdot)$ and $(\cdots)$ denote the enstrophy curves for a T/S wave generated by a non-interactive psuedo-particle over a rigid and compliant surfaces with Kramer stiffness, and a half and quarter of the Kramer stiffness respectively. $(\bullet)$ represents the location where the disturbance breaks into two. The body force is Type *MO*, R=1000, W=88.0 and positioned at z=2.314 (non-dimensional units). The computation is two-dimensional.

receptivity process is complete shortly after the disturbance has broken into two parts, and the growing T/S wavepacket induced at the wall has been initiated. The minimum value of the enstrophy can be viewed as a reflection of the efficiency of the receptivity process. The larger the value of the minimum, the more powerful the process. Figure A.5 demonstrates a significant reduction in enstrophy (receptivity) over the compliant wall. One may expect that the initial amplitude of the T/S waves would be greater as the motion of the surface acts as large roughness elements. For the Reynolds Number ranges studied this was not observed. (In this case, it may be that the motion of the

wall can feed or sustain the T/S wavepacket.) A brief study into the effects of compliance revealed that the phenomenon was sustained until the wall stiffness falls below quarter of the Kramer surface value. This is a relatively soft surface, (and probably impractical for actual use in marine environments).

A brief, but incomplete investigation into the case where a compliant panel is embedded in a rigid surface revealed that, for the most part, the particle could pass over the leading and trailing edges without any significant detrimental effect to the T/S and particle-wake wavepackets. The T/S wavepacket, generated on the rigid surface is of a sufficiently low amplitude to pass over the junction largely unaffected. At higher forcing frequencies it may not be unreasonable to assume that the leading-edge join may prompt the faster-moving body-force wavepacket to initiate an additional, more powerful wavepacket, that is detrimentally affected when the original T/S wavepacket catches up with it. The secondary wavepacket is largely a result of the combination of the large displacement at the leading edge join and the body force. Alternatively, an increased degree of scattering may be prompted at the join. At this stage this is speculation, and Fourier analysis at the joins revealed no additional modes of behaviour.

At present, our premliminary findings show that, over a Kramer surface the disturbances pass over the join in the conventional manner, i.e. the magnitude of the T/S waves rises at the leading edge and falls over the panel, and then rises once it leaves (Figure A.6). As a result, we show that this phenomenon is unaffected by the panel ends. Further work is necessary to ascertain how far-reaching the effects of the join are. The effect of the oscillating pseudo-particle over compliant walls and panels when its frequency is above cut-off frequency is also of interest.

The phenonemon is largely unaltered when a constant, moving psuedo-particle, (i.e. Type MC), is modelled. The only difference is that the magnitude of the response is reduced as a result of reduced wall forcing.

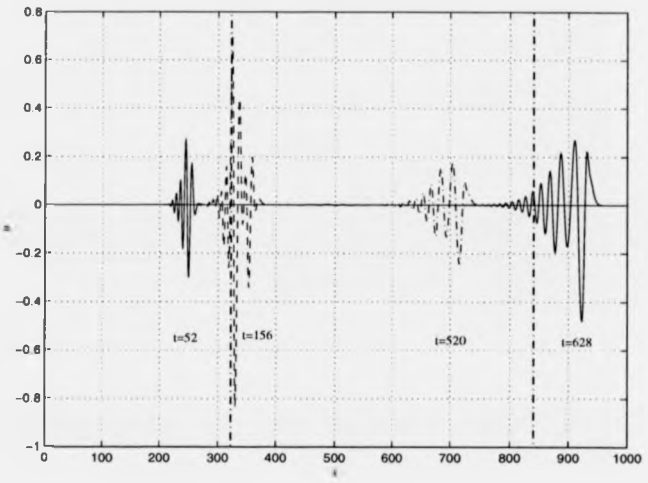

Figure A.6: Temporal evolution of wall-wavepacket over a compliant panel generated by a travelling, oscillating, psuedo-particle that is unaffected by the boundary layer. The body force is Type MO, R=1000, W=88.0 and positioned at z=2.314 (non-dimensional units). The computation is two-dimensional. The panel joins at x=320 and 830 are indicated by bold dash-dot lines.

A.3 Particle Interaction in a Boundary Layer

Having established the effect of a particle moving with the freestream speed, our attention now focuses on a particle whose motion is influenced by the motion of the wall and growth of the boundary layer in the presence of wall compliance. The simple model for the particle dynamics described in §A.1 is implemented. This is sufficient to trace the trajectory of the particle when under the influence of the displacement of the compliant wall.

Figure A.7(a) traces the disturbances and position of the psuedo-particle at time intervals over a rigid surface. The Reynolds Number of the flow is approximately, R=1000. The pseudo-particle is of type IP, and initially located just outside the

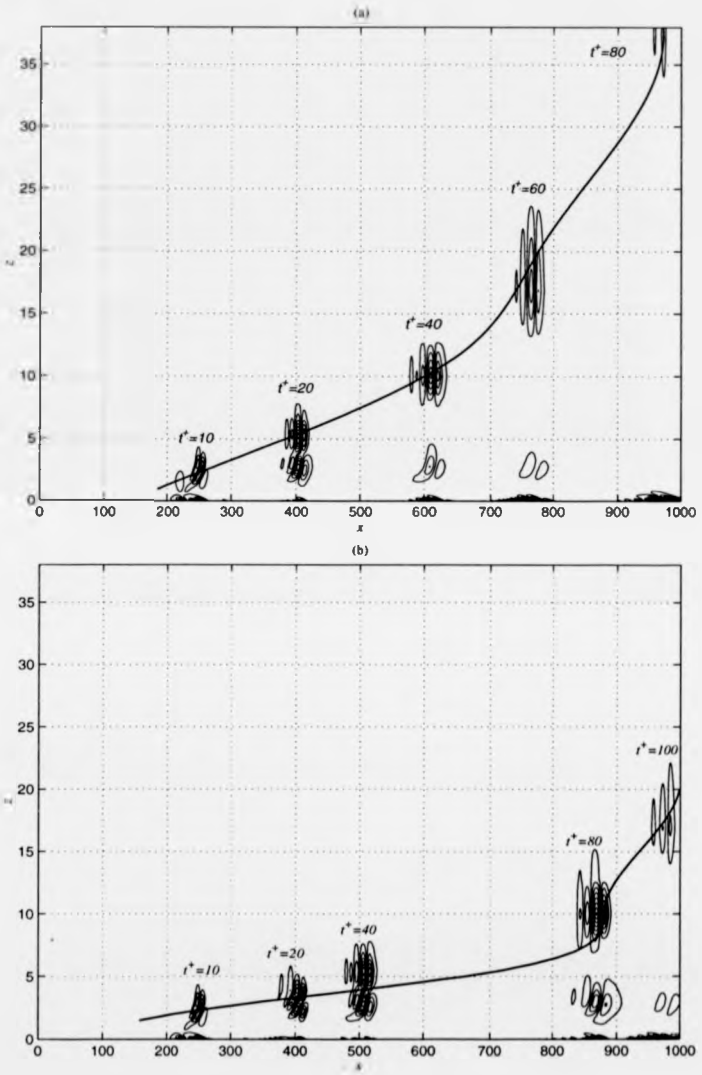

Figure A.7: Temporal evolution of T/S wavepacket over a (a) rigid wall and (b) a compliant wall generated by a travelling, non-oscillating, puesdo-particle interacting with the boundary layer. The body force is Type IP, R=1000 and positioned at z=2.314 (non-dimensional units). The computation is two-dimensional.

boundary layer, at x=2.314. Note that the particle is three-dimensional (i.e. spherical), but only constrained to move in the z-x plane. The particle generates freestream vorticity as it travels in its wake in much the same way as the 'non-interactive' particle in §A.2. At an early stage, $t^+ \approx 10$, the disturbance breaks into two parts as before; namely, a locally suppressed T/S wavepacket near the wall, which is responsible for transition to turbulence, and the pseudo-particle wavepacket which is generated in its wake and travels downstream and decays at a faster rate. The latter has less influence on the flow after the T/S wavepacket is induced.

Comparison with the behaviour of the particle in the previous section clearly shows that the disturbance breaks into two components earlier, and that the growth rate and amplitude of the induced T/S wall-wavepacket is reduced (Figure A.8). This is a result

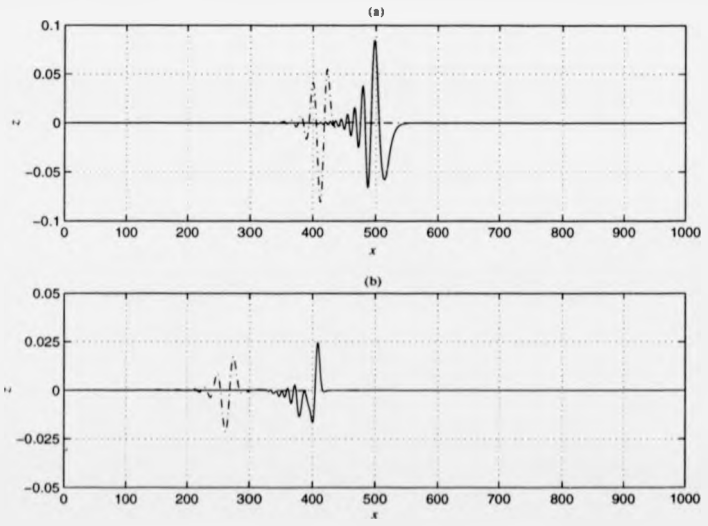

Figure A.8: Evolution of T/S wavepackets, generated by an interactive (−·), and non-interactive, (−) particle over a (a) rigid and (b) compliance wall at t^+=35. The body force is Type *IP*, R=1000 and positioned at z=2.314 (non-dimensional units). The computation is two-dimensional.

of the influence the boundary layer exerts on the particle; as it moves downstream, it interacts with the growing boundary layer such that it is, (almost immediately and violently), ejected away from the wall and out of the boundary layer. As a result, as the particle is now considerably further away from the effects of the wall. Accordingly, any initial effect that the particle has on the initiation of the T/S wavepacket is considerably reduced. As a result, the growth and amplitude of the T/S wavepacket is locally suppressed. The trajectory of the particle away from the wall becomes increasingly steep with increasing Reynolds Number, resulting in further reduction in T/S wavepacket amplitude, due to a reduced influence in its generation. Figure A.9 plots the neutral-

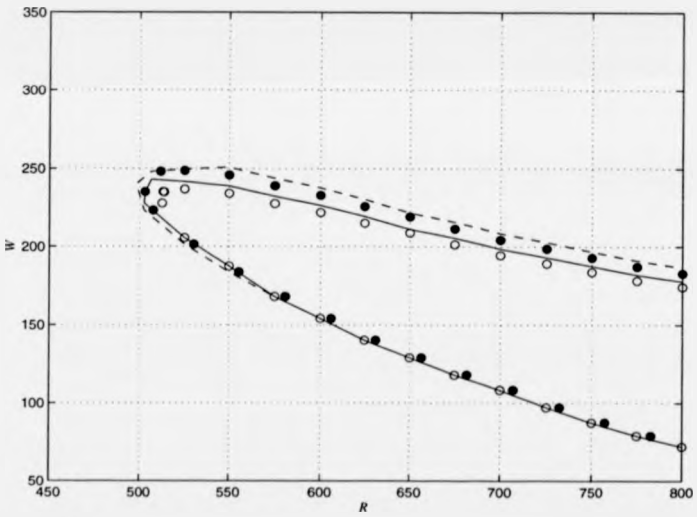

Figure A.9: Neutral-Stability Curves for particle-induced T/S disturbance over rigid and compliant surfaces. (−) and (− −) denotes stability curve for a T/S wave generated by a non-interactive psuedo-particle over a rigid and compliant surface respectively. (○) and (●) denotes the neutral-stability curve for a T/S wave generated by an interative psuedo-particle over a rigid and compliant surface respectively.

stability curve for the T/S disturbance near the wall, if the wavepacket were allowed to

develop. The nature of the T/S wavepacket is reflected by the (slightly) higher critical Reynolds Number.

A similar observation is made for a compliant surface. Figure A.7(b) plots the disturbance at a comparable Reynolds Number and boundary-layer thickness over a Kramer-type compliant surface with identical properties to that in §A.2. Again, the disturbance breaks into a T/S wavepacket and the pseudo-particle disturbance. The T/S disturbance near the wall is slow to evolve, compared to the pseudo-particle disturbance which rapidly moves downstream and is ejected away from the wall, reducing its influence. Comparison with the rigid surface reveals that the effect of wall compliance results in an even greater suppression of the T/S disturbance, its amplitude is considerably reduced after sufficient time has elapsed for the wall motion to tune itself to the frequency of the T/S wave. The slightly higher critical Reynolds Number observed, (Figure A.9), may be due to the reduced initial effect that the particle has on the initiation of the T/S wavepacket before breaking into two parts. Examination of the particle trajectories also highlights an additional benefit of wall compliance. A comparison of the trace of the particle trajectories over rigid and compliant surfaces reveals much shallower paths for the latter. In other words, the particle remains in the boundary layer over the compliant wall for longer. The fact that the speed of the body force and its wavepacket is reduced owes more to the motion of the surface than any other viscous/drag mechanisms. As a result, this is a clear demonstration of the far-reaching effects that wall compliance has; the wall can selectively tune itself locally to suppress the motion of both the particle and the T/S wavepacket. Eventually, however, the particle can no longer be sustained as the growth of the boundary layer and motion of the wall, forces the disturbance further away from the wall, out of the boundary layer.

Figure A.10 plots the enstrophy of the disturbance as a measure of the receptivity. The trace can be interpreted in the same manner as for Figure A.5. It is clear that compliant surfaces are less receptive to such a route to transition. The effect of increasing compliance does not necessarily sustain this behaviour, particularly as

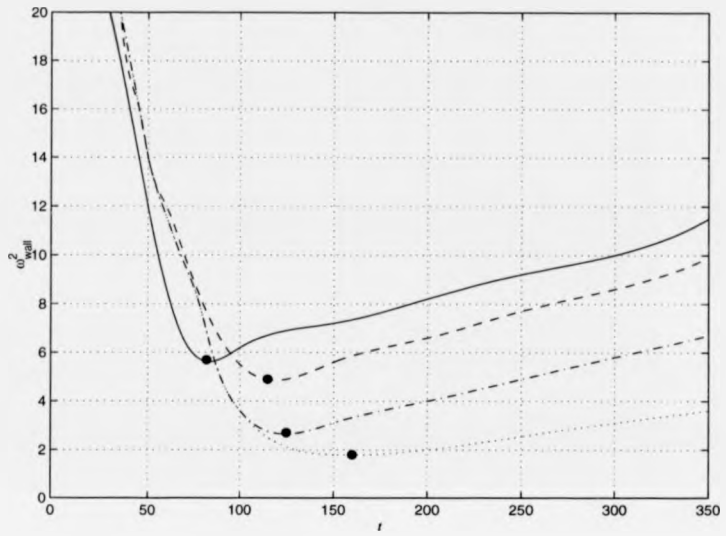

Figure A.10: Variation of wall enstrophy, (ω_w^2), with time, (t) for the particle-induced T/S disturbance over rigid and compliant surfaces. $(-)$, $(--)$, $(-\cdot)$ and $(\cdots)$ denote the enstrophy curves for a T/S wave generated by an interactive psuedo-particle over rigid and compliant surfaces with Kramer stiffness, and half and a quarter of the Kramer stiffness respectively. $(\bullet)$ represents the location where the disturbance breaks into two. The body force is Type IP, R=1000, and positioned at z=2.314 (non-dimensional units). The computation is two-dimensional.

softer surfaces can move in such a way as to act as large roughness elements promoting transition to turbulence significantly earlier. This requires careful study, as the motion of the surface could selectively enhance the induced disturbance or generate its own fluid- and/or wall-based waves. However, if the surface properties are chosen such that the motion of the wall can match that of the pseudo-particle, there is no reason, in principle why the particle cannot remain in the flow in the same way as observed in §A.2.

Replacing the wall with a finite compliant panel reveals some interesting effects.

When the boundary layer has been prescribed such that the body force moves downstream over the rigid surface, inducing a T/S wavepacket in the same way as in §A.2. When it reaches and enters the boundary layer, the particle is over the panel and begins to be repelled away from the wall. The wavepacket induced at the wall behaves in a similar fashion as in §A.2 and its amplitude is reduced over the panel. As it nears the vicinity of the leading edge, it rises and then rapidly falls over the bulk of the panel. A Fourier analysis at the leading edge reveals no evidence that any scattering occurs as a result, and besides it could have few or no far-reaching effects on the faster-moving body-force disturbance on the panel. The particle, once it has left the panel, displays a rapid increase in the amplitude of its disturbance accompanied by subsequent ejection away from the wall.

For the case where the psuedo-particle remains in the boundary layer over a rigid surface, when it meets the leading edge it is violently pushed out further away from the wall. This is certainly due to the mismatch at the leading-edge join, the displacement of the wall is now greater than zero and this represents a considerable obstacle in the flow to the particle. The change in the flow field in this region has far reaching effects, influencing the motion of the particle, i.e. pushing it further away from the wall.) It is interesting to note that once the body force is over the panel, and the compliant wall modifies its motion over a certain distance, the rate of ejection of the particle and its growth rate is slowed, demonstrating the far-reaching effects of wall compliance. The T/S wavepacket produced at the wall behaves in the conventional manner, (only travels and develops at a much slower rate).

A.4 Summary

We have succeeded in coupling the wall, fluid and particle aspects of the code together. The model for the particle dynamics is relatively simple, containing only the basic hydrodynamic lift, drag and buoyancy forces acting on the particle. The particle was modelled as a body force and termed a psuedo-particle. Despite the preliminary nature of the study, and the obvious need for further code development and in-depth analysis, a hitherto unknown receptivity mechanism was observed.

(i). Effect of a non interactive particle

Results suggest that boundary layers over compliant walls are much less receptive to disturbance generation by particles than those over rigid walls. Oscillating and constant, moving, pseudo-particles were implemented to stimulate particle-induced receptivity in laminar boundary layers. For the case where an oscillating pseudo-particle moves downstream, the disturbance created breaks into two parts; one continues to travel with the particle, whilst the other is a T/S wavepacket which travels more slowly than the particle, but grows as it travels downstream. This is responsible for initating transition-to-turbulence and apparently has not not been previously reported. The compliant wall is less receptive to disturbances generated by such a travelling psuedo-particle.

(ii). Effect of a particle interacting with boundary-layer

The present model for particle dynamics is successfully employed to study particle perturbations generated at the wall. The behaviour observed appears to be similar to that for a moving pseudo-particle, where its motion is unaffected by the presence of the boundary layer. The psuedo-particle wake is locally suppressed at the wall over rigid and compliant surfaces. This may be partly explained by the fact that the influence of the particle is reduced owing to the effect of the wall in ejecting the pseudo-particle away from the surface along a less steep trajectory. For the case of embedded panels, the effect of the leading edge appears to provide an additional source of disturbance, pushing the particle out considerably and more violently, earlier in its trajectory. (If

the disturbance at the leading-edge junction was excessively strong compared with the disturbance produced by the particle, the particle would be immediately ejected.)

Bibliography

ACARLAR, M.S. & SMITH, C.R. 1987 A study of hairpin vortices in a laminar boundary-layer. Part I: Hairpin vortices generated by a hemisphere protuberance. *J. Fluid Mech.* **175**, 1.

AIZIN, L.B. & POLYAKOV, N. F. 1979 Acoustic generation of Tollmien-Schlichting waves over local unevenness of surfaces immersed in streams. *Russian Preprint No. 17. USSR Acad.Sci. Div, Inst. Theoretical. Appl. Mech, Novosibirsk.*

ANDERSSON, A., BERGGREN, M. & HENNINGSON, D. S. 1999 Optimal disturbances and bypass transition in boundary-layers. *Phys. Fluids.* **1**, 134.

ARNAL, D. & CASALIS, G. 2000 Laminar-turbulent transition prediction in three-dimensional flows. *Prog. Aero. Sci* **36**, 173.

BABENKO, V. V. & SURKINA, R. M. 1969 Some hydrodynamic features of dolphin swimming. *Bionika* **3**, 19 (in Russian).

BABENKO, V. V. & CARPENTER, P. W. 2003 Dolphin Hydrodynamics. In *IUTAM Symp. on Flow Past Highly Compliant Boundaries and in Collapsible Tubes* Eds. P.W. Carpenter & T.J. Pedley, pp. 293-322 Kluwer, Dordrecht.

BELANGER, F. P., HERBERT, TH. & SPALART, P. R. 1992 Linear and nonlinear stability of the Blasius boundary layer. *J. Fluid Mech.* **242**, 441.

BENJAMIN, T. B. 1960 Effects of a flexible surface on hydrodynamic stability. *J. Fluid Mech.* **9**, 513.

BENJAMIN, T. B. 1963 The threshold classification of unstable disturbance in flexible surfaces bounding inviscid flows. *J. Fluid Mech.* **16**, 436.

Berlin, S. & Henningson, D. S. 1999 A non-linear mechanism for receptivity of free stream disturbances. *Phys. Fluids.* **11**, 3749.

Bertolotti, F. P. 1997 Response of the Blasius boundary-layer to free stream vorticity. *Phys. Fluids.* **9**, 2286.

Blackwelder, R. F., Browand, F.K., Fischer, C. & Tanaguichi, P. 1992 Initiation of turbulent spots in laminar boundary-layer by rigid particulates. *Bull. Am. Phys. Soc.* **37**, 1812.

Boiko, A. V., Westin, K. J. A., Klingmann, B. G. B., Kozlov, V. V. & Alfredsson, P. H. 1994 Experiments in a boundary-layer subject to free stream turbulence. Part II: The role of T/S waves in the transition process. *J. Fluid Mech.* **281**, 219.

Bridges, T. J. & Morris, P. J. 1984 Differential eigenvalue problems in which the parameter appears nonlinearly. *J. Comp. Phys.* **55**, 437.

Briggs, R. J. 1964 *Electron-Stream Interaction with Plasmas.* MIT Press.

Breuer K. S. & Haritonidis, J. H. 1990 The evolution of a localised disturbance in a laminar boundary layer. Part 1. Weak disturbances. *J. Fluid Mech.* **220**, 568.

Breuer, K. S. & Landhal, M. T. 1990 The evolution of a localised disturbance in a laminar boundary layer. Part 2. Strong disturbances. *J. Fluid Mech.* **220**, 595.

Breuer, K. S., Denitis, E. G., Gunnarsson, J. & Ullmar, M. 1996 Linear and non-linear evolution of boundary-layer instabilities generated by acoustic receptivity mechanisms. *Phys. Fluids.* **8**, 1415.

Butler, K. M. & Farrell, B. F. 1992 Three-dimensional optimal perturbations in viscous shear flow. *Phys. Fluids.* **4**, 1637.

Butler, K. M. & Farrell, B. F 1993 Optimal perturbations and streak spacing in wall-bounded turbulent shear flow *Phys. Fluids.* **5**, 774.

Carpenter, P.W. 1990 Status of transition delay using compliant walls. *Prog. Astro. Aero.* **123**, 79.

Carpenter, P.W. 1993 Optimization of multiple-panel compliant walls for delay of laminar-turbulent transition. *AIAA J.* **31**, 1187.

CARPENTER, P.W. 1998 Current status of the use of wall compliance for laminar flow control. *Expt. Therm. Fluid Sci.* **16**, 133.

CARPENTER, P.W. & GARRAD, A. D. 1985 The hydrodynamic stability of flow over Kramer-type compliant surfaces. Part I: Tollmien-Schlichting instabilities. *J. Fluid Mech.* **155**, 465.

CARPENTER, P.W. & GARRAD, A. D. 1986 The hydrodynamic stability of flow over Kramer-type compliant surfaces. Part II: Flow-induced surface instabilities. *J. Fluid Mech.* **170**, 199.

CARPENTER, P.W. & MORRIS, P. J. 1990 The effects of anisotropic wall compliance on boundary layer stability and transition. *J. Fluid Mech.* **218**, 171.

CARPENTER, P. W., DAVIES, C.& LUCEY, A. D. 2000 Hydrodynamics & compliant walls. Does the dolphin have a secret? *Current Sci.* **9**, 758.

CARPENTER, P. W., LUCEY, A. D. & DAVIES, C. 2001 Progress on the use of compliant walls for laminar-flow control. *J. Aircraft.* **38**, 504.

CARPENTER, P. W., THOMAS, P. J. & NAGATA, M. 2003 Rotating flows over compliant walls. In *IUTAM Symp. on Flow Past Highly Compliant Boundaries and in Collapsible Tubes* Eds. P.W. Carpenter & T.J. Pedley, pp. 167-187 Kluwer, Dordrecht.

CHEN, C.P., GOLAND, Y. & RESHOTKO, E. 1979 Generation rate of turbulent patches in the laminar boundary- layer of a submersible. *Prog. Astro & Aero.* **72**, 73.

CHOI, H., MOIN, P. & KIM, J. 1994 Active turbulence control for drag reduction in wall-bounded flows. *J. Fluid Mech.* **262**, 75.

CHOI, K-S. 1989 Near-wall structure of turbulent boundary layer with riblets. *J. Fluid Mech.* **208**, 417.

CHOI, K-S 2003 Experimental research on turbulent flow over compliant walls. In *IUTAM Symp. on Flow Past Highly Compliant Boundaries and in Collapsible Tubes* Eds. P.W. Carpenter & T.J. Pedley, pp. 275-292 Kluwer, Dordrecht.

CHOI, K-S., YANG, X., CLAYTON, B. R., GLOVER, E. J., ATLAR, M., SEMENOV, B. N. & KULIK, V. M. 1997 Turbulent drag reduction using compliant surfaces. *Proc. R. Soc. Lond. A.* **453**, 2229.

CHOI, K-S, LE-HUU-NHO, E., CLAYTON, B. R. & ESCUDIER, M. P. 2001 Turbulent boundary-layer structure over a compliant surface. *IUTAM Symp. on Flow In Collapsible Tubes & Past Other Highly Compliant Boundaries* 26-30th March, 2001, University of Warwick, Coventry, U.K., Ed. P.W. Carpenter & T.J. Pedley. *In Abstract Book.*

CHOUDHARI, M. & STREETT, C.L. 1992 A finite Reynolds number approach for the prediction of boundary layer receptivity in localised regions. *Phys. Fluids.* **4**(11), 2495.

CLIFT, R., GRACE, J. R. & WEBER, M. E. 1978 *Bubbles, Drops & Particles.* Academic Press, London.

COLES, D. 1956 The law of the wake in the turbulent boundary layer. *J. Fluid Mech.* **1**, 191.

COLLEY, A.J; THOMAS, P.J; CARPENTER, P.W. & COOPER, A.J. 1999 An experimental study of boundary layer transition over a rotating compliant disc. *Phys. Fluids.* **11**(11), 3340.

COLLEY, A.J; THOMAS, P.J; & CARPENTER, P.W. 2000 Experiments on boundary-layer transition over a rotating compliant disc- New experimental method. *4th EUROMECH Fluid Mechanics Conference*, 19th-23rd November, 2000, Eindhoven, The Netherlands. *In Abstract Book.*

CORKE, T. C., BAR SEVER, A. & MORKOVIN, M. V. 1986 Experiments on transition enhancement by distributed roughness. *Phys. Fluids.* **29**, 3199. CROUCH, J. D. 1992 Non-localised receptivity of boundary-layers. *J. Fluid Mech.* **224**, 567.

CROUCH, J.D. 1994 Distributed excitation of Tollmien-Schlichting waves by vortical free stream disturbances. *Phys. Fluids.* **6**, 217.

CROWE, C. T., SOMMERFELD, M., & TSUJI, Y. 1998 Multiphase flows with droplets and particles. CRC Press, Boca Raton, FL, U.S.

CUI, J., PATEL, V. C. & LIN, C-L. 2003 Prediction of flow over rough surfaces using a force field in large eddy simulation. *Trans. ASME. J. Fluid. Eng.* **125**, 2.

DAVIES, C. 1995 Evolution of Tollmien-Schlichting waves over a compliant panel. PhD Thesis, University of Warwick, Coventry, U.K.

DAVIES, C. & CARPENTER, P. W. 1997 Numerical simulation of Tollmien-Schlichting waves over finite compliant panels. *J. Fluid Mech.* **335**, 361.

DAVIES, C. & CARPENTER, P. W. 2001 A novel velocity-vorticity formulation of the Navier-Stokes equations with applications to boundary layer disturbance evolution. *J. Comp. Phys.* **172**, 119.

DONOHUE, G.L., TIEDERMAN, W.G. & REISCHMAN, R.G. 1972 Flow visualisation of the near-wall region in a drag reducing channel flow. *J. Fluid Mech.* **56**, 559.

DUNCAN, J.H. 1986 The response of an incompressible, viscoelastic coating to pressure fluctuations in a turbulent boundary layer. *J. Fluid Mech.* **171**, 339.

DUNCAN, J.H. & SIRKIS, J.S. 1992 The generation of wave patterns on isotropic coatings by pressure fluctuations in a turbulent boundary layer. *J. Sound Vib.* **157**, 243.

ECKELMAN, L.D., FORTUNA, G. & HANRATTY, T.J. 1972 Drag reduction and the wavelength of flow-orientated wall eddies. *Nature* **236**, 94.

ELFOSSON, P.A., KAWAKAMI, M. & ALFREDSSON, P. H. 1999 Experiments on the stability of streamwise streaks in plane Poiseuille flow. *Phys. Fluids.* **11**, 134.

ENDO, T. & HIMENO, R. 2001a Direct numerical simulation of turbulent flow over a compliant surface. *J. Turb.* **2**, 001.

ENDO, T. & HIMENO, R. 2001b Direct numerical simulation of turbulent flow over a compliant surface. *RIKEN Rev.* **40**, 7.

FALCO, R. E. 1977 Coherent motions in the outer region of turbulent boundary-layers. *Phys. Fluids.* **20**, s124.

FASEL, H. 1976 Investigation of the stability of boundary layers by a finite difference model of the Navier-Stokes equations. *J. Fluid Mech.* **78**, 355.

FASEL, H. 1980 Recent developments in the numerical solution to the Navier-Stokes and hydrodynamic stability problems. In *Computational Fluid Dynamics* pp. 167, Hemisphere, London

FASEL, H. & KONZELMANN, U. 1990 Non-parallel stability of a flat plate boundary layer using the complete Navier-Stokes equations. *J. Fluid Mech.* **221**, 311.

FASEL, H., RIST, U. & KONZELMANN, U. 1990 Numerical investigation of the three-dimensional development in boundary-layer transition. *AIAA J.* **28**, 29.

FASEL, H. 2002 Numerical Investigation of the interaction of the Klebanoff-mode with a Tollmien-Schlichting wave. *J. Fluid Mech.* **450**, 1.

FLORYAN, J. M. 1997 Stability of wall-bounded shear layers in the presence of simulated surface roughness. *J. Fluid Mech.* **335**, 29.

GAD-EL-HAK, M. 1998 Compliant coatings: The simpler alternative. *Expt. Therm. Fluid. Sci.* **16**, 141.

GAD-EL-HAK, M. 2002 Compliant coatings for drag reduction. *Prog. Aero. Sci.* **38**, 77.

GAD-EL-HAK, M., BLACKWELDER, R.F. & RILEY, J.J. 1984 On the interaction of compliant coatings with boundary-layer flows. *J. Fluid Mech* **140**, 257.

GAD-EL-HAK, M. & HUSSAIN, F. 1986 Coherent structures in a turbulent boundary layer. Part 1: generation of 'artificial' bursts. *Phys. Fluids.* **29**, 2124.

GASTER, M. 1965 On the generation of spatially growing waves in a boundary-layer. *J. Fluid Mech.* **22**, 433.

GASTER, M. 1987 Is the dolphin a red herring? *Proceedings of IUTAM Symp. on Turbulence Mangement & Relaminarization, Bangalore, India* Ed. H.W. Liepmann & R. Narashimha, Springer-Verlag, New York, pp. 609-304.

GOLDSTEIN, M.E. 1983 The evolution of acoustic waves into Tollmien-Schlichting waves near the leading edge. *J. Fluid Mech.* **127**, 59.

GOLDSTEIN, M. E., SOCKOL, P. M. & SANZ, J. 1983 The evolution of Tollmien-Schlichting waves near the leading edge. Part II: Numerical determination of amplitudes. *J. Fluid Mech.* **129**, 443.

GOLDSTEIN, M. E. 1985 The scattering of acoustic waves into Tollmien-Schlichting waves by small streamwise variations in surface geometry. *J. Fluid Mech.* **154**, 509.

GOLDSTEIN, M. E. & HULTGREN, L. S. 1989 Boundary-layer receptivity to long-wave freestream disturbances. *Annu. Rev. Fluid Mech.* **21**, 137.

GRAY, J. 1936 Studies in Animal Locomotion: VI. The propulsive powers of the dol-

phin. *J. Expt. Biol.* **13**, 192.

GROSSKREUTZ, R. 1971 Wechselwirkungen zwischen turbulenten Grenzschichten und weichen Wänden. *MPI für Stronrömungsforschung und der AVA*, Göttingen, Germany, Mitt No.53.

GROSSKREUTZ, R. 1975 An attempt to control boundary layer turbulence with non-isotropic compliant walls. *University Science, Journal Dar es Salaam.* **1**, 65.

HALL, G, R. 1967 Interaction of the wake from bluff bodies with an initially laminar boundary-layer. *AIAA J.* **5**, 1386.

HENNINGSON, D. S., LUNDBLADH, A. & JOHANSSON, A. V. 1993 A mechanism for bypass transition from localised disturbances in wall bounded-shear flows. *J. Fluid Mech.* **250**, 169.

JACOBS, R. G. & DURBIN, P. A. 1998 Shear sheltering and the continuous spectrum of the Orr-Sommerfeld equation. *Phys. Fluids.* **10**, 2006.

JACOBS, R.G. & DURBIN, P.A. 2001 Simulations of bypass transition. *J. Fluid Mech.* **428**, 185.

JOSLIN, R. D., MORRIS, J. P., & CARPENTER, P. W. 1991 Role of three-dimensional instabilities in compliant wall boundary-layer transition. *AIAA J.* **29**, 1603.

JOHANSSON, A. V., ALFREDSSON, P. H. & KIM, J. 1991 Evolution and dynamics of shear layer structure in near-wall turbulence. *J. Fluid Mech.* **224**, 579.

KACHANOV, Y.S., KOZLOV, V. V. & LEVCHENKO, V. Y. 1975 Generation and development of small disturbances in laminar boundary-layer under the action of acoustic fields. *Izv. Sib. Otd. Akad. Nauk.* **13**(3), 18.

KACHANOV, Y. S. 1996 Experimental studies of three-dimensional instability of boundary layers. *AIAA Paper*, 96-1978.

KACHANOV, Y. S. 2000 Three-dimensional receptivity of boundary layers. *Eur. J. Mech B-Fluids.* **19**, 723.

KENDALL, J. M. 1981 Laminar boundary layer velocity distortion by surface roughness: Effect upon stability. *AIAA Paper*, 81-0195.

KENDALL, J. M. 1985 Experimental study of disturbances produced in a pre-transitional

laminar boundary layer by weak free stream turbulence. *AIAA Paper*, 85-1695.

KENDALL, J. M. 1991 Studies on laminar boundary-layer receptivity to free stream turbulence near a leading edge. *Trans. ASME J. FED.* **114**, 23.

KENDALL, J. M. 1998 Experiments on boundary-layer receptivity to free stream. *AIAA Paper*, 98-0530.

KERSCHEN, E.J 1989 Boundary-layer receptivity. *AIAA Paper*, 89-1109.

KIM, J. & LIM, J. 2000 A linear process in wall-bounded turbulent shear flows. *Phys. Fluids.* **12**, 1885.

KLEBANOFF, P.S. 1971 Effect of free-stream turbulence on a laminar boundary layer. *Bull. Amer. Phys. Soc.* **10**(11), 1323.

KLEBANOFF, P.S., CLEVELAND, W.G. & TIDSTROM, K.D. 1992 On the evolution of a turbulent boundary-layer induced by a three-dimensional roughness element. *J. Fluid Mech.* **237**, 101.

KLINE, S.J., REYNOLDS, W.C, SCHRAUB, F.A. & RUNDSTADLER, P.W, 1967 The structure of turbulent boundary layer. *J. Fluid Mech.* **30**, 741.

KLOKER, M., KONZELMANN, U. & FASEL, H. 1993 Outflow boundary conditions for spatial Navier-Stokes simulations of transition boundary layers. *AIAA J.* **31**, 620.

KORSORYGIN, V. S. & POLYAKOV, N. F. 1990 Autodestruction of unstable waves in a laminar boundary-layer. *Russian Reprint 11-17, ITPM, Akad. Nauk USSR, Sib. Otd., Novosibirsk.*

KRAMER, M. O. 1957 Boundary-layer stabilization by distributed damping. *J. Aeronau. Sci.* **24**, 459.

KRAMER, M. O. 1960a Boundary-layer stabilization by distributed damping. *J. Aero/Space. Sci.* **27**(1), 69.

KRAMER, M. O. 1960b Boundary-layer stabilization by distributed damping. *J. Am. Soc. Nav. Engrs.* **72**(2), 25.

KRAMER, M. O. 1962 Boundary-layer stabilization by distributed damping. *J. Am. Soc. Nav. Engrs.* **74**(5), 341.

KRAMER, M. O. 1965 Hydrodynamics of the dolphin. *Adv. Hydrosci.* **2**, 111.

KULIK, V.M., POGUDA, I.S & SEMENOV, B.M. 1991 Experimental invetsigation of one-layer viscoelastic coatings action on turbulent friction and wall pressure pulsations. In *Recent developments in turbulence management* Ed. K-S. Choi, pp.263-289. Kluwer, Dordrecht.

LANDHAL, M. T. 1962 On the stability of a laminar incompressible boundary layer over a flexible surface. *J. Fluid Mech.* **13**, 609.

LANDHAL, M. T. 1990 On sublayer streaks. *J. Fluid Mech.* **212**, 593.

LAUCHLE, G. C., PETRIE, H. L. & STINEBERG, D. R. 1995 Laminar flow performance of a heated body in particle-laden water. *Expt. Fluids.* **19**, 305.

LEE, T., FISHER, M. & SCHWARZ, W. H. 1993 Investigation of the stable interaction of a passive compliant surface with a turbulent boundary layer. *J. Fluid Mech.* **257**, 373.

LEEHEY 1980 Influence of environment in laminar boundary layer control. *Viscous Flow Drag Reduction Vol.72, 4* Ed. G. Hough.

LESSEN, M. & GANGWANI, S. T. 1976 Effects of small amplitude wall waviness upon the stability of the laminar boundary layer. *Phys. Fluids.* **19**, 510.

LOCKERBY, D. 2001 Numerical simulation of boundary-layer control using MEMS actuation. PhD Thesis, University of Warwick, Coventry, U.K.

LOTH, E. 2000 Numerical approaches for motion of dispersed particles, droplets and bubbles. *Prog. Engy. Comb Sci.* **26**, 161.

LUCEY, A. D. & CARPENTER, P. W. 1992 A numerical simulation of the interaction of a compliant wall and inviscid flow. *J. Fluid Mech.* **234**, 121.

LUCEY, A. D. & CARPENTER, P. W. 1993a The hydroelastic stability of three-dimensional disturbances of a finite compliant wall. *J. Sound Vib.* **165**, 527.

LUCEY, A. D. & CARPENTER, P. W. 1993b Evolution of disturbances on a fluid-loaded compliant panel with orthotropic properties. In *Extended Abstracts for the First Conference of the ACME*, Ed. N. Bicanic, INME, University College, Swansea, Wales U.K.

LUCEY, A. D. & CARPENTER, P. W. 1995 Boundary layer instability over compliant

walls: Comparison between theory and experiment. *Phys. Fluids.* **7**, 2355.

LUMLEY, J.L. 1973 Drag reduction in turbuloent flow by polymer additives. *J. Polymer Sci. Macromol. Rev.* **7**, 263.

LUO, X.Y. & PEDLEY, T.J. (1995) A numerical simulation of unsteady flow in a 2D collapsible channel. *J. Fluid Mech.* **314**, 191.

MADIGOSKY, W. M., LEE, G. F., HAUN, J., BORKAT, F. & KATAOKA, R. 1986 Acoustic surface-wave measurements on live bottle-nosed dolphins. *J. Acoust. Soc. Amer.* **77**(1), 153.

MEITZ, H. L. 1996 Numerical investigation of suction in a transitional flat-plate boundary layer. PhD Thesis, University of Arizona, U.S.

MEITZ, H. L. & FASEL, H. F. 2000 A compact-difference scheme for the Navier-Stokes equations in velocity-vorticity formulation. *J. Comp. Phys.* **157**, 371.

METCALFE, R.W., BATTISTONI, F., EKEROOT, J. & ORSZAG, S.A. 1991 Evolution of boundary-layer flow over a compliant wall during transition to turbulence. *Proc. Royal Aero. Soc.* 36.1-36.4.

MOCHIZUKI, M. 1961 Smoke observation on boundary-layer transition caused by a spherical roughness element. *J. Phys. Soc. Japan.* **16**, 995.

MORKOVIN, M. V. 1969a On the many faces of transition. In *Viscous Drag Reduction* Ed. C.S. Wells, Plenum Press, New York.

MORKOVIN, M. V. 1969b Critical evaluation of transition from laminar to turbulent shear layer with emphasis on hypersonically travelling bodies. *Airforce Flight Dyn. Lab Rep:AFTDL-TR-68-149.*

MORKOVIN, M. V. 1990 On roughness-induced transition: facts, views and spectulations. In *Instabilty & Transition* Ed. M. Y. Hussaini & R. G. Voigt, vol. 2, pp: 258-267, ICASE/NASA LARC Series, Springer.

MORKOVIN, M. V. & RESHOTKO, E. 1990 Dialogue on progress and issues in stability and transition research. In *Laminar Turbulent Transition* Ed. D. Arnal & R. Michel, Springer, Berlin.

MORSI, S.A. & ALEXANDER, A.J. 1972 An investigation of particle trajectories in

two-phase flow systems. *J. Fluid Mech.* **55**, 193.

NISHIOKA, M. & MORKOVIN, M.V. 1986 Boundary-layer receptivity to unsteady pressure gradients: Experiments & Overview. *J. Fluid Mech.* **171**, 219.

OLDAKER, D.K. & TIEDERMAN, W.G. 1977 Spatial structure of the viscous sublayer in drag-reducing channel flows. *Phys. Fluids.* **20**, s133.

REMPFER, D., PARSONS, L., XU, S. & LUMLEY, J. 2003 Theoretical approaches to the effect of wall compliance on turbulent flow. In *IUTAM Symp. on Flow Past Highly Compliant Boundaries and in Collapsible Tubes* Eds. P.W. Carpenter & T.J. Pedley, pp. 231-252 Kluwer, Dordrecht.

RESHOTKO, E. 1984 Disturbances in a laminar boundary layer due to distributed surface roughness. *Proc. IUTAM Symp: Turbulence & Chaotic Phenomena* Ed. T. Tatsumi, pp. 39-46, Elsevier, Holland.

RESHOTKO, E. & LEVENTHAL, L. 1981 Preliminary experimental study of disturbances in a laminar boundary layer due to distributed surface roughness. *AIAA Paper,* 81-1224.

RIDGWAY, S.H. & CARDER, D.A. 1993 Features of dolphin skin with potential hydrodynamic importance. *IEEE Eng in. Med. Biol.* **12**, 83.

RILEY, J.J, GAD-EL-HAK, M. & METCALFE, R. W. 1988 Compliant coatings. *Annu. Rev. Fluid Mech.* **20**, 393.

RUBEN, A. I. 1985 On the generation of Tollmien-Schlichting waves by sound. *Fluid Dyn.* **19**, 709.

SAIKI, E.M. & BIRINGEN, S. 1997 Spatial numerical simulation of boundary-layer transition: Effects of a spherical particle. *J. Fluid Mech.* **345**, 133.

SARIC, W.S., HOOS, J.A. & RADEZTSKY, R.H. 1991 Boundary-layer receptivity of sound with roughness. Boundary layer stability and transition to turbulence. *Trans. ASME J. Fluid Eng.* **114**, 17.

SARIC, W.S., REED, H.L. & KERSCHEN, E.J. 2002 Boundary-layer receptivity to freestream disturbances. *Annu. Rev. Fluid Mech.* **34**, 291.

SCHLICHTING, H. 1979 *Boundary-Layer Theory.* 7th Ed. McGraw-Hill, New York.

SCHLICHTING, H. & GERSTEN, K. 2000 *Boundary-Layer Theory.* 8th Revised and Enlarged Edition. Springer-Verlag, Berlin.

SCHUBAUER, G. B. & SKRAMSTAD, H. K. 1943 Laminar boundary layer oscillations and stability of laminar flow. *NBS Res. Paper 1772* Washington D.C.

SEN, P. K. & ARORA, D. S. 1988 On the stability of laminar boundary-layer flow over a flat-plate with a compliant surface. *J. Fluid Mech.* **197**, 201.

SHAPIRO, P. J. 1977 The influence of sound upon laminar boundary layer instability. *MIT Acoust. Vib. Lab. Rep. 83458-83560-1*, Mass. Inst. Tech. U.S.

SHIROLKAR, J. S., COIMBRA, C. F. M., & QUIREZ MCQUAY, M. 1996 Fundamental aspects of modelling turbulent particle dispersion in dilute flows. *Prog. Engy Comb Sci.* **22**, 363.

SINGH, K. & LUMLEY, J. L. 1971 Effects of roughness on the velocity in a laminar boundary layer. *Appl. Sci. Res.* **24**, 168.

SPALDING, D. B. 1961 A single formula for the 'Law of the Wall'. *ASME J. Appl. Mech.* **28**, 455.

SURESHKUMAR, R., BERIS, A.N. & HANDLER, R. A. 1997 Direct numerical simulation of the turbulent channel flow of a polymer solution. *Phys. Fluids.* **9**, 743.

TADJFAR, M., RESHOTKO, E., DYBBS, A. & EDWARDS, R. V. 1985 Velocity measurements within boundary layer roughness using index matching. *Intl. Symp. on Laser Anemometry, ASME FED:33, 59* Ed. A. Dybbs & P.A. Pfund.

TAMILARASAN, M. & CHOI, K-S. 2001 Drag reduction in turbulent pipe flows using compliant coating. *IUTAM Symp. on Flow In Collapsible Tubes & Past Other Highly Compliant Boundaries* 26-30th March, 2001, University of Warwick, Coventry, U.K., Ed. P.W. Carpenter & T.J. Pedley. *In Abstract Book.*

TIEDERMAN, W.G., LUCHIK, T.S. & BOGARD, D.G. 1985 Wall layer structure and drag reduction. *J. Fluid Mech.* **156**, 419.

VINCENT, D. C. & PETRIE, H. L. 1993 Transition induced by a spherical particle in a laminar boundary-layer. *AIAA Paper,* 93-2902.

WESTIN, K. J. A., BOIKO, A. V., KLINGMANN, B. G. B., KOZLOV, V. V. &

ALFREDSSON, P. H. 1994 Experiments in a boundary-layer subject to free stream turbulence. Part I: Boundary-layer structure and receptivity. *J. Fluid Mech.* **281**, 193.

WIPLIER, O. & EHRENSTEIN, U. 2000 Numerical simulation of linear & nonlinear disturbance evolution in a boundary layer with compliant walls. *J. Fluids Struct.* **14**, 157.

WU, X., LEIB, S. J. & GOLDSTEIN, M. E. 1997 On the nonlinear evolution of a pair of oblique Tollmien-Schlichting waves in boundary layers. *J. Fluid Mech.* **340**, 361.

YEO, K.S. 1986 The stability of flows over flexible surfaces. PhD Thesis, University of Cambridge, U.K.

YEO, K.S. 1990 The hydrodynamic stability of boundary layer flow over a class of anisotropic compliant walls. *J. Fluid Mech.* **220**, 125.

YEO, K.S. 1992 The three dimensional stability of boundary-layer flow over compliant walls. *J. Fluid Mech.* **238**, 537.

YEO, K. S., ZHAO, H.Z. & KHOO, B. C. 2001 Turbulent boundary layer over a compliant surface: absolute and convective instabilities. *J. Fluid Mech.* **449**, 141.

ZHIGULEV, V.N. & FEDEROV, A. V. 1987 Boundary-layer receptivity to acoustic disturbances. *J. Appl. Mech. Tech. Phys.* **28**, 1.

ZHOU, M. D., LIU, D. P. & BLACKWELDER, R. F. 1994 An experimental study of receptivity of acoustic waves in laminar boundary-layers. *Expt. in Fluids* **17**, 1.

ZOUESHTIAGH, F., ALI, R., COLLEY, A. J., THOMAS, P. J. & CARPENTER, P. W. 2003 Laminar-Turbulent Boundary-Layer Transition over a Rough Rotating Disc. *Accepted for publication in Phys. Fluids.*